AD-A274 136

INCORPORATION OF CARRIER PHASE
GLOBAL POSITIONING SYSTEM MEASUREMENTS
INTO THE NAVIGATION REFERENCE SYSTEM
FOR IMPROVED PERFORMANCE

THESIS

Neil P. Hansen, B.Sc. Electrical Engineering
Captain, Canadian Forces (Air)

AFIT/GE/ENG/93D-40

93-31063

93 12 22 176

Best Available Copy

INCORPORATION OF CARRIER PHASE

GLOBAL POSITIONING SYSTEM MEASUREMENTS

INTO THE NAVIGATION REFERENCE SYSTEM

FOR IMPROVED PERFORMANCE

THESIS

Presented to the Faculty of the Graduate School of Engineering

of the Air Force Institute of Technology

Air University

In Partial Fulfillment of the

Requirements for the Degree of

Master of Science in Electrical Engineering

Neil P. Hansen, B.Sc. Electrical Engineering

Captain, Canadian Forces (Air)

December 1993

Accesion For	
NTIS CRA&I	☑
DTIC TAB	☐
Unannounced	☐
Justification_____	
By_____	
Distribution /	
Availability Codes	
Dist	Avail and / or Special
A-1	

Preface

This thesis is the first of what may be a series of carrier-phase GPS related theses and the fifth in a series of theses devoted to modeling and improving the Completely Integrated Reference Instrumentation System (CIRIS) and the Navigation Reference System (NRS) used by the Central Inertial Guidance Test Facility (CIGTF), Hollomon AFB, New Mexico in order to validate the accuracy of inertial navigation systems (INS's). The theory and results contained in this research is not limited to this one application, however. The theory, material, and results can be applied to any area of research involving the integration of INS's with GPS, Differential GPS, Carrier-Phase GPS, and even ground transponder systems using an Extended Kalman Filter. As GPS is one of the most reliable, accurate, and cost effective navigation aids available to both the public and the miliary, I hope the results of this research can provide a contribution to the world of aerospace navigation.

Of course, this thesis would not have been possible without the help of a few key individuals. First of all is my thesis committee members Dr. Peter Maybeck, Capt Ron Delap, and especially my thesis advisor LCol Bob Riggins. Their astute comments and guidance help me understand the complexities of inertial navation systems, the Global Positioning System, and integration using a Kalman Filter. Their efforts certainly kept me on track and on time.

My thesis track predecessors, Captains Negast, Solomon, Snodgrass, and Stacey, deserve a pat on the back for their ground breaking work on the CIRIS and NRS models. Without these models, I could not have completed one tenth of the work I did!

The folks out a Hollomon AFB, including Mr. Scott Dance and LCol Dicker, must be recognized for their assistance in building the carrier-phase GPS model and for allowing me to continue my research for them out at Hollomon for the six months following graduation. That makes one more Canadian winter I don't have to endure!

ii

It would not be fair to not mention my classmates in the Guidance and Control track, Capt Dave Lane, Capt Pat Grondin, Capt Jim Fitch, Capt Greg Schiller, Capt Bob Nielsen, Capt Vince Reyna, Lt Kevin Boyum, Lt Mike Logan, Lt Mark Keating, 2Lt Chip Mosle, and 2Lt Odell Reynolds. These people helped me navigate through the unending complexities of the controls classes and understand the subtleties of UNIX and Matlab. Without them, I could not have even made it to the thesis.

I would also like to thank the members of the Wright-Patterson base ice hockey team for letting me play on the team and putting up with my less than "Canadian" hockey skills. These games and practices provided a well needed outlet from the AFIT workload.

And finally a special thanks goes to Mr. Don Smith who kept the Navigation Lab computers running in spite of the antics of the computer-illiterate students, of which I am one, who were using them. Every time there was a problem, which was much of the time, Don was there to fix it for us. Thanks Don for your efforts and patience over the last year.

Table of Contents

Page

List of Figures

List of Tables

List of Plots

Abstract

In order to quantify the performance and accuracy of existing navigation systems, the U.S. Air Force has been using the Completely Integrated Reference Instrumentation System (CIRIS) as a baseline. CIRIS combines the information from an inertial navigation unit, a barometric altimeter, and a range and range-rate system of ground transponders to obtain a highly accurate navigation solution. The accuracy of CIRIS, however, will soon be inadequate as a reference standard against which modern and future navigation systems can be compared to. This research explores the possibilities of enhancing CIRIS by adding measurements obtained from the Global Position System (GPS). Pure pseudorange measurement updates to the CIRIS Extended Kalman Filter form the basis of the Navigation Reference System (NRS). Applying differential corrections to the pseudorange measurements forms the basis of the Enhanced Navigation Reference System (ENRS). Though these filters are explored in this research, the bulk of the material is dedicated to the addition of Carrier-Phase GPS measurements to the existing ENRS to form the Precision Navigation Reference System (PNRS). Analysis of these three systems is performed using a Kalman filter development software package known as Multimode Simulation for Optimal Filter Evaluation (MSOFE). The performance of the three filters are compared as well as the PNRS's performance when subjected to large and small cycle slips. Results of the simulations indicate that the PNRS can provide an improved navigation solution over CIRIS, the NRS, and the ENRS. Results of the cycle slip simulations indicate that the PNRS filter is stable for large cycle slips and small cycle slips are negligible in the computation of the navigation solution.

INCORPORATION OF CARRIER PHASE GLOBAL POSITIONING SYSTEM MEASUREMENTS INTO THE NAVIGATION REFERENCE SYSTEM FOR IMPROVED PERFORMANCE

I. Introduction

Currently the Central Inertial Guidance Test Facility (CIGTF), 46th Test Group, located at Holloman Air Force Base in New Mexico, provides the United States Air Force with the ability to develop and test new and existing inertial navigation systems. In order to provide a reliable benchmark to which the systems under test are compared, CIGTF employs the use of the Navigation Reference System (NRS). The NRS uses the Range/Range-rate System (RRS) and the Global Positioning System (GPS) as measurement updates to an Extended Kalman Filter (EKF) modelling the error dynamics of a Litton LN-93 Inertial Navigation System (INS) as well as the error dynamics of the RRS and GPS. The EKF state estimates provide a navigation solution correction for the LN-93 INS. By using such a configuration, which is commonly known as a feedforward configuration, the NRS currently can achieve one or more orders of magnitude better accuracy than the system under test. The NRS configuration, as used by CIGTF, is depicted in Figure 1-1.

The operation of the NRS involves flight testing the system under test in conjunction with the NRS. The systems are flown through the flight profile of interest over the RRS transponder range and the output navigation solutions of both are recorded on a data storage medium for post flight evaluation. The NRS records its raw data only and does not provide on-line real-time Kalman filter solutions. The data is then processed post-flight to form the NRS EKF solution which can then be compared to the system under test.

1.1 Background

The NRS has remained an adequate benchmark for current inertial navigation system testing due to the incorporation of GPS and RRS measurements through the EKF. However,
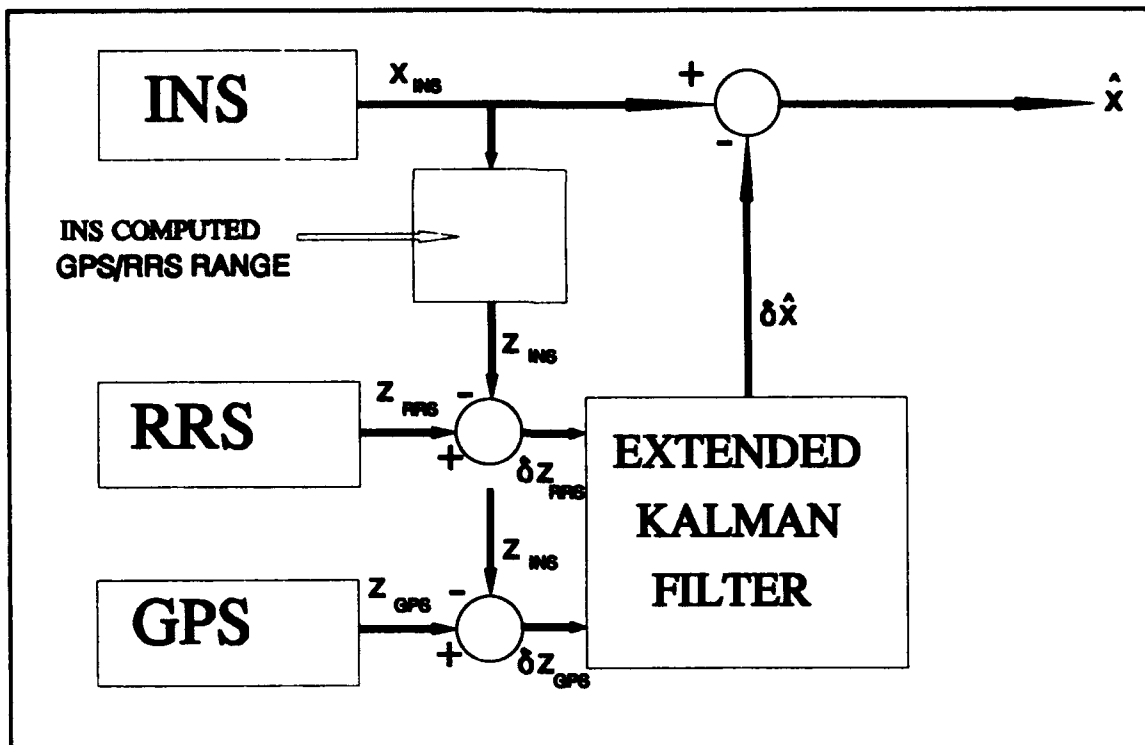
Figure 1-1 NRS Configuration.

today's inertial navigation systems are approaching the accuracy levels of the NRS. Many companies are now developing embedded INS/GPS systems which can have accuracies that far exceed previous standard levels. For the NRS to remain an adequate benchmark, it should be able to provide at least one order of magnitude better accuracy than the system under test; to achieve this goal, the NRS systems and algorithms must be enhanced.

One method of accuracy enhancement is to improve the quality of the measurement updates to the EKF. This quality is measured by the strength of the measurement noise as well as how well this measurement can be computed using linear combinations of EKF states. Research into the accuracy of GPS measurements and the GPS error state models is an ever growing field. New technologies and new algorithms are being studied that improve the GPS measurement accuracies by significant amounts. By making use of some of these new technologies, the accuracy of the NRS may be improved.

1-2

In 1991, William Negast, who was a student at the Air Force Institute of Technology (AFIT), designed and simulated a scheme to incorporate Differential GPS (DGPS) measurements into the NRS as his Masters thesis (1). This system, currently being tested in full by CIGTF, is known as the Enhanced Navigation Reference System (ENRS).

There exists another technique of GPS measurement enhancement. This technique exploits Carrier Phase GPS (CPGPS). CPGPS forms its range measurement, not from the GPS satellite data, but from measurements of the phase shift of the GPS code carrier wave. CPGPS promises extremely high accuracies and is now under consideration by CIGTF to be the next generation of reference system.

1.2 Problem Definition

By using Carrier Phase GPS measurement updates to the EKF, which are corrected by using the differential GPS techniques of the ENRS (see Chapter III), it should be possible to enhance the accuracy of the navigation solution of the NRS. This thesis specifically focuses on the development and testing of a post-processing EKF of 70 or fewer states to augment the ENRS navigation solution with Carrier Phase GPS phase-range measurements. This NRS configuration will be known as the Precision Navigation Reference System (PNRS). This thesis will also explore the phenomenon of carrier phase cycle slip (see later in this chapter and in Chapter IV for an explanation of cycle slip). Note that an EKF is developed instead of an optimal smoothing algorithm, due to the limited computer storage capacity available to CIGTF. A smoothing algorithm requires a forward pass and a backwards pass through the data in order to compute the optimal state estimates. While this technique may produce better results, it requires much more time and computer memory to execute. The EKF developed for this system is limited to 70 or fewer states in order to ensure a maximum 24 hour post-processing turn around time. These limitations are required by CIGTF.

1.3 Summary of Previous Research

Much work has been put into the development of simulation models for the NRS and its predecessor, the Completely Integrated Reference Instrumentation System (CIRIS), for AFIT and CIGTF research. The culmination of work completed by past AFIT masters degree students Joe Solomon (2), Britt Snodgrass (3), Richard Stacey (4), and William Negast (1) (as their Masters theses) has resulted in a working NRS simulation programmed into the Multimode Simulation for Optimal Filter Evaluation (MSOFE) software tool (5).

William Negast (1) also completed the initial studies of incorporating DGPS measurements into the NRS. His results indicated that DGPS could provide a marked improvement over the current reference system and would provide a satisfactory reference system for testing current aircraft inertial navigation systems.

It is known that the CPGPS technique can be used to compute user position and velocity information by measuring the phase shift of satellite carrier waves (6: section 4.15). Since the phase of a signal can be measured accurately to about 1%, and since the wavelength of one cycle of the L-band GPS carrier wave is about 20 cm, it is theoretically possible to measure the position of a CPGPS receiver to millimeter accuracy (7) assuming all other error sources are negligible. This can be compared to 1 to 2 meter accuracy for conventional code-phase GPS receivers using differential corrections.

The carrier phase measurement equation has been derived in several different sources (6: section 8.2 and 8.3; 8; 9). The phase of a reference wave generated inside the GPS receiver is beat (subtracted) from the satellite transmitted carrier wave. The result is a measure of the phase shift the transmitted signal experienced in transit from the satellite to the receiver. Given knowledge of the number of integer cycles between the satellite and receiver, the fractional phase shift, and the frequency of transmission, the receiver can compute the range between the satellite and itself. This computed range, or phase-range, can then be used to

calculate the receiver's position in three dimensions in the same manner as conventional code-phase GPS measurements.

Research has also been performed in the area of single, double, and triple difference techniques for Carrier Phase GPS measurements (6: sections 8.4 through 8.10; 8; 9). The between-satellite single difference results in the cancellation of the user clock bias term. The between-receivers single difference results in the cancellation of the satellite clock error term and will also significantly reduce the effects of the atmospheric delay error terms. This is the same technique used with conventional differential code-phase GPS. The between-time epoch single difference results in the cancellation of the phase ambiguity term (see Chapter IV for a description of phase ambiguity) as well as significantly reducing the effects of the atmospheric delay error terms. The between-receiver/satellite double difference cancels out both the common satellite clock error and receiver clock error terms. The between-receiver/time epoch double difference cancels out both the common satellite clock error term and the phase ambiguity term. The between-satellite/time epoch double difference cancels out both the common user clock error term and the phase ambiguity term. Triple differencing causes not only both the user clock and satellite clock error terms to drop out, but the phase ambiguity term to drop out as well. For a more in-depth explanation of the differencing techniques, see Chapter IV, Section 4.4.

Carrier Phase GPS has been successfully used in the areas of static surveying (10) and low dynamic positioning (11). The results of these tests show promise for this form of position measurement. Some problems encountered that need to be addressed are bandwidth and cycle slip. The receiver bandwidth must be such that the receiver does not lose lock on the carrier wave even during dynamic maneuvers. The more dynamic the maneuvers, the wider the bandwidth must be, but this also causes a decrease in the signal-to-noise ratio of the carrier wave (and if the signal-to-noise ratio becomes too low, the receiver can lose lock).

Loss of lock can cause a phenomenon known as *cycle slip*. When the satellite carrier signal is reacquired following a loss of lock by the carrier phase receiver, several integer cycles may have been missed or a jump in the true number of integer cycles may occur. This is known as cycle slip. Cycle slips will cause the range measurement equation to be biased by the range equivalent of the number of integer cycles "slipped". Chapter IV Section 4.5 presents a more in-depth discussion of cycle slip.

1.4 Assumptions

The full order NRS model developed for MSOFE by Solomon, Snodgrass, Stacey, and Negast (hereafter to be called simply the Negast model) will be assumed to be an accurate enough representation of the real NRS performance to be deemed the system truth model for simulation purposes. It has been documented by Stacey (4) that the Litton barometric altimeter model (part of the LN-93 model) did not perform as the true representation of the real barometric altimeter. Stacey attempted to correct this problem by using a higher order barometric altimeter model. This new model, however, also did not perform as a true representation, and Negast reverted back to the original single state model. It will be assumed for this thesis that this single state model is an adequate representation of the real barometric altimeter. It should be noted, however, that Litton is currently working on a new and better model.

It is not known at this time which differencing method, if any, CIGTF will wish to use to incorporate the CPGPS measurements into their reference system. After some discussion with CIGTF personnel (12), it was decided to construct the PNRS model utilizing the ENRS model (which incorporates differential corrections to the NRS) as a base. This technique is similar to the between-receivers single difference. If other differencing techniques are required later, they can be easily incorporated into the models developed in this research and theoretically should produce a more accurate solution.

1-6

CPGPS measurement updates computed by MSOFE in the PNRS simulation studies will be of the form of differentially corrected phase-range. The simulation studies will also include differentially corrected code-phase GPS measurement updates. This requires that the simulation assume that a carrier phase receiver is available that provides these quantities as its output and that an accurate ground based differential receiver is available. These measurement updates are computed within MSOFE using operator-programmable noise variance levels; therefore, an actual receiver or receiver data are not required for the simulation studies.

1.5 Thesis Objectives and Methodology

The MSOFE software tool is completely self-contained. No external data is required to perform a complete simulation study of the proposed models. A two-hour fighter flight profile, complete with all measured and computed navigation data, is simulated using a computer program called PROFGEN and stored in a file that can be read in by the MSOFE software routine. The data in this file serves as the true navigation solution. A full order truth model, computed inside MSOFE, calculates the true error states of the LN-93 INS and adds them along with some user-defined white noise terms (such as one might find in any real world system) to the true navigation data. This results in a simulation of the actual LN-93 INS outputs. MSOFE also computes the true RRS and GPS (and/or DGPS and/or CPGPS) measurements plus additive user-defined white measurement noise to simulate the actual RRS and GPS measurements. Using the EKF model, MSOFE computes the filter-predicted errors of the INS, RRS, and GPS, and subtracts the INS predicted errors from the simulated actual INS data to produce the optimal estimate of the navigation solution. This MSOFE configuration is depicted in Figure 1-2. Note the similarities and differences between this figure and Figure 1-1, the actual NRS configuration. GPS satellite data is simulated inside MSOFE and this simulation is depicted in Figure 1-2 as the "Orbit Data" block.
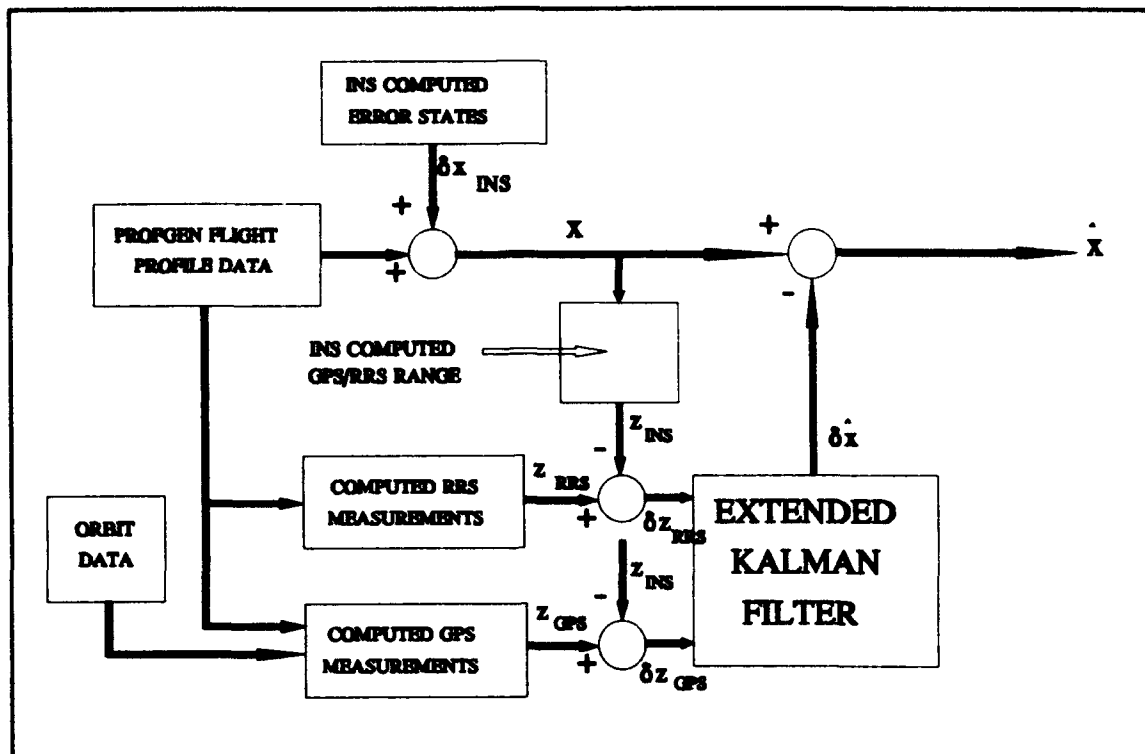
Figure 1-2 MSOFE NRS Simulation Configuration.

This thesis research will commence by rebuilding and tuning the Negast NRS truth and filter simulation models inside the MSOFE software tool on AFIT's Sun Sparc 2 computer systems. It should be noted that Negast and his predecessors utilized the MSOFE software tool on AFIT's VAX computer system. The VAX is no longer being supported by AFIT, and therefore the models must all be transferred over to the Sun Sparc 2's. Once transferred, these models must be verified by comparing them to Negast's results (1) and data from the Avionics Section of the Wright Laboratories, Wright Patterson Air Force Base, Dayton, Ohio. The finalized version of the Negast NRS truth and filter simulation software model will serve as the model of the current NRS and a benchmark for comparing further research as well. Development of the NRS truth and filter model is presented in Chapter III, Section 3.5.

This NRS model will then be modified to incorporate differential GPS corrections. The result will be similar to Negast's ENRS truth and filter models. These simulation models will

then be tuned and the results compared to the NRS results. Development of the ENRS truth and filter models is presented in Chapter III, Section 3.6.

Carrier Phase GPS measurements will then be incorporated into the ENRS model to form the PNRS model. Simulation studies of this configuration will then be performed. The strengths of the driving noise terms for the EKF truth model and the covariances of the true measurement noise terms must be determined for the carrier phase additions. The other driving and measurement noise terms will remain the same as in the Negast final ENRS model. This model will then be tuned using the standard Kalman filter tuning techniques, which are outlined in Chapter II of this thesis. Once this PNRS model has been tuned, its results will be compared to the NRS filter model results, and the amount of improvement (or degradation) in performance and accuracy will be determined. It is also of interest to compare the PNRS results to the ENRS results. The development of the PNRS truth and filter models is presented in Chapter IV, Section 4.1.

Following verification of the models, research into detection and correction of the cycle slip phenomenon will commence. A methodology to simulate cycle slips within the MSOFE truth model will be developed, and the PNRS model will then be subjected to simulated cycle slips. The results of these simulations will show the filter's ability to recover from cycle slips and will determine the form for the detection and correction algorithm, if one is required. Development of the cycle slip simulation is presented in Chapter IV, Section 4.5.

1.6 Conclusion

This thesis is divided into six chapters. Chapter I has overviewed the goals and methodology of this research. Chapter II gives the reader an overview of the extended Kalman filter (EKF) derivation as well as tuning and model reduction techniques. Chapter III presents the NRS and the ENRS truth, filter, and measurement models. Chapter IV presents the PNRS truth, filter, and measurement models, as well as provide more detail on carrier phase

GPS measurements, differencing techniques, and cycle slips. Chapter V presents the results of the simulation studies and Chapter VI provides conclusions and recommendations.

The PNRS is expected to show an improvement in accuracy over the NRS and the ENRS. The objective of this research is to explore the possibility of enhanced performance of the NRS by incorporating CPGPS measurements into the ENRS. This thesis will no doubt be only the first in a series of carrier phase GPS related theses.

II. Extended Kalman Filtering

2.1 Overview.

This chapter is meant as an overview or review of the Extended Kalman Filter (EKF) dynamics, measurement, propagation, and update equations. A brief discussion on filter reduction and tuning is also presented. For those readers who are not familiar with the Kalman filter, it is suggested to review Dr. Peter Maybeck's textbooks (13, 14, 15) on stochastic control in which robust derivations of the EKF equations and discussions of state reduction and filter tuning are presented.

2.2 The Extended Kalman Filter Equations.

The error state model of the NRS is a set of non linear state-space differential equations. Due to this non linearity, a linear Kalman filter cannot be used. Instead, the Extended Kalman Filter, which allows relinearization about the optimal state estimate at each measurement update time, will be implemented for this thesis research. Many of the following equations were taken from (14).

To begin the derivation of the EKF, it must be assumed that the dynamics of the system in question can be described as a set of non linear continuous-time differential equations of the form:

$$\dot{x}(t) = f[x(t),t] + G(t)w(t) \tag{2-1}$$

The state dynamics matrix $f[x(t),t]$ is, in general, a non linear function of the state vector $x(t)$ and time t. The noise distribution matrix $G(t)$ is set equal to the identity matrix I and the white Gaussian noise $w(t)$ is defined with mean:

$$m_w = E[w(t)] = 0 \tag{2-2}$$

2-1

and noise strength $Q(t)$:

$$E[w(t)w^T(t+\tau)] = Q(t)\delta(\tau) \tag{2-3}$$

It is also assumed that a discrete-time measurement update is available at each sample time t_i and is of the form:

$$z(t_i) = h[x(t_i), t_i] + v(t_i) \tag{2-4}$$

Where $z(t_i)$ represents the measurement update, $h[x(t_i), t_i]$ is a non linear function of the state vector x and time t_i, and the discrete-time Gaussian white noise vector $v(t_i)$ is defined as zero-mean with covariance:

$$E[v(t_i)v(t_j)^T] = \begin{cases} R(t_i) & \text{for } t_i = t_j \\ 0 & \text{for } t_i \neq t_j \end{cases} \tag{2-5}$$

In order for the Kalman filter to produce an "optimal" state estimate, these non linear equations (Eq. (2-1) and Eq. (2-4)) must be linearized. The method described in (13) will be used to linearize these equations. The following is an overview of this linearization technique.

A nominal state trajectory, $x_n(t)$ is defined to satisfy:

$$\dot{x}_n(t) = f[x_n(t), t] \tag{2-6}$$

starting with the initial condition of $x_n(t_o)=x_{no}$; where the matrix $f[x_n(t), t]$ is specified in Equation (2-1). The nominal measurement updates are defined as:

$$z_n(t_i) = h[x_n(t_i), t_i] \tag{2-7}$$

where $z_n(t_i)$ is the nominal measurement update at time t_i and the matrix $h[x_n(t_i), t_i]$ is specified in Equation (2-4). The "perturbation" of the actual state from this nominal state trajectory is defined by subtracting (2-6) from (2-1):

$$[\dot{x}(t) - \dot{x}_n(t)] = f[x(t), t] - f[x_n(t), t] + G(t)w(t) \tag{2-8}$$

We can now define the left hand side of (2-8) as the perturbation state $\delta \dot{x}(t)$ and approximate the right hand side to first order using a Taylor series expansion of the form:

$$f(x) = f(x_n) + \frac{\partial f(x)}{\partial x}\bigg|_{x=x_n} \cdot \delta x + H.O.T. \qquad (2\text{-}9)$$

Equation (2.8) then becomes:

$$\delta \dot{x}(t) = F[t;x_n(t)] \cdot \delta x(t) + G(t)w(t) \qquad (2\text{-}10)$$

Where the matrix $F[t;x_n(t)]$ is defined as:

$$F[t;x_n(t)] = \frac{\partial f[x(t),t]}{\partial x}\bigg|_{x(t)=x_n(t)} \qquad (2\text{-}11)$$

The perturbed discrete-time measurement update equation is derived is a similar fashion and is expressed as:

$$\delta z(t_i) = H[t_i;x_n(t_i)] + v(t_i) \qquad (2\text{-}12)$$

Where the matrix $H[t_i;x_n(t_i)]$ is defined as:

$$H[t_i;x_n(t_i)] = \frac{\partial h[x(t_i),t_i]}{\partial x}\bigg|_{x(t)=x_n(t)} \qquad (2\text{-}13)$$

The non linear continuous-time dynamics and measurement equations have now been converted to "perturbation" or "error" state equations. An estimate of the total state of interest can be computed using:

$$\hat{x}(t) = x_n(t) + \delta \hat{x}(t) \qquad (2\text{-}14)$$

The above expressions can now be used in a linearized Kalman filter. However if the "true" state values deviate a significant amount from the nominal trajectory, large unacceptable errors can result. For this reason the EKF is used in applications where perturbation techniques alone cannot suffice. The EKF allows relinearization of the state

dynamics vector **f** along with the newly declared nominal trajectory, and measurement vector **h** about the newly declared optimal state estimate $\hat{x}(t_i^+)$ at each measurement update time t_i. This relinearization process allows for improved robustness and performance of the Kalman filter.

The state estimate and covariance equations are propagated from time t_i to time t_{i+1} by integrating the following equations:

$$\dot{\hat{x}}(t/t_i) = f[\hat{x}(t/t_i),t] \tag{2-15}$$

$$\dot{P}(t/t_i) = F[t;\hat{x}(t/t_i)]P(t/t_i) \\ + P(t/t_i)F^T[t;\hat{x}(t/t_i)] + G(t)Q(t)G^T(t) \tag{2-16}$$

where:

$$F[t;\hat{x}(t/t_i)] = \left.\frac{\partial f[x(t),t]}{\partial x}\right|_{x(t)=\hat{x}(t/t_i)} \tag{2-17}$$

and starting from the initial conditions:

$$\hat{x}(t_i/t_i) = \hat{x}(t_i^+) \tag{2-18}$$

$$P(t_i/t_i) = P(t_i^+) \tag{2-19}$$

where $\hat{x}(t_i^+)$ and $P(t_i^+)$ are the results of the previous measurement update cycle. Discrete-time measurements are incorporated into the EKF by the following equations:

$$K(t_i) = P(t_i^-)H^T[(t_i);\hat{x}(t_i^-)] \cdot \\ \{H[(t_i);\hat{x}(t_i^-)]P(t_i^-)H^T[(t_i);\hat{x}(t_i^-)] + R(t_i)\}^{-1} \tag{2-20}$$

$$\hat{x}(t_i^+) = \hat{x}(t_i^-) + K(t_i)\{z_i - h[\hat{x}(t_i^-);t_i]\} \tag{2-21}$$

$$P(t_i^+) = P(t_i^-) - K(t_i)H[t_i; \hat{x}(t_i^-)]P(t_i^-) \qquad (2\text{-}22)$$

where:

$$H[t_i; \hat{x}(t_i^-)] = \left. \frac{\partial h[x(t_i), t_i]}{\partial x} \right|_{x(t_i) = \hat{x}(t_i^-)} \qquad (2\text{-}23)$$

and the notation (t/t_i) denotes "at time t based on measurements through time t_i".

These EKF equations are programmed into the MSOFE software tool (5) for optimal error state estimation. Note that the MSOFE tool uses the U-D factored form of the EKF propagation and update equations for improved numeric stability. For more information on the U-D Factored form, see (13).

2.3 Kalman Filter Order Reduction.

Filter order reduction is the process by which a number of states of a Kalman filter are eliminated or absorbed into other (presumably more dominant) states. Order reduction causes the filter to be sub-optimal as compared to the filter based upon the truth model or full order model, however is necessary in many cases due to limited computational speed or computer memory. An example of this would be running a Kalman filter real-time in a small aircraft navigation computer, which would be considerably more difficult than real-time in, say, an AFIT Sun workstation. The aircraft navigation computer may have less memory, slower computation speed, and other priorities to which it must attend. For this thesis research, a post-processing technique will be used (that is the Kalman filter does not have to run real-time). However, CIGTF requires that the filter order be 70 states or less, to allow for a maximum 24 hour processing time. This is based on usage of a Hewlett-Packard minicomputer running a 10-run Monte Carlo analysis of a 2-hour aircraft flight profile.

Proper selection of the states to be eliminated (or possibly simplified) is critical. It is necessary to retain (or minimize the effects on) computed position and velocity estimates when selecting possible candidates for order reduction. The next few paragraphs offer some general recommendations for filter order reduction and how these recommendations pertain to this thesis research.

In the NRS INS error dynamics model, there are 10 states that cannot be eliminated. They are 3 position states, 3 velocity states, 3 attitude states, and the barometric altimeter state. These 10 states are of prime interest in aircraft navigation filters as they contain the information required by the aircrew for navigation. The LN-93 INS error model (16) uses these 10 states plus 83 more. These remaining 83 states are not of primary interest, but they contribute to the accuracy of the first 10. These 83 can then be considered for order reduction.

Often a literature search can turn up documents to assist the design engineer in his (or her) selection of states. A previous investigation into the LN-93 model order reduction was done by Lewantowicz and Keen and documented in (17). This paper presents four different reduced order models for the LN-93, ranging from 41 states down to 17 states. All four performed reasonably well; however, it should be noted that it is the design engineer's choice to determine how reasonable the reduced-order model really is. The previously defined "Negast" model, as used by Negast (1), his 3 predecessors (2, 3, 4), and Juan Vasquez (18), used the results of this paper for filter order reduction. For consistency, the results of this paper will also be used to form the basis of the truth and reduced-order filter model for this thesis research.

At this point it should be noted that the NRS MSOFE model, as used by Negast and Vasquez, has been transferred to AFIT's Sun workstations (as opposed to AFIT's VAX computer) by the Wright Labs Avionics section, William Mosle (AFIT, GE-93D), and this author. Much of the work of this thesis research and that of Mosle (19) will be to reverify the

filter order reductions previously defined by Negast and used by Vasquez. This verification will be performed using the MSOFE software tool and good engineering insight.

A tool as powerful as MSOFE can be used to assist the design engineer in the selection of states that can be eliminated, simplified, or absorbed into others. MSOFE can also be used in other ways. It is known that even a well-tuned full order filter may not adequately track the truth model state dynamics. This inadequacy of the filter model is generally attributed to the observability (or lack of observability) of some states. Maybeck (13) states that unobservable states should not be used in the filter dynamics model. The filter's estimate of these states generally never follow the true (truth) value, even though the filter's covariance values might indicate a properly tuned filter. Using MSOFE gives the design engineer the opportunity to assess the performance of the filter accurately under a wide range of conditions, using either Monte Carlo or covariance analysis techniques. Though Maybeck recommends the use of the covariance analysis technique for linear or linearized Kalman filters, this technique is not useful for the EKF implementation and not practical on large order filters (due to the time required to run a covariance analysis on a large order filter). The Monte Carlo analysis technique can provide good results more quickly and can be used as a benchmark for further analysis. Often designers use Monte Carlo techniques to produce adequate results and then further refine the filter's performance using covariance analysis. Due to the use of the EKF and time constraints on this research, only the Monte Carlo technique will be used to define the filter's performance.

The procedure above presents generalized Kalman filter order reduction techniques as applied to the NRS model. This procedure is in no way all-inclusive or all-encompassing but is strictly intended to help the inexperienced reader understand the methodology and reasoning behind the NRS filter order reduction.

2.4 *Tuning of a Kalman Filter*.

A Kalman filter proves to be the optimal state estimator of a system that has dynamics and measurement equations which can be described as linear, driven by white Gaussian noise and deterministic inputs (13). If one were to construct a full order filter model, its dynamics noise strength and measurement noise covariances would normally be identical to those of the truth model (or those of the true system, if one could compute these). When this full order filter is reduced, either by removing states or by combining states, the strengths of these noise terms must be adjusted. In the case of non linear dynamics and/or measurement equations, even the full order EKF derived above is only optimal in a first order perturbation sense. Due to this, the dynamics and measurement noise strengths of the full order filter as well as those of any reduced order filter must be adjusted to compensate for not only the state reductions but the non linear effects as well. The process of adjusting these noise strengths is called "tuning" a Kalman filter. Next, a brief overview of the rationale behind the tuning process of the NRS EKF (as applicable to this thesis research) is presented.

Tuning consists of the adjustment of variables in two matrices: the dynamics noise strength matrix $Q(t)$ and the measurement noise covariance matrix $R(t_i)$. These values are tuned until the filter (whether full order or reduced order) closely tracks ("close" depends on the required performance level and engineering discretion) the truth model dynamics. Generally, as the filter order is reduced, these values of Q and R are increased.

There are three reasons why the Q values must be tuned. The first of these reasons is to keep the Kalman filter gain (or some partition of the gain) from becoming zero. This phenomenon can occur in linear, linearized, and extended Kalman filters when the filter becomes too confident and begins to rely increasingly on its own dynamics model and to reject the information in measurement updates. If the gain $K(t_i) = 0$ from Equation (2-14), then no update information will be incorporated into $x(t_i^+)$ or $P(t_i^+)$ in Equations (2-15) and (2-16). In

order to prevent this situation from occurring, the Q value corresponding to those states showing this property can be artificially increased to a point where the gain K never becomes zero.

The second reason for tuning of the dynamics noise strength matrix Q is to keep the filter covariance matrix P from attaining any negative eigenvalues. This is a problem with numeric stability and computational precision and is somewhat fixed to the computer being used. It occurs when the range of numbers the filter computes is large (for example some states could be in the order of 10^{-10} and others in the order of 10^{+10}). The truth model state variances of the states that show this phenomenon are often zero. It should be noted that the filter may give a good estimate of the state even when the computed covariance value is negative. Increasing the noise terms for these states will keep the covariance positive and generally does not degrade the filter's performance. Also, the tuning values in the "real world" are often different from the tuning values used in simulation.

The third reason is to compensate for filter order reduction and any non linear effects. When a state is eliminated or absorbed into another, the remaining states that were effected by the now removed state are compensated for losing some of their precision by increasing their uncertainty (that is, by increasing their Q values). Non linear effects in linearized/extended Kalman filters are compensated for by increasing the Q values of the affected states. The more non linear the state, the more the required increase in the Q value.

The measurement noise matrix $R(t_i)$ must be tuned for two reasons. The first is to compensate for non linear effects (if the measurement equation had to be linearized). Note that a linear Kalman filter can only use measurement equations that are a linear combination of states. The second reason is due to filter order reduction. If a state that is part of the measurement equation is eliminated/absorbed, it is necessary to increase the R value

associated with that measurement, thereby increasing its uncertainty, to compensate for the missing information.

The tuning procedure is far from trivial. In fact, it is probably the most time-consuming step in Kalman filter design. Adjustments of the **Q** and **R** matrices must be done iteratively and good engineering insight must be used. The rationale presented here in this thesis research is not universal to all Kalman filters but was intended as an overview of why tuning is required and how the final values were derived for the NRS EKF.

2.5 Summary.

An understanding of the EKF is important for engineers and designers who wish to study modern aircraft navigation systems. In this chapter the equations for the EKF, as well as a description of the state reduction and tuning process as they apply to the NRS, were presented. The reader is encouraged to seek other literature sources such as Maybeck's textbooks (13, 14, 15) or Stacey's thesis (4), which offer a broader and more complete description of the EKF as applied to the NRS and the CIRIS, if more information is required.

III. The Navigation Reference System

3.1 Overview:

This chapter will overview some of the theory and equations of the Navigation Reference System (NRS) and the Enhanced Navigation Reference System (ENRS). The NRS MSOFE model, first developed by Stacey (4), and the ENRS MSOFE model, developed by Negast (1), will also be reviewed. The goal of this chapter will be to present the NRS and ENRS truth models and reduced order filter models that will be used for this thesis research. These NRS and ENRS models will be implemented in MSOFE and run on AFIT's Sun workstations in order to verify their performance. Note that the NRS model will be developed in conjunction with Mosle (19), as his thesis research model is similar. The incorporation of carrier-phase GPS measurements will be accomplished in Chapter IV of this thesis.

The NRS and ENRS models can be partitioned into three distinct sections: the LN-93 INS error state model, the RRS error state model, and the GPS (or DGPS) error state model. Each of these sections will be discussed separately.

3.2 The Litton LN-93 Error State Models:

3.2.1 The 93-state model. A 93-error-state model of the LN-93 was developed by Litton and documented in (16). This section will summarize this model; however, the reader is encouraged to review the Litton documentation if in-depth information is required.

This model is broken into six categories. The first category is the general error states and can be described as combinations of other states in the model. Position, velocity, platform tilt, and vertical channel errors are in this category. Note that these are the states of primary interest as described in Chapter II. The second category consists of states that can be described by first order Markov processes. Gyro and accelerometer errors, which are time-

correlated exponential errors, and the baro-altimeter error state are included in this category. Gyro and accelerometer bias errors, which can be modelled as unknown constants, form the third and fourth category. The first-order Markov processes of the gyro and accelerometer thermal transients form the fifth category and the sixth is the gyro compliance errors modelled as unknown constants. In partitioned vector form, the 93-state model is:

$$\delta x = [\delta x_1 \; \delta x_2 \; \delta x_3 \; \delta x_4 \; \delta x_5 \; \delta x_6]^T \qquad (3\text{-}1)$$

where:

δx represents a 93 x 1 column vector of error states.

δx_1 represents category 1 errors consisting of 13 position, velocity, attitude, and vertical channel errors.

δx_2 represents category 2 errors consisting of 16 gyro, accelerometer, and baro-altimeter first-order Markov error states.

δx_3 represents category 3 errors consisting of 18 gyro bias errors.

δx_4 represents category 4 errors consisting of 22 accelerometer bias errors.

δx_5 represents category 5 errors consisting of 6 initial thermal transient errors for the gyros and accelerometers.

δx_6 represents category 6 errors consisting of 18 gyro compliance error states.

In state space form, this 93-state model is of the form:

$$
\begin{bmatrix} \delta \dot{x}_1 \\ \delta \dot{x}_2 \\ \delta \dot{x}_3 \\ \delta \dot{x}_4 \\ \delta \dot{x}_5 \\ \delta \dot{x}_6 \end{bmatrix} =
\begin{bmatrix}
F_{11} & F_{12} & F_{13} & F_{14} & F_{15} & F_{16} \\
0 & F_{22} & 0 & 0 & 0 & 0 \\
0 & 0 & 0 & 0 & 0 & 0 \\
0 & 0 & 0 & 0 & 0 & 0 \\
0 & 0 & 0 & 0 & F_{55} & 0 \\
0 & 0 & 0 & 0 & 0 & 0
\end{bmatrix}
\cdot
\begin{bmatrix} \delta x_1 \\ \delta x_2 \\ \delta x_3 \\ \delta x_4 \\ \delta x_5 \\ \delta x_6 \end{bmatrix}
+
\begin{bmatrix} w_1 \\ w_2 \\ 0 \\ 0 \\ 0 \\ 0 \end{bmatrix}
\qquad (3\text{-}2)
$$

A complete state listing of the 93 states is included in Appendix A as Tables A-1 through A-6. Appendix B, Tables B-1 through B-8, contains a listing of all the non-zero entries of the F(t)

matrix of Equation (3.2). Also, the non-zero entries of the dynamics driving noise matrix, $Q(t)$, are presented in Tables B-9 and B-10.

3.2.2 The 39-State Model. Negast (1: sec 3.4) reduced the 93-state LN-93 model to a 41-state model, following the recommendations of Lewantowicz and Keen (17). Upon close inspection of this 41-state model, which was also used by Vasquez (18), it was discovered that 2 states, numbers 40 and 41, were identical to state 39 and in fact were never used. These two states were thus removed, making Negast's 41-state model the same as the 39-state model used in this thesis research. This state reduction will significantly reduce the computation time needed for an analysis of the NRS and ENRS, but does effect the accuracy of the error-states of primary interest, according to the results of Lewantowicz and Keen and Negast. The 39-state model used for this research is presented later in Section 3.5: *Integration to Form the NRS Truth and Filter Models.*

3.3 The RRS Error State Model.

The Range/Range-rate System consists of an airborne transmitter/receiver and a number of ground based transponders. The transmitter/receiver interrogates the transponders and processes the resulting information to produce a navigation solution. By interrogating three or more ground transponders, the user can obtain a three-dimensional position and velocity fix. The RRS information can also be used as measurement updates to a navigation Kalman filter. This is the manner in which the RRS is incorporated into the NRS and ENRS.

A detailed explanation of the RRS is presented in both Stacey (4) and Negast (1). The following sections will overview the RRS MSOFE error state model equations and measurement equations. If more detail is required, the reader is encouraged to review the above references.

3.3.1 RRS MSOFE Model Equations. The RRS error state model consists of 26 states divided into seven categories: the first category is for two error states that are common to all transponders and the remaining six categories are made up of four states each for the transponder-dependant states. The MSOFE model for this thesis research models only six transponders, while in reality there are many more located in New Mexico and along the flight tracks used by CIGTF for flight tests. Additional transponders can be added to the MSOFE simulation; however, this would make the simulation more burdensome. It may also be possible to incorporate transponder "switching" which would require only a few transponders to be modelled in MSOFE and the program can then choose which transponders to use at any time.

The two states of the common category are simple random biases that model the effects of the interrogator hardware calibration errors in both range and velocity. The state space model for this is:

$$\delta \dot{\mathbf{x}}_{common} = \begin{bmatrix} \delta \dot{x}_{br} \\ \delta \dot{x}_{bv} \end{bmatrix} = \begin{bmatrix} 0 & 0 \\ 0 & 0 \end{bmatrix} \cdot \begin{bmatrix} \delta x_{br} \\ \delta x_{bv} \end{bmatrix} \tag{3-3}$$

where:

δx_{br} ▲ range equivalent of the interrogator bias
δx_{bv} ▲ velocity equivalent of the interrogator bias

The initial state estimates and covariances for these states are:

$$\delta \hat{\mathbf{x}}_{common}(t_o) = 0 \tag{3-4}$$

and

$$\mathbf{P}_{br,bv}(t_o) = \begin{bmatrix} 1 \ ft^2 & 0 \\ 0 & 10^{-4} \ \frac{ft^2}{sec^2} \end{bmatrix} \tag{3-5}$$

Each individual transponder has four error states associated with it. Three of these are due to the uncertainty in the transponder surveyed position and are modelled as random biases. The remaining one is due to atmospheric propagation delays the signal experiences between the interrogator and transponder. This state is modelled as a first order Markov process. The state space model of these four states is:

$$
\begin{bmatrix} \delta \dot{x}_i \\ \delta \dot{y}_i \\ \delta \dot{z}_i \\ \delta \dot{R}_{atm-i} \end{bmatrix} = \begin{bmatrix} 0 & 0 & 0 & 0 \\ 0 & 0 & 0 & 0 \\ 0 & 0 & 0 & 0 \\ 0 & 0 & 0 & -\frac{1}{\tau} \end{bmatrix} \cdot \begin{bmatrix} \delta x_i \\ \delta y_i \\ \delta z_i \\ \delta R_{atm-i} \end{bmatrix} + \begin{bmatrix} w_{xi} \\ w_{yi} \\ w_{zi} \\ w_{atm-i} \end{bmatrix}
\tag{3-6}
$$

Where the subscript i denotes transponder number 1 through 6 and $\tau = 300$ seconds is the transponder atmospheric error state time constant.

The initial conditions for these states are:

$$
\delta \hat{x}_{x,y,z,atm}(t_o) = 0
\tag{3-7}
$$

with:

$$
P_{x,y,z,atm}(t_o) = \begin{bmatrix} 25 \ ft^2 & 0 & 0 & 0 \\ 0 & 25 \ ft^2 & 0 & 0 \\ 0 & 0 & 25 \ ft^2 & 0 \\ 0 & 0 & 0 & 100 \ PPM^2 \end{bmatrix}
\tag{3-8}
$$

and:

$$
E[w_{x,y,z,atm}] = 0
\tag{3-9}
$$

$$
E[w_{x,y,z,atm}(t) w_{x,y,z,atm}(t + \tau)] = \begin{bmatrix} 0 & 0 & 0 & 0 \\ 0 & 0 & 0 & 0 \\ 0 & 0 & 0 & 0 \\ 0 & 0 & 0 & \frac{2\sigma_{atm}^2}{300} \end{bmatrix} \cdot \delta(\tau)
\tag{3-10}
$$

3-5

The value of $\sigma^2_{atm} = 10^{-10}$ ft^2. Equations (3-3) through (3-10) were developed by Cubic Corporation, the designers of the RRS for CIGTF. The numeric values presented are based on actual data from static and dynamic measurement analysis of the RRS (2). As there are six transponders used in this thesis research, there are six sets of the Equations (3-6) through (3-10). Table A-7 in Appendix A gives a complete listing of all 26 RRS states as used in this thesis research.

3.3.2 The RRS Range Measurement Equation. The NRS utilizes the RRS computed range from the interrogator to each transponder as the basis for its measurement update to the Kalman filter. The RRS computes this range by measuring the time delay between the transmission of the interrogation pulse and the receiving of the response from the transponder. This time delay is divided by two (to account for the "round trip" of the signal) and multiplied by the speed of light to produce the uncorrected range measurement. This measurement can then be corrected in order to compensate for propagation delays due to the atmosphere and errors introduced by equipment biases. The uncorrected range measurement as obtained from the RRS is modelled as:

$$R_{RRS} = R_t + \delta R_{atm} + \delta R_{br} + v \qquad (3-11)$$

where:

R_{RRS} = RRS range measurement (transponder to interrogator)

R_t = True (but unknown) range (transponder to interrogator)

δR_{atm} = range error due to atmospheric delay

δR_{br} = range error due to equipment calibration biases

v = zero mean white Gaussian measurement noise

In order to formulate a difference measurement, as described in Chapter II, two sources of range information must be obtained. The second range measurement will come

from the computed range between the INS-indicated user position and the transponder surveyed position. The INS-indicated user position can be expressed as the 3-dimensional vector (in the Litton ECEF frame):

$$\mathbf{X}_U = \begin{bmatrix} x_U \\ y_U \\ z_U \end{bmatrix}^{ECEF} \tag{3-12}$$

and the true RRS transponder surveyed position is represented by:

$$\mathbf{X}_r = \begin{bmatrix} x_T \\ y_T \\ z_T \end{bmatrix}^{ECEF} \tag{3-13}$$

The calculated range from the user (INS) to the transponder is then:

$$R_{INS} = \left| \mathbf{X}_U - \mathbf{X}_r \right| = \sqrt{(x_U - x_T)^2 + (y_U - y_T)^2 + (z_U - z_T)^2} \tag{3-14}$$

Equation (3-14) above is a non linear measurement that can be "linearized" by using a first order perturbation (Taylor series) about the true value. The result is a first order approximation of R_{INS} expressed as the sum of R_t and the errors in user and transponder position:

$$R_{INS} = R_t + \left. \frac{\partial R_{INS}(\mathbf{x}_r, \mathbf{x}_u)}{\partial \mathbf{x}_r} \right|_{(\mathbf{x}_r, \mathbf{x}_u)_{true}} \cdot \delta \mathbf{X}_T + \left. \frac{\partial R_{INS}(\mathbf{x}_r, \mathbf{x}_u)}{\partial \mathbf{x}_u} \right|_{(\mathbf{x}_r, \mathbf{x}_u)_{true}} \cdot \delta \mathbf{X}_U \tag{3-15}$$

Substitution of Equation (3-14) into (3-15) and evaluation of the partial derivatives yields the INS-derived range approximation as:

$$\begin{aligned} R_{INS} = R_t &- \frac{x_T - x_u}{|R_{INS}|} \cdot \delta x_U - \frac{y_T - y_u}{|R_{INS}|} \cdot \delta y_U - \frac{z_T - z_u}{|R_{INS}|} \cdot \delta z_U \\ &+ \frac{x_T - x_u}{|R_{INS}|} \cdot \delta x_T + \frac{y_T - y_u}{|R_{INS}|} \cdot \delta y_T + \frac{z_T - z_u}{|R_{INS}|} \cdot \delta z_T \end{aligned} \tag{3-16}$$

The difference measurement, δz, can now be formed as the difference between Equation (3-11) and (3-16):

$$\delta z = R_{INS} - R_{RRS} = -\frac{x_T-x_u}{|\mathbf{R}_{ou}|} \cdot \delta x_U - \frac{y_T-y_u}{|\mathbf{R}_{ou}|} \cdot \delta y_U - \frac{z_T-z_u}{|\mathbf{R}_{ou}|} \cdot \delta z_U$$
$$+ \frac{x_T-x_u}{|\mathbf{R}_{ou}|} \cdot \delta x_T + \frac{y_T-y_u}{|\mathbf{R}_{ou}|} \cdot \delta y_T + \frac{z_T-z_u}{|\mathbf{R}_{ou}|} \cdot \delta z_T \qquad (3\text{-}17)$$
$$- \delta R_{atm} - \delta R_{br} - v$$

The range measurement noise v has been determined (for the truth model) to have a variance of 4 ft^2 when the measurement interval is 6 seconds (2, 3). Of special interest is the fact that the true range R_t, which was present in both Equations (3-11) and (3-16), has been cancell $\mathbf{d}$ out due to the differencing. This is important as the true range is unknown. Equation (3-17) is now in the form required to be used as a measurement update for an EKF as described in Chapter II. The terms δx_U, δy_U, δz_U, δx_T, δy_T, δz_T, δR_{atm}, and δR_{br} are states or linear combinations of states in our error state model, and the coefficient terms appear in the **H** matrix of the measurement update. It is also important to note that these updates are performed in the Litton ECEF frame. The choice of frame is arbitrary but must be consistent throughout the simulation. The Litton ECEF frame seemed a reasonable choice as it was already coded into MSOFE by the Wright Laboratory Avionics Division.

3.4 The GPS Code-Phase Error State Model:

The Global Positioning System is a highly accurate, stand-alone navigation system capable of all-weather, world-wide navigation. GPS utilizes 24 satellites orbiting in 6 orbital planes with an orbit period of close to 12 hours and at a radius of about 10,000 nautical miles. Each satellite continuously broadcasts its navigation message, including satellite identification (pseudo-random code), orbital position data, and timing information, on two L-band frequencies. The GPS receiver is able to compute the uncorrected range, known as pseudorange, between itself and a satellite by measuring the time delay between the

transmission of the satellite navigation message and the reception of the message at the receiver. This pseudorange is corrupted by errors such as user clock bias and drift, atmospheric (ionospheric and tropospheric) delays, code-loop errors, satellite clock errors, and satellite orbital position errors. Using pseudorange measurements from at least four satellites, the GPS receiver can compute user position as well as the user clock bias. Four satellites are required in order to compute the user's X, Y, and Z position as well as the dominate error source: user clock bias.

GPS is meant to be used in a stand-alone configuration, however, this thesis research uses GPS pseudorange measurements as updates to the EKF in a manner similar to the RRS measurement updates.

3.4.1 GPS MSOFE Model Equations. The GPS error state model, first developed by Solomon (2) and then revised by Stacey (4), consists of 30 states divided into five categories: one category for 2 common (receiver-dependent) states, and four categories of 7 states each for satellite-dependent states. The MSOFE model tracks all 24 GPS satellite orbital positions and chooses the best four that are "in view" (above a user selectable elevation angle) based on computed Position Dilution of Precision (PDOP). Only four satellite pseudorange measurements are passed on to the EKF.

The two common states are the user clock bias and user clock drift states. The state space model for this category is:

$$\begin{bmatrix} \dot{x}_{Uclk-b} \\ \dot{x}_{Uclk-dr} \end{bmatrix} = \begin{bmatrix} 0 & 1 \\ 0 & 0 \end{bmatrix} \cdot \begin{bmatrix} x_{Uclk-b} \\ x_{Uclk-dr} \end{bmatrix} \tag{3-18}$$

where: x_{Uclk-b} = range equivalent of user (receiver) clock bias

$x_{Uclk-dr}$ = velocity equivalent of user (receiver) clock drift

The initial state estimates and covariances for these states are (3):

$$\begin{bmatrix} \hat{x}_{Uclk-b}(t_o) \\ \hat{x}_{Uclk-dr}(t_o) \end{bmatrix} = 0 \qquad (3\text{-}19)$$

and:

$$P_{Uclk-b, Uclk-dr}(t_o) = \begin{bmatrix} 9 \times 10^{14} \text{ ft}^2 & 0 \\ 0 & 9 \times 10^{10} \frac{ft^2}{sec^2} \end{bmatrix} \qquad (3\text{-}20)$$

It should be noted that the large initial uncertainties associated with these two states are representative of the normal receiver clock bias and drifts associated with both military and civilian GPS receivers. Until a good estimate of the user clock bias is determined, it remains the largest and most dominant source of error in the GPS measurements.

The seven states of the satellite-dependent categories are: δR_{cl} - code range quantization error (code loop error), δR_{trop} - tropospheric propagation delay, δR_{iono} - ionospheric propagation delay, δR_{Sclk} - satellite clock error, and δx_S, δy_S, and δz_S - the x, y, and z components of the GPS satellite position error. Each GPS receiver utilizes a pair of interacting tracking loops. One of these loops is the code tracking loop and is a source of range measurement error. Code loop error is modelled as a first order Markov process (20) with an exponential autocorrelation function. Both the tropospheric and ionospheric propagation delay errors can be modelled and significantly reduced by the GPS receiver; however, the contribution to the error of these two states is still significant. Both these states are modelled as first order Markov processes with different time constants. The remaining four states, satellite clock error and position error, are due mainly to errors in the ephemeris data received and are modelled as random biases. It should be noted that pseudorange measurements only provide new information along the line-of-sight from user to satellite and the satellite position error is modelled in three dimensions. This can lead to observability problems in these states.

This argument will be employed later in obtaining a reduced-order GPS error model. The state space model for the satellite-dependent states is:

$$
\begin{bmatrix} \delta\dot{R}_{cl} \\ \delta\dot{R}_{trop} \\ \delta\dot{R}_{iono} \\ \delta\dot{R}_{Sclk} \\ \delta\dot{x}_S \\ \delta\dot{y}_S \\ \delta\dot{z}_S \end{bmatrix} = \begin{bmatrix} -1 & 0 & 0 & 0 & 0 & 0 & 0 \\ 0 & -\frac{1}{500} & 0 & 0 & 0 & 0 & 0 \\ 0 & 0 & -\frac{1}{1500} & 0 & 0 & 0 & 0 \\ 0 & 0 & 0 & 0 & 0 & 0 & 0 \\ 0 & 0 & 0 & 0 & 0 & 0 & 0 \\ 0 & 0 & 0 & 0 & 0 & 0 & 0 \\ 0 & 0 & 0 & 0 & 0 & 0 & 0 \end{bmatrix} \cdot \begin{bmatrix} \delta R_{cl} \\ \delta R_{trop} \\ \delta R_{iono} \\ \delta R_{Sclk} \\ \delta x_S \\ \delta y_S \\ \delta z_S \end{bmatrix} + \begin{bmatrix} w_{cl} \\ w_{trop} \\ w_{iono} \\ 0 \\ 0 \\ 0 \\ 0 \end{bmatrix}
\tag{3-21}
$$

with:

$$
P(t_o) = \begin{bmatrix} 0.25 & 0 & 0 & 0 & 0 & 0 & 0 \\ 0 & 1.0 & 0 & 0 & 0 & 0 & 0 \\ 0 & 0 & 1.0 & 0 & 0 & 0 & 0 \\ 0 & 0 & 0 & 25 & 0 & 0 & 0 \\ 0 & 0 & 0 & 0 & 25 & 0 & 0 \\ 0 & 0 & 0 & 0 & 0 & 25 & 0 \\ 0 & 0 & 0 & 0 & 0 & 0 & 25 \end{bmatrix} ft^2
\tag{3-22}
$$

and:

$$
E[w(t)] = 0
\tag{3-23}
$$

$$
E[w(t)w(t+\tau)] = \begin{bmatrix} 0.5 & 0 & 0 & 0 & 0 & 0 & 0 \\ 0 & 0.004 & 0 & 0 & 0 & 0 & 0 \\ 0 & 0 & 0.004 & 0 & 0 & 0 & 0 \\ 0 & 0 & 0 & 0 & 0 & 0 & 0 \\ 0 & 0 & 0 & 0 & 0 & 0 & 0 \\ 0 & 0 & 0 & 0 & 0 & 0 & 0 \\ 0 & 0 & 0 & 0 & 0 & 0 & 0 \end{bmatrix} \cdot \delta(\tau) \frac{ft^2}{sec}
\tag{3-24}
$$

Equations (3-19) through (3-34) are typical of a military 5-channel GPS receiver operating on P-code. The GPS 30-state error model is completely specified in Appendix A, Table A-8.

3.4.2 GPS Pseudorange Measurement Equation. The NRS utilizes the GPS receiver-computed pseudorange to each of four satellites as a basis for the Kalman filter measurement updates in much the same fashion as the RRS measurements are used. As mentioned earlier, there exist errors in the pseudorange measurement. The computed range is corrupted by atmospheric delays (as the signal must travel a great distance through both the upper and lower atmospheres) and timing errors. The raw, or uncorrected, pseudorange measurement equation is modelled as:

$$R_{GPS} = R_t + \delta R_{cl} + \delta R_{trop} + \delta R_{iono} + \delta R_{Sclk} + \delta R_{Uclk} + v \qquad (3\text{-}25)$$

where:

R_{GPS} = GPS pseudorange measurement (from satellite to user)

R_t = true (and unknown) range from satellite to user

δR_{cl} = range error due to code loop error

δR_{trop} = range error due to tropospheric delay

δR_{iono} = range error due to ionospheric delay

δR_{Sclk} = range error due to satellite clock error

δR_{Uclk} = range error due to user clock error

v = zero mean white Gaussian measurement noise

As in Equation (3-11), the RRS measurement equation, the GPS measurement equation contains both the true range, which can never be known exactly, and terms which reflect sources of uncertainty which are inherent to GPS pseudorange measurements.

Also as in the case of the RRS measurement, in order to formulate a difference measurement, two sources of GPS pseudorange information must be obtained. The second measurement again comes from the computed range from the INS-indicated position of the user to the satellite. The satellite's position is computed using the satellite ephemeris data. The satellite position, which can be represented by the three dimensional vector

$$X_s = \begin{bmatrix} x_s \\ y_s \\ z_s \end{bmatrix}^{ECEF} \qquad (3\text{-}26)$$

is subtracted from the INS-indicated user position, and the calculated range from the user to the satellite is:

$$R_{INS} = \sqrt{(x_U - x_S)^2 + (y_U - y_S)^2 + (z_U - z_S)^2} \qquad (3\text{-}27)$$

This non linear equation can be "linearized" in the same fashion as Equation (3-14) was. The result is a first order approximation of R_{INS} expressed as a sum of R_t and the uncertainties in user and satellite position:

$$R_{INS} = R_t + \frac{\delta R_{ins}(x_U, x_s)}{\delta x_s}\bigg|_{(x_U, x_s)\,nom} \cdot \delta X_s + \frac{\delta R_{ins}(x_U, x_s)}{\delta x_U}\bigg|_{(x_U, x_s)\,nom} \cdot \delta X_U \qquad (3\text{-}28)$$

When Equation (3-27) is substituted into (3-28) and the partial derivatives are evaluated, the INS-derived pseudorange approximation becomes:

$$\begin{aligned} R_{INS} = R_t &- \frac{x_s - x_U}{|\underline{R}|} \cdot \delta x_U - \frac{y_s - y_U}{|\underline{R}|} \cdot \delta y_U - \frac{z_s - z_U}{|\underline{R}|} \cdot \delta z_U \\ &+ \frac{x_s - x_U}{|\underline{R}|} \cdot \delta x_S + \frac{y_s - y_U}{|\underline{R}|} \cdot \delta y_S + \frac{z_s - z_U}{|\underline{R}|} \cdot \delta z_S \end{aligned} \qquad (3\text{-}29)$$

The GPS pseudorange difference measurement is formed by subtracting Equation (3-25) from Equation (3-29):

$$\begin{aligned} \delta z = R_{INS} - R_S = &- \frac{x_s - x_U}{|\underline{R}|} \cdot \delta x_U - \frac{y_s - y_U}{|\underline{R}|} \cdot \delta y_U - \frac{z_s - z_U}{|\underline{R}|} \cdot \delta z_U \\ &+ \frac{x_s - x_U}{|\underline{R}|} \cdot \delta x_S + \frac{y_s - y_U}{|\underline{R}|} \cdot \delta y_S + \frac{z_s - z_U}{|\underline{R}|} \cdot \delta z_S \\ &- \delta R_{cl} - \delta R_{trop} - \delta R_{iono} - \delta R_{Sclk} \\ &- \delta R_{Uclk} - v \end{aligned} \qquad (3\text{-}30)$$

The pseudorange measurement noise variance used by Negast is 9 ft^2 (for the truth model) when the GPS pseudorange measurements occur every 10 seconds (20). This thesis

research will use the same value for the variance and the measurement cycle time. As in the RRS case, the true range R_t drops out in the differencing, the measurement δz is a linear combination of states of the error state model, and the coefficients in Equation (3-30) appear in the H matrix of the measurement update. These updates are also performed in the Litton ECEF frame.

3.5 Integration to Form the NRS Truth and Filter Models.

3.5.1 The NRS Truth Model. The 39-state LN-93, 26-state RRS, and 30-state GPS error models are integrated to form a 95-state error model for the NRS. This model was used as the truth model by both Negast (1) and Vasquez (18). It will also be used as the truth model for this thesis research. Appendix A, Tables A-11 through A-14, contains a complete listing of the 95 NRS truth states. Note that the states were re-ordered (the RRS range bias and velocity bias states and the GPS clock bias and drift states were moved to states 12 through 15) in order to facilitate further state reductions.

3.5.2 The NRS Filter Model. The 39-state LN-93 model and the 26-state RRS model were integrated along with the two GPS common states, user clock bias and user clock drift, to form the 67-state NRS filter model. This is one of the filter models used by Negast (1) for the NRS. Note that the requirement of 70 or fewer states is met, as this filter uses only 67 states. This filter model is the same as the NRS truth model with states 68 through 95 removed. Tables A-11 through A-13 contain a listing of all 67 states of the NRS filter model.

3.6 The Enhanced Navigation Reference System (ENRS).

The Enhanced Navigation System (ENRS) employs differential corrections to the GPS raw pseudorange data collected by the NRS. The Differential GPS corrections researched by
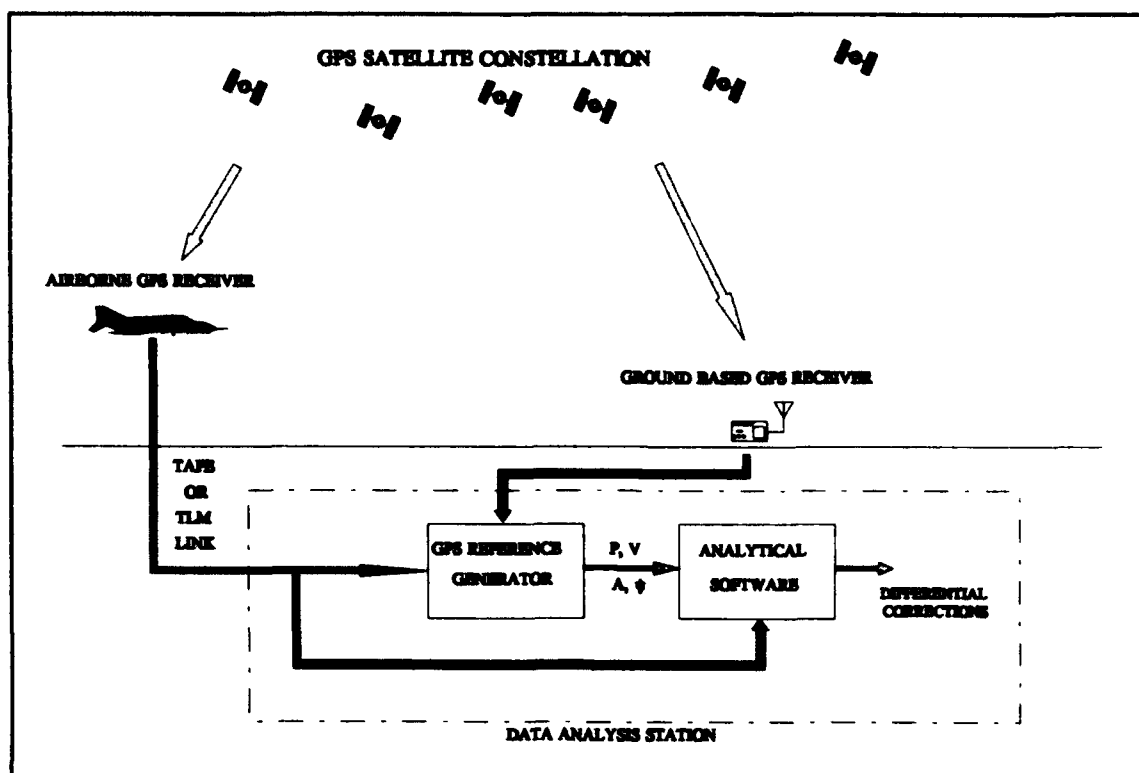
Figure 3-1: DGPS Data Analysis/Reference Station

tracking the same satellites as the ABR (a good assumption if the ABR is within the CIRIS test range). This is an important assumption as the between-receivers removed or reduced errors must have a high correlation. Using differential corrections in this manner, the satellite clock error is removed (as it is common to both receivers) and the satellite position errors are greatly reduced. The atmospheric propagation errors can also be greatly reduced, depending upon the distance between the ABR and the GBR (even up to 200 miles). Atmospheric errors are still reduced for flights that exceed 200 miles distance between the ABR and GBR. The largest remaining error, as in the case of GPS pseudorange measurements, is the ABR clock bias.

Using this knowledge of how DGPS is implemented at CIGTF, a new DGPS error state model can be developed *assuming differential corrections have already been applied to the ABR raw pseudorange measurements.*

3-16

3.6.1 Differential GPS MSOFE Error State Model. The DGPS model is virtually identical to the code-phase GPS model, with the exception that the satellite clock state and the code-loop error state have been removed for all four satellite-dependent categories. With the removal of these eight, the DGPS model is now composed of 22 states. It should be noted that removal of the code-loop error states is justified in that compensation is provided by the measurement noise variance in the pseudorange measurement as implemented in Negast's thesis and this thesis research (12).

The DGPS model is, as in the case of GPS, broken into five categories: ABR-dependent (common) states, and five satellite-dependent states. The names of the states remain the same and, except for the removed states, they remain in the same order. The ABR-dependent states are modeled as:

$$\begin{bmatrix} \dot{x}_{Uclk\text{-}b} \\ \dot{x}_{Uclk\text{-}dr} \end{bmatrix} = \begin{bmatrix} 0 & 1 \\ 0 & 0 \end{bmatrix} \cdot \begin{bmatrix} x_{Uclk\text{-}b} \\ x_{Uclk\text{-}dr} \end{bmatrix} \qquad (3\text{-}31)$$

with:

$\quad x_{Uclk\text{-}b}$ = range equivalent of ABR clock bias

$\quad x_{Uclk\text{-}dr}$ = velocity equivalent of ABR clock drift

The initial state estimates and covariances for these states are:

$$\begin{bmatrix} \hat{x}_{Uclk\text{-}b}(t_o) \\ \hat{x}_{Uclk\text{-}dr}(t_o) \end{bmatrix} = 0 \qquad (3\text{-}32)$$

and

$$P_{Uclk\text{-}b,Uclk\text{-}dr}(t_o) = \begin{bmatrix} 9.0\text{x}10^{14} \ ft^2 & 0 \\ 0 & 9.0\text{x}10^{10} \ \frac{ft^2}{sec^2} \end{bmatrix} \qquad (3\text{-}33)$$

As was noted earlier, until the ABR clock bias and drift errors are determined, they remain the dominant error source in the DGPS model.

The satellite-dependent states are modelled as:

$$
\begin{bmatrix} \delta\dot{R}_{trop} \\ \delta\dot{R}_{iono} \\ \delta\dot{x}_S \\ \delta\dot{y}_S \\ \delta\dot{z}_S \end{bmatrix} = \begin{bmatrix} -\frac{1}{500} & 0 & 0 & 0 & 0 \\ 0 & -\frac{1}{1500} & 0 & 0 & 0 \\ 0 & 0 & 0 & 0 & 0 \\ 0 & 0 & 0 & 0 & 0 \\ 0 & 0 & 0 & 0 & 0 \end{bmatrix} \cdot \begin{bmatrix} \delta R_{trop} \\ \delta R_{iono} \\ \delta x_S \\ \delta y_S \\ \delta z_S \end{bmatrix} + \begin{bmatrix} w_{trop} \\ w_{iono} \\ 0 \\ 0 \\ 0 \end{bmatrix}
$$

(3-34)

where:

δR_{trop} = range equivalent of tropospheric delay

δR_{iono} = range equivalent of ionospheric delay

δx_S = satellite x position error

δy_S = satellite y position error

δz_S = satellite z position error

The initial state estimates are zero and the initial state covariances are (4):

$$
P_{DGPS}(t_o) = \begin{bmatrix} 1.0 & 0 & 0 & 0 & 0 \\ 0 & 1.0 & 0 & 0 & 0 \\ 0 & 0 & 0.35 & 0 & 0 \\ 0 & 0 & 0 & 0.35 & 0 \\ 0 & 0 & 0 & 0 & 0.35 \end{bmatrix} ft^2
$$

(3-35)

with

$$
E[w_{DGPS}(t)] = 0
$$

(3-36)

and

$$
E[w_{DGPS}(t)w_{DGPS}(t+\tau)] = \begin{bmatrix} 0.001 & 0 & 0 & 0 & 0 \\ 0 & 0.0004 & 0 & 0 & 0 \\ 0 & 0 & 0 & 0 & 0 \\ 0 & 0 & 0 & 0 & 0 \\ 0 & 0 & 0 & 0 & 0 \end{bmatrix} \frac{ft^2}{sec} \cdot \delta(\tau)
$$

(3-37)

Note that these states have significantly less error contribution after differential corrections are applied. The values for the initial variances and the atmospheric error dynamics driving

3-18

noise strengths were obtained by Negast from (21). Negast modelled these slightly more conservatively than was recommended to Negast by CIGTF. The complete 22-state DGPS error state vector is specified in Appendix A as Table A-9.

3.6.2 Differential GPS Pseudorange Measurement Equation. After application of the differential corrections to the raw pseudorange measurements from the ABR, the GPS measurement equation (Eq. (3-25)) becomes:

$$R_{DGPS} = R_t + \delta R_{trop} + \delta R_{iono} + \delta R_{Uclk} + v \tag{3-38}$$

where:

R_{DGPS} = DGPS pseudorange measurement

R_t = true range (unknown)

δR_{trop} = range error due to tropospheric delay

δR_{iono} = range error due to ionospheric delay

δR_{Uclk} = range error due to ABR clock error

v = zero mean white Gaussian measurement noise

As in the case of both the RRS measurement and the GPS measurement, two sources of DGPS pseudorange information are required to formulate a difference measurement. The second measurement will again come from the computed pseudorange using the INS-indicated user position and the satellite position calculated from the GPS ephemeris data. This derivation is identical to Equations (3-26) through (3-29). The DGPS pseudorange difference measurement is then computed by subtracting Equation (3-38) from Equation (3-29):

$$\delta z = R_{INS} - R_S = -\frac{x_s - x_u}{|R_{ins}|} \delta x_U - \frac{y_s - y_u}{|R_{ins}|} \delta y_U - \frac{z_s - z_u}{|R_{ins}|} \delta z_U$$
$$+ \frac{x_s - x_u}{|R_{ins}|} \delta x_S + \frac{y_s - y_u}{|R_{ins}|} \delta y_S + \frac{z_s - z_u}{|R_{ins}|} \delta z_S \tag{3-39}$$
$$- \delta R_{trop} - \delta R_{iono} - \delta R_{Uclk} - v$$

The DGPS pseudorange measurement noise variance is 9 ft² (truth model) when the measurements occur every 10 seconds. As in the case of GPS and RRS measurements, the true range value R_t dropped out in the differencing, the measurement δz is a linear combination of error states of our model, and the coefficients of Equation (3-39) appear in the H matrix of the measurement update. DGPS measurements are performed in the Litton ECEF frame.

3.7 The ENRS Truth and Filter Models.

3.7.1 The ENRS Truth Model. The 39-state LN-93 model, the 26-state RRS model, and the 22-state DGPS model are merged to form the 87-state ENRS truth model. This is the ENRS truth model researched and simulated by Negast. Appendix A, Tables A-11 through A-13 and Table A-15, contains a complete listing of the 87 ENRS truth states.

3.7.2 The ENRS Filter Model. The 39-state LN-93 model, the 26-state RRS model, and the two receiver-dependent states of the DGPS model were merged to form the 67-state ENRS filter model. This model is virtually identical, except for the values of the dynamics driving noise strength terms $Q(t)$ and the initial covariance terms $P(t_o)$, to the NRS filter model used in this thesis research. This is the ENRS filter model used by Negast in his thesis research. A complete listing of the 67 states is presented in Appendix A, Tables A-11 through A-13.

3.8 Other Measurements.

3.8.1 Velocity. In general, an aircraft INS would receive velocity measurement updates from either a doppler radar, GPS doppler range-rate, and/or RRS doppler range-rate. Negast (1) attempted to incorporate RRS and GPS doppler range-rate measurement updates to the NRS filter but was somewhat unsuccessful. Velocity updates are required in order to keep the

filter model stable, and therefore an "ad-hoc" velocity measurement update was incorporated. The origin of this measurement model can be found in the Mosle (19) - Vasquez (18) thesis line. In this model, the filter is fed directly the true value of the velocity error (i.e., the truth model value of states 7, 8, and 9) with some additive measurement noise. Future research will be required to rectify this problem.

3.8.2 Barometric Altimeter. Any unaided INS is unstable in the vertical channel. For this reason, manufacturers generally incorporate some form of altitude aiding in order to stabilize this channel. The barometric altimeter model used in this thesis and other, previous theses, is a one-state model developed by Litton and documented in (16).

3.9 Summary.

This chapter presented the development of the 95-state NRS truth model, the 87-state ENRS truth model, and the 67-state NRS and ENRS filter models. Development of the measurement update equations for the RRS, GPS, and DGPS are also presented. Simulation results and discussions of these results are presented in detail in Chapter 5 of this thesis research.

of the signal from the satellite and time t represents the receiver clock time of reception of the signal at the receiver. The total transit time δt from satellite to receiver is then:

$$\delta t = t - T \tag{4-2}$$

If we take $\Phi(t)=\Phi(T+\delta t)$ and expand it about T in a Taylor series (see Equation (2-9)), we obtain:

$$\Phi(T + \delta t) = \Phi(T) + \frac{\partial \Phi(\tau)}{\partial \tau}\bigg|_{\tau=T} \cdot \delta t + H.O.T. \tag{4-3}$$

The first derivative of $\Phi(T)$ with respect to time is equal to the frequency f. Since the GPS reference and satellite transmitted carrier frequency oscillators are highly stable over short time intervals (such as δt), the second order and higher terms of Equation (4-3) will be negligible and the frequency term f will be constant. Equation (4-3) then becomes the phase/frequency relation:

$$\Phi(T + \delta t) = \Phi(T) + f \cdot \delta t \tag{4-4}$$

Substitution of Equation (4-2) into (4-4) and noting that $\Phi(T + \delta t) = \Phi_R(t)$ and $\Phi(T) = \Phi^k(T)$, the following is obtained:

$$\Phi_R(t) = \Phi^k(T) + f \cdot (t-T) \tag{4-5}$$

which can be re-arranged to form:

$$\Phi = \Phi^k(T) - \Phi_R(t) = -f \cdot (t-T) \tag{4-6}$$

It would now be useful to obtain an expression relating the transmit time T to the received time t. It should be noted that these two clocks are independent of each other and are offset from the true GPS time by some small error. If the true GPS time at the time of reception is represented by t_{GPS}, then the reception time can be related to true GPS time by:

$$t_{GPS} = t + dt \tag{4-7}$$

where dt represents the user clock offset from true GPS time. The transmission time T can be related to this same t_{GPS} by its offset term, dT, plus the time it takes for the RF signal to propagate from the satellite to the receiver. This propagation time is computed using the true range divided by the speed of light and compensated for the ionospheric delay and the tropospheric delay. At this point it should be noted that the ionosphere, although causes a delay in the code-phase GPS signal, actually advances the phase of the carrier signal making it appear as though the signal is traveling faster than the speed of light (6: sec 9.05 and 9.06; 22). The total time of propagation is then calculated using:

$$\text{Propagation time} = \frac{(\rho - d_{iono} + d_{trop})}{c} \qquad (4\text{-}8)$$

where: ρ = true range, satellite to user

c = speed of light

d_{iono} = range equivalent of ionospheric delay term

d_{trop} = range equivalent of tropospheric delay term

The relation between the transmission time T of the signal and the true GPS time of Equation (4-7) is then:

$$t_{GPS} = T + dT + \frac{(\rho - d_{iono} + d_{trop})}{c} \qquad (4\text{-}9)$$

The relationship between the transmission time T and the reception time t is then obtained by setting Equation (4-7) equal to Equation (4-9):

$$T + dT + \frac{(\rho - d_{iono} + d_{trop})}{c} = t + dt \qquad (4\text{-}10)$$

Equation (4-10) can then be re-arranged to obtain:

$$t - T = dT - dt + \frac{(\rho - d_{iono} + d_{trop})}{c} \qquad (4\text{-}11)$$

Substitution of Equation (4-11) into Equation (4-6), the carrier phase observation equation is obtained:

$$\Phi = -f \cdot (dT - dt) - \left(\frac{f}{c}\right) \cdot (\rho - d_{iono} + d_{trop}) \qquad (4\text{-}12)$$

Equation (4-12) indicates that the carrier phase observation equation is a function of the user and satellite clock biases, the frequency of transmission, the true range, and the ionospheric and tropospheric delay terms.

4.2.2 Phase-Range Measurement Equation. The GPS carrier frequencies (L1 and L2) are in the L-band (1.2 to 1.6 GHz). The wavelength range of the L-band is therefore 18 to 25 centimeters. The observed carrier-phase quantity is a measure of the phase-shift; that is, it represents only a fractional part of one wavelength. The total phase-range measurement at some time epoch t would then be equal to this fractional part, Φ_{frac}, plus an integer number of phase cycles from the initial time, t_o, to the time epoch t (which is continuously measured and accounted for by the receiver), $\Phi_{int}(t_o, t)$, plus an integer phase ambiguity term N. Note that $\Phi_{int}(t_o, t_o)$ represents the receiver's initial estimate of the number of integer phase cycles. The ambiguity term, sometimes referred to as the *cycle ambiguity*, is the difference between the true integer count at time t and the current integer count at time t measured by the receiver. If the receiver started with perfect knowledge of the integer count, this ambiguity term would be equal to zero. If no cycle slips (see Chapter I and later in this chapter for a description of cycle slip) were to occur, then this N term would remain constant. Figure 4-1 is a pictorial description of how Φ_{total} is formulated.

The total phase can then be represented by:

$$\Phi_{total}(t) = \Phi_{frac}(t) + \Phi_{int}(t_o, t) + N(t) \qquad (4\text{-}13)$$

4-4
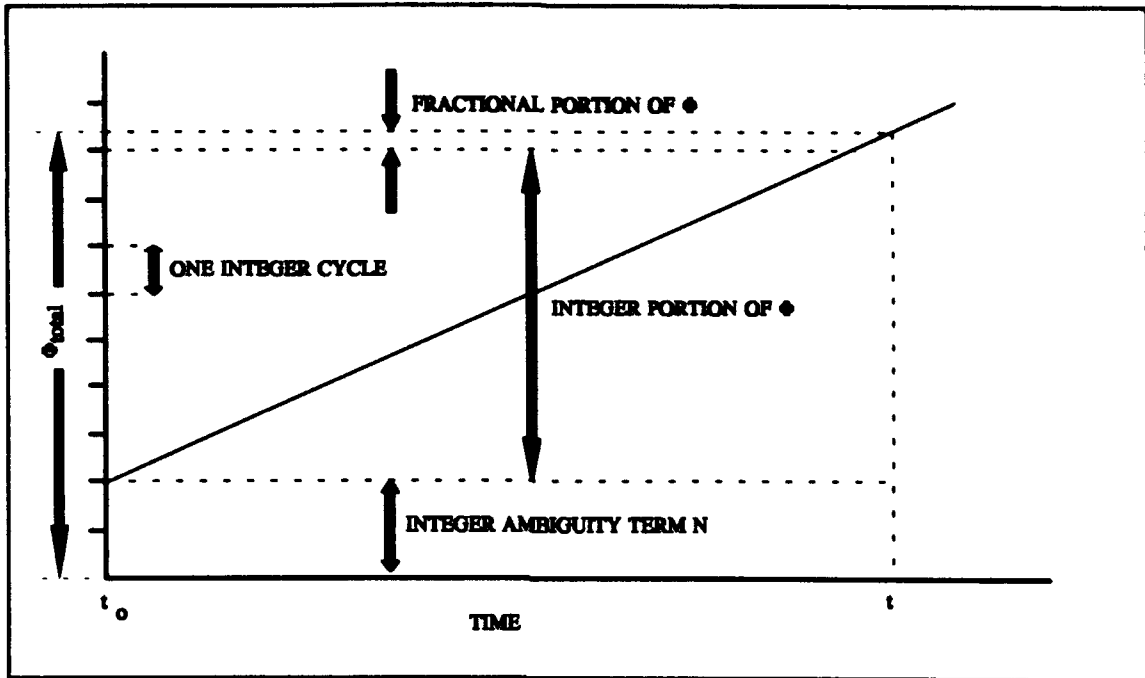
Figure 4-1: Pictorail Formulation of Φ_{total} (no cycle slip)

Note that N is treated as a time varying integer in order to account for cycle slips. As long as the receiver maintains its integer cycle count, then there is only one cycle ambiguity per satellite.

The measured phase-range (Φ of Equation (4-12)) is equal to the sum of the integer count at epoch t and the fractional observation at epoch t:

$$\Phi_{measured}(t) = \Phi_{frac}(t) + \Phi_{int}(t_o, t) \tag{4-14}$$

Therefore the total phase-range at time epoch t is:

$$\Phi_{total}(t) = \Phi_{measured}(t) + N(t) \tag{4-15}$$

The measured phase-range equation for the GPS carrier phase observable is then:

$$\Phi_{measured} = -f \cdot (dT - dt) - \left(\frac{f}{c}\right) \cdot (\rho - d_{iono} + d_{trop}) - N(t) \tag{4-16}$$

4-5

By multiplying Equation (4-16) through by the wavelength $\lambda = c/f$ and representing the phase-range measurement (in length units) as $\Phi = -\lambda \Phi_{total}$, the carrier phase-range equation for each satellite then becomes:

$$\Phi(t) = \rho + c \cdot (dT - dt) - d_{iono} + d_{trop} + \lambda \cdot N(t) \qquad (4\text{-}17)$$

where: $\Phi(t)$ = the phase-range measurement at time epoch t
  ρ = the true (but unknown) range from satellite to user
  c = the speed of light
  dt = the user clock offset
  dT = satellite clock offset
  λ = the carrier frequency wavelength
  N(t) = the integer phase ambiguity term at time epoch t
  d_{iono} = the range equivalent ionospheric delay term
  d_{trop} = the range equivalent tropospheric delay term

According to (6: sec 8.3), the error terms that appear in Equation (4-17) above are the same as those that affect GPS code-phase pseudorange measurements (Equation (3-25)) except for the negative sign on the ionospheric delay and the appearance of the phase ambiguity term N. It should be noted at this point that the user and satellite clock bias terms in Equation (4-17) (dt and dT) are time offsets from true GPS time; the MSOFE models these parameters as range-equivalent to the error caused by the offsets. Due to this difference, the MSOFE measurement equation will have both terms positive rather than dT-dt. This sign convention must be maintained throughout the simulation. The sign of the ionospheric delay term, however, is not changed as it is modelled as a first order Markov process. Using the notation of Chapter III then, Equation (4-17) can be rewritten to:

$$R_{CPGPS} = R_t + \delta R_{Uclk} + \delta R_{Sclk} - \delta R_{iono} + \delta R_{trop} + \delta R_N + v \qquad (4\text{-}18)$$

where: R_{CPGPS} = Carrier Phase-range measurement
  δR_N = Range equivalent of the cycle ambiguity term N(t)
  v = zero mean white Gaussian measurement noise

and the rest is the same as for Equation (3-25). Note the addition of the v term representing zero-mean white Gaussian measurement noise. The variance of the measurement noise depends on the type of receiver being used in the application. Most carrier phase receivers can measure a phase difference to 1 to 2 percent accuracy. The wavelength of a GPS L-band carrier signal is approximately 9.75 inches (25 centimeters) and therefore, using the more conservative 2% accuracy, a carrier phase receiver can measure to within 0.02 x 9.75 in. = 0.195 inches (0.01625 feet). If this value of 0.01625 feet represents the one-sigma error standard deviation (which is a more conservative error model than using it as the 2 or greater sigma standard deviation), then the measurement noise error variance would be $R(t_i) =$ $(0.01625)^2 = 2.641 \times 10^{-4} \text{ ft}^2$. This measurement noise variance is approximately 341,000 times better than the GPS and DGPS measurement noise variance (recall that the GPS and DGPS measurement noise variance is 9 ft^2).

Data from the ground-based receiver (GBR; see Chapter III) can now be used to correct the above phase-range equation exactly as was done in Chapter III with the GPS pseudorange equation (Eq. (3-25)) to produce the DGPS pseudorange equation (Eq. (3-38)). Recall that the differential corrections removed the satellite clock error completely and significantly reduced the atmospheric delay errors. Differential corrections will have no effect on the phase ambiguity term. After differential corrections have been applied, the phase-range equation is:

$$R_{CPGPS} = R_t + \delta R_{Uclk} - \delta R_{iono} + \delta R_{trop} + \delta R_N + v \qquad (4\text{-}19)$$

As in the cases of the RRS, GPS, and DGPS measurements, a difference measurement is required. The second source of CPGPS phase-range measurement will come from the INS-indicated position and the satellite-computed position, just as in the GPS and DGPS code-phase measurements. The derivation of this is presented in Chapter III, Equations (3-26)

through (3-29). The CPGPS phase-range difference measurement is formed by subtracting Equation (4-19) from Equation (3-29) to obtain:

$$
\begin{aligned}
\delta z = R_{INS} - R_{CPGPS} = &-\frac{x_s - x_u}{|R|} \cdot \delta x_U - \frac{y_s - y_u}{|R|} \cdot \delta y_U - \frac{z_s - z_u}{|R|} \cdot \delta z_U \\
&+ \frac{x_s - x_u}{|R|} \cdot \delta x_S + \frac{y_s - y_u}{|R|} \cdot \delta y_S + \frac{z_s - z_u}{|R|} \cdot \delta z_S \\
&- \delta R_{trop} + \delta R_{iono} - \delta R_{Uclk} \\
&- \delta R_N - v
\end{aligned}
\tag{4-20}
$$

The phase-range measurement updates will occur every 10 seconds to coincide with GPS code-phase measurement updates. Note that, as in all previous measurement cases, the true range term R_t drops out in the differencing, the measurement δz is a linear combination of error states, and the coefficients of Equation (4-19) appear in the H matrix of the measurement update cycle. These updates are performed in the Litton ECEF frame.

4.3 The PNRS Model:

4.3.1 The Truth Model. The Precision Navigation Reference System will utilize the existing model of the ENRS with the addition of carrier phase GPS. Carrier phase GPS requires the addition of four states to the truth model; the four phase ambiguity terms δR_{N1} through δR_{N4} (one for each satellite). These additional states are presented in Appendix A, Table A-10. In the truth model and without cycle slips, these terms are modelled as time-invariant random biases:

$$
\begin{bmatrix} \delta \dot{R}_{N1} \\ \delta \dot{R}_{N2} \\ \delta \dot{R}_{N3} \\ \delta \dot{R}_{N4} \end{bmatrix} = \begin{bmatrix} 0 & 0 & 0 & 0 \\ 0 & 0 & 0 & 0 \\ 0 & 0 & 0 & 0 \\ 0 & 0 & 0 & 0 \end{bmatrix} \cdot \begin{bmatrix} \delta R_{N1} \\ \delta R_{N2} \\ \delta R_{N3} \\ \delta R_{N4} \end{bmatrix}
\tag{4-21}
$$

with initial state estimates and covariance:

$$
\delta \hat{R}_N = 0
\tag{4-22}
$$

4-8

$$P_{R_x}(t_o) = \begin{bmatrix} 13 & 0 & 0 & 0 \\ 0 & 13 & 0 & 0 \\ 0 & 0 & 13 & 0 \\ 0 & 0 & 0 & 13 \end{bmatrix} ft^2 \qquad (4\text{-}23)$$

The value of 13 ft^2 for the initial state covariance was derived using the idea that the *initial* differentially corrected carrier phase measurement cannot be more accurate than the *initial* differentially corrected code-phase measurement. Recall that Equation (3-38) is the DGPS code-phase measurement equation and Equation (4-19) is the differentially corrected CPGPS carrier phase measurement equation. If $R_{DGPS}(t_o)$ is equal to $R_{CPGPS}(t_o)$, and the measurements are using the same satellite and user-clock (a good assumption, as most carrier phase receivers can also produce a code-phase measurement), then Equation (3-38) - Equation (4-19) produces:

$$R_{DGPS}(t_o) - R_{CPGPS}(t_o) = 0 = 2\delta R_{iono}(t_o) - \delta R_N(t_o) + v_{DGPS}(t_o) - v_{CPGPS}(t_o) \qquad (4\text{-}24)$$

where the true range $R_t(t_o)$, the tropospheric delay $\delta R_{trop}(t_o)$, and the user clock error $\delta R_{Udk}(t_o)$, which are common to both measurements, cancel. Solving for $\delta R_N(t_o)$, the following is obtained:

$$\delta R_N(t_o) = 2\delta R_{iono}(t_o) + v_{DGPS}(t_o) - v_{CPGPS}(t_o) \qquad (4\text{-}25)$$

To calculate the initial variance of $\delta R_N(t_o)$, which is $E[(\delta R_N(t_o))^2]$, both sides of Equation (4-25) are squared and the expected value is taken. Note that the time designation (t_o) has been dropped in Equation (4-26):

$$\begin{aligned} E[(\delta R_N)^2] &= E[(2\delta R_{iono} + v_{DGPS} - v_{CPGPS})^2] \\ &= E[(4\delta R_{iono}^2 + v_{DGPS}^2 + v_{CPGPS}^2 + 4\delta R_{iono}v_{DGPS} - 4\delta R_{iono}v_{CPGPS} + 2v_{DGPS}v_{CPGPS})] \quad (4\text{-}26) \\ &= 4E[\delta R_{iono}^2] + E[v_{DGPS}^2] + E[v_{CPGPS}^2] + 4E[\delta R_{iono}v_{DGPS}] - 4E[\delta R_{iono}v_{CPGPS}] \\ &\qquad\qquad\qquad\qquad\qquad\qquad\qquad\qquad\qquad + 2E[v_{DGPS}v_{CPGPS}] \end{aligned}$$

Since the v terms in Equation (4-26) are defined as white Gaussian processes with zero mean, then the v terms will be independent and uncorrelated from each other and the δR_{iono} term

This allows the separation of the cross terms of Equation (4-26) and, since $E[v] = 0$, the cross terms cancel out. The remaining terms have all been previously defined as:

$E[(\delta R_{iono})^2]$ $= 1 \text{ ft}^2$ (see Equation (3-35))

$E[v_{DGPS}{}^2]$ $= 9 \text{ ft}^2$ (see Section 3.6.2)

$E[v_{CPGPS}{}^2]$ $= 2.641 \times 10^{-4} \text{ ft}^2$ (see Section 4.2.2)

The computed value for $E[(\delta R_N)^2]$ using Equation (4-26) is then:

$$E[(\delta R_N)^2] = 4(1) + 9 + 2.641 \times 10^{-4} \approx 13 \text{ ft}^2 \qquad (4\text{-}27)$$

Note that this derivation is only valid at the initial time t_0 to produce the initial covariance matrix $P_{R_N}(t_0)$.

These four states occupy states 68 through 71 of the PNRS truth model. The error state vector for the PNRS truth model is completely specified in Appendix A, Tables A-16 through A-19. Note that the GPS satellite-dependent states, states 68-95 of the NRS truth model and states 68-87 of the ENRS truth model, are now states 72-91 of the PNRS truth model. This change was accomplished in order to facilitate data reduction in the MSOFE software.

4.3.2 The Filter Model. The phase-range measurement of Equation (4-18) and the truth model phase-range is biased by the phase ambiguity term δR_N. If cycle slips were not to occur, then this would remain a simple constant (but unknown) bias and may not require repeated estimation in the filter model. However, cycle slips are likely to occur, so this term must be estimated and compensated for in the filter. The addition of these four states increases the filter dimension from 67 states to 71 states. Recall that one of the CIGTF requirements was to have a filter of 70 or fewer states. This 71 state filter violates this requirement, however, further studies into filter order reduction can probably produce a filter

of under 70 states. These four states will be modelled in the filter as random biases with some additive zero mean white Gaussian noise:

$$
\begin{bmatrix} \delta \dot{R}_{N1} \\ \delta \dot{R}_{N2} \\ \delta \dot{R}_{N3} \\ \delta \dot{R}_{N4} \end{bmatrix} = \begin{bmatrix} 0 & 0 & 0 & 0 \\ 0 & 0 & 0 & 0 \\ 0 & 0 & 0 & 0 \\ 0 & 0 & 0 & 0 \end{bmatrix} \cdot \begin{bmatrix} \delta R_{N1} \\ \delta R_{N2} \\ \delta R_{N3} \\ \delta R_{N4} \end{bmatrix} + \begin{bmatrix} w_{N1} \\ w_{N2} \\ w_{N3} \\ w_{N4} \end{bmatrix}
\tag{4-28}
$$

where

$$
E[w_{N}(t)] = 0
\tag{4-29}
$$

and

$$
E[w_{N}(t)w_{N}(t+\tau)] = \begin{bmatrix} a & 0 & 0 & 0 \\ 0 & b & 0 & 0 \\ 0 & 0 & c & 0 \\ 0 & 0 & 0 & d \end{bmatrix} \cdot \delta(\tau)
\tag{4-30}
$$

Where the values for a, b, c, and d (the noise variances) will be defined by tuning this filter model. The complete PNRS filter error state vector is presented in Appendix A, Tables A-16 through A-19 (ignore all states above 71).

4.4 Differencing Technique (6).

4.4.1 The Single Difference.
There are three forms of the single difference: the between-receivers single difference, the between-satellites single difference, and the between-time-epochs single difference. The between-receivers single difference is formed by subtracting the phase-range measurement from one receiver from that of another, presumably close-by, receiver that is tracking the same satellite. If the first receiver's measurement is represented by (using Equation (4-18)):

$$
R_1 = R_{t_1} + \delta R_{Uclk_1} + \delta R_{Sclk} - \delta R_{iono_1} + \delta R_{trop_1} + \delta R_{N_1} + v_1
\tag{4-31}
$$

and the second receiver's measurement is represented by:

4-11

$$R_2 = R_{t_2} + \delta R_{Uclk_2} + \delta R_{Sclk} - \delta R_{iono_2} + \delta R_{trop_2} + \delta R_{N_2} + v_2 \qquad (4\text{-}32)$$

then subtracting R_2 from R_1 would result in the cancellation of the common satellite clock bias term δR_{Sclk}. If the variable prefix SD_R represents the between-receivers single difference of that variable (ie: $SD_R(R) = R_1\text{-}R_2$) then the between-receiver single difference is:

$$SD_R(R) = SD_R(R_t) + SD_R(\delta R_{Uclk}) - SD_R(\delta R_{iono}) + \\ SD_R(\delta R_{trop}) + SD_R(\delta R_N) + v \qquad (4\text{-}33)$$

The single difference of the measurement noise term v will not change its characteristics (that is, it remains a zero-mean, white Gaussian process; however, its statistics do change) and therefore $SD(v)$ can be represented by v. The measurement $SD_R(R)$ is then a measurement of the relative distance between the two receivers. This single differencing method is very similar to Differential GPS and thus will greatly reduce the error contributions of the atmospheric delay terms δR_{iono} and δR_{trop} (depending on how close the receivers are to each other). This method requires the two receivers to be tracking the same set of at least four satellites in order to produce a reduced error navigation solution. Figure 4-2 depicts the between-receivers single difference.

The between-satellites single difference is computed by subtracting the phase-range measurement from one satellite from that of another satellite, where the measurements are made by the same receiver. If the first measurement is represented by:

$$R_1 = R_{t_1} + \delta R_{Uclk} + \delta R_{Sclk_1} - \delta R_{iono_1} + \delta R_{trop_1} + \delta R_{N_1} + v_1 \qquad (4\text{-}34)$$

and the second by:

$$R_2 = R_{t_2} + \delta R_{Uclk} + \delta R_{Sclk_2} - \delta R_{iono_2} + \delta R_{trop_2} + \delta R_{N_2} + v_2 \qquad (4\text{-}35)$$

Then this single difference, $SD_S(R)$, would result in the cancellation of the common user clock bias term δR_{Uclk}:
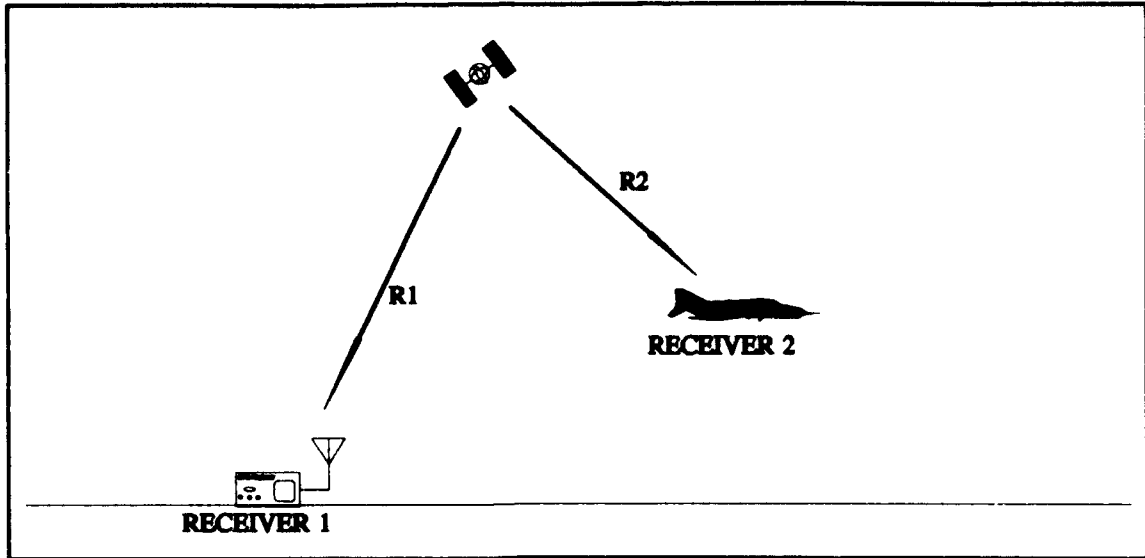
Figure 4-2: Between-Receivers Single Difference

$$SD_S(R) = SD_S(R_t) + SD_S(\delta R_{Sclk}) - SD_S(\delta R_{iono}) + \\ SD_S(\delta R_{trop}) + SD_S(\delta R_N) + v$$

(4-36)

This measurement $SD_S(R)$ is a measurement of the relative distance between the two satellites. Figure 4-3 depicts the between-satellites single difference.

The between-time-epochs, or Doppler, single difference is formed by subtracting the phase-range measurement made by the receiver at one time epoch, t_1, from that of another time epoch, t_2, using the same receiver and satellite. The result is a cancellation of the time-invariant phase ambiguity term δR_N. Note that the user clock bias error and satellite clock bias error would also cancel if they were time-invariant. These terms, however have a time-varying drift associated with them and therefore are not time invariant. The between time epoch single difference, $SD_t(R)$, is then:

$$SD_t(R) = SD_t(R_t) + SD_t(\delta R_{Uclk}) + SD_t(\delta R_{Sclk}) - \\ SD_t(\delta R_{iono}) + SD_t(\delta R_{trop}) + v$$

(4-37)
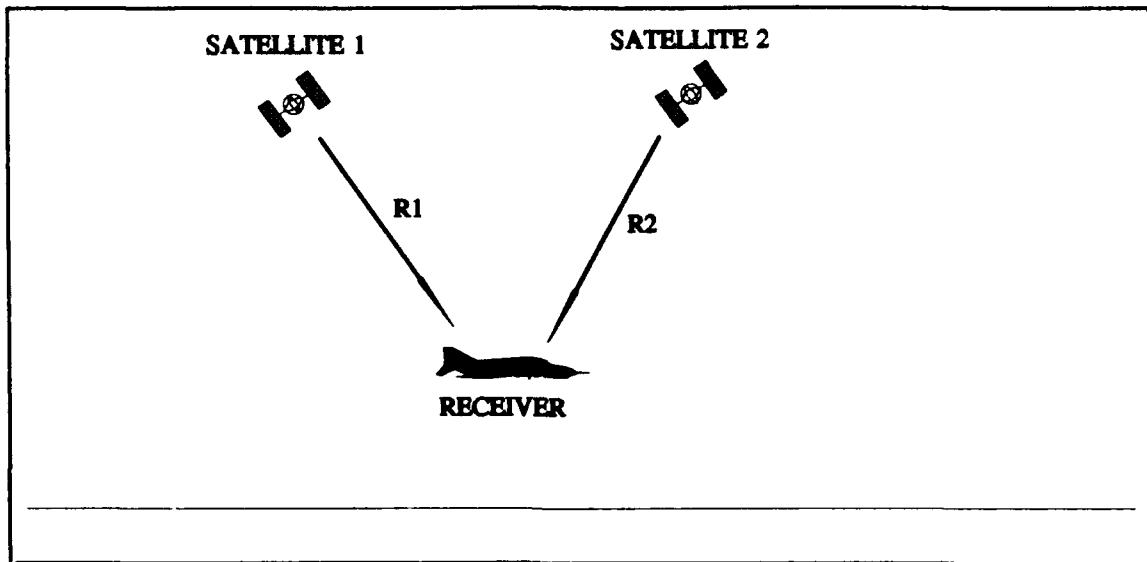
Figure 4-3: Between-Satellites Single Difference

Recall that δR_N is only time-invariant if no cycle slips were to occur during the time interval t_1 to t_2. If a cycle slip were to occur during this time interval, then the resulting single difference equation would be biased by an amount equal to the number of integer cycles "slipped". Figure 4-4 depicts the between-time-epochs single difference.

4.4.2 The Double Difference. The double difference is formed by subtraction of two single difference measurements. There are three forms of the double difference: between-receivers/time-epochs, between-satellites/time-epochs, and between-receivers/satellites. The between-receivers/time-epochs double difference is formed by subtracting the between-receivers single difference measurement at one time-epoch from that of another later time-epoch. The same measurement can be formed by subtracting the between-time-epochs single difference measurement of one receiver from that of another receiver, using the same time-epoch and tracking the same satellite. The result is the cancellation of both the time-invariant phase ambiguity term and the satellite clock error term and the reduction in error contribution from the atmospheric delay terms:
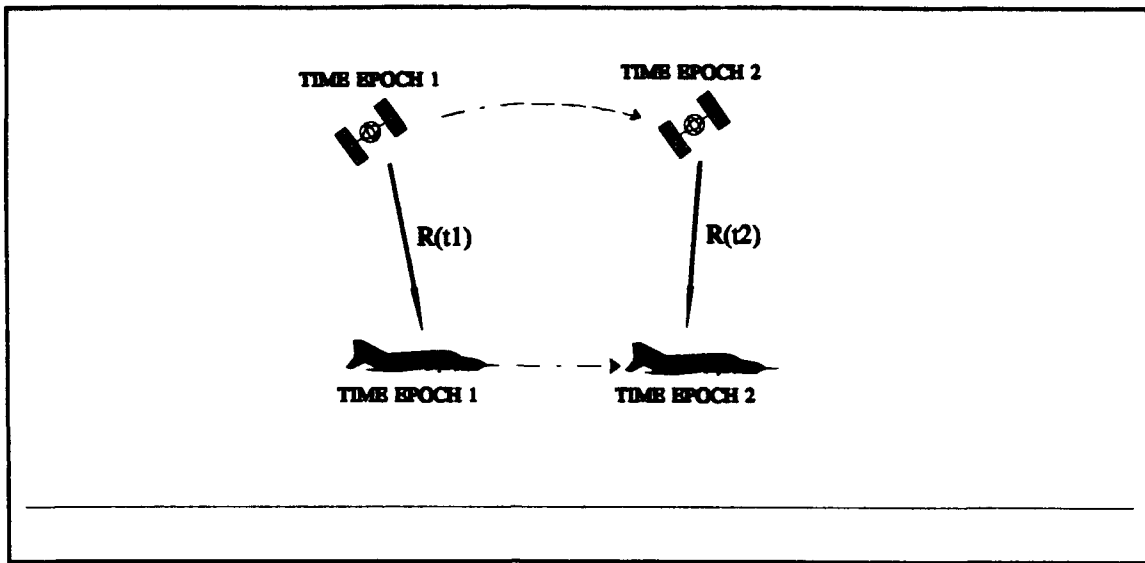
Figure 4-4: Between-Time-Epochs Single Difference

$$DD_{Rt} (R) = DD_{Rt} (\delta R_t) + DD_{Rt} (\delta R_{Uclk}) - DD_{Rt} (\delta R_{iono}) + DD_{Rt} (\delta R_{trop}) + v \qquad (4\text{-}38)$$

The between-satellites/time-epochs double difference measurement is formed by subtracting the between-satellites single difference measurement of one time-epoch from that of another later time-epoch. The same measurement can be obtained by subtracting the between-time-epochs single difference measurement of one satellite from that of another satellite using the same time-epoch and receiver. The result is the cancellation of the user clock error term and the time-invariant phase ambiguity term:

$$DD_{St} (R) = DD_{St} (\delta R_t) + DD_{St} (\delta R_{Sclk}) - DD_{St} (\delta R_{iono}) + DD_{St} (\delta R_{trop}) + v \qquad (4\text{-}39)$$

The between-receivers/satellites double difference is formed by subtracting a between-receivers single difference measurement from another using the same two receivers but two different satellites. The same measurement can be formed by subtracting a between-satellites single difference from another, using the same pair of satellites but two different receivers. The result is the cancellation of both the satellite clock bias error term and the user clock bias error term and the reduction in error contribution from the atmospheric terms:

4-15

$$DD_{RS}(\delta R) = DD_{RS}(R_t) - DD_{RS}(\delta R_{iono}) + DD_{RS}(\delta R_{trop}) + DD_{RS}(\delta R_N) + v \qquad (4\text{-}40)$$

4.4.3 The Triple Difference. If a between-receivers/satellites double difference measurement at one time-epoch t_1 is subtracted from another double difference measurement at time-epoch t_2 (where $t_2 > t_1$), the triple difference is formed. Triple differencing not only removes the satellite clock and user clock bias terms and reduces the atmospheric delay terms, but it also removes the time-invariant phase ambiguity term δR_N:

$$TD(R) = TD(R_t) - TD(R_{iono}) + TD(R_{trop}) + v \qquad (4\text{-}41)$$

Table 4-1 summarizes the effects of single, double, and triple differencing on the phase-range measurement equation.

Observation	Terms Eliminated	Terms Reduced
Between Rx Single Difference	Satellite clock term	Ionospheric and tropospheric delay terms
Between SV Single Difference	User clock term	
Between Time Single Difference	Phase ambiguity term	Ionospheric and tropospheric delay terms
DD_{Rt} Double Difference	Satellite clock term Phase ambiguity term	Ionospheric and tropospheric delay terms
DD_{St} Double Difference	User clock term Phase ambiguity term	
DD_{RS} Double Difference	Satellite clock term User clock term	Ionospheric and tropospheric delay terms
Triple Difference	Satellite clock term User clock term Phase ambiguity term	Ionospheric and tropospheric delay terms

Table 4-1: Effects of Differencing Techniques.

where Rx means receiver, SV means Satellite Vehicle, DD refers to the double difference, and the subscript Rt means between receivers/time-epochs, St means between satellites/time-epochs, and RS means between receivers/satellites.

4.5 Cycle Slips.

If, for any reason, the carrier signal from a GPS satellite to the receiver is interrupted, the receiver will begin to reacquire the signal. When the signal is reacquired, the fractional part of the measurement remains unchanged. However, the receiver may lock onto a different integer phase cycle of the transmission than it had before the interruption, while believing it to be unchanged. If this were to happen, then there would be a "jump" in the phase-range measurement equivalent to the number of integer phase cycles "jumped" or "slipped". This phenomenon, which can be quite frequent (on the order of 1 per minute of operation) (6: sec 9.10) is known as *cycle slip*.

The occurrence of cycle slips cannot be predicted, as they are caused by many different things. Terrain, weather, multipath reflections, jamming or spoofing, noise bursts, and signal blockage are among the causes of cycle slip. The use of single differences, double differences, and triple differences can assist in the detection of cycle slips.

In the phase-range measurement equation developed in this chapter for this thesis research, Equation (4-19), a cycle slip would cause a jump in the phase-range measurement R_{CPGPS}. This can be interpreted as a change in the cycle ambiguity term δR_N. Since δR_N is continuously estimated in the EKF, it is possible to account and correct for cycle slips through the estimation of this error term.

4.5.1 Simulation of Cycle Slips. In order to test the filter's robustness to cycle slips, they must be simulated in a realistic manner in the truth model. At this point it is convenient to recall that, for no cycle slips, the δR_N term of the truth model is constant over the entire

4-17

simulation. A cycle slip can then be simulated as a step bias or sudden change of this term.

Note that a bias in this truth state does not affect the other truth states in the MSOFE

simulation software and therefore does not affect the truth position, velocity, or attitude states.

Since δR_N is measured in range units (feet), this bias would have to be in the form of the

range equivalent of the number of cycles "slipped". If K represents the number of integer

cycles "slipped" (K can be either positive or negative), then the cycle slip simulation would be

of the form:

$$\delta R_N(t^+) = \delta R_N(t^-) + K \cdot \lambda \qquad (4\text{-}42)$$

where: t^+ represents the time just after the cycle slip occurs

t^- represents the time just before the cycle slip occurs

K represents the integer number of cycles "slipped" (+ or -)

λ represents the wavelength of the carrier signal

Using information gained in conversations with Mr. Scott Dance of CIGTF (12) and Dr.

Frank Von Graas, a leading expert in the area of carrier-phase GPS, of Ohio University (23),

realistic cycle slips were developed for this simulation. Cycle slips can appear in two different

ways. One is a small cycle slip which is the result of a sudden and quick burst of noise in the

GPS receiver at the frequency of the carrier signal. The other is a large cycle slip which is

generally preceded by a sustained loss of lock on a particular GPS satellite. When the receiver

regains lock, the phase ambiguity term has changed (as the range between the satellite and

receiver has changed). Most loss-of-lock occurrences on GPS satellites are caused by aircraft

maneuvers that block the incoming signal. These blockages last a short time (3 to 10 seconds,

in general, depending on the maneuver). Longer loss-of-lock's can occur due to terrain,

weather, etc. It is logical then that simulations of this type of cycle slip should be preceded

by a loss-of-lock on a particular satellite. This can be performed in MSOFE by not performing

the update for a particular satellite phase-range measurement, as well as that same satellite's differential pseudorange measurement, for a period of time.

With these in mind, the tuned PNRS MSOFE simulation can then be programmed to simulate loss-of-lock and cycle slips of any magnitude, at any time epoch, and on any satellite. Chapter 5 will discuss the timing and range values used for the simulated cycle slips.

4.5.2 Cycle Slip Correction. Since the filter receives measurement updates from the RRS and code-phase GPS as well as the carrier-phase GPS, it is possible that cycle slips below some threshold value may be tolerable and possibly negligible in the filter's calculation of position, velocity, and attitude (as well as the other states). In this case, the filter could be self-correcting and cycle slips may not pose a problem. It is also possible that larger cycle slips may be self-correcting. Though these larger cycle slips may result in large errors in the navigation solution, the filter may be stable and these errors may return to nominal.

Cycle slips can be treated as biases in the satellite phase-range and detection algorithms such as the Chi^2, Generalized Maximum Likelihood (GLR), and multiple-model adaptation can be employed to quickly detect them. These techniques are currently being explored in general by Mosle (19) as his AFIT Masters degree research.

4.6 Summary.

This chapter presented the development of the 91-state PNRS truth model and the 71-state filter model. Theory and development of the carrier-phase GPS measurement updates and how they are integrated into the ENRS to form the PNRS were also presented. Some ideas about cycle slip simulation, detection, and correction were also presented. Simulation results and discussion of these results are discussed in Chapter 5 of this thesis.

Chapter V. Filter Implementation Results

5.1 Overview.

This chapter presents the results of the simulation studies of the NRS, the ENRS, and the PNRS filters developed in Chapters III and IV of this thesis. Evaluations of each filter's performance is presented, as well as a comparison of accuracy between these filters and those evaluated by Negast. The results of the simulation runs are in the form of state-error plots and are presented in Appendices D through F. Cycle slips, as described in Chapter IV, are simulated and the results presented, also in the form of state-error plots, in Appendices G through J. As will be seen, this PNRS filter is able to recover very well from the simulated cycle slips.

These state-error plots show the results of a 15-run Monte-Carlo average of the state-error (truth state value minus the filter state estimate), the state-error average ± its true 1σ value (σ being the standard deviation) calculated from the Monte-Carlo runs, and the filter predicted ± 1σ value. In an optimally tuned filter, the filter-predicted 1σ should be roughly equivalent to this true error 1σ. A more conservatively tuned filter would have the filter-predicted 1σ greater than the true error 1σ. This chapter also presents the final tuning parameters ($Q(t)$ and $R(t_i)$) used for each of these three filters.

5.2 Tuning Parameters.

A complete listing of the tuning parameters used for the NRS, ENRS, and PNRS filters is presented in Appendix C. Note that the truth model $Q(t)$ and $R(t_i)$ values for each of the filter states are also presented for comparison. A glossary of the Appendix C tables is presented below in Table 5-1.

Each of the three filters is conservatively tuned. Though the tuning could be improved, this conservative tuning is acceptable for this simulation study. Note that all the cycle slip

simulations were performed using a more conservatively tuned PNRS filter than the PNRS simulation of Appendix F. This was done due to the fact that the tuning process took quite some time to accomplish and the cycle slip simulations could be run during this process. Since the objective of these simulations was to explore the cycle slip phenomenon and not to define the accuracy of the filter when subjected to cycle slips, then this conservative tuning is acceptable. All cycle slip simulations were run with the same filter parameters.

Filter	Q(t) Tables	R(t,) Table
67-State NRS	C-1 through C-3	C-4
67-State ENRS	C-5 through C-7	C-8
71-State PNRS	C-9 through C-11	C-12

Table 5-1: Glossary of Appendix C Tables

5.3 The 67-State NRS Filter.

Appendix D presents the results of the NRS simulation study. The MSOFE simulation software model was put through the 2-hour (7200 sec) flight profile shown in Plot D-1 (a), (b), and (c). A complete 7200-second flight profile, 15-run Monte-Carlo MSOFE simulation on the Sun SPARC 2 workstations took approximately 60 hours to complete. Plot D-2 shows the errors in the filter-computed longitude and latitude, Plot D-3 shows the errors in the filter-computed altitude and barometric altitude, and Plot D-4 shows the errors in the three filter-computed inertial platform tilt states. Note that the LN-93 INS utilizes the wander angle method for navigation solution computation and thus these states had to be transformed to the North-West-Up navigation frame for presentation. Plot D-5 shows the errors in the three filter-computed velocity states, Plot D-6 shows the errors in the filter-computed RRS range bias, velocity bias, and atmospheric propagation delay states, and Plot D-7 shows the errors in the three filter-computed RRS transponder surveyed position (X, Y, and Z) errors. Note that

the RRS atmospheric delay and the X, Y, and Z position errors are transponder-dependent (see Chapter III), and thus there is one of these states for each of the six transponders modelled in the simulation. These plots only show the errors for transponder #1 but are representative of all six transponders. Plot D-8 shows the errors in the filter-computed GPS user clock bias and user clock drift states.

For each of these plots, a computed temporal average of the true 1σ can be made and compared to that of Negast's 69-state NRS filter results (1: Appendix F). These temporal averages are computed starting from time = 60 sec (to allow transient effects to die down) to the end of the flight profile, time = 7200 sec. These temporal averages are presented below in Table 5-2 (along with the temporal averages of the ENRS and PNRS as implemented in this thesis research). It can be seen from this comparison that this NRS filter appears to be worse than Negast's equivalent NRS filter. It should be noted, however, that many errors were found and corrected by this author and Mosle (19) in the MSOFE code utilized by Vasquez and Negast. These errors could easily account for the large discrepancies seen in some of these states. Due to these errors, it is not practical to compare the results of this thesis to those of Negast or any others.

5.4 The 67-State ENRS Filter.

Appendix E presents the results of the 67-state ENRS (differential GPS) MSOFE simulation study. This appendix is laid out exactly the same as Appendix D, so as to facilitate comparison between these results and those of the 67-state NRS filter of Appendix D.

Differential corrections, as described in Chapter III, not only improve the accuracy of the GPS pseudorange measurements, but also, by way of removing the code-loop and satellite clock bias error contributions, and significantly reducing the effects of the atmosphere, allow the filter model to match the truth model more closely. Thus, an improvement in the accuracy of this filter over the NRS should be expected, especially in the filter estimation of the GPS

(a)

	Long. (ft)	Lat. (ft)	Alt. (ft)	Baro. (ft)	NTilt (deg)	WTilt (deg)	AzTilt (deg)
Negast's NRS	4.21	3.28	9.04	-	5.9×10^{-4}	3.8×10^{-4}	5.1×10^{-3}
NRS	7.54	7.10	10.52	37.61	3.0×10^{-4}	3.0×10^{-4}	2.2×10^{-4}
ENRS	1.64	1.71	6.63	36.54	3.0×10^{-4}	2.9×10^{-4}	1.9×10^{-4}
PNRS	1.47	1.62	6.00	36.31	3.0×10^{-4}	3.0×10^{-4}	2.2×10^{-4}

(b)

	NVel. (ft/sec)	WVel. (ft/sec)	VVel. (ft/sec)	XpRnge (ft)	XpVel. (ft/sec)	XpAtm (ft)
Negast's NRS	0.026	0.033	0.070	-	-	-
NRS	0.10	0.10	0.10	5.07	0.0068	0.105
ENRS	0.10	0.10	0.10	1.82	0.0091	0.090
PNRS	0.10	0.10	0.10	1.76	0.0072	0.106

(c)

	RRS X (ft)	RRS Y (ft)	RRS Z (ft)	GPS B. (ft)	GPS D. (ft/sec)
Negast's NRS	-	-	-	-	-
NRS	4.23	4.55	2.68	4.73	0.0016
ENRS	2.37	2.03	1.23	1.18	0.0012
PNRS	3.88	2.96	1.42	0.89	0.0009

Table 5-2: Comparison of NRS, ENRS, and PNRS True Error 1σ

user clock bias and drift states. Again, temporal averages of the true 1σ errors for each state of interest for this ENRS filter are tabulated in Table 5-2, along with the corresponding NRS temporal averages. Note that significant improvements, from 1.2 to 4.6 times, are seen in almost every state.

The barometric altimeter and the three velocity states see almost no improvement, as they are estimated using the barometric altimeter measurement and velocity measurement updates (see Chapter III, Section 3.8) that occur every two seconds (as opposed to every six seconds for the RRS and every ten seconds for the GPS) and do not change from the NRS to the ENRS filters. The frequency and accuracy of these measurements stabilize these states over the entire flight profile, regardless of any other measurement updates. The three platform tilt states see little to no improvement, as the GPS and RRS measurements, which inherently add information to the position and velocity states, contribute very little to the INS platform tilt states. The INS model itself calculates the tilt errors and the INS model does not change from the NRS to the ENRS. This would indicate that there is little to no coupling between the position/velocity states and the platform tilt angle states. Due to the errors found in the Negast/Vasquez MSOFE code described in Section 5.3, this ENRS filter will not be compared to Negast's ENRS filter.

5.5 The 71-State PNRS Filter.

Appendix F presents the results of the 71-state PNRS MSOFE simulation study. This filter was put through the same 2-hour flight profile used for both the NRS and ENRS simulations in this thesis research. The plots of Appendix F are laid out exactly as in the previous two appendices (D and E), in order to facilitate comparison between filters. Note that there are an additional four plots: the four satellite phase ambiguity terms (in range equivalent format) which are not present in the NRS or the ENRS filters.

It can be seen from Table 5-2 that the PNRS is, as expected, more accurate for the most part than the ENRS, but not by much. The addition of high accuracy carrier-phase GPS measurements improves the EKF's ability to estimate all the states, however the additional uncertainty associated with the phase ambiguity states reduces the effects of the high accuracy measurements. It is for this reason that the improvement over the ENRS is not greater. As in the case of the ENRS, there is little to no improvement in the barometric altimeter state (Plot F-3 (a)), the three tilt states (Plot F-4), and the three velocity states (Plot F-5), for the same reasons as discussed earlier. The reader should note that tuning plays a large role in the accuracy of a Kalman filter and that better fine tuning of the PNRS filter will result in better accuracy. The RRS transponder surveyed position errors (in X, Y, and Z), Plot F-7, come out less accurate in the PNRS than in the ENRS. The reason for this is not clear. With the addition of a high accuracy carrier-phase measurement to the already existing RRS and DGPS measurements, it was expected that all the states would show an improvement. The improvement seen in the position states (latitude, longitude, and altitude) should have inherently produced a better estimate of the RRS transponder X, Y, and Z surveyed positions (through the RRS measurements). Further exploration of this problem is required and should be included as a task in further AFIT research using this MSOFE simulation model.

5.6 Cycle Slips.

Two types of cycle slips were simulated for this thesis research: a "small" cycle slip and a "large" cycle slip. Referring back to the discussion on cycle slip simulation in Chapter IV, a "small" cycle slip can be interpreted as a slip caused by a strong noise burst at the GPS signal carrier frequency. This would appear as an almost instantaneous change in the true phase ambiguity term on the order of 10 or fewer feet. A "large" cycle slip can be interpreted as a slip caused by reacquisition of a GPS satellite following a period of signal loss. This would appear as a loss of a particular GPS signal for a period of time followed by a change in

the true phase ambiguity term proportional to the change in receiver-satellite range over the outage period.

Before presenting the results of the cycle slip simulations, the PNRS MSOFE model was subjected to a simulated loss of code-phase and carrier-phase measurements from satellite #1. Appendix G presents the results of this study in the same order and format as the previous appendices. Measurements from satellite #1 were "turned off" at time = 400 seconds and "turned on" at time = 600 seconds (with the next satellite #1 GPS measurements being processed at time = 610 seconds). In this time period, measurements from only three GPS satellites were being processed by the EKF. In an integrated INS/GPS navigation system, the loss of a satellite would result in the filter's inability to compute the user clock bias term (3 equations from the 3 remaining satellites and 4 unknowns: X, Y, Z, and user clock bias). The computed navigation solution would then follow the user clock bias drift and their errors would grow in time. However, the inclusion of transponder measurement updates allows this filter to compute the aircraft X, Y, and Z position independent of the GPS measurements and therefore, theoretically, only one satellite measurement would be required to compute the user clock bias term. Using all the measurements produces an overdetermined solution and by losing one satellite, some of the accuracy of this solution would be lost. This is seen in the filter-computed state estimates in Appendix G. Note that, without satellite #1 measurements, satellite #1's phase ambiguity error (Plot G-9 (a)) grows exponentially, indicating that this state is only observable through the satellite #1 measurement updates. States associated with the RRS do not show this error, as the RRS continues to operate throughout this time period.

5.6.1 Large Cycle Slip Simulation. Appendix H presents the results of a large cycle slip simulation. The cycle slip was simulated using a 20-second loss of satellite #1, followed by a 30,000 foot change in the true phase ambiguity term for satellite #1. The time period of 20 seconds was chosen, as this is a good estimate of an extended GPS signal outage. Any

longer than 20 to 30 seconds and most receivers would attempt to acquire a different satellite. The amount of 30,000 feet was chosen, as this is approximately the change in true receiver-satellite range in the MSOFE simulation. This can be seen from Plot 5-1. This plot shows the delta-range (or rate-of-change of true range) for satellite #1 used in this study. The time period of the outage is time = 400 to time = 420 seconds, where the delta-range is approximately constant at 1500 feet/sec; 1500 feet/sec x 20 sec = 30,000 feet. Note that only the first 1000 seconds of the flight profile and error plots are presented in Appendix H. The plots of Appendix H are laid out exactly as those in the previous appendices for ease of comparison.
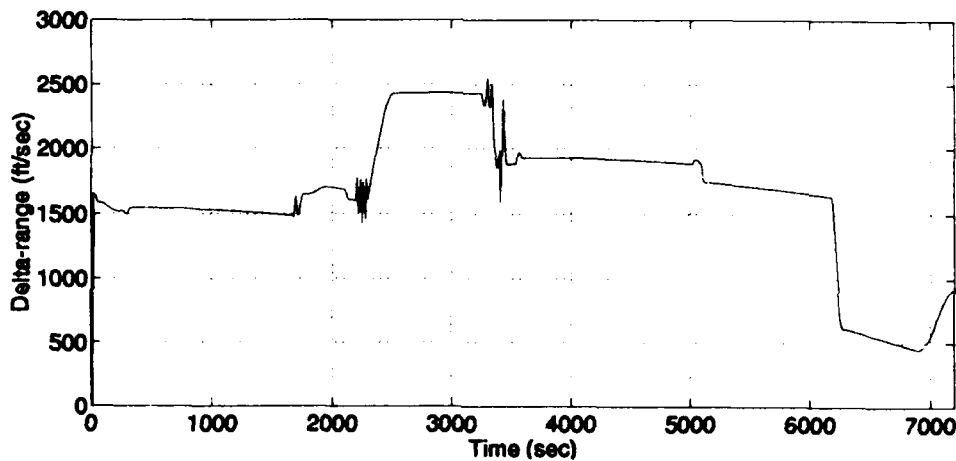
Plot 5-1: Satellite #1 True Delta-range

Appendix I presents the same results as Appendix H but with a "zoomed" time scale. Instead of showing the entire 1000 seconds of data, Appendix I shows only from time = 400 to time = 500 seconds. This allows closer inspection of the effects of this large cycle slip. Appendix I is laid out exactly as the previous appendices for ease of comparison.

There are several points of particular interest in these results. The first is that the 30,000 foot bias was applied at time = 400 sec but did not become observable in the navigation solution until time = 430 seconds. During the 20-second satellite #1 outage, this drastic change in the true phase ambiguity is unobservable in any state except for the satellite #1

5-8

phase ambiguity error, Plots H-9 (a) and I-9 (a). In fact, this cycle slip is not observable until the next measurement update from satellite #1 at time = 430 seconds (recall that GPS updates are performed every 10 seconds).

The next point of interest is that, at time = 430 seconds, when the corrupted measurement is incorporated into the EKF, there are large changes in all the states, including the RRS states (except the RRS velocity bias state, Plots H-8 (b) and I-8 (b)). This indicates that the phase ambiguity errors are observable in all the states (except RRS velocity bias). The navigation solution states, position and velocity, show errors that would be unacceptable to the user: as much as 800 feet in horizontal position, 1200 feet in altitude, and 2 feet/second in velocity.

The next and most significant point of interest is that, after satellite #1 is reacquired, every state begins to converge back to zero error! This indicates that, even with this large cycle slip, the EKF is stable and the navigation solution will return to its nominal error values. It can be seen from the Appendix H plots that this return to nominal error may take several minutes; however, the reader should note that no detection or correction scheme was employed in this simulation and that any such scheme could easily reduce these minutes to seconds. The addition of a detection/correction scheme would of course add complexity to the overall system, but, this addition complexity can be justified by the improved performance. This is the sort of decision that a navigation system design engineer must make.

5.6.2 Small Cycle Slip Simulation. Appendix J presents the results of a small cycle slip simulation. A cycle slip of 10 feet was applied at time = 400 seconds, with no loss of GPS satellite signals. This appendix is laid out exactly as the previous appendices for ease of comparison. This cycle slip cannot be distinguished in any of the plots of Appendix J, except in the satellite #1 phase ambiguity error, Plot J-9 (a). This plot also shows that, at time = 410 seconds, the time of the next GPS update, this phase ambiguity error is back to its nominal

value. These results indicate that small cycle slips are indistinguishable from the measurement and process noise of the filter and are "lost in the noise".

5.7 Summary.

More accurate measurement updates result in a more accurate EKF estimation of the states. This is obvious from the results of the NRS, ENRS, and PNRS studies. The high accuracy carrier phase measurements in the PNRS result in this filter being the most accurate of the three. The accuracy of the PNRS is not significantly better than the ENRS due to the additional uncertainty attributed to the phase ambiguity states.

The effect of large cycle slips, though far from negligible, is less of a problem than one may tend to believe (it helps, of course, to have an integrated INS/GPS/RRS navigation system!). The stability of the EKF in this PNRS simulation brings all the cycle slip error corrupted states back to a nominal error value within seconds or minutes (depending on the state). The incorporation of a cycle slip detector, though adding complexity to the overall system, would certainly aid in the EKF's recovery from these large errors. Small cycle slips, in the order of 10 feet, are "lost in the noise" and are negligible in the computation of the navigation solution.

Chapter VI. Conclusions and Recommendations

6.1 Overview.

This chapter presents conclusions drawn during this thesis research on all three filter and cycle slip simulations. Also, recommendations to assist future AFIT research that use this thesis as a reference and for further AFIT research in the area of carrier-phase GPS are presented.

6.2 Conclusions.

6.2.1 The NRS Filter.
Though the NRS filter developed and simulated in this thesis did not match the equivalent NRS filter of Negast, the errors found (see Chapter V) in the Negast/Vasquez MSOFE code easily account for the discrepancies. This NRS filter actually performed worse than Negast's; however, it produced more "realistic" results and was deemed sufficient to use as a baseline for evaluating the performance of the ENRS and PNRS.

6.2.2 The ENRS Filter.
As Negast found in his ENRS simulation (1), the addition of differential corrections to the GPS pseudorange measurement updates greatly increased the accuracy of the filter. These improvements ranged from 1.2 to 4.6 times better. The conclusion that can be drawn from this is that DGPS measurement updates to the NRS improve the accuracy enough to allow the ENRS to be used as an adequate reference system to test current navigation systems.

6.2.3 The PNRS Filter.
From the results presented in Chapter V and in Appendix F, it can be seen that the addition of high accuracy carrier-phase GPS measurements, using a between-receivers single difference technique, increased the accuracy of the reference system.

Although "orders of magnitude" improvements were not seen, this one result is enough to justify further research into the use of carrier-phase GPS.

6.2.4 Cycle Slips. The results of the cycle slip simulation tests of Chapter V allow this one very important conclusion to be drawn: carrier-phase GPS cycle slips, whether large or small, do not cause this PNRS filter to become unstable. In fact, small cycle slips can become "lost in the noise" and never become observable in the navigation solution. With the filter's ability to estimate the phase ambiguity term at each measurement update time, the filter is always able to converge back to a navigation solution with nominal errors. It would be interesting to see if this convergence time can be greatly decreased with the addition of some kind of detection and correction algorithm in the filter.

6.3 Recommendations.

There are many recommendations to pass on to future AFIT researchers. Some of these recommendations involve the simulation of the filters using the MSOFE software tool developed and used in this thesis research. The following contains the most important recommendations, as determined by the author and the thesis committee members.

6.3.1 Velocity-Aiding Measurements. As mentioned in Chapter III, the velocity measurement updates to all three filters simulated in this thesis were not realistic. Negast and his predecessors discovered that incorporation of RRS and GPS delta-range measurements did not produce satisfactory results. If realistic velocity measurements are required, which may or may not be the case, then some form of realistic velocity measurement (for example, a doppler radar set) must be simulated in the MSOFE software in place of the present velocity measurements.

6.3.2 GPS Satellite Selection and Switching. In the "real world", GPS receivers will change GPS satellites based on best computed GDOP, or else one or more satellites may set or move out of view. When this action of changing satellites was simulated in the MSOFE software, large biases and errors were seen in the state-error plots. This thesis continued with the use of the same four satellites for the entire 2-hour flight profile; however, if satellite switching is desired in future simulations, then this section of the MSOFE software must be examined closely and any errors or problems corrected.

6.3.3 Order Reduction of the Filter. With the current truth and filter model sizes, an entire 15-run Monte Carlo, 2-hour flight profile run takes over 60 hours to complete on AFIT's SUN SPARC 2 workstations. Though the recent addition of two SPARC 10 workstations may decrease the run time somewhat, it is still much longer than it may have to be. Negast recommended (1: Ch 6) that the RRS filter model be reduced from 26 states to 2. It may also be possible to reduce the order of the LN-93 INS filter model, though this thesis contains no supporting evidence for this. Some evidence of the impact of these reductions can be seen in Vasquez (18) and Mosle (19). Filter order reductions may allow the researcher to spend more time investigating the filter's performance and less time tuning.

6.3.4 Cycle Slip Detection and Correction. Although the results of the cycle slip simulations indicated that the filter is stable and will always converge back to its nominal error values, the time lag for this convergence in some states is unacceptable for real-time aircraft navigation. Perhaps a future AFIT thesis student can look into developing an algorithm for the detection and subsequent correction of large carrier-phase GPS cycle slips.

6.3.5 RRS Transponder Position Errors. In Chapter V, a problem with the PNRS's ability to estimate the RRS transponder surveyed position errors was presented. It does not

seem reasonable that this filter would be worse at estimating these states than the ENRS filter. This indicates that there is some problem with either the MSOFE Fortran code of either filter, or a fundamental problem to do with how MSOFE computes and propagates these states in the truth and filter models. This problem must be investigated in the future if this model is to be used for further AFIT research.

Appendix A. Error State Model Definitions

This appendix contains tabular listings of the 93-state LN-93, 26-state RRS, 30-state GPS, 22-state DGPS, 4 additional PNRS error states, 95-state NRS truth, 87-state ENRS truth, 9- state PNRS truth, 67-state NRS/ENRS filter, and 71-state PNRS filter models.

A.1 Litton LN-93 INS 93-State Model.

Tables A-1 through A-6 list the LN-93 error model as defined in the Litton CDRL (15). It should be noted that this document contains some errors (1: Appendix A; 4) that have been corrected in this appendix. Note that the error states are divided into the six categories described in Chapter III.

A.2 RRS 26-State Model.

Table A-7 presents the 26 states of the RRS error state model as used in this thesis research. These states are extracted from (3). Note that 26 states are required to model the error characteristics of 6 ground based transponders and the airborne interrogator.

A.3 GPS 30-State Model.

Table A-8 presents the 30 states of the GPS error state model as used in this thesis research. These states are extracted from (24) and defined in (25). Note that 30 states are required to model the error characteristics of 4 orbiting GPS satellites and the airborne receiver.

A.4 DGPS 22-State Model.

Table A-9 presents the 22 states of the DGPS error state model as used in this thesis research. The state reduction from the 30-state GPS error model is presented in Chapter III of this thesis and in (1). Note that 22 states are required to model the error characteristics of 4 orbiting GPS satellites and the airborne receiver after differential corrections have been applied.

A.5 4 Additional CPGPS States.

Table A-10 presents the 4 additional CPGPS states as used in this thesis research. These four addition states are augmented to the 22-state DGPS model to form the CPGPS model. Four additional states are required to model the phase ambiguity terms for the four orbiting GPS satellites.

A.6 95-State NRS Truth Model.

Tables A-11 through A-14 present the 95 states of the NRS truth model as used in this thesis research. This is the so called "Negast" model of the NRS that was derived by Negast (1) and his predecessors (2, 3, 4) and based on the recommendations of Lewantowicz and Keen (17). This model is made up of 39 INS, 26 RRS, and 30 GPS states.

A.7 87-State ENRS Truth Model.

Tables A-11 through A-13 and Table A-15 present the 87 states of the ENRS truth model as used in this thesis research. This model is a reduced form of the NRS truth model using 39 INS, 26 RRS, and 22 DGPS states. This model was developed and tested by Negast (1).

A.8 91-State PNRS Truth Model.

Tables A-16 through A-20 present the 91 states of the ENRS truth model as used in this thesis research. This model is the ENRS truth model augmented with the four additional states of the CPGPS model. This model is made up of 39 INS, 26 RRS, 22 DGPS, and 4 CPGPS states.

A.9 67-State NRS/ENRS Filter Models.

Tables A-11 through A-13 present the 67 states of the NRS/ENRS filter models as used in this thesis research. These models are a reduced form of the NRS truth model and were developed and tested by Negast (1). These models are the same and are made up of 39 INS, 26 RRS, and 2 GPS states.

A.10 71-State PNRS Filter Model.

Tables A-16 through A-18 and Table A-20 present the 71 states of the PNRS filter model as used in this thesis research. This filter model is the NRS/ENRS 67-state filter model augmented with the four additional CPGPS states. This model is made up of 39 INS, 26 RRS, 2 GPS, and 4 CPGPS states.

State Number	State Symbol	Definition
1	$\delta\theta_X$	X component of vector angle from true to computer frame
2	$\delta\theta_Y$	Y component of vector angle from true to computer frame
3	$\delta\theta_Z$	Z component of vector angle from true to computer frame
4	ϕ_X	X component of vector angle from true to platform frame
5	ϕ_Y	Y component of vector angle from true to platform frame
6	ϕ_Z	Z component of vector angle from true to platform frame
7	δV_X	X component of error in computed velocity
8	δV_Y	Y component of error in computed velocity
9	δV_Z	Z component of error in computed velocity
10	δh	Error in vehicle altitude above reference ellipsoid
11	δh_L	Error in lagged inertial altitude
12	δS_3	Error in vertical channel aiding state
13	δS_4	Error in vertical channel aiding state

Table A-1: 93-State INS Model,
Category 1: General Error States

State Number	State Symbol	Definition
14	b_{X_c}	X component of gyro correlated drift rate
15	b_{Y_c}	Y component of gyro correlated drift rate
16	b_{Z_c}	Z component of gyro correlated drift rate
17	v_{X_c}	X component of accelerometer & velocity quantizer correlated noise
18	v_{Y_c}	Y component of accelerometer & velocity quantizer correlated noise
19	v_{Z_c}	Z component of accelerometer & velocity quantizer correlated noise
20	δg_X	X component of gravity vector errors
21	δg_Y	Y component of gravity vector errors
22	δg_Z	Z component of gravity vector errors
23	δh_B	Total baro-altimeter correlated error
24	b_{X_t}	X component of gyro trend
25	b_{Y_t}	Y component of gyro trend
26	b_{Z_t}	Z component of gyro trend
27	v_{X_t}	X component of accelerometer trend
28	v_{Y_t}	Y component of accelerometer trend
29	v_{Z_t}	Z component of accelerometer trend
30	b_X	X component of gyro drift rate repeatability
31	b_Y	Y component of gyro drift rate repeatability
32	b_Z	Z component of gyro drift rate repeatability
33	S_{gx}	X component of gyro scale factor error
34	S_{gy}	Y component of gyro scale factor error
35	S_{gz}	Z component of gyro scale factor error
36	χ_1	X gyro misalignment about Y axis
37	χ_2	Y gyro misalignment about X axis
38	χ_3	Z gyro misalignment about X axis
39	v_1	X gyro misalignment about Z axis
40	v_2	Y gyro misalignment about Z axis
41	v_3	Z gyro misalignment about Y axis

Table A-2: 93-State INS Model
Category 2: 1ˢᵗ Order Markov Process Error States

State Number	State Symbol	Definition
42	D_{XXX}	X gyro scale factor non linearity
43	D_{YYY}	Y gyro scale factor non linearity
44	D_{ZZZ}	Z gyro scale factor non linearity
45	S_{Qbx}	X gyro scale factor asymmetry error
46	S_{Qby}	Y gyro scale factor asymmetry error
47	S_{Qbz}	Z gyro scale factor asymmetry error

Table A-3: 93-State INS Model
Category 3: Gyro Bias Error States

State Number	State Symbol	Definition
48	∇_{bx}	X component of accelerometer bias repeatability
49	∇_{by}	Y component of accelerometer bias repeatability
50	∇_{bz}	Z component of accelerometer bias repeatability
51	S_{Ax}	X component of accelerometer & velocity quantizer scale factor error
52	S_{Ay}	Y component of accelerometer & velocity quantizer scale factor error
53	S_{Az}	Z component of accelerometer & velocity quantizer scale factor error
54	S_{QAx}	X component of accelerometer & velocity quantizer scale factor asymmetry
55	S_{QAx}	Y component of accelerometer & velocity quantizer scale factor asymmetry
56	S_{QAx}	Z component of accelerometer & velocity quantizer scale factor asymmetry
57	f_{XX}	Coefficient of error proportional to square of measured acceleration
58	f_{YY}	Coefficient of error proportional to square of measured acceleration
59	f_{ZZ}	Coefficient of error proportional to square of measured acceleration
60	f_{XY}	Coefficient of error proportional to products of acceleration along & orthogonal to accelerometer sensitive axis
61	f_{XZ}	Coefficient of error proportional to products of acceleration along & orthogonal to accelerometer sensitive axis
62	f_{YX}	Coefficient of error proportional to products of acceleration along & orthogonal to accelerometer sensitive axis
63	f_{YZ}	Coefficient of error proportional to products of acceleration along & orthogonal to accelerometer sensitive axis
64	f_{ZX}	Coefficient of error proportional to products of acceleration along & orthogonal to accelerometer sensitive axis
65	f_{ZY}	Coefficient of error proportional to products of acceleration along & orthogonal to accelerometer sensitive axis
66	μ_1	X accelerometer misalignment about Z axis
67	μ_2	Y accelerometer misalignment about Z axis
68	μ_3	Z accelerometer misalignment about Y axis
69	σ_3	Z accelerometer misalignment about X axis

Table A-4: 93-State INS Model,
Category 4: Accelerometer Bias Error States

State Number	State Symbol	Definition
70	∇_{X_q}	X component of accelerometer bias thermal transient
71	∇_{Y_q}	Y component of accelerometer bias thermal transient
72	∇_{Z_q}	Z component of accelerometer bias thermal transient
73	b_{X_q}	X component of initial gyro drift rate bias thermal transient
74	b_{Y_q}	Y component of initial gyro drift rate bias thermal transient
75	b_{Z_q}	Z component of initial gyro drift rate bias thermal transient

Table A-5: 93-State INS Model,
Category 5: Thermal Transient Error States

State Number	State Symbol	Definition
76	F_{XYZ}	X gyro compliance term
77	F_{XYY}	X gyro compliance term
78	F_{XYX}	X gyro compliance term
79	F_{XZY}	X gyro compliance term
80	F_{XZZ}	X gyro compliance term
81	F_{XZX}	X gyro compliance term
82	F_{YZX}	Y gyro compliance term
83	F_{YZZ}	Y gyro compliance term
84	F_{YZY}	Y gyro compliance term
85	F_{YXZ}	Y gyro compliance term
86	F_{YXX}	Y gyro compliance term
87	F_{YXY}	Y gyro compliance term
88	F_{ZXY}	Z gyro compliance term
89	F_{ZXX}	Z gyro compliance term
90	F_{ZXZ}	Z gyro compliance term
91	F_{ZYX}	Z gyro compliance term
92	F_{ZYY}	Z gyro compliance term
93	F_{ZYZ}	Z gyro compliance term

Table A-6: 93-State INS Model,
Category 6: Gyro Compliance Error States

State Number	State Symbol	Definition
1	δR_b	Range Error due to equipment bias
2	δv_b	Velocity Error due to equipment bias
3	δP_{T1x}	Transponder 1 X component of position error
4	δP_{T1y}	Transponder 1 Y component of position error
5	δP_{T1z}	Transponder 1 Z component of position error
6	δR_{T1a}	Transponder 1 range error due to atmospheric propagation
7	δP_{T2x}	Transponder 2 X component of position error
8	δP_{T2y}	Transponder 2 Y component of position error
9	δP_{T2z}	Transponder 2 Z component of position error
10	δR_{T2a}	Transponder 2 range error due to atmospheric propagation
11	δP_{T3x}	Transponder 3 X component of position error
12	δP_{T3y}	Transponder 3 Y component of position error
13	δP_{T13z}	Transponder 3 Z component of position error
14	δR_{T3a}	Transponder 3 range error due to atmospheric propagation
15	δP_{T4x}	Transponder 4 X component of position error
16	δP_{T4y}	Transponder 4 Y component of position error
17	δP_{T4z}	Transponder 4 Z component of position error
18	δR_{T4a}	Transponder 4 range error due to atmospheric propagation
19	δP_{T5x}	Transponder 5 X component of position error
20	δP_{T5y}	Transponder 5 Y component of position error
21	δP_{T5z}	Transponder 5 Z component of position error
22	δR_{T5a}	Transponder 5 range error due to atmospheric propagation
23	δP_{T6x}	Transponder 6 X component of position error
24	δP_{T6y}	Transponder 6 Y component of position error
25	δP_{T6z}	Transponder 6 Z component of position error
26	δR_{T6a}	Transponder 6 range error due to atmospheric propagation

Table A-7: 26-State RRS Error Model

State Number	State Symbol	Definition
1	$\delta R_{clk\ u}$	User clock bias
2	$\delta D_{clk\ u}$	User clock drift
3	δR_{cloop1}	SV 1 code loop error
4	δR_{trop1}	SV 1 tropospheric error
5	δR_{ion1}	SV 1 ionospheric error
6	δR_{clk1}	SV 1 clock error
7	δX_1	SV 1 X component of position error
8	δY_1	SV 1 Y component of position error
9	δZ_1	SV 1 Z component of position error
10	δR_{cloop2}	SV 2 code loop error
11	δR_{trop2}	SV 2 tropospheric error
12	δR_{ion2}	SV 2 ionospheric error
13	δR_{clk2}	SV 2 clock error
14	δX_2	SV 2 X component of position error
15	δY_2	SV 2 Y component of position error
16	δZ_2	SV 2 Z component of position error
17	δR_{cloop3}	SV 3 code loop error
18	δR_{trop3}	SV 3 tropospheric error
19	δR_{ion3}	SV 3 ionospheric error
20	δR_{clk3}	SV 3 clock error
21	δX_3	SV 3 X component of position error
22	δY_3	SV 3 Y component of position error
23	δZ_3	SV 3 Z component of position error
24	δR_{cloop4}	SV 4 code loop error
25	δR_{trop4}	SV 4 tropospheric error
26	δR_{ion4}	SV 4 ionospheric error
27	δR_{clk4}	SV 4 clock error
28	δX_4	SV 4 X component of position error
29	δY_4	SV 4 Y component of position error
30	δZ_4	SV 4 Z component of position error

Table A-8: 30-State GPS Error Model

State Number	State Symbol	Definition
1	$\delta R_{clk\ u}$	User clock bias
2	$\delta D_{clk\ u}$	User clock drift
3	δR_{trop1}	SV 1 tropospheric error
4	δR_{ion1}	SV 1 ionospheric error
5	δX_1	SV 1 X component of position error
6	δY_1	SV 1 Y component of position error
7	δZ_1	SV 1 Z component of position error
8	δR_{trop2}	SV 2 tropospheric error
9	δR_{ion2}	SV 2 ionospheric error
10	δX_2	SV 2 X component of position error
11	δY_2	SV 2 Y component of position error
12	δZ_2	SV 2 Z component of position error
13	δR_{trop3}	SV 3 tropospheric error
14	δR_{ion3}	SV 3 ionospheric error
15	δX_3	SV 3 X component of position error
16	δY_3	SV 3 Y component of position error
17	δZ_3	SV 3 Z component of position error
18	δR_{trop4}	SV 4 tropospheric error
19	δR_{ion4}	SV 4 ionospheric error
20	δX_4	SV 4 X component of position error
21	δY_4	SV 4 Y component of position error
22	δZ_4	SV 4 Z component of position error

Table A-9: 22-State DGPS Error Model

State Number	State Symbol	Definition
1	δR_{N1}	SV 1 range equivelent cycle ambiguity term
2	δR_{N2}	SV 2 range equivelent cycle ambiguity term
3	δR_{N3}	SV 3 range equivelent cycle ambiguity term
4	δR_{N4}	SV 4 range equivelent cycle ambiguity term

Table A-10: Additional PNRS Error States

State Number	State Symbol	Definition	Related State
1	$\delta\theta_X$	X comp. of vector angle from true to computer frame	INS 1
2	$\delta\theta_Y$	Y comp. of vector angle from true to computer frame	INS 2
3	$\delta\theta_Z$	Z comp. of vector angle from true to computer frame	INS 3
4	ϕ_X	X comp. of vector angle from true to platform frame	INS 4
5	ϕ_Y	Y comp. of vector angle from true to platform frame	INS 5
6	ϕ_Z	Z comp. of vector angle from true to platform frame	INS 6
7	δV_X	X component of error in computed velocity	INS 7
8	δV_Y	Y component of error in computed velocity	INS 8
9	δV_Z	Z component of error in computed velocity	INS 9
10	δh	Error in vehicle altitude above reference ellipsoid	INS 10
11	δh_B	Total baro-altimeter correlated error	INS 23
12	δR_b	Range error due to RRS equipment bias	RRS 1
13	δv_b	Velocity error due to RRS equipment bias	RRS 2
14	$\delta R_{clk\ u}$	GPS user clock bias	GPS 1
15	$\delta D_{clk\ u}$	GPS user clock drift	GPS 2
16	δh_L	Error in lagged inertial altitude	INS 11
17	δS_3	Error in vertical channel aiding state	INS 12
18	δS_4	Error in vertical channel aiding state	INS 13
19	∇_{Xc}	X comp. of accelerometer & velocity quantizer correlated noise	INS 17
20	∇_{Yc}	Y comp. of accelerometer & velocity quantizer correlated noise	INS 18
21	∇_{Zc}	Z comp. of accelerometer & velocity quantizer correlated noise	INS 19
22	δg_X	X component of gravity vector errors	INS 20
23	δg_X	Y component of gravity vector errors	INS 21
24	δg_X	Z component of gravity vector errors	INS 22

Table A-11: States 1-24 of 95/87-State NRS/ENRS Truth and 67-State Filter Models

State Number	State Symbol	Definition	Related State
25	b_X	X component of gyro drift rate repeatability	INS 30
26	b_Y	Y component of gyro drift rate repeatability	INS 31
27	b_Z	Z component of gyro drift rate repeatability	INS 32
28	S_{gx}	X component of gyro scale factor error	INS 33
29	S_{gy}	Y component of gyro scale factor error	INS 34
30	S_{gz}	Z component of gyro scale factor error	INS 35
31	∇_{bx}	X component of accelerometer bias repeatability	INS 48
32	∇_{by}	Y component of accelerometer bias repeatability	INS 49
33	∇_{bz}	Z component of accelerometer bias repeatability	INS 50
34	S_{Ax}	X component of accelerometer & velocity quantizer scale factor error	INS 51
35	S_{Ay}	Y component of accelerometer & velocity quantizer scale factor error	INS 52
36	S_{Az}	Z component of accelerometer & velocity quantizer scale factor error	INS 53
37	S_{QAx}	X component of accelerometer & velocity quantizer scale factor asymmetry	INS 54
38	S_{QAy}	Y component of accelerometer & velocity quantizer scale factor asymmetry	INS 55
39	S_{QAz}	Z component of accelerometer & velocity quantizer scale factor asymmetry	INS 56
40	μ_1	X accelerometer misalignment about Z axis	INS 66
41	μ_2	Y accelerometer misalignment about Z axis	INS 67
42	μ_3	Z accelerometer misalignment about Y axis	INS 68
43	σ_1	X accelerometer misalignment about Y axis	INS 69

Table A-12: States 25-43 of 95/87-State NRS/ENRS Truth and 67-State Filter Models

State Number	State Symbol	Definition	Related State
44	δP_{T1x}	Transponder 1 X component of position error	RRS 3
45	δP_{T1y}	Transponder 1 Y component of position error	RRS 4
46	δP_{T1z}	Transponder 1 Z component of position error	RRS 5
47	δP_{T1a}	Transponder 1 range error due to atm propagation	RRS 6
48	δP_{T2x}	Transponder 2 X component of position error	RRS 7
49	δP_{T2y}	Transponder 2 Y component of position error	RRS 8
50	δP_{T2z}	Transponder 2 Z component of position error	RRS 9
51	δP_{T2a}	Transponder 2 range error due to atm propagation	RRS 10
52	δP_{T3x}	Transponder 3 X component of position error	RRS 11
53	δP_{T3y}	Transponder 3 Y component of position error	RRS 12
54	δP_{T3z}	Transponder 3 Z component of position error	RRS 13
55	δP_{T3a}	Transponder 3 range error due to atm propagation	RRS 14
56	δP_{T4x}	Transponder 4 X component of position error	RRS 15
57	δP_{T4y}	Transponder 4 Y component of position error	RRS 16
58	δP_{T4z}	Transponder 4 Z component of position error	RRS 17
59	δP_{T4a}	Transponder 4 range error due to atm propagation	RRS 18
60	δP_{T5x}	Transponder 5 X component of position error	RRS 19
61	δP_{T5y}	Transponder 5 Y component of position error	RRS 20
62	δP_{T5z}	Transponder 5 Z component of position error	RRS 21
63	δP_{T5a}	Transponder 5 range error due to atm propagation	RRS 22
64	δP_{T6x}	Transponder 6 X component of position error	RRS 23
65	δP_{T6y}	Transponder 6 Y component of position error	RRS 24
66	δP_{T6z}	Transponder 6 Z component of position error	RRS 25
67	δP_{T6a}	Transponder 6 range error due to atm propagation	RRS 26

Table A-13: States 44-67 of 95/87-State NRS/ENRS Truth and 67-State Filter Models

State Number	State Symbol	Definition	Related State
68	δR_{cloop1}	SV 1 code loop error	GPS 3
69	δR_{trop1}	SV 1 tropospheric error	GPS 4
70	δR_{ion1}	SV 1 ionospheric error	GPS 5
71	δR_{clk1}	SV 1 clock error	GPS 6
72	δX_1	SV 1 X component of position error	GPS 7
73	δY_1	SV 1 Y component of position error	GPS 8
74	δZ_1	SV 1 Z component of position error	GPS 9
75	δR_{cloop2}	SV 2 code loop error	GPS 10
76	δR_{trop2}	SV 2 tropospheric error	GPS 11
77	δR_{ion2}	SV 2 ionospheric error	GPS 12
78	δR_{clk2}	SV 2 clock error	GPS 13
79	δX_2	SV 2 X component of position error	GPS 14
80	δY_2	SV 2 Y component of position error	GPS 15
81	δZ_2	SV 2 Z component of position error	GPS 16
82	δR_{cloop3}	SV 3 code loop error	GPS 17
83	δR_{trop3}	SV 3 tropospheric error	GPS 18
84	δR_{ion3}	SV 3 ionospheric error	GPS 19
85	δR_{clk3}	SV 3 clock error	GPS 20
86	δX_3	SV 3 X component of position error	GPS 21
87	δY_3	SV 3 Y component of position error	GPS 22
88	δZ_3	SV 3 Z component of position error	GPS 23
89	δR_{cloop4}	SV 4 code loop error	GPS 24
90	δR_{trop4}	SV 4 tropospheric error	GPS 25
91	δR_{ion4}	SV 4 ionospheric error	GPS 26
92	δR_{clk4}	SV 4 clock error	GPS 27
93	δX_4	SV 4 X component of position error	GPS 28
94	δY_4	SV 4 Y component of position error	GPS 29
95	δZ_4	SV 4 Z component of position error	GPS 30

Table A-14: States 68-95 of 95-State NRS Truth Model

State Number	State Symbol	Definition	Related State
68	δR_{trop1}	SV 1 tropospheric error	DGPS 3
69	δR_{ion1}	SV 1 ionospheric error	DGPS 4
70	δX_1	SV 1 X component of position error	DGPS 5
71	δY_1	SV 1 Y component of position error	DGPS 6
72	δZ_1	SV 1 Z component of position error	DGPS 7
73	δR_{trop2}	SV 2 tropospheric error	DGPS 8
74	δR_{ion2}	SV 2 ionospheric error	DGPS 9
75	δX_2	SV 2 X component of position error	DGPS 10
76	δY_2	SV 2 Y component of position error	DGPS 11
77	δZ_2	SV 2 Z component of position error	DGPS 12
78	δR_{trop3}	SV 3 tropospheric error	DGPS 13
79	δR_{ion3}	SV 3 ionospheric error	DGPS 14
80	δX_3	SV 3 X component of position error	DGPS 15
81	δY_3	SV 3 Y component of position error	DGPS 16
82	δZ_3	SV 3 Z component of position error	DGPS 17
83	δR_{trop4}	SV 4 tropospheric error	DGPS 18
84	δR_{ion4}	SV 4 ionospheric error	DGPS 19
85	δX_4	SV 4 X component of position error	DGPS 20
86	δY_4	SV 4 Y component of position error	DGPS 21
87	δZ_4	SV 4 Z component of position error	DGPS 22

Table A-15: States 68-87 of 87-State ENRS Truth Model

State Number	State Symbol	Definition	Related State
1	$\delta\theta_X$	X comp. of vector angle from true to computer frame	INS 1
2	$\delta\theta_Y$	Y comp. of vector angle from true to computer frame	INS 2
3	$\delta\theta_Z$	Z comp. of vector angle from true to computer frame	INS 3
4	ϕ_X	X comp. of vector angle from true to platform frame	INS 4
5	ϕ_Y	Y comp. of vector angle from true to platform frame	INS 5
6	ϕ_Z	Z comp. of vector angle from true to platform frame	INS 6
7	δV_X	X component of error in computed velocity	INS 7
8	δV_Y	Y component of error in computed velocity	INS 8
9	δV_Z	Z component of error in computed velocity	INS 9
10	δh	Error in vehicle altitude above reference ellipsoid	INS 10
11	δh_B	Total baro-altimeter correlated error	INS 23
12	δR_b	Range error due to RRS equipment bias	RRS 1
13	δv_b	Velocity error due to RRS equipment bias	RRS 2
14	$\delta R_{clk\,u}$	GPS user clock bias	GPS 1
15	$\delta D_{clk\,u}$	GPS user clock drift	GPS 2
16	δh_L	Error in lagged inertial altitude	INS 11
17	δS_3	Error in vertical channel aiding state	INS 12
18	δS_4	Error in vertical channel aiding state	INS 13
19	∇_{Xc}	X comp. of accelerometer & velocity quantizer correlated noise	INS 17
20	∇_{Yc}	Y comp. of accelerometer & velocity quantizer correlated noise	INS 18
21	∇_{Zc}	Z comp. of accelerometer & velocity quantizer correlated noise	INS 19
22	δg_X	X component of gravity vector errors	INS 20
23	δg_X	Y component of gravity vector errors	INS 21
24	δg_X	Z component of gravity vector errors	INS 22

Table A-16: States 1-24 of 91-State PNRS Truth and 71-State Filter Models

State Number	State Symbol	Definition	Related State
25	b_X	X component of gyro drift rate repeatability	INS 30
26	b_Y	Y component of gyro drift rate repeatability	INS 31
27	b_Z	Z component of gyro drift rate repeatability	INS 32
28	S_{gx}	X component of gyro scale factor error	INS 33
29	S_{gy}	Y component of gyro scale factor error	INS 34
30	S_{gz}	Z component of gyro scale factor error	INS 35
31	∇_{bx}	X component of accelerometer bias repeatability	INS 48
32	∇_{by}	Y component of accelerometer bias repeatability	INS 49
33	∇_{bz}	Z component of accelerometer bias repeatability	INS 50
34	S_{Ax}	X component of accelerometer & velocity quantizer scale factor error	INS 51
35	S_{Ay}	Y component of accelerometer & velocity quantizer scale factor error	INS 52
36	S_{Az}	Z component of accelerometer & velocity quantizer scale factor error	INS 53
37	S_{QAx}	X component of accelerometer & velocity quantizer scale factor asymmetry	INS 54
38	S_{QAy}	Y component of accelerometer & velocity quantizer scale factor asymmetry	INS 55
39	S_{QAz}	Z component of accelerometer & velocity quantizer scale factor asymmetry	INS 56
40	μ_1	X accelerometer misalignment about Z axis	INS 66
41	μ_2	Y accelerometer misalignment about Z axis	INS 67
42	μ_3	Z accelerometer misalignment about Y axis	INS 68
43	σ_1	X accelerometer misalignment about Y axis	INS 69

Table A-17: States 25-43 of 91-State PNRS Truth and 71-State Filter Models

State Number	State Symbol	Definition	Related State
44	δP_{T1x}	Transponder 1 X component of position error	RRS 3
45	δP_{T1y}	Transponder 1 Y component of position error	RRS 4
46	δP_{T1z}	Transponder 1 Z component of position error	RRS 5
47	δP_{T1a}	Transponder 1 range error due to atm propagation	RRS 6
48	δP_{T2x}	Transponder 2 X component of position error	RRS 7
49	δP_{T2y}	Transponder 2 Y component of position error	RRS 8
50	δP_{T2z}	Transponder 2 Z component of position error	RRS 9
51	δP_{T2a}	Transponder 2 range error due to atm propagation	RRS 10
52	δP_{T3x}	Transponder 3 X component of position error	RRS 11
53	δP_{T3y}	Transponder 3 Y component of position error	RRS 12
54	δP_{T3z}	Transponder 3 Z component of position error	RRS 13
55	δP_{T3a}	Transponder 3 range error due to atm propagation	RRS 14
56	δP_{T4x}	Transponder 4 X component of position error	RRS 15
57	δP_{T4y}	Transponder 4 Y component of position error	RRS 16
58	δP_{T4z}	Transponder 4 Z component of position error	RRS 17
59	δP_{T4a}	Transponder 4 range error due to atm propagation	RRS 18
60	δP_{T5x}	Transponder 5 X component of position error	RRS 19
61	δP_{T5y}	Transponder 5 Y component of position error	RRS 20
62	δP_{T5z}	Transponder 5 Z component of position error	RRS 21
63	δP_{T5a}	Transponder 5 range error due to atm propagation	RRS 22
64	δP_{T6x}	Transponder 6 X component of position error	RRS 23
65	δP_{T6y}	Transponder 6 Y component of position error	RRS 24
66	δP_{T6z}	Transponder 6 Z component of position error	RRS 25
67	δP_{T6a}	Transponder 6 range error due to atm propagation	RRS 26

Table A-18: States 44-67 of 91-State PNRS Truth and 71-State Filter Models

State Number	State Symbol	Definition	Related State
68	δR_{N1}	SV 1 range equivelent cycle ambiguity term	CPGPS 1
69	δR_{N2}	SV 2 range equivelent cycle ambiguity term	CPGPS 2
70	δR_{N3}	SV 3 range equivelent cycle ambiguity term	CPGPS 3
71	δR_{N4}	SV 4 range equivelent cycle ambiguity term	CPGPS 4
72	δR_{trop1}	SV 1 tropospheric error	DGPS 3
73	δR_{ion1}	SV 1 ionospheric error	DGPS 4
74	δX_1	SV 1 X component of position error	DGPS 5
75	δY_1	SV 1 Y component of position error	DGPS 6
76	δZ_1	SV 1 Z component of position error	DGPS 7
77	δR_{trop2}	SV 2 tropospheric error	DGPS 8
78	δR_{ion2}	SV 2 ionospheric error	DGPS 9
79	δX_2	SV 2 X component of position error	DGPS 10
80	δY_2	SV 2 Y component of position error	DGPS 11
81	δZ_2	SV 2 Z component of position error	DGPS 12
82	δR_{trop3}	SV 3 tropospheric error	DGPS 13
83	δR_{ion3}	SV 3 ionospheric error	DGPS 14
84	δX_3	SV 3 X component of position error	DGPS 15
85	δY_3	SV 3 Y component of position error	DGPS 16
86	δZ_3	SV 3 Z component of position error	DGPS 17
87	δR_{trop4}	SV 4 tropospheric error	DGPS 18
88	δR_{ion4}	SV 4 ionospheric error	DGPS 19
89	δX_4	SV 4 X component of position error	DGPS 20
90	δY_4	SV 4 Y component of position error	DGPS 21
91	δZ_4	SV 4 Z component of position error	DGPS 2

Table A-19: States 68-91 of 91-State PNRS Truth Model and
States 68-71 of 71-State Filter Model

Appendix B. LN-93 INS Error State Model Dynamics Matrix

(4)

Tables B-1 through B-8 contain a complete listing of the LN-93 INS error state dynamics matrix (F matrix) developed by Litton. This matrix is a 93 x 93 array that contains a large number of zeros. Only the non-zero elements of this matrix are presented in these tables.

Each of these tables present one of the eight sub-arrays of the F matrix presented in Equation (3-2) of Chapter III.

Note that the revised barometric altimeter model used in this thesis research is not presented in this set of F matrix elements. These elements were extracted directly from the Litton documentation (16).

A notational convention (4) is to label the elements of the sensor-to-true transformation matrix, C_S^t, as C_{ij} where i represents the row number and j represents the column number of the matrix.

Tables B-9 and B-10 presents the Q(t) matrix developed by Litton. This is also a 93 x 93 array that contains mostly zero. Only the non-zero elements are presented in these tables.

Element	Term	Element	Term	Element	Term
(1,3)	$-\rho_Y$	(1,8)	$-C_{RY}$		
(2,3)	$-\rho_X$	(2,7)	C_{RX}		
(3,1)	ρ_Y	(3,2)	$-\rho_X$		
(4,2)	$-\Omega_Z$	(4,3)	Ω_Y	(4,5)	ω_{itz}
(4,6)	$-\omega_{ity}$	(4,8)	$-C_{RY}$		
(5,1)	Ω_Z	(5,3)	$-\Omega_X$	(5,4)	$-\omega_{itz}$
(5,6)	ω_{itx}	(5,7)	C_{RX}		
(6,1)	$-\Omega_Y$	(6,2)	Ω_X	(6,4)	ω_{ity}
(6,5)	$-\omega_{itx}$				
(7,1)	$-2V_Y\Omega_Y - 2V_Z\Omega_Z$	(7,2)	$2V_Y\Omega_X$	(7,3)	$2V_Z\Omega_Y$
(7,5)	$-A_Z$	(7,6)	A_Y	(7,7)	$-V_Z C_{RX}$
(7,8)	$2\Omega_Z$	(7,9)	$-\rho_Y - 2\Omega_Y$		
(8,1)	$2V_X\Omega_Y$	(8,2)	$-2V_X\Omega_X - 2V_Z\Omega_Z$	(8,3)	$2V_Z\Omega_Y$
(8,4)	A_Z	(8,6)	$-A_X$	(8,7)	$-2\Omega_Z$
(8,8)	$-V_Z C_{RY}$	(8,9)	$\rho_X + 2\Omega_X$		
(9,1)	$2V_X\Omega_Z$	(9,2)	$2V_Y\Omega_Z$	(9,3)	$-2V_Y\Omega_Y - 2V_X\Omega_X$
(9,4)	$-A_Y$	(9,5)	A_X	(9,7)	$\rho_Y + 2\Omega_Y + V_X C_{RX}$
(9,8)	$-\rho_X - 2\Omega_X + V_Y C_{RY}$	(9,10)	$2g_0/a$	(9,11)	$-k_2$
(9,12)	-1	(9,13)	k_2		
(10,9)	1	(10,11)	$-k_1$	(10,13)	$k_1 - 1$
(11,10)	1	(11,11)	-1		
(12,11)	k_3	(12,13)	$-k_3$		
(13,10)	k_4	(13,11)	$-k_4$	(13,13)	$k_4 - 1$

Table B-1: Elements of the Dynamics Submatrix F_{11}

Element	Term	Element	Term	Element	Term
(4,14)	C_{11}	(4,15)	C_{12}	(4,16)	C_{13}
(4,24)	$C_{11}t$	(4,25)	$C_{12}t$	(4,26)	$C_{13}t$
(5,14)	C_{21}	(5,15)	C_{22}	(5,16)	C_{23}
(5,24)	$C_{21}t$	(5,25)	$C_{22}t$	(5,26)	$C_{23}t$
(6,14)	C_{31}	(6,15)	C_{32}	(6,16)	C_{33}
(6,24)	$C_{31}t$	(6,25)	$C_{32}t$	(6,26)	$C_{33}t$
(7,17)	C_{11}	(7,18)	C_{12}	(7,19)	C_{13}
(7,20)	1	(7,27)	$C_{11}t$	(7,28)	$C_{12}t$
(7,29)	$C_{31}t$				
(8,17)	C_{21}	(8,18)	C_{22}	(8,19)	C_{23}
(8,21)	1	(8,27)	$C_{21}t$	(8,28)	$C_{22}t$
(8,29)	$C_{23}t$				
(9,17)	C_{31}	(9,18)	C_{32}	(9,19)	C_{33}
(9,22)	1	(9,23)	k_2	(9,27)	$C_{31}t$
(9,28)	$C_{32}t$	(9,29)	$C_{33}t$		
(10,23)	k_1	(12,23)	$-k_3$	(13,23)	$k_4 / 600$

Table B-2: Elements of the Dynamics Submatrix F_{12}

Element	Term	Element	Term	Element	Term
(4,30)	C_{11}	(4,31)	C_{12}	(4,32)	C_{13}
(4,33)	$C_{11}\omega_{ibx}$	(4,34)	$C_{12}\omega_{iby}$	(4,35)	$C_{13}\omega_{ibz}$
(4,36)	$C_{11}\omega_{ibz}$	(4,37)	$-C_{12}\omega_{ibx}$	(4,38)	$C_{13}\omega_{iby}$
(4,39)	$-C_{11}\omega_{iby}$	(4,40)	$C_{12}\omega_{ibx}$	(4,41)	$-C_{13}\omega_{ibx}$
(4,42)	$C_{11}\omega^2_{ibx}$	(4,43)	$C_{12}\omega^2_{iby}$	(4,44)	$C_{13}\omega^2_{ibz}$
(4,45)	$\tfrac{1}{2}C_{11}\lvert\omega_{ibx}\rvert$	(4,46)	$\tfrac{1}{2}C_{12}\lvert\omega_{iby}\rvert$	(4,47)	$\tfrac{1}{2}C_{13}\lvert\omega_{ibz}\rvert$
(5,30)	C_{21}	(5,31)	C_{22}	(5,32)	C_{23}
(5,33)	$C_{21}\omega_{ibx}$	(5,34)	$C_{22}\omega_{iby}$	(5,35)	$C_{23}\omega_{ibz}$
(5,36)	$C_{21}\omega_{ibz}$	(5,37)	$-C_{22}\omega_{ibx}$	(5,38)	$C_{23}\omega_{iby}$
(5,39)	$-C_{21}\omega_{iby}$	(5,40)	$C_{22}\omega_{ibx}$	(5,41)	$-C_{23}\omega_{ibx}$
(5,42)	$C_{21}\omega^2_{ibx}$	(5,43)	$C_{22}\omega^2_{iby}$	(5,44)	$C_{23}\omega^2_{ibz}$
(5,45)	$\tfrac{1}{2}C_{21}\lvert\omega_{ibx}\rvert$	(5,46)	$\tfrac{1}{2}C_{22}\lvert\omega_{iby}\rvert$	(5,47)	$\tfrac{1}{2}C_{23}\lvert\omega_{ibz}\rvert$
(6,30)	C_{31}	(6,31)	C_{32}	(6,32)	C_{33}
(6,33)	$C_{31}\omega_{ibx}$	(6,34)	$C_{32}\omega_{iby}$	(6,35)	$C_{33}\omega_{ibz}$
(6,36)	$C_{31}\omega_{ibz}$	(6,37)	$-C_{32}\omega_{ibx}$	(6,38)	$C_{33}\omega_{iby}$
(6,39)	$-C_{31}\omega_{iby}$	(6,40)	$C_{32}\omega_{ibx}$	(6,41)	$-C_{33}\omega_{ibx}$
(6,42)	$C_{31}\omega^2_{ibx}$	(6,43)	$C_{32}\omega^2_{iby}$	(6,44)	$C_{33}\omega^2_{ibz}$
(6,45)	$\tfrac{1}{2}C_{31}\lvert\omega_{ibx}\rvert$	(6,46)	$\tfrac{1}{2}C_{32}\lvert\omega_{iby}\rvert$	(6,47)	$\tfrac{1}{2}C_{33}\lvert\omega_{ibz}\rvert$

Table B-3: Elements of the Dynamics Submatrix F_{12}

Element	Term	Element	Term	Element	Term
(7,48)	C_{11}	(7,49)	C_{12}	(7,50)	C_{13}
(7,51)	$C_{11}A_z^{\ B}$	(7,52)	$C_{12}A_y^{\ B}$	(7,53)	$C_{13}A_z^{\ B'}$
(7,54)	$C_{11}|A_z^{\ B}|$	(7,55)	$C_{12}|A_y^{\ B}|$	(7,56)	$C_{13}|A_z^{\ B'}|$
(7,57)	$C_{11}A_x^{\ B'}$	(7,58)	$C_{12}A_y^{\ B'}$	(7,59)	$C_{13}A_z B^{\varepsilon}$
(7,60)	$C_{11}A_x^{\ B}A_y^{\ B}$	(7,61)	$C_{11}A_z^{\ B}A_x^{\ B}$	(7,62)	$C_{12}A_y^{\ B}A_x^{\ B}$
(7,63)	$C_{12}A_y^{\ B}A_z^{\ B}$	(7,64)	$C_{13}A_x^{\ B}A_z^{\ B}$	(7,65)	$C_{13}A_y^{\ B}A_z^{\ B}$
(7,66)	$C_{11}A_y^{\ B}$	(7,67)	$-C_{12}A_x^{\ B}$	(7,68)	$C_{13}A_y^{\ B}$
(7,69)	$C_{13}A_x^{\ B}$				
(8,48)	C_{21}	(8,49)	C_{22}	(8,50)	C_{23}
(8,51)	$C_{21}A_z^{\ B}$	(8,52)	$C_{22}A_y^{\ B}$	(8,53)	$C_{23}A_z^{\ B'}$
(8,54)	$C_{21}|A_x^{\ B}|$	(8,55)	$C_{22}|A_y^{\ B}|$	(8,56)	$C_{23}|A_z^{\ B'}|$
(8,57)	$C_{21}A_x^{\ B'}$	(8,58)	$C_{22}A_y^{\ B'}$	(8,59)	$C_{23}A_z B^{\varepsilon}$
(8,60)	$C_{21}A_x^{\ B}A_y^{\ B}$	(8,61)	$C_{21}A_x^{\ B}A_x^{\ B}$	(8,62)	$C_{22}A_y^{\ B}A_x^{\ B}$
(8,63)	$C_{22}A_y^{\ B}A_z^{\ B}$	(8,64)	$C_{23}A_x^{\ B}A_z^{\ B}$	(8,65)	$C_{23}A_y^{\ B}A_z^{\ B}$
(8,66)	$C_{21}A_y^{\ B}$	(8,67)	$-C_{22}A_x^{\ B}$	(8,68)	$C_{23}A_y^{\ B}$
(8,69)	$C_{23}A_x^{\ B}$				
(9,48)	C_{31}	(9,49)	C_{32}	(9,50)	C_{33}
(9,51)	$C_{31}A_x^{\ B}$	(9,52)	$C_{32}A_y^{\ B}$	(9,53)	$C_{33}A_z^{\ B'}$
(9,54)	$C_{31}|A_x^{\ B}|$	(9,55)	$C_{32}|A_y^{\ B}|$	(9,56)	$C_{33}|A_z^{\ B'}|$
(9,57)	$C_{31}A_x^{\ B'}$	(9,58)	$C_{32}A_y^{\ B'}$	(9,59)	$C_{33}A_z B^{\varepsilon}$
(9,60)	$C_{31}A_x^{\ B}A_y^{\ B}$	(9,61)	$C_{31}A_x^{\ B}A_z^{\ B}$	(9,62)	$C_{32}A_y^{\ B}A_x^{\ B}$
(9,63)	$C_{32}A_y^{\ B}A_z^{\ B}$	(9,64)	$C_{33}A_x^{\ B}A_z^{\ B}$	(9,65)	$C_{33}A_y^{\ B}A_z^{\ B}$
(9,66)	$C_{31}A_y^{\ B}$	(9,67)	$-C_{32}A_x^{\ B}$	(9,68)	$C_{33}A_y^{\ B}$
(9,69)	$C_{33}A_x^{\ B}$				

Table B-4: Elements of the Dynamics Submatrix F_{14}

Element	Term	Element	Term	Element	Term
(4,73)	C_{11}	(4,74)	C_{12}	(4,75)	C_{13}
(5,73)	C_{21}	(5,74)	C_{22}	(5,75)	C_{23}
(6,73)	C_{31}	(6,74)	C_{32}	(6,75)	C_{33}
(7,73)	C_{11}	(7,74)	C_{12}	(7,75)	C_{13}
(8,73)	C_{21}	(8,74)	C_{22}	(8,75)	C_{23}
(9,73)	C_{31}	(9,74)	C_{32}	(9,75)	C_{33}

Table B-5: Elements of the Dynamics Submatrix F_{15}

Element	Term	Element	Term	Element	Term
(4,76)	$C_{11}A_y{}^B\omega_{ibz}$	(4,77)	$C_{11}A_y{}^B\omega_{iby}$	(4,78)	$C_{11}A_y{}^B\omega_{ibx}$
(4,79)	$C_{11}A_z{}^B\omega_{iby}$	(4,80)	$C_{11}A_z{}^B\omega_{ibz}$	(4,81)	$C_{11}A_z{}^B\omega_{ibx}$
(4,82)	$C_{12}A_z{}^B\omega_{ibx}$	(4,83)	$C_{12}A_z{}^B\omega_{ibz}$	(4,84)	$C_{12}A_z{}^B\omega_{iby}$
(4,85)	$C_{12}A_x{}^B\omega_{ibz}$	(4,86)	$C_{12}A_x{}^B\omega_{ibx}$	(4,87)	$C_{12}A_x{}^B\omega_{iby}$
(4,88)	$C_{13}A_x{}^B\omega_{iby}$	(4,89)	$C_{13}A_x{}^B\omega_{ibx}$	(4,90)	$C_{13}A_x{}^B\omega_{ibz}$
(4,91)	$C_{13}A_y{}^B\omega_{ibx}$	(4,92)	$C_{13}A_y{}^B\omega_{iby}$	(4,93)	$C_{13}A_y{}^B\omega_{ibz}$
(5,76)	$C_{21}A_y{}^B\omega_{ibz}$	(5,77)	$C_{21}A_y{}^B\omega_{iby}$	(5,78)	$C_{21}A_y{}^B\omega_{ibx}$
(5,79)	$C_{21}A_z{}^B\omega_{iby}$	(5,80)	$C_{21}A_z{}^B\omega_{ibz}$	(5,81)	$C_{21}A_z{}^B\omega_{ibx}$
(5,82)	$C_{22}A_z{}^B\omega_{ibx}$	(5,83)	$C_{22}A_z{}^B\omega_{ibz}$	(5,84)	$C_{22}A_z{}^B\omega_{iby}$
(5,85)	$C_{22}A_x{}^B\omega_{ibz}$	(5,86)	$C_{22}A_x{}^B\omega_{ibx}$	(5,87)	$C_{22}A_x{}^B\omega_{iby}$
(5,88)	$C_{23}A_x{}^B\omega_{iby}$	(5,89)	$C_{23}A_x{}^B\omega_{ibx}$	(5,90)	$C_{23}A_x{}^B\omega_{ibz}$
(5,91)	$C_{23}A_y{}^B\omega_{ibx}$	(5,92)	$C_{23}A_y{}^B\omega_{iby}$	(5,93)	$C_{23}A_y{}^B\omega_{ibz}$
(6,76)	$C_{31}A_y{}^B\omega_{ibz}$	(6,77)	$C_{31}A_y{}^B\omega_{iby}$	(6,78)	$C_{31}A_y{}^B\omega_{ibx}$
(6,79)	$C_{31}A_z{}^B\omega_{iby}$	(6,80)	$C_{31}A_z{}^B\omega_{ibz}$	(6,81)	$C_{31}A_z{}^B\omega_{ibx}$
(6,82)	$C_{32}A_z{}^B\omega_{ibx}$	(6,83)	$C_{32}A_z{}^B\omega_{ibz}$	(6,84)	$C_{32}A_z{}^B\omega_{iby}$
(6,85)	$C_{32}A_x{}^B\omega_{ibz}$	(6,86)	$C_{32}A_x{}^B\omega_{ibx}$	(6,87)	$C_{32}A_x{}^B\omega_{iby}$
(6,88)	$C_{33}A_x{}^B\omega_{iby}$	(6,89)	$C_{33}A_x{}^B\omega_{ibx}$	(6,90)	$C_{33}A_x{}^B\omega_{ibz}$
(6,91)	$C_{33}A_y{}^B\omega_{ibx}$	(6,92)	$C_{33}A_y{}^B\omega_{iby}$	(6,93)	$C_{33}A_y{}^B\omega_{ibz}$

Table B-6: Elements of the Dynamics Submatrix F_{16}

Element	Term	Element	Term	Element	Term
(14,14)	$-\beta_{b_{xc}}$	(15,15)	$-\beta_{b_{yc}}$	(16,16)	$-\beta_{b_{zc}}$
(17,17)	$-\beta_{V_{xc}}$	(18,18)	$-\beta_{V_{yc}}$	(19,19)	$-\beta_{V_{zc}}$
(20,20)	$-\beta_{g_{xz}}$	(21,21)	$-\beta_{g_{zy}}$	(22,22)	$-\beta_{g_{zz}}$
(23,23)	$-\beta_{g_{hc}}$				

Table B-7: Elements of the Dynamics Submatrix F_{22}

Element	Term	Element	Term	Element	Term
(70,70)	$-\beta_{V_{xq}}$	(71,71)	$-\beta_{V_{yq}}$	(72,72)	$-\beta_{V_{zq}}$
(73,73)	$-\beta_{b_{xq}}$	(74,74)	$-\beta_{b_{yq}}$	(75,75)	$-\beta_{b_{zq}}$

Table B-8: Elements of the Dynamics Submatrix F_{88}

Element	Term	Element	Term
(4,4)	$\sigma^2_{\eta bx}$	(5,5)	$\sigma^2_{\eta by}$
(6,6)	$\sigma^2_{\eta bz}$	(7,7)	$\sigma^2_{\eta Ax}$
(8,8)	$\sigma^2_{\eta Ay}$	(9,9)	$\sigma^2_{\eta Az}$

Table B-9: Elements of the Process Noise Submatrix $\mathbf{Q}_{11}$

Element	Term	Element	Term
(14,14)	$2\beta_{bxc}\sigma^2_{bxc}$	(15,15)	$2\beta_{byc}\sigma^2_{byc}$
(16,16)	$2\beta_{bzc}\sigma^2_{bzc}$	(17,17)	$2\beta_{Vxc}\sigma^2_{Vxc}$
(18,18)	$2\beta_{Vyc}\sigma^2_{Vyc}$	(19,19)	$2\beta_{Vzc}\sigma^2_{Vzc}$
(20,20)	$2\beta_{\delta gx}\sigma^2_{\delta gx}$	(21,21)	$2\beta_{\delta gy}\sigma^2_{\delta gy}$
(22,22)	$2\beta_{\delta gz}\sigma^2_{\delta gz}$	(23,23)	$2\beta_{\delta bc}\sigma^2_{\delta bc}$

Table B-10: Elements of the Process Noise Submatrix $\mathbf{Q}_{22}$

Appendix C. Filter Tuning Parameters Q(t) and R(t)

This appendix contains a complete listing of the filter tuning parameters for the NRS, ENRS, and PNRS filters as used in this thesis research. These parameters are laid out in Tables C-1 through C-9 (Q(t) values) and C-10 through C-12 (R(t) values). The truth model dynamics driving noise and measurement noise variances for the corresponding filter state are also provided for comparison.

State Number	Truth Model Value	Filter Q Value	Units
1	0	0.5×10^{-14}	$(\text{arc-sec})^2/\text{sec}$
2	0	0.5×10^{-14}	$(\text{arc-sec})^2/\text{sec}$
3	0	1×10^{-15}	$(\text{arc-sec})^2/\text{sec}$
4	190.4×10^{-15}	9.52×10^{-13}	$(\text{arc-sec})^2/\text{sec}$
5	190.4×10^{-15}	9.52×10^{-13}	$(\text{arc-sec})^2/\text{sec}$
6	190.4×10^{-15}	1.618×10^{-11}	$(\text{arc-sec})^2/\text{sec}$
7	102.9×10^{-9}	1.544×10^{-3}	ft^2/sec^3
8	102.9×10^{-9}	1.544×10^{-3}	ft^2/sec^3
9	102.9×10^{-9}	11.32×10^{-3}	ft^2/sec^3
10	0	20.0	ft^2/sec
11	33.34	1667	ft^2/sec
12	0	7.5	ft^2/sec
13	0	1×10^{-10}	ft^2/sec^3
14	0	7.5	ft^2/sec
15	0	1×10^{-8}	ft^2/sec^3
16	0	1×10^{-6}	ft^2/sec
17	0	1×10^{-6}	ft^2/sec
18	(time-varying)[1]	(time-varying)[2]	ft^2/sec^5
19	2.7451×10^{-11}	2.7451×10^{-11}	$\mu\text{g}^2/\text{sec}$
20	2.7451×10^{-11}	2.7451×10^{-11}	$\mu\text{g}^2/\text{sec}$
21	2.7451×10^{-11}	2.7451×10^{-11}	$\mu\text{g}^2/\text{sec}$
22	1.9548	1.9508	$\mu\text{g}^2/\text{sec}$
23	1.9548	1.9508	$\mu\text{g}^2/\text{sec}$
24	1.9548	1.9508	$\mu\text{g}^2/\text{sec}$

Table C-1: States 1-24 of NRS Filter Tuning Parameters Q(t)

State Number	Truth Model Value	Filter Q Value	Units
25	0	1×10^{-10}	$(\text{deg/hr})^2/\text{sec}$
26	0	1×10^{-10}	$(\text{deg/hr})^2/\text{sec}$
27	0	0	$(\text{deg/hr})^2/\text{sec}$
28	0	1×10^{-10}	%/sec
29	0	1×10^{-10}	%/sec
30	0	0	%/sec
31	0	1×10^{-8}	$\mu g^2/\text{sec}$
32	0	1×10^{-8}	$\mu g^2/\text{sec}$
33	0	1×10^{-8}	$\mu g^2/\text{sec}$
34	0	1×10^{-8}	%/sec
35	0	1×10^{-8}	%/sec
36	0	1×10^{-8}	%/sec
37	0	1×10^{-8}	%/sec
38	0	1×10^{-8}	%/sec
39	0	1×10^{-8}	%/sec
40	0	1×10^{-8}	$(\text{arc-sec})^2/\text{sec}$
41	0	1×10^{-8}	$(\text{arc-sec})^2/\text{sec}$
42	0	1×10^{-8}	$(\text{arc-sec})^2/\text{sec}$
43	0	1×10^{-8}	$(\text{arc-sec})^2/\text{sec}$

Table C-2: States 25-43 of NRS Filter Tuning Parameters Q(t)

State Number	Truth Model Value	Filter Q Value	Units
44	0	2×10^{-3}	ft^2/sec
45	0	2×10^{-3}	ft^2/sec
46	0	2×10^{-3}	ft^2/sec
47	6.667×10^{-13}	6.667×10^{-6}	ft^2/sec
48	0	2×10^{-3}	ft^2/sec
49	0	2×10^{-3}	ft^2/sec
50	0	2×10^{-3}	ft^2/sec
51	6.667×10^{-13}	6.667×10^{-6}	ft^2/sec
52	0	2×10^{-3}	ft^2/sec
53	0	2×10^{-3}	ft^2/sec
54	0	2×10^{-3}	ft^2/sec
55	6.667×10^{-13}	6.667×10^{-6}	ft^2/sec
56	0	2×10^{-3}	ft^2/sec
57	0	2×10^{-3}	ft^2/sec
58	0	2×10^{-3}	ft^2/sec
59	6.667×10^{-13}	6.667×10^{-6}	ft^2/sec
60	0	2×10^{-3}	ft^2/sec
61	0	2×10^{-3}	ft^2/sec
62	0	2×10^{-3}	ft^2/sec
63	6.667×10^{-13}	6.667×10^{-6}	ft^2/sec
64	0	2×10^{-3}	ft^2/sec
65	0	2×10^{-3}	ft^2/sec
66	0	2×10^{-3}	ft^2/sec
67	6.667×10^{-13}	6.667×10^{-6}	ft^2/sec

Table C-3: States 44-67 of NRS Filter Tuning Parameters Q(t)

State Number	Truth Model Value	Filter Q Value	Units
1	0	0.1×10^{-14}	$(\text{arc-sec})^2/\text{sec}$
2	0	0.1×10^{-14}	$(\text{arc-sec})^2/\text{sec}$
3	0	1×10^{-15}	$(\text{arc-sec})^2/\text{sec}$
4	190.4×10^{-15}	9.52×10^{-13}	$(\text{arc-sec})^2/\text{sec}$
5	190.4×10^{-15}	9.52×10^{-13}	$(\text{arc-sec})^2/\text{sec}$
6	190.4×10^{-15}	1.618×10^{-11}	$(\text{arc-sec})^2/\text{sec}$
7	102.9×10^{-9}	1.544×10^{-3}	ft^2/sec^3
8	102.9×10^{-9}	1.544×10^{-3}	ft^2/sec^3
9	102.9×10^{-9}	11.32×10^{-3}	ft^2/sec^3
10	0	25.0	ft^2/sec
11	33.34	1667	ft^2/sec
12	0	2.0	ft^2/sec
13	0	1×10^{-10}	ft^2/sec^3
14	0	1.0	ft^2/sec
15	0	1×10^{-9}	ft^2/sec^3
16	0	1×10^{-6}	ft^2/sec
17	0	1×10^{-6}	ft^2/sec
18	(time-varying)[note 1]	(time-varying)[note 2]	ft^2/sec^5
19	2.7451×10^{-11}	2.7451×10^{-11}	$\mu g^2/\text{sec}$
20	2.7451×10^{-11}	2.7451×10^{-11}	$\mu g^2/\text{sec}$
21	2.7451×10^{-11}	2.7451×10^{-11}	$\mu g^2/\text{sec}$
22	1.9548	1.9508	$\mu g^2/\text{sec}$
23	1.9548	1.9508	$\mu g^2/\text{sec}$
24	1.9548	1.9508	$\mu g^2/\text{sec}$

Table C-4: States 1-24 of ENRS Filter Tuning Parameters Q(t)

State Number	Truth Model Value	Filter Q Value	Units
25	0	1×10^{-10}	$(deg/hr)^2/sec$
26	0	1×10^{-10}	$(deg/hr)^2/sec$
27	0	0	$(deg/hr)^2/sec$
28	0	1×10^{-10}	%/sec
29	0	1×10^{-10}	%/sec
30	0	0	%/sec
31	0	1×10^{-8}	$\mu g^2/sec$
32	0	1×10^{-8}	$\mu g^2/sec$
33	0	1×10^{-8}	$\mu g^2/sec$
34	0	1×10^{-8}	%/sec
35	0	1×10^{-8}	%/sec
36	0	1×10^{-8}	%/sec
37	0	1×10^{-8}	%/sec
38	0	1×10^{-8}	%/sec
39	0	1×10^{-8}	%/sec
40	0	1×10^{-8}	$(arc\text{-}sec)^2/sec$
41	0	1×10^{-8}	$(arc\text{-}sec)^2/sec$
42	0	1×10^{-8}	$(arc\text{-}sec)^2/sec$
43	0	1×10^{-8}	$(arc\text{-}sec)^2/sec$

Table C-5: States 25-43 of ENRS Filter Tuning Parameters Q(t)

State Number	Truth Model Value	Filter Q Value	Units
44	0	2×10^{-3}	ft^2/sec
45	0	2×10^{-3}	ft^2/sec
46	0	2×10^{-3}	ft^2/sec
47	6.667×10^{-13}	6.667×10^{-6}	ft^2/sec
48	0	2×10^{-3}	ft^2/sec
49	0	2×10^{-3}	ft^2/sec
50	0	2×10^{-3}	ft^2/sec
51	6.667×10^{-13}	6.667×10^{-6}	ft^2/sec
52	0	2×10^{-3}	ft^2/sec
53	0	2×10^{-3}	ft^2/sec
54	0	2×10^{-3}	ft^2/sec
55	6.667×10^{-13}	6.667×10^{-6}	ft^2/sec
56	0	2×10^{-3}	ft^2/sec
57	0	2×10^{-3}	ft^2/sec
58	0	2×10^{-3}	ft^2/sec
59	6.667×10^{-13}	6.667×10^{-6}	ft^2/sec
60	0	2×10^{-3}	ft^2/sec
61	0	2×10^{-3}	ft^2/sec
62	0	2×10^{-3}	ft^2/sec
63	6.667×10^{-13}	6.667×10^{-6}	ft^2/sec
64	0	2×10^{-3}	ft^2/sec
65	0	2×10^{-3}	ft^2/sec
66	0	2×10^{-3}	ft^2/sec
67	6.667×10^{-13}	6.667×10^{-6}	ft^2/sec

Table C-6: States 44-67 of ENRS Filter Tuning Parameters Q(t)

State Number	Truth Model Value	Filter Q Value	Units
1	0	0.5×10^{-14}	$(\text{arc-sec})^2/\text{sec}$
2	0	0.5×10^{-14}	$(\text{arc-sec})^2/\text{sec}$
3	0	1×10^{-15}	$(\text{arc-sec})^2/\text{sec}$
4	190.4×10^{-15}	9.52×10^{-13}	$(\text{arc-sec})^2/\text{sec}$
5	190.4×10^{-15}	9.52×10^{-13}	$(\text{arc-sec})^2/\text{sec}$
6	190.4×10^{-15}	1.618×10^{-11}	$(\text{arc-sec})^2/\text{sec}$
7	102.9×10^{-9}	1.544×10^{-3}	ft^2/sec^3
8	102.9×10^{-9}	1.544×10^{-3}	ft^2/sec^3
9	102.9×10^{-9}	11.32×10^{-3}	ft^2/sec^3
10	0	15.0	ft^2/sec
11	33.34	1667	ft^2/sec
12	0	1.5	ft^2/sec
13	0	1×10^{-10}	ft^2/sec^3
14	0	1.0	ft^2/sec
15	0	1×10^{-9}	ft^2/sec^3
16	0	1×10^{-6}	ft^2/sec
17	0	1×10^{-6}	ft^2/sec
18	(time-varying)[note 1]	(time-varying)[note 2]	ft^2/sec^5
19	2.7451×10^{-11}	2.7451×10^{-11}	$\mu\text{g}^2/\text{sec}$
20	2.7451×10^{-11}	2.7451×10^{-11}	$\mu\text{g}^2/\text{sec}$
21	2.7451×10^{-11}	2.7451×10^{-11}	$\mu\text{g}^2/\text{sec}$
22	1.9548	1.9508	$\mu\text{g}^2/\text{sec}$
23	1.9548	1.9508	$\mu\text{g}^2/\text{sec}$
24	1.9548	1.9508	$\mu\text{g}^2/\text{sec}$

Table C-7: States 1-24 of PNRS Filter Tuning Parameters Q(t)

State Number	Truth Model Value	Filter Q Value	Units
25	0	1×10^{-10}	$(deg/hr)^2/sec$
26	0	1×10^{-10}	$(deg/hr)^2/sec$
27	0	0	$(deg/hr)^2/sec$
28	0	1×10^{-10}	$\%/sec$
29	0	1×10^{-10}	$\%/sec$
30	0	0	$\%/sec$
31	0	1×10^{-8}	$\mu g^2/sec$
32	0	1×10^{-8}	$\mu g^2/sec$
33	0	1×10^{-8}	$\mu g^2/sec$
34	0	1×10^{-8}	$\%/sec$
35	0	1×10^{-8}	$\%/sec$
36	0	1×10^{-8}	$\%/sec$
37	0	1×10^{-8}	$\%/sec$
38	0	1×10^{-8}	$\%/sec$
39	0	1×10^{-8}	$\%/sec$
40	0	1×10^{-8}	$(arc\text{-}sec)^2/sec$
41	0	1×10^{-8}	$(arc\text{-}sec)^2/sec$
42	0	1×10^{-8}	$(arc\text{-}sec)^2/sec$
43	0	1×10^{-8}	$(arc\text{-}sec)^2/sec$

Table C-8: States 25-43 of PNRS Filter Tuning Parameters Q(t)

State Number	Truth Model Value	Filter Q Value	Units
44	0	2×10^{-3}	ft^2/sec
45	0	2×10^{-3}	ft^2/sec
46	0	2×10^{-3}	ft^2/sec
47	6.667×10^{-13}	6.667×10^{-6}	ft^2/sec
48	0	2×10^{-3}	ft^2/sec
49	0	2×10^{-3}	ft^2/sec
50	0	2×10^{-3}	ft^2/sec
51	6.667×10^{-13}	6.667×10^{-6}	ft^2/sec
52	0	2×10^{-3}	ft^2/sec
53	0	2×10^{-3}	ft^2/sec
54	0	2×10^{-3}	ft^2/sec
55	6.667×10^{-13}	6.667×10^{-6}	ft^2/sec
56	0	2×10^{-3}	ft^2/sec
57	0	2×10^{-3}	ft^2/sec
58	0	2×10^{-3}	ft^2/sec
59	6.667×10^{-13}	6.667×10^{-6}	ft^2/sec
60	0	2×10^{-3}	ft^2/sec
61	0	2×10^{-3}	ft^2/sec
62	0	2×10^{-3}	ft^2/sec
63	6.667×10^{-13}	6.667×10^{-6}	ft^2/sec
64	0	2×10^{-3}	ft^2/sec
65	0	2×10^{-3}	ft^2/sec
66	0	2×10^{-3}	ft^2/sec
67	6.667×10^{-13}	6.667×10^{-6}	ft^2/sec
68	0	0.5 [note 3]	ft^2/sec
69	0	0.5 [note 3]	ft^2/sec
70	0	0.5 [note 3]	ft^2/sec
71	0	0.5 [note 3]	ft^2/sec

Table C-9: States 44-71 of PNRS Filter Tuning Parameters Q(t)

Measurement	Truth Model Value	Filter R Value	Units
RRS	4.0	6.0	ft^2
GPS	9.0	300.0	ft^2
Velocity	0.02	0.02	$(ft/sec)^2$
Baro-altimeter	2500.0	2500.0	ft^2

Table C-10: Measurement Noise Variance $R(t_i)$ for NRS Filter

Measurement	Truth Model Value	Filter R Value	Units
RRS	4.0	6.0	ft^2
DGPS	9.0	30.0	ft^2
Velocity	0.02	0.02	$(ft/sec)^2$
Baro-altimeter	2500.0	2500.0	ft^2

Table C-11: Measurement Noise Variance $R(t_i)$ for ENRS Filter

Measurement	Truth Model Value	Filter R Value	Units
RRS	4.0	6.0	ft^2
DGPS	9.0	30.0	ft^2
CPGPS	2.641×10^{-4}	3.0×10^{-4}	ft^2
Velocity	0.02	0.02	$(ft/sec)^2$
Baro-altimeter	2500.0	2500.0	ft^2

Table C-12: Measurement Noise Variance $R(t_i)$ for PNRS Filter

Notes:

1) Time varying from 0 to 26.9667

2) Time varying from 0.1062 to 26.9646

3) The PNRS filter for the cycle slip and loss-of-satellite simulations used a value of 5.0 ft^2/sec

C-11

Appendix D. NRS Simulation Results

This appendix presents the results of the NRS MSOFE simulation study. The simulation utilized the 95-state NRS truth model and 67-state NRS filter model derived in Chapter III of this thesis research. The results are presented in the form of 8 plots:

Plot D-1   (a) - Flight Profile Longitude
                      (b) - Flight Profile Latitude
                      (c) - Flight Profile Altitude

Plot D-2   (a) - Longitude Error
                      (b) - Latitude Error

Plot D-3   (a) - Altitude Error
                      (b) - Barometric Altitude Error

Plot D-4   (a) - North Tilt Error
                      (b) - West Tilt Error
                      (c) - Azimuth Tilt Error

Plot D-5   (a) - North Velocity Error
                      (b) - West Velocity Error
                      (c) - Vertical Velocity Error

Plot D-6   (a) - RRS Range Bias Error
                      (b) - RRS Velocity Bias Error
                      (c) - RRS Atmospheric Propagation Delay Error

Plot D-7   (a) - RRS X Position Survey Error
                      (b) - RRS Y Position Survey Error
                      (c) - RRS Z Position Survey Error

Plot D-8   (a) - GPS User Clock Bias Error
                      (b) - GPS User Clock Drift Error

Each plot shows the results of a 15-run Monte Carlo average of the truth state minus the filter state for the entire 2 hour flight profile, the true +/- one sigma standard deviation of the Monte Carlo simulation, and the filter predicted +/- one sigma standard deviation.

The following is a legend for the 8 plots:

Line Style	Description
————————————	15 Monte Carlo run mean
··	mean + and - true 1σ
- - - - - - - - - - - - - - - - - - - -	+ and - filter-predicted 1σ

Plot D-1: Flight Profile

D-3

Plot D-2: Longitude/Latitude Errors

(a)

(b)
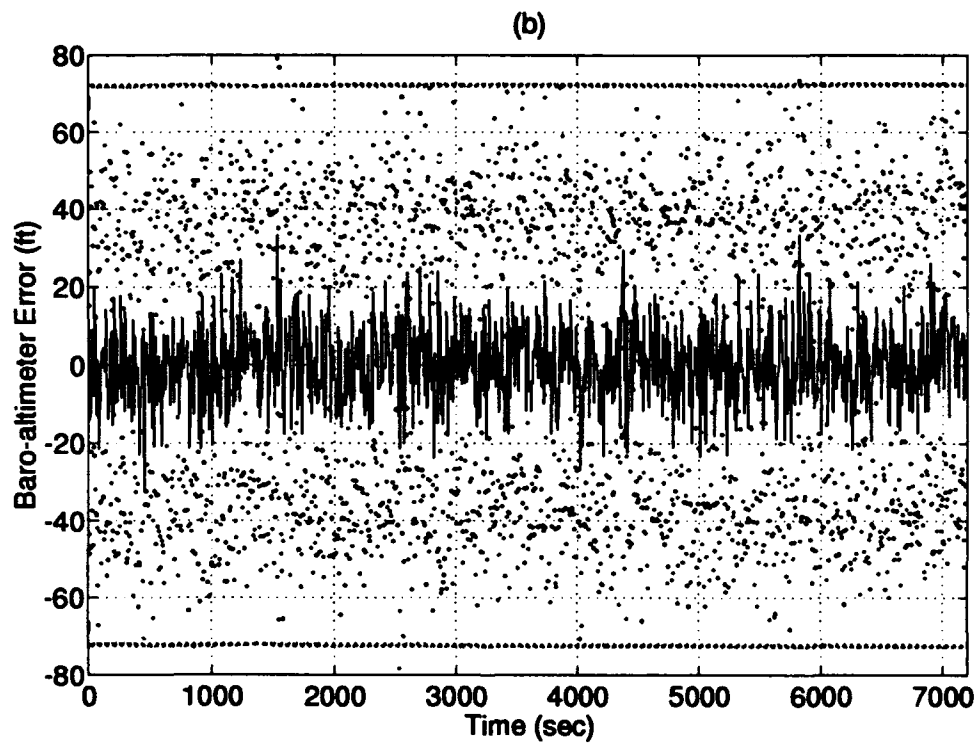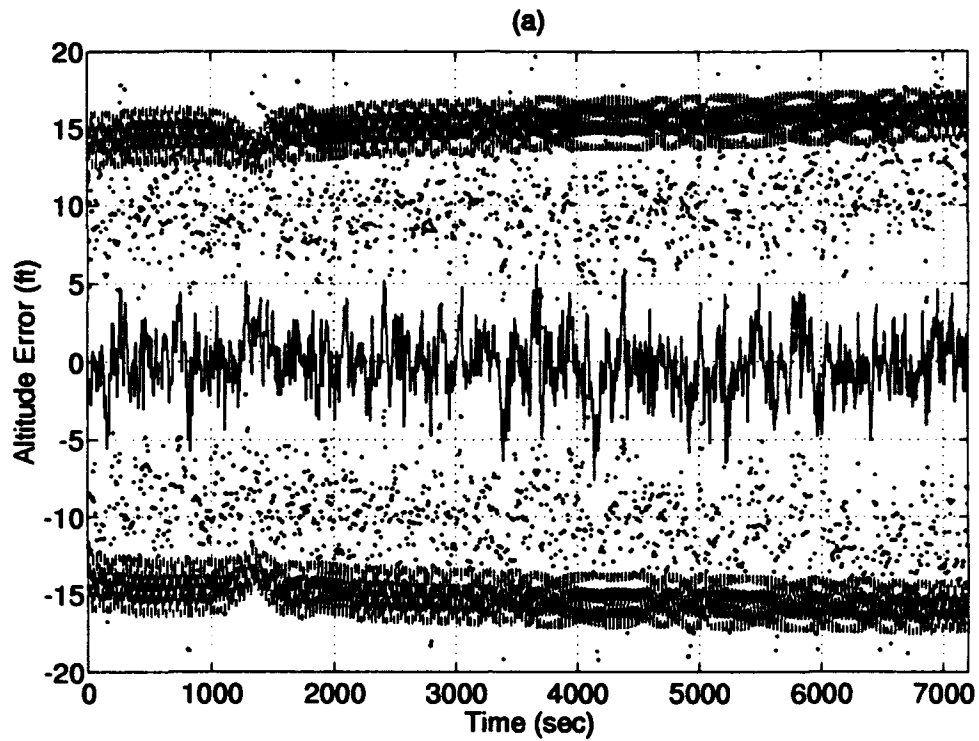
Plot D-3: Altitude/Barometric Altitude Errors
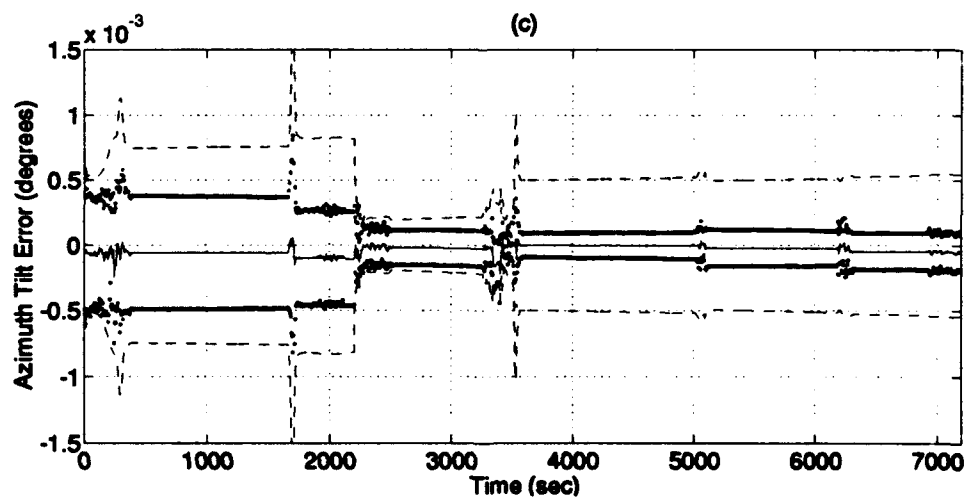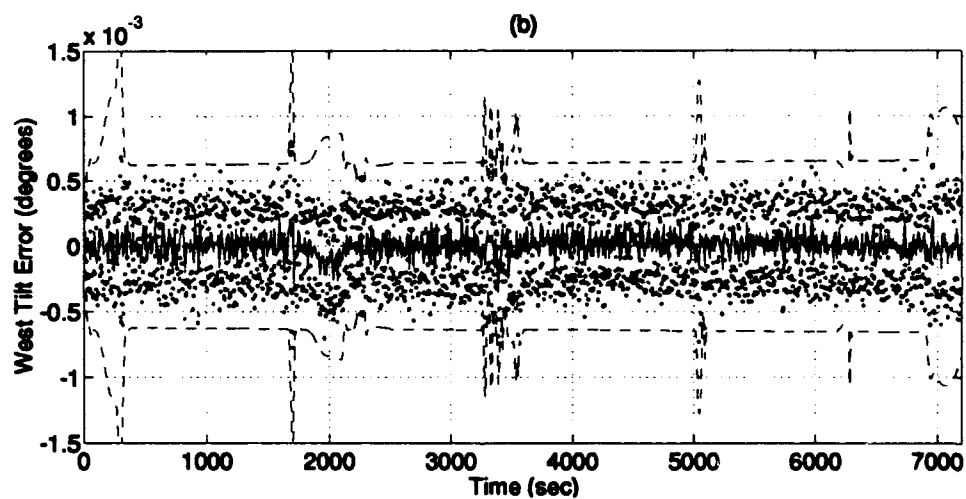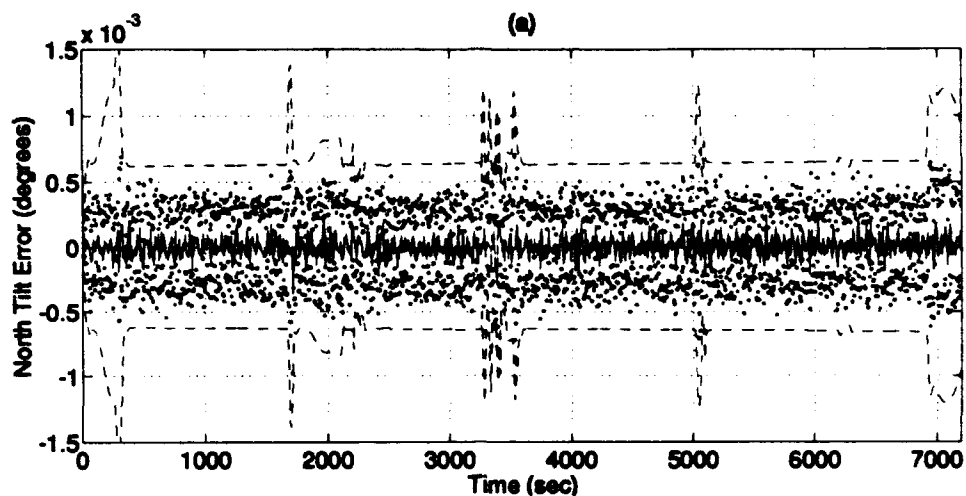
Plot D-4: North/West/Azimuth Tilt Errors
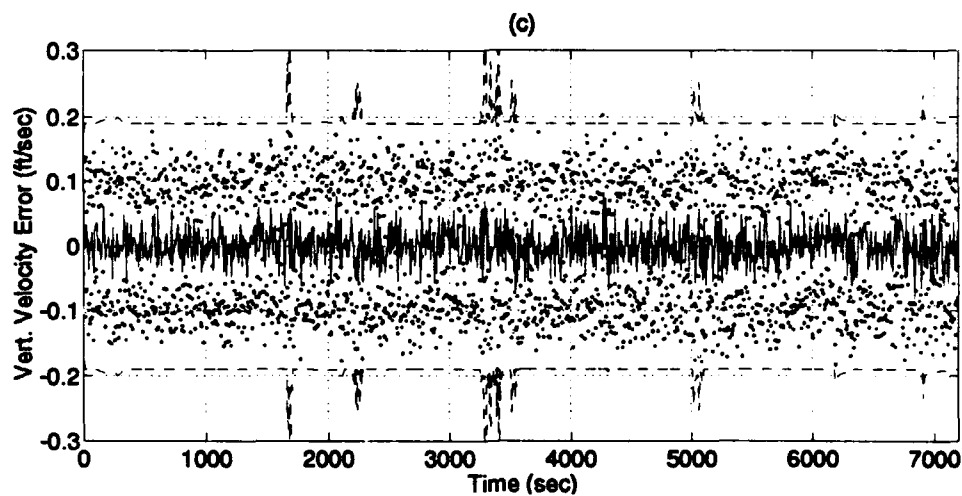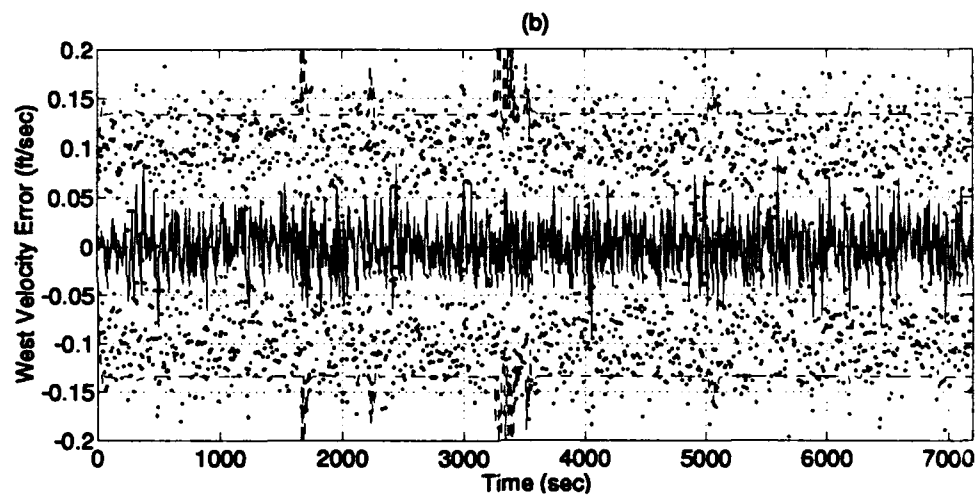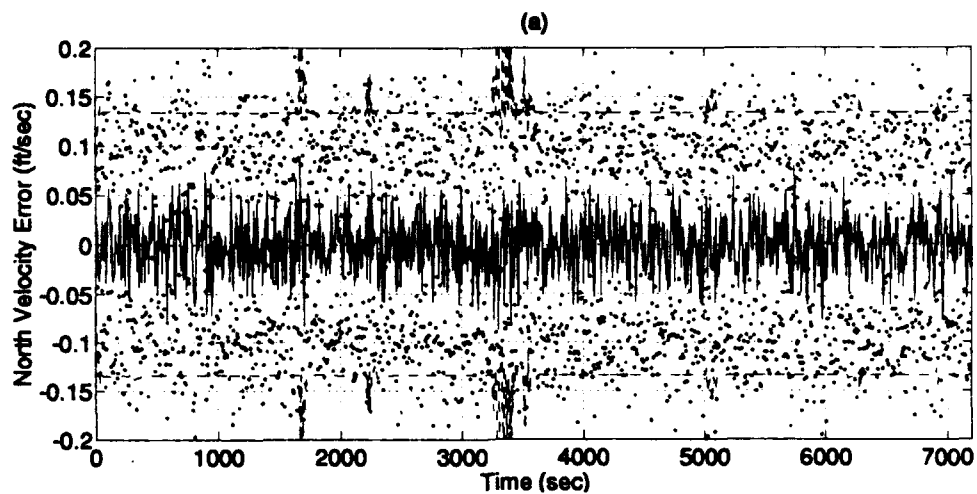
Plot D-5: North/West/Vertical Velocity Errors

(a)

(b)

(c)
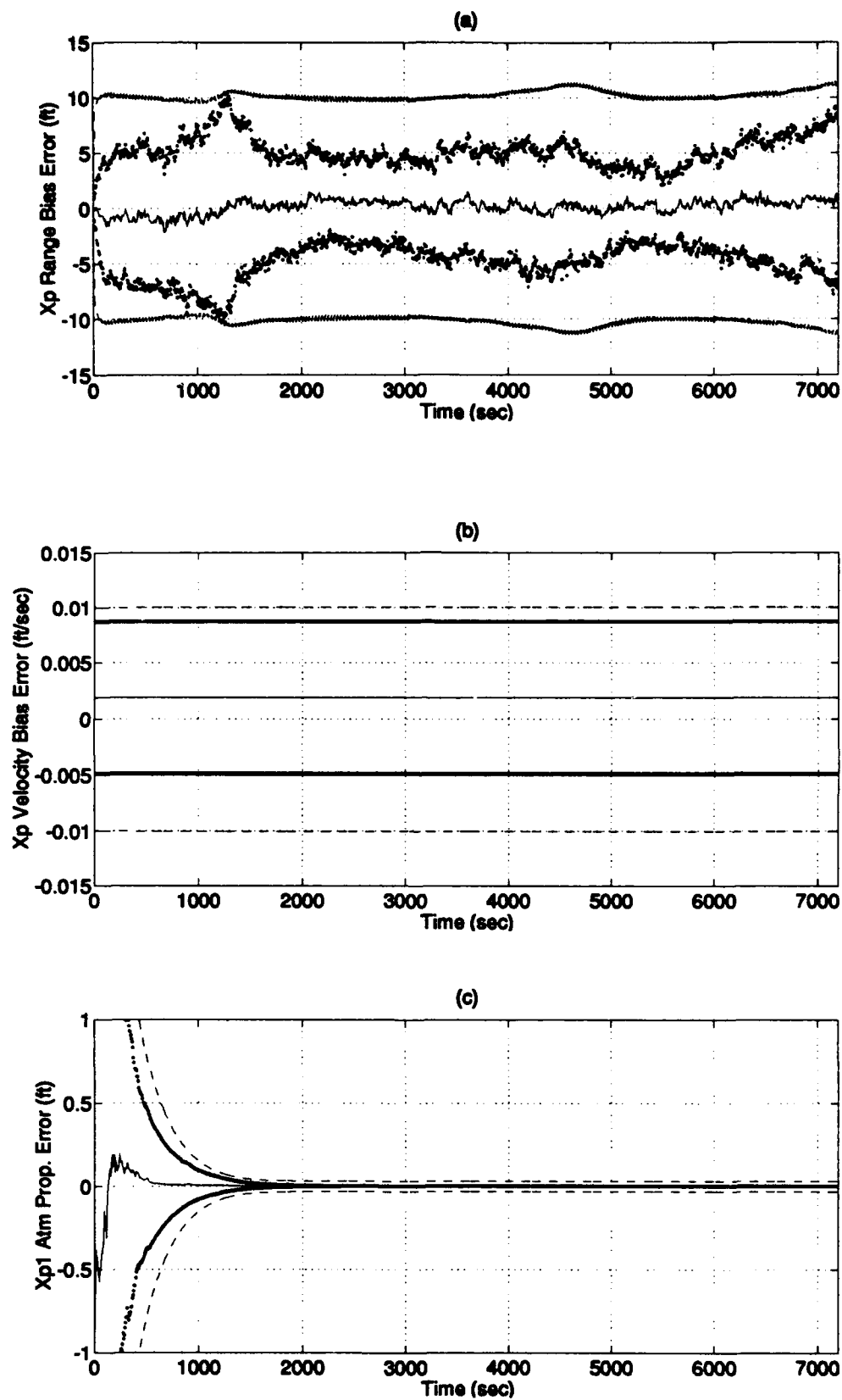
Plot D-6: RRS Range bias/Velocity bias/Atmospheric propagation delay Errors

(a)

(b)

(c)
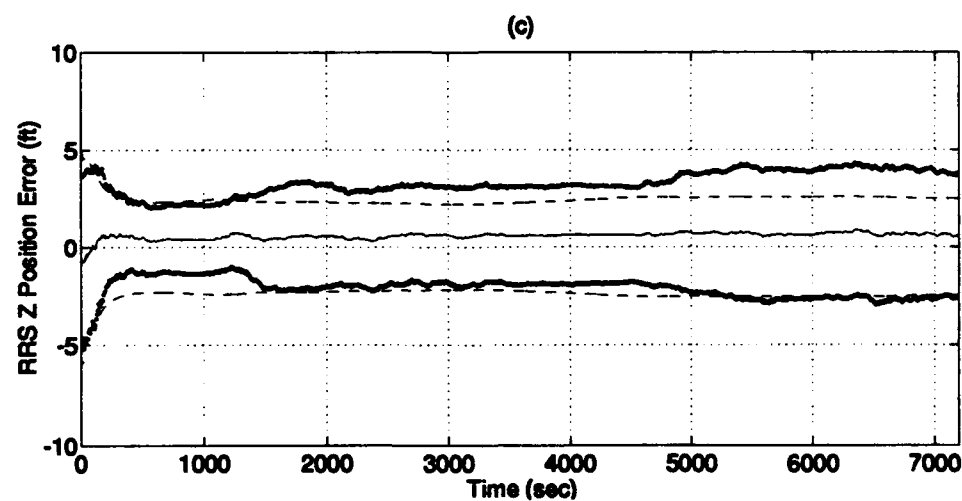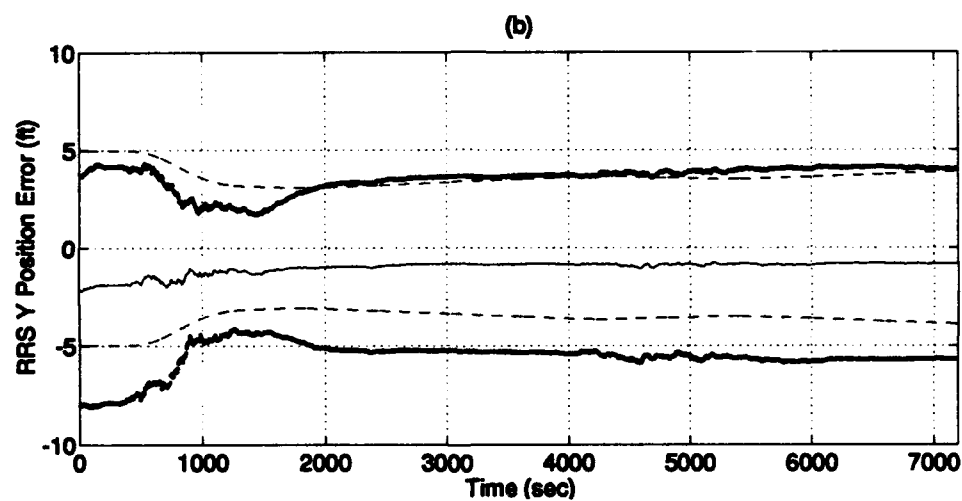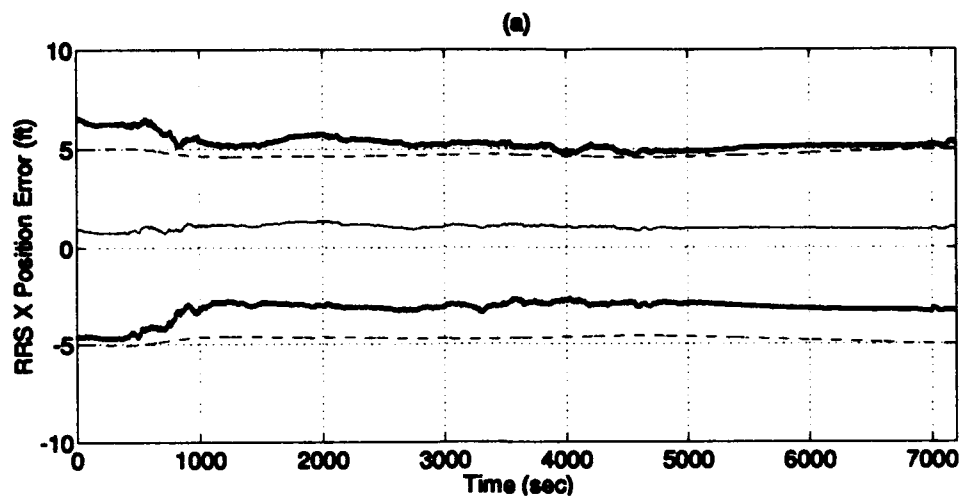
Plot D-7: RRS X/Y/Z Surveyed Position Errors

D-9

(a)

(b)
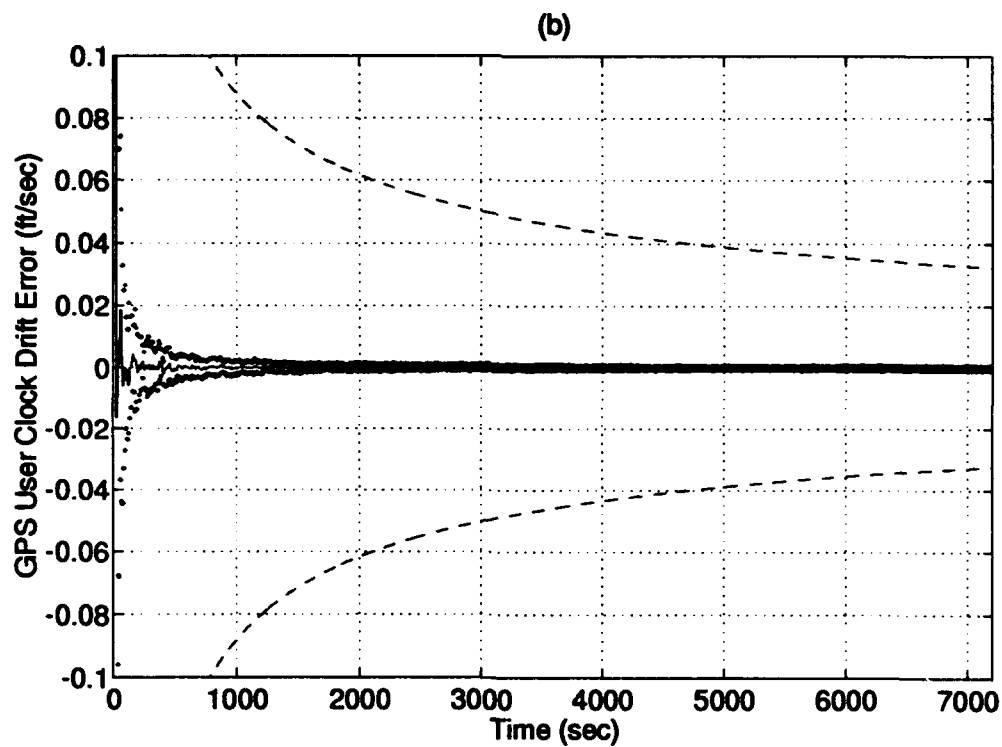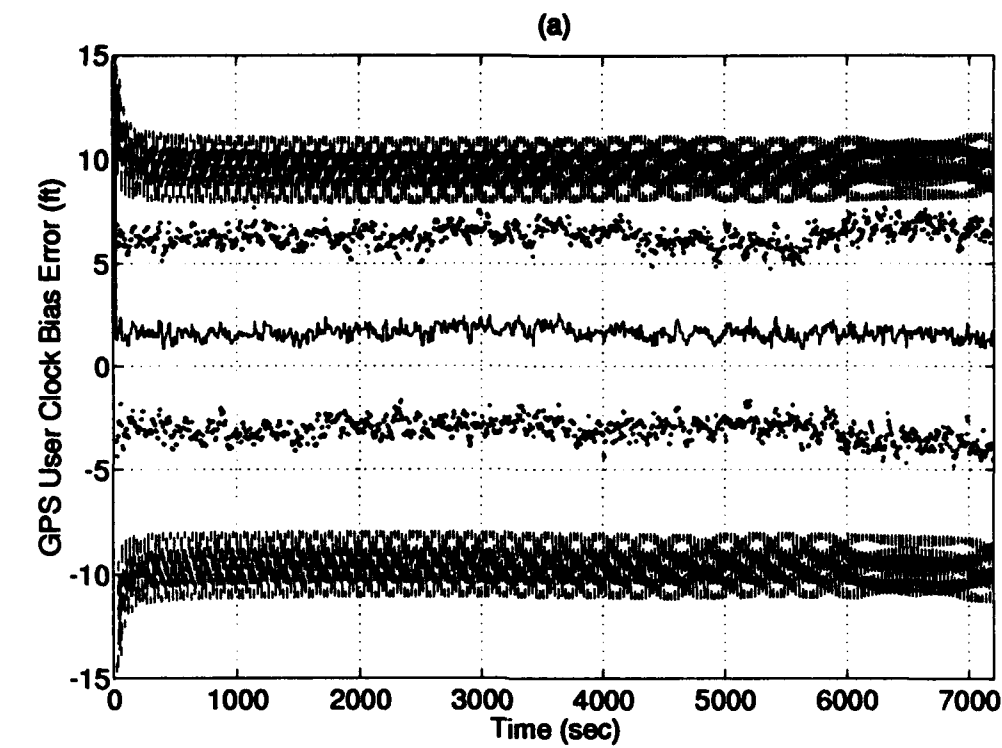
Plot D-8: GPS User Clock Bias/Drift Errors

D-10

Appendix E. ENRS Simulation Results

This appendix presents the results of the ENRS MSOFE simulation study. The simulation utilized the 87-state ENRS truth model and 67-state ENRS filter model derived in Chapter III of this thesis research. The results are presented in the form of 8 plots:

Plot E-1	(a) - Flight Profile Longitude
	(b) - Flight Profile Latitude
	(c) - Flight Profile Altitude
Plot E-2	(a) - Longitude Error
	(b) - Latitude Error
Plot E-3	(a) - Altitude Error
	(b) - Barometric Altitude Error
Plot E-4	(a) - North Tilt Error
	(b) - West Tilt Error
	(c) - Azimuth Tilt Error
Plot E-5	(a) - North Velocity Error
	(b) - West Velocity Error
	(c) - Vertical Velocity Error
Plot E-6	(a) - RRS Range Bias Error
	(b) - RRS Velocity Bias Error
	(c) - RRS Atmospheric Propagation Delay Error
Plot E-7	(a) - RRS X Position Survey Error
	(b) - RRS Y Position Survey Error
	(c) - RRS Z Position Survey Error
Plot E-8	(a) - GPS User Clock Bias Error
	(b) - GPS User Clock Drift Error

Each plot shows the results of a 15-run Monte Carlo average of the truth state minus the filter state for the entire 2 hour flight profile, the true +/- one sigma standard deviation of the Monte Carlo simulation, and the filter predicted +/- one sigma standard deviation.

The following is a legend for the 8 plots:

| Line Style	Description
————————	15 Monte Carlo run mean
····························	mean + and - true 1σ
- - - - - - - - - - - - - -	+ and - filter-predicted 1σ

Plot E-1: Flight Profile

(a)

(b)

Plot E-2: Longitude/Latitude Errors

E-4

(a)

(b)
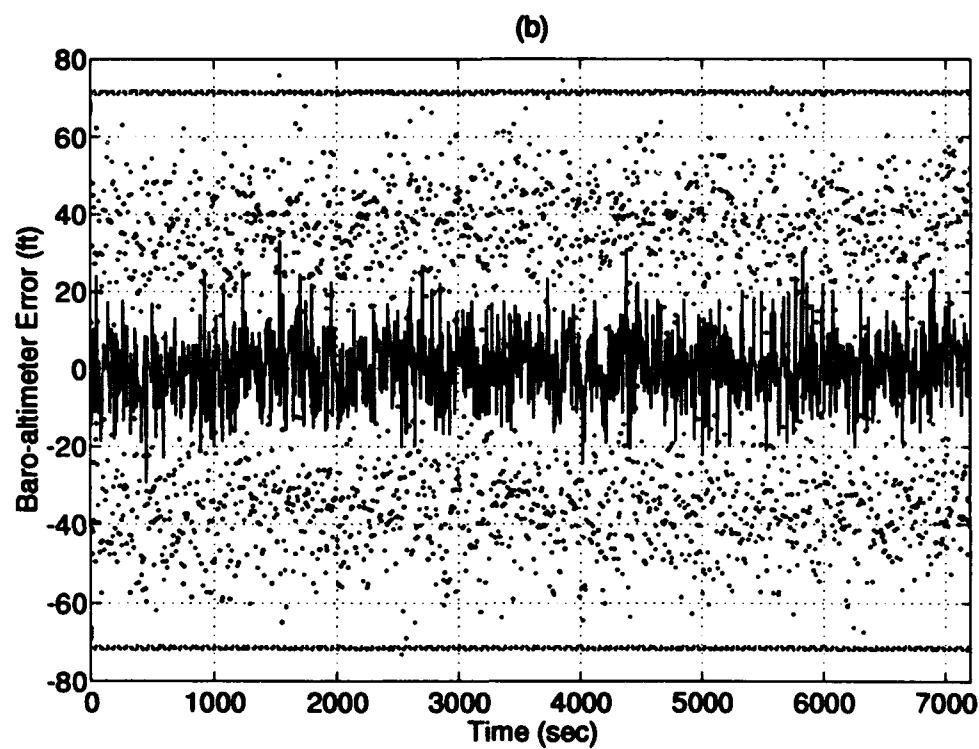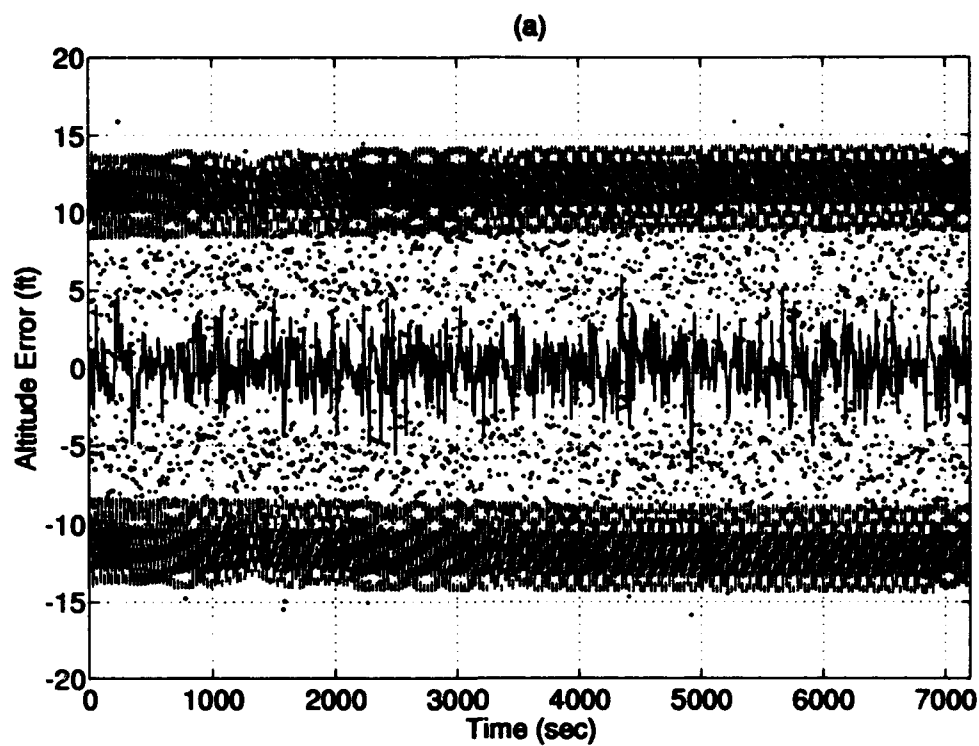
Plot E-3: Altitude/Barometric Altitude Errors
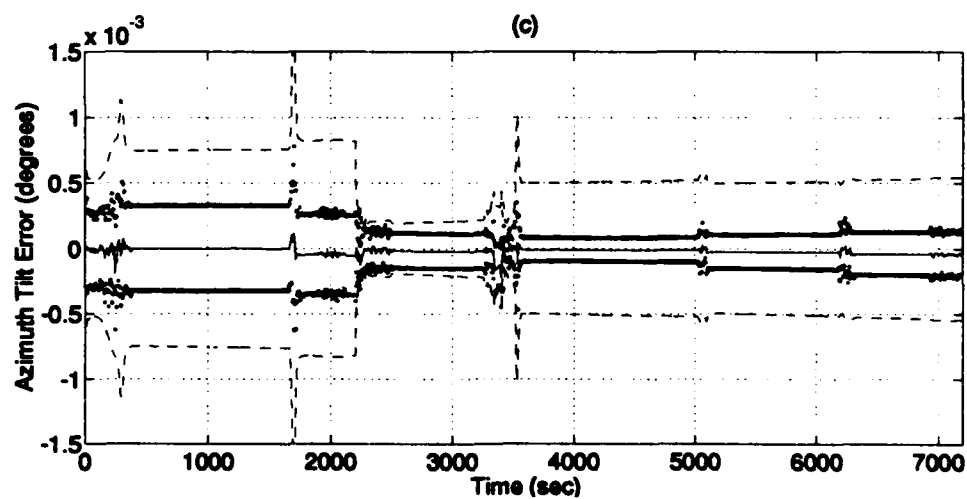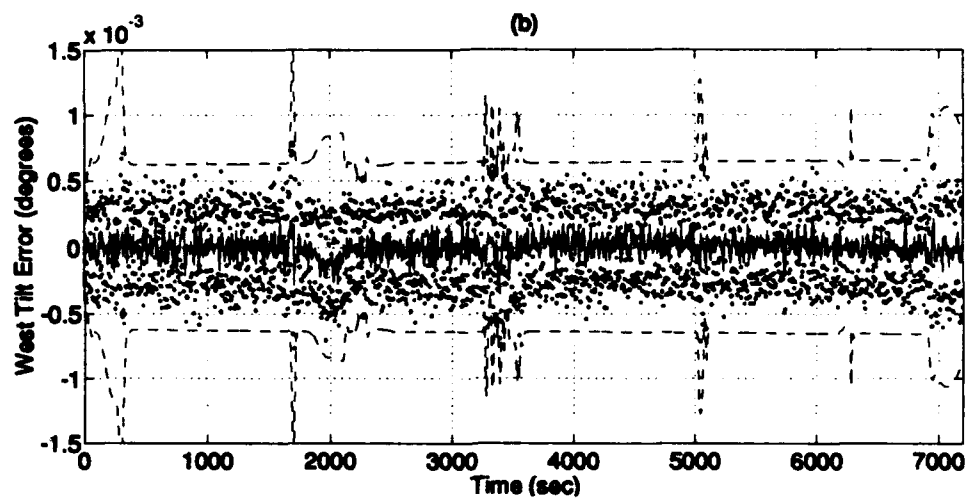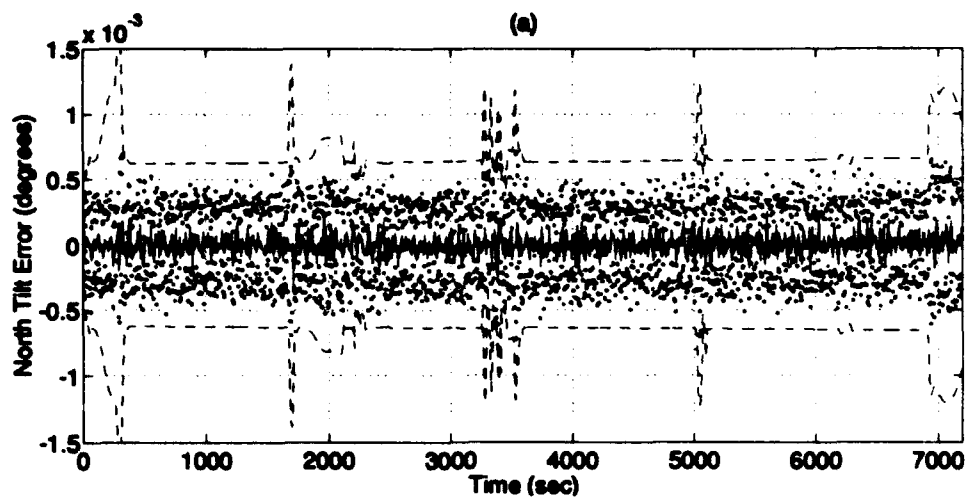
Plot E-4: North/West/Azimuth Tilt Errors

E-6

(a)

(b)

(c)
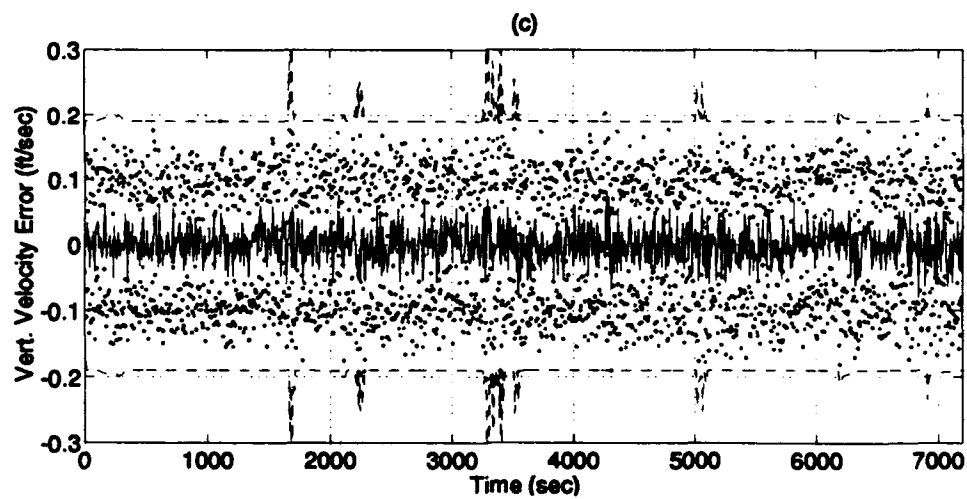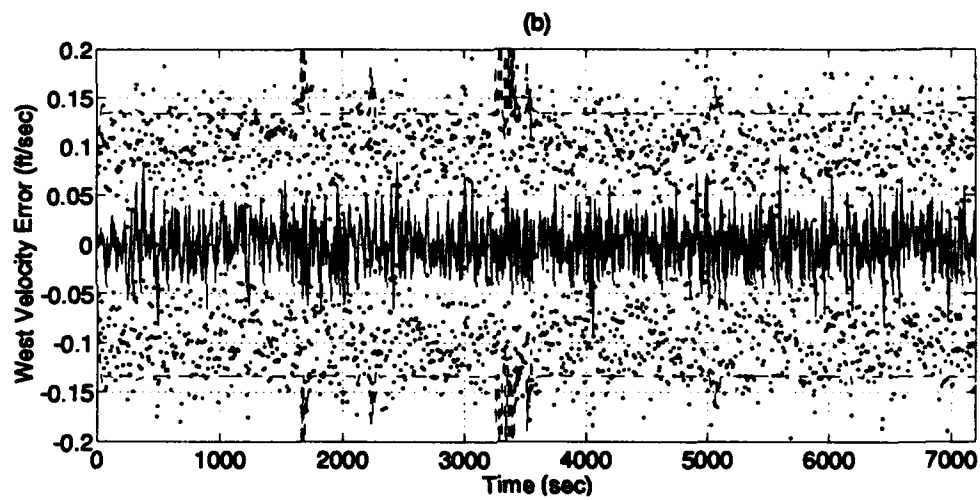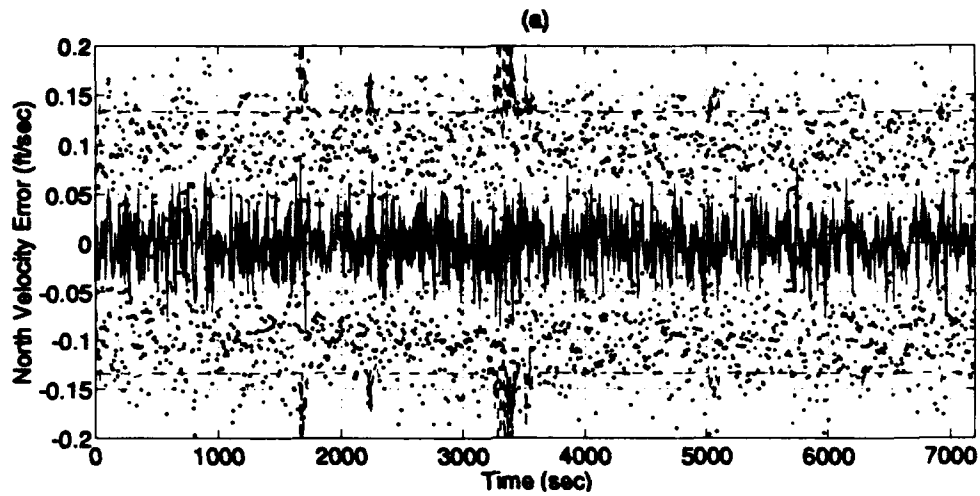
Plot E-5: North/West/Vertical Velocity Errors
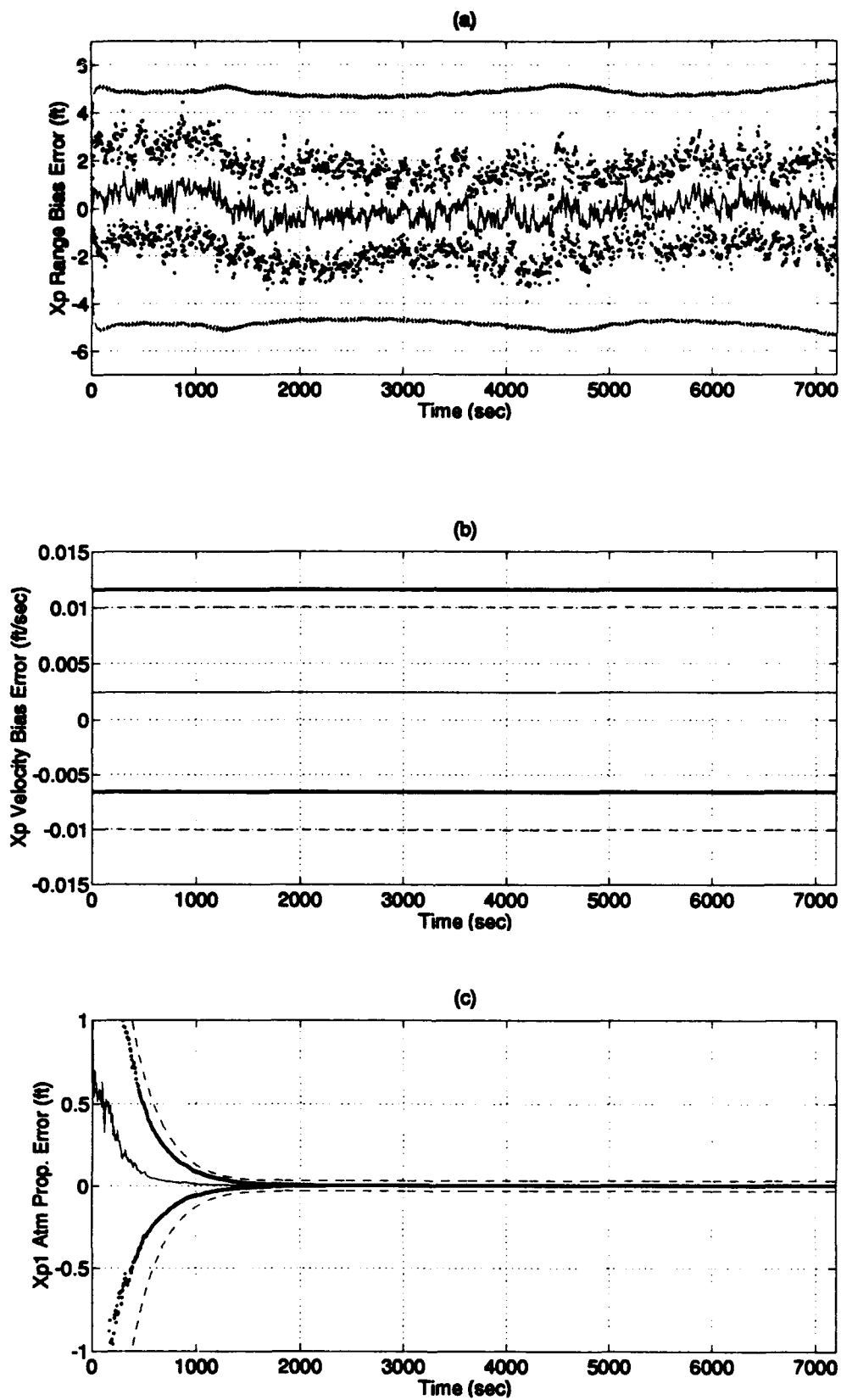
Plot E-6: RRS Range bias/Velocity bias/Atmospheric propagation delay Errors
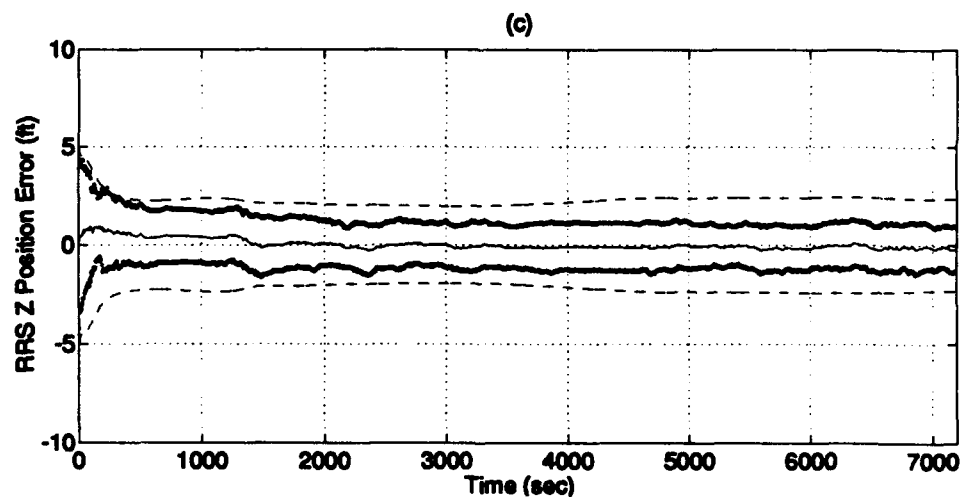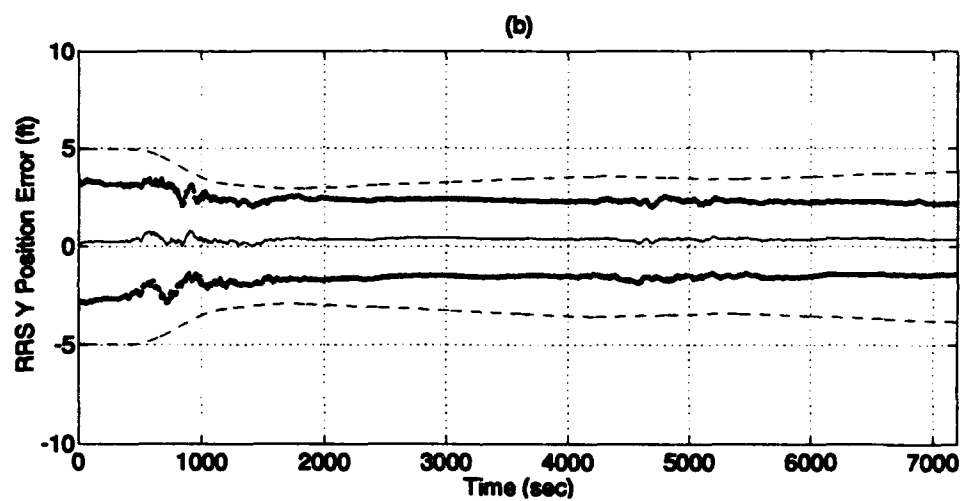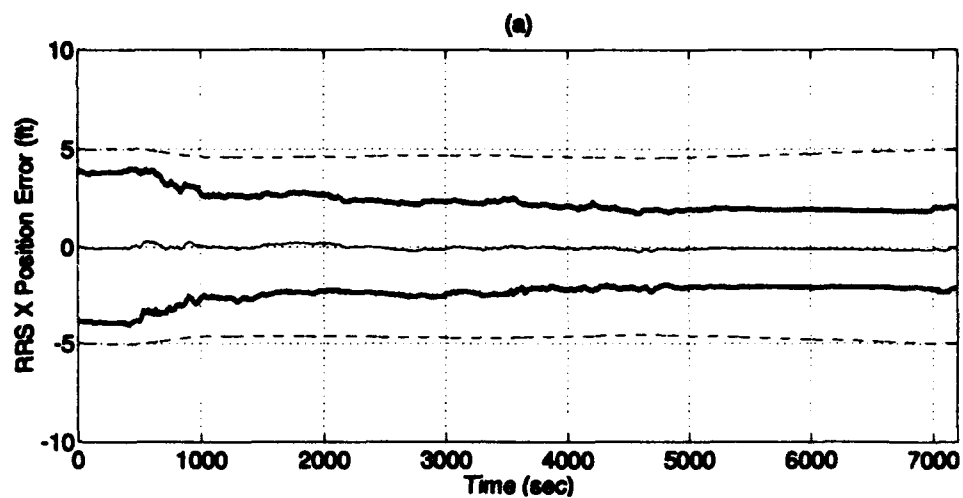
Plot E-7: RRS X/Y/Z Surveyed Position Errors

(a)

(b)
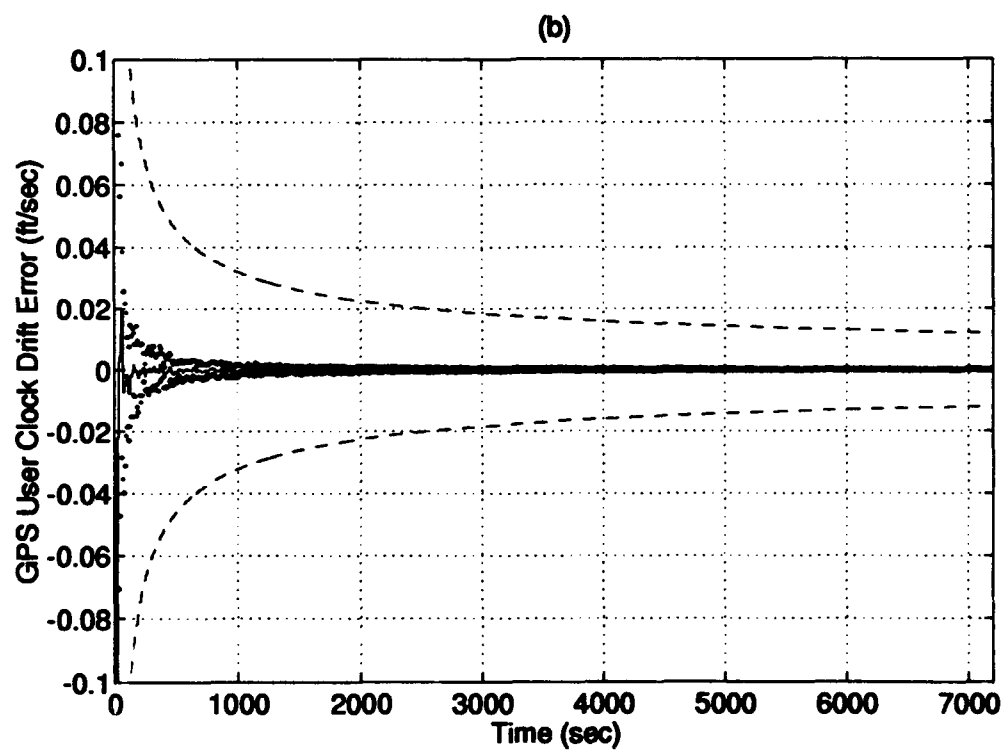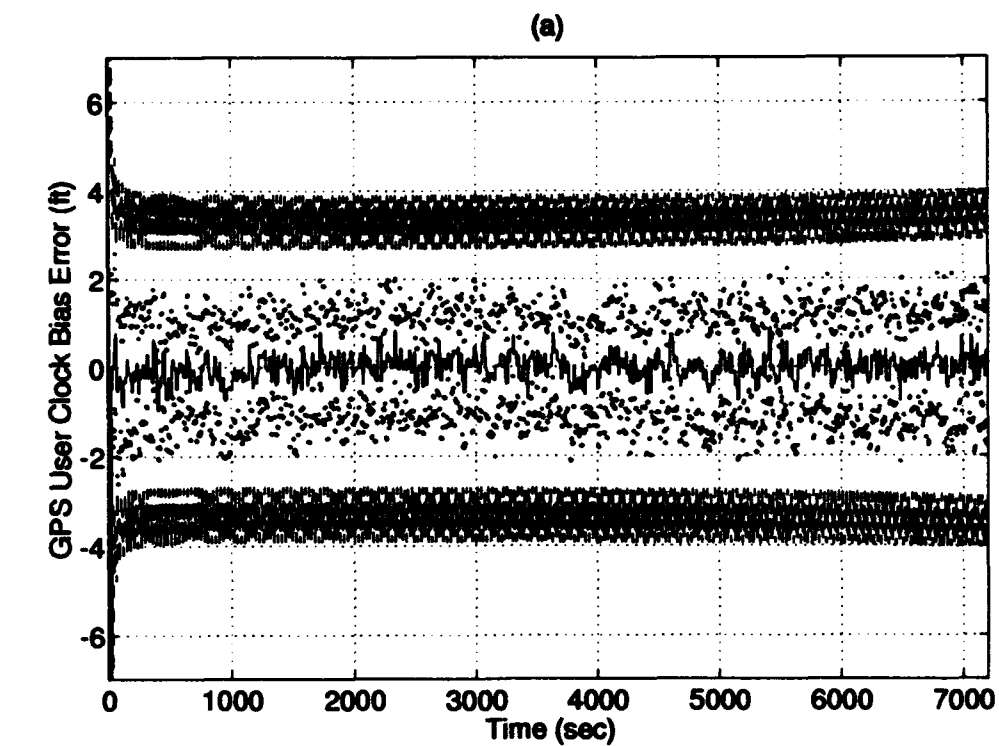
Plot E-8: GPS User Clock Bias/Drift Errors

E-10

Appendix F. PNRS Simulation Results

This appendix presents the results of the PNRS MSOFE simulation study (not including cycle slips). The simulation utilized the 91-state PNRS truth model and 71-state PNRS filter model derived in Chapter IV of this thesis research. The results are presented in the form of 10 plots:

Plot F-1   (a) - Flight Profile Longitiude
                       (b) - Flight Profile Latitude
                       (c) - Flight Profile Altitude

Plot F-2   (a) - Longitude Error
                       (b) - Latitude Error

Plot F-3   (a) - Altitude Error
                       (b) - Barometric Altitude Error

Plot F-4   (a) - North Tilt Error
                       (b) - West Tilt Error
                       (c) - Azimuth Tilt Error

Plot F-5   (a) - North Velocity Error
                       (b) - West Velocity Error
                       (c) - Vertical Velocity Error

Plot F-6   (a) - RRS Range Bias Error
   (b) - RRS Velocity Bias Error
                       (c) - RRS Atmospheric Propagation Delay Error

Plot F-7   (a) - RRS X Position Survey Error
                       (b) - RRS Y Position Survey Error
                       (c) - RRS Z Position Survey Error

Plot F-8   (a) - GPS User Clock Bias Error
                       (b) - GPS User Clock Drift Error

Plot F-9   (a) - GPS Satellite 1 Phase Ambiguity Error
                       (b) - GPS Satellite 2 Phase Ambiguity Error

Plot F-10   (a) - GPS Satellite 3 Phase Ambiguity Error
                       (b) - GPS Satellite 4 Phase Ambiguity Error

Each plot shows the results of a 15-run Monte Carlo average of the truth state minus the filter state for the entire 2 hour flight profile, the true +/- one sigma standard deviation of the Monte Carlo simulation and the filter predicted +/- one sigma standard deviation.

The following is a legend for the 10 plots:

Line Style	Description
————————————	15 Monte Carlo run mean
····································	mean + and - true 1σ
--------------------------------	+ and - filter-predicted 1σ
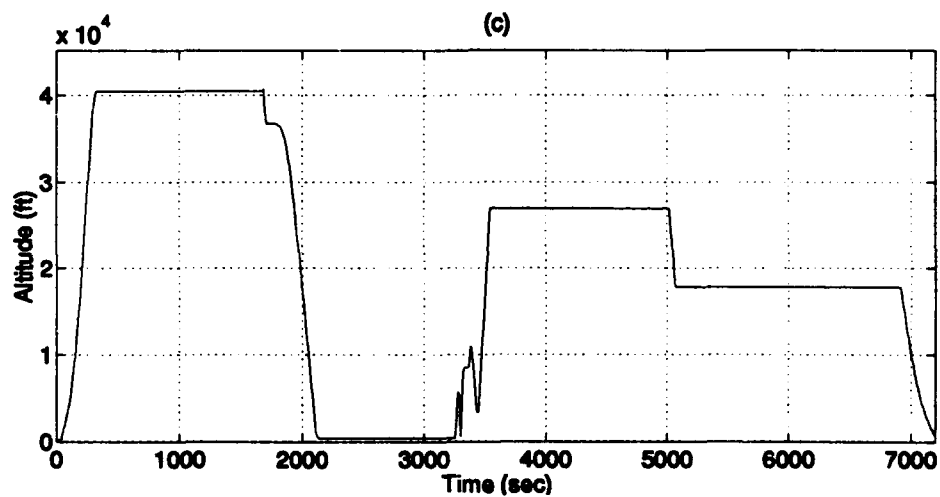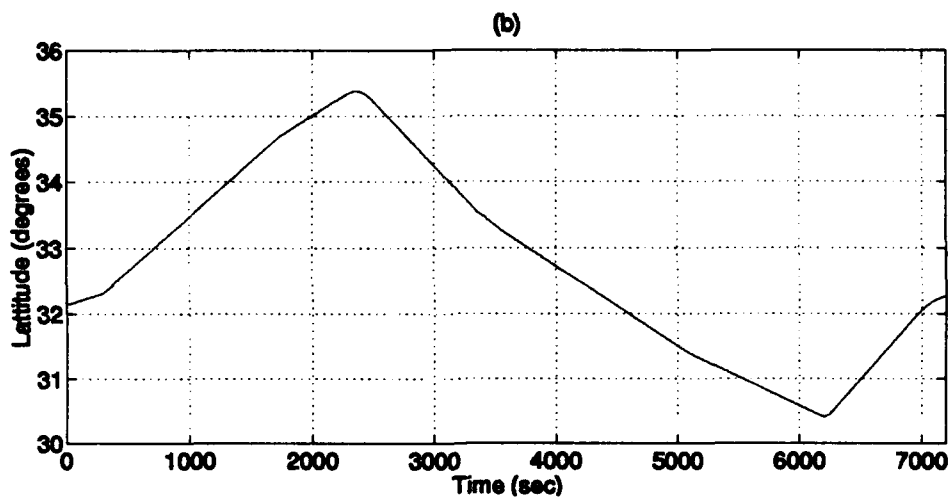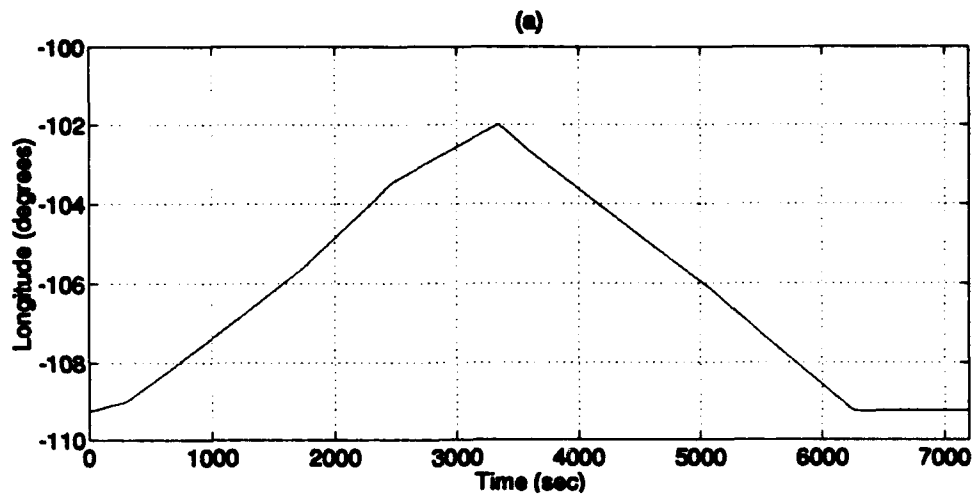
Plot F-1: Flight Profile

F-3
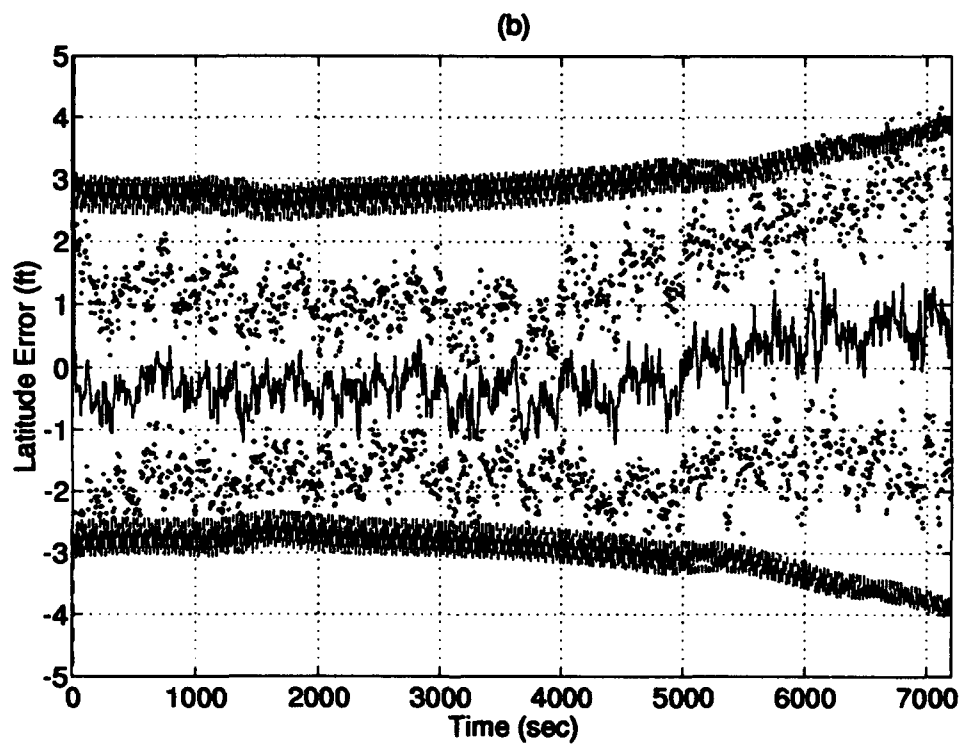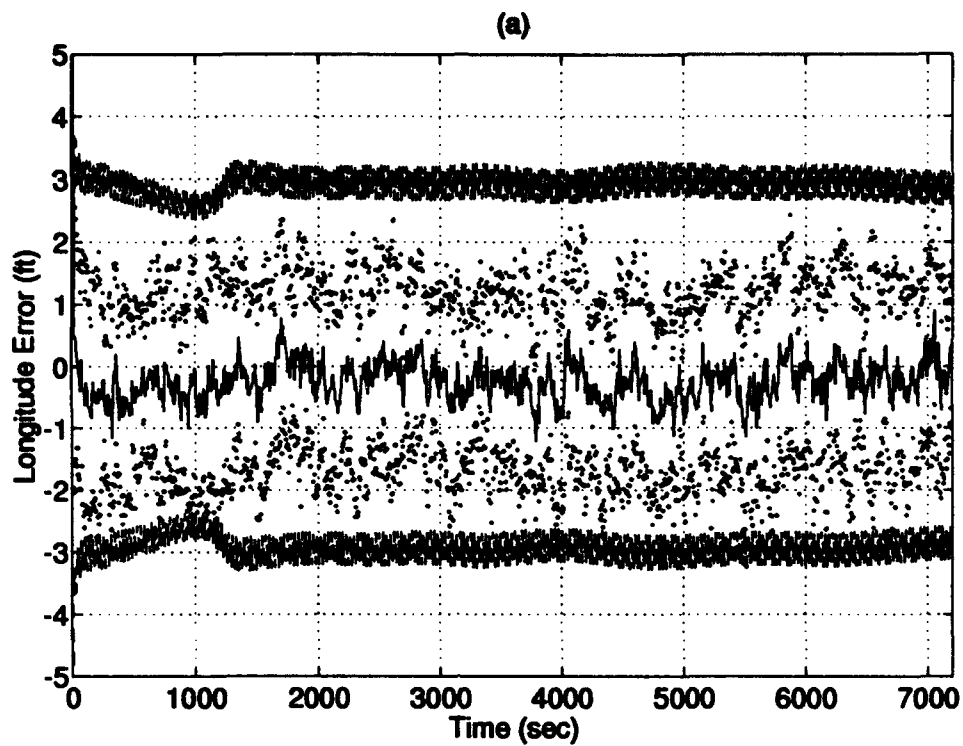
Plot F-2: Longitude/Latitude Errors

F-4
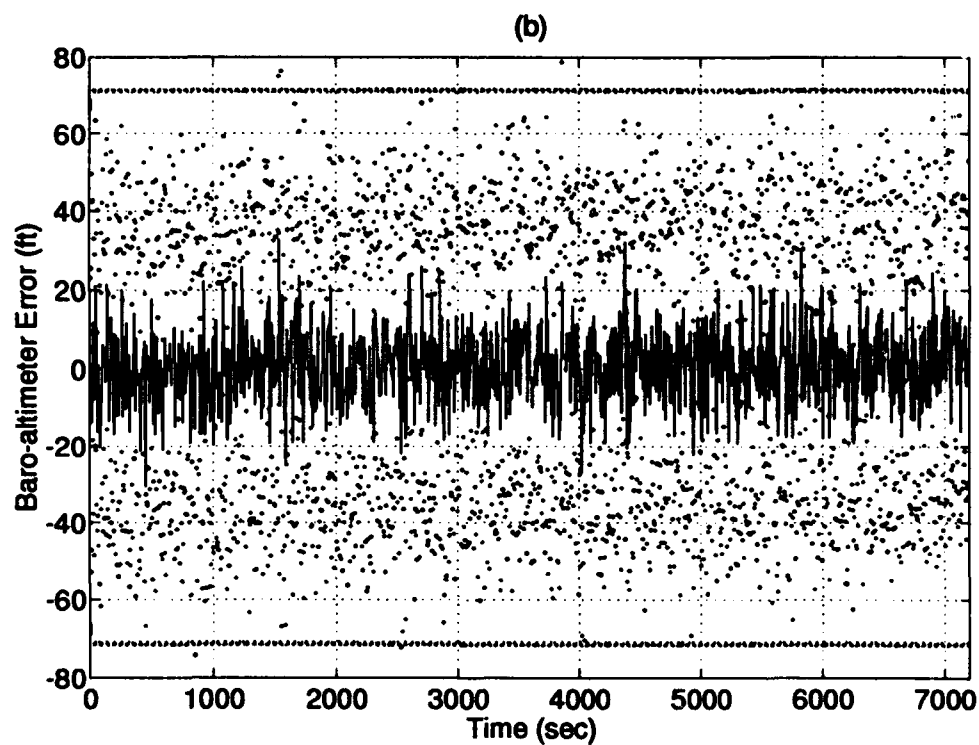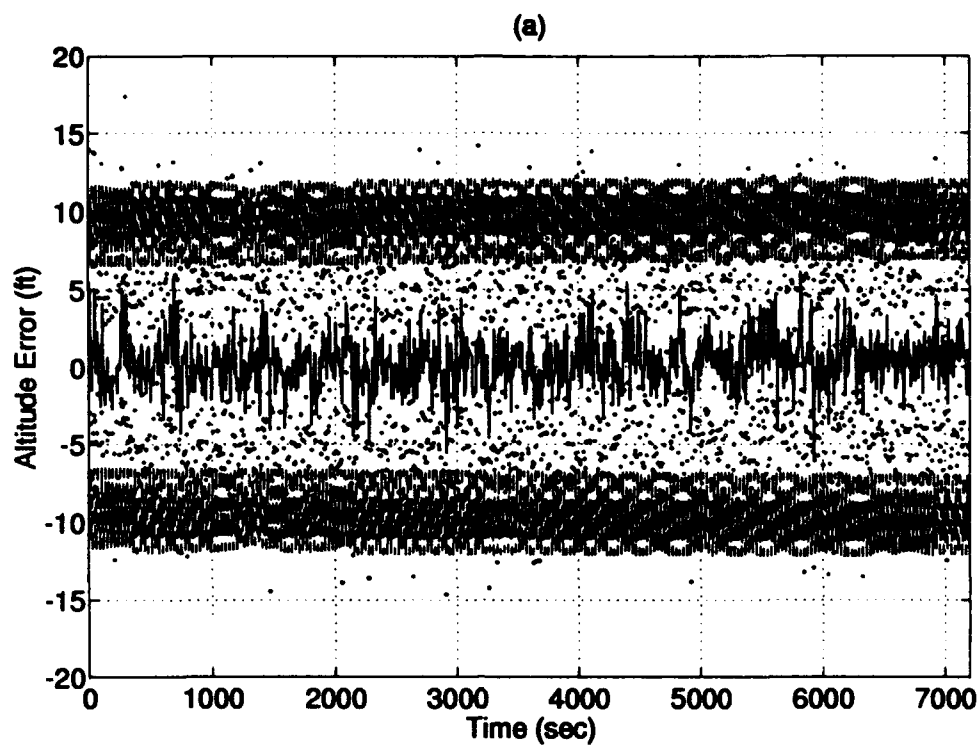
Plot F-3: Altitude/Barometric Altitude Errors
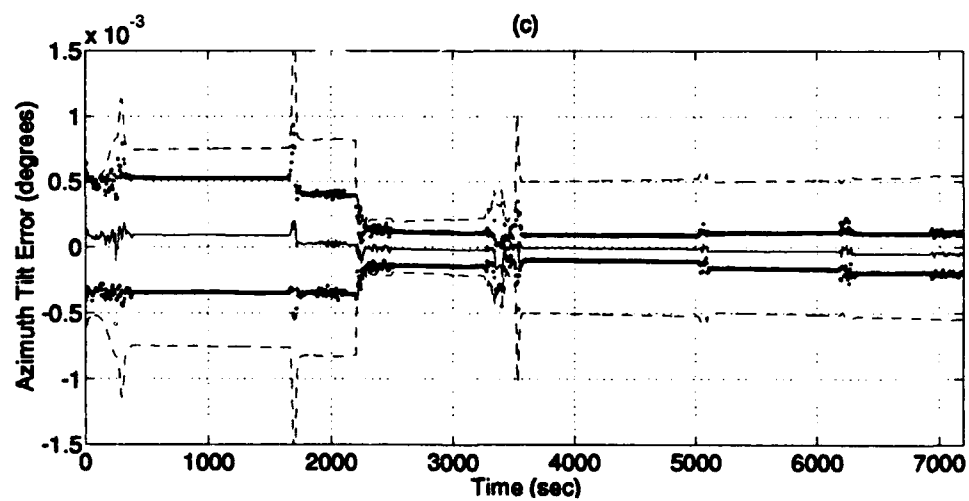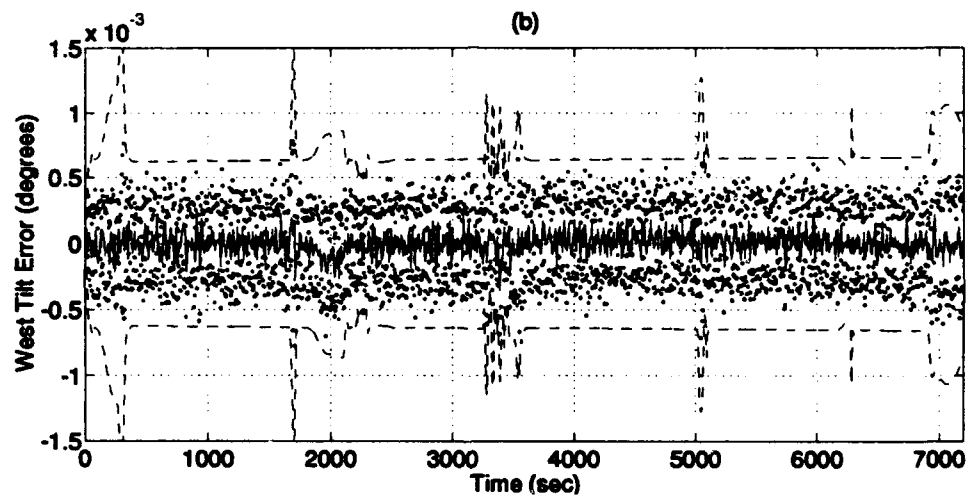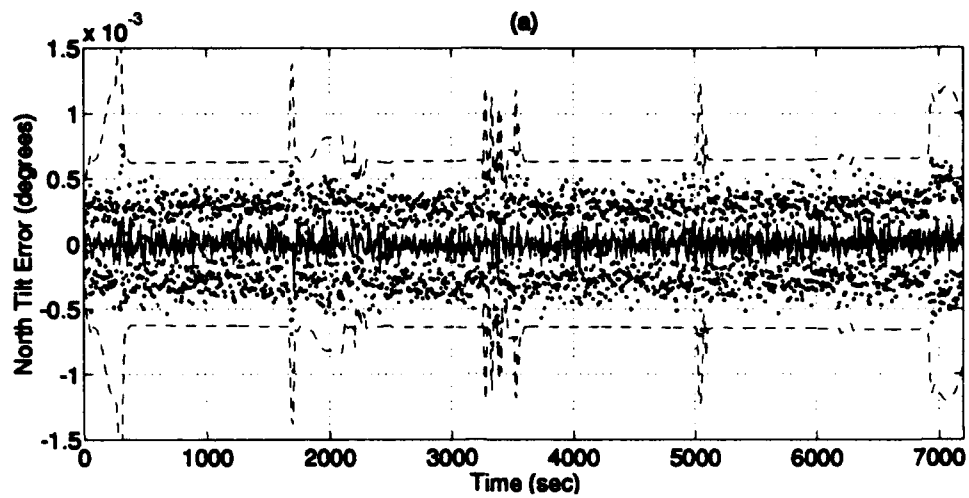
Plot F-4: North/West/Azimuth Tilt Errors

F-6
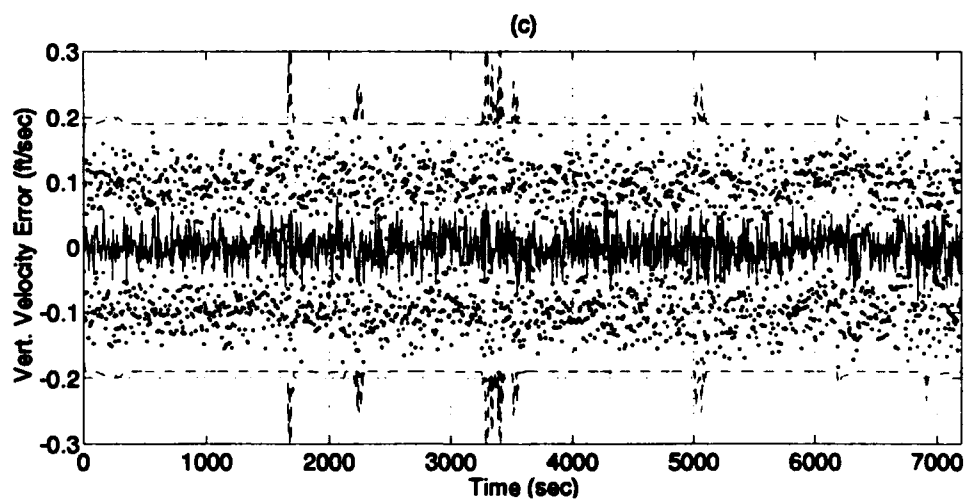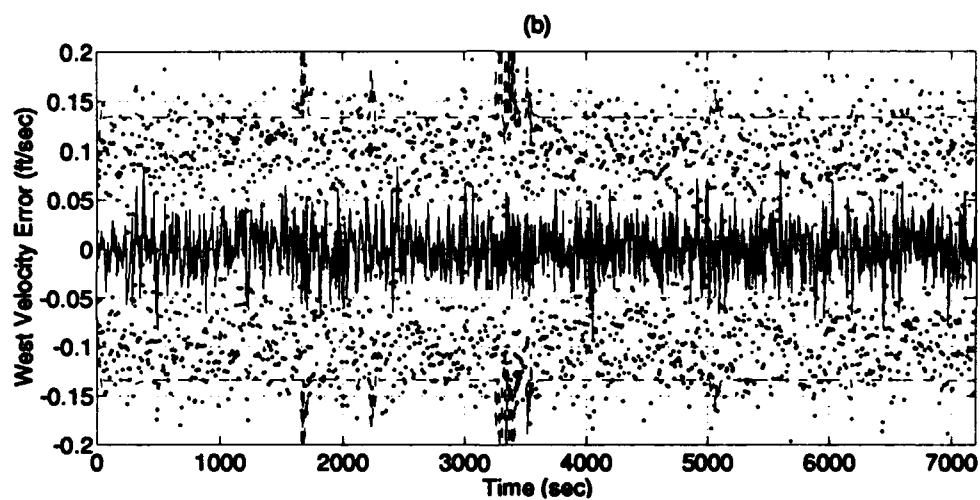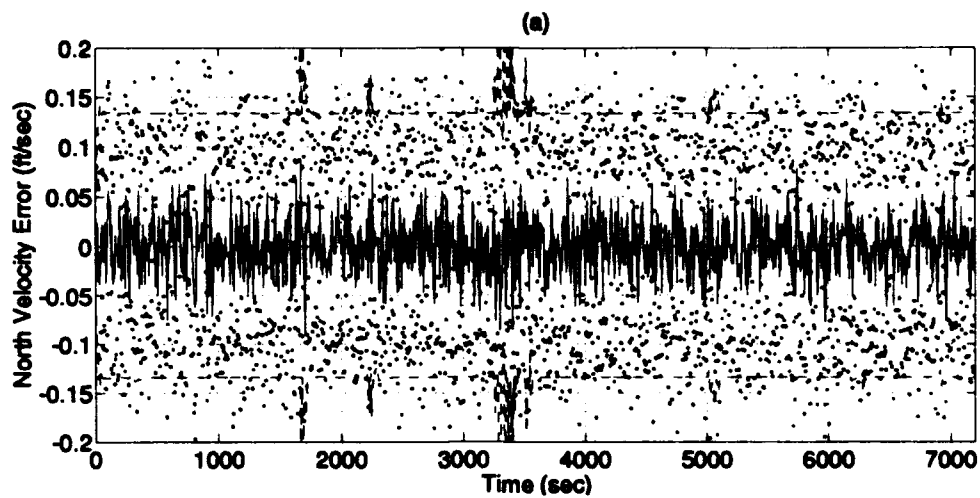
Plot F-5: North/West/Vertical Velocity Errors

F-7
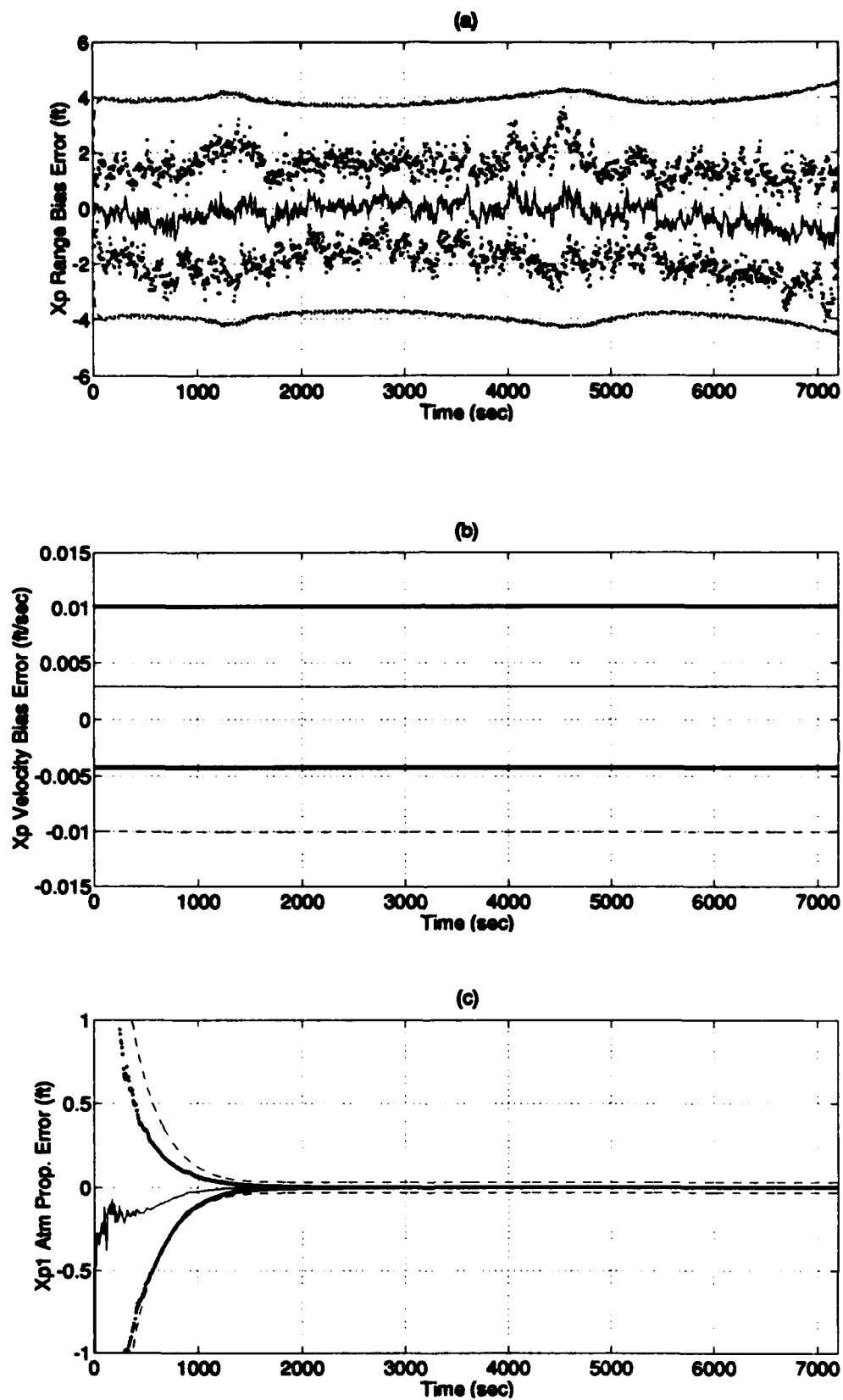
Plot F-6: RRS Range bias/Velocity bias/Atmospheric propagation delay Errors
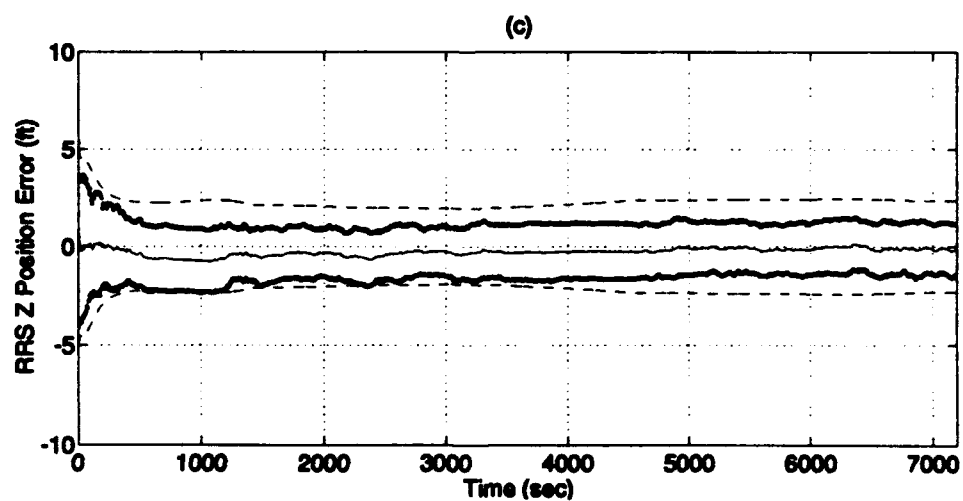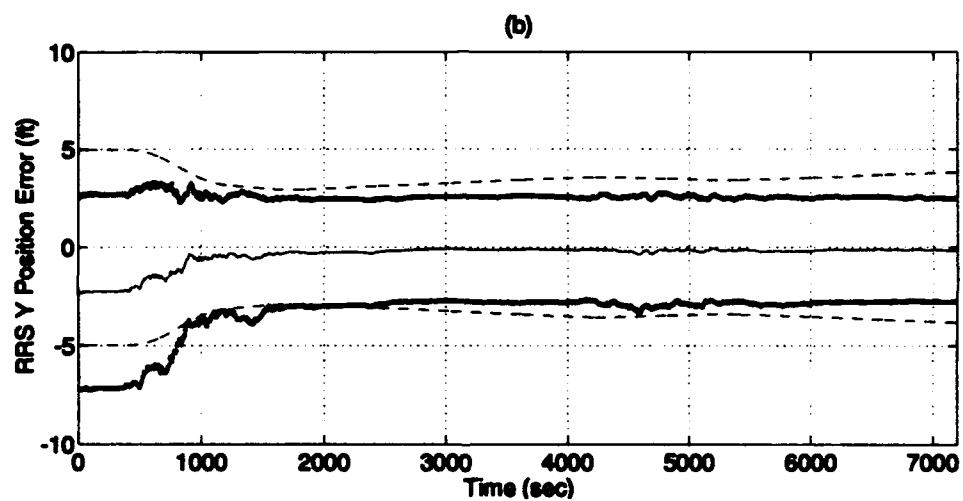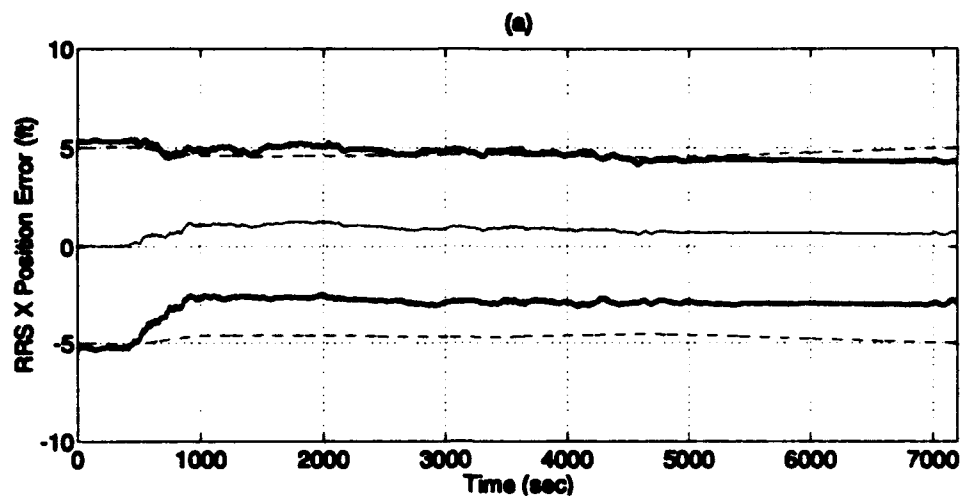
Plot F-7: RRS X/Y/Z Surveyed Position Errors

F-9

(a)

(b)
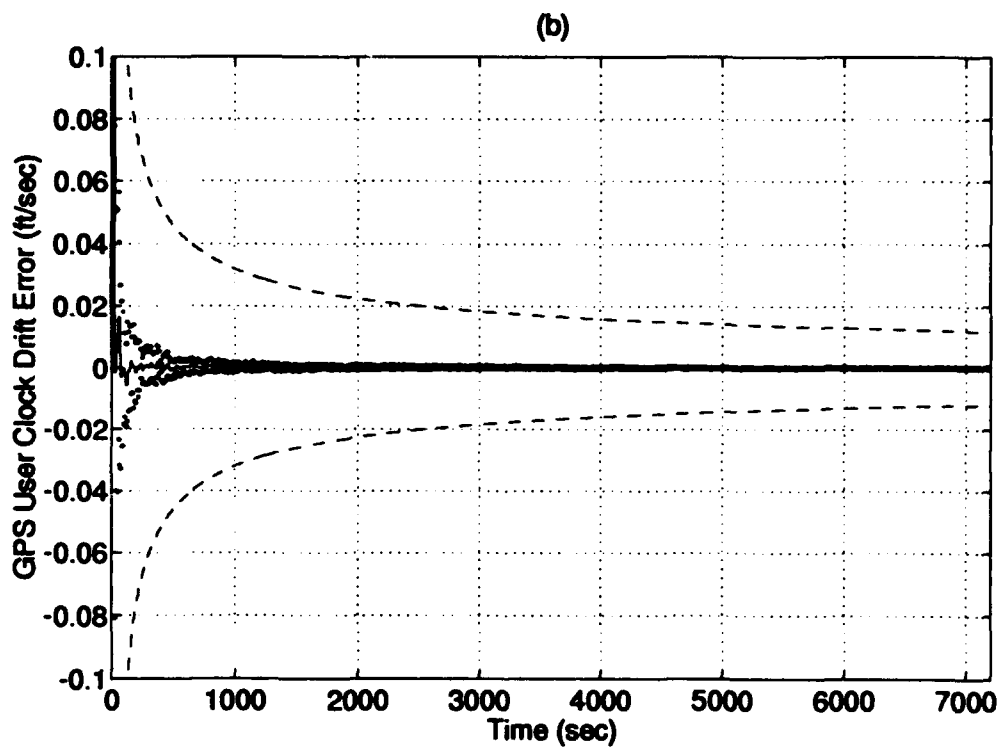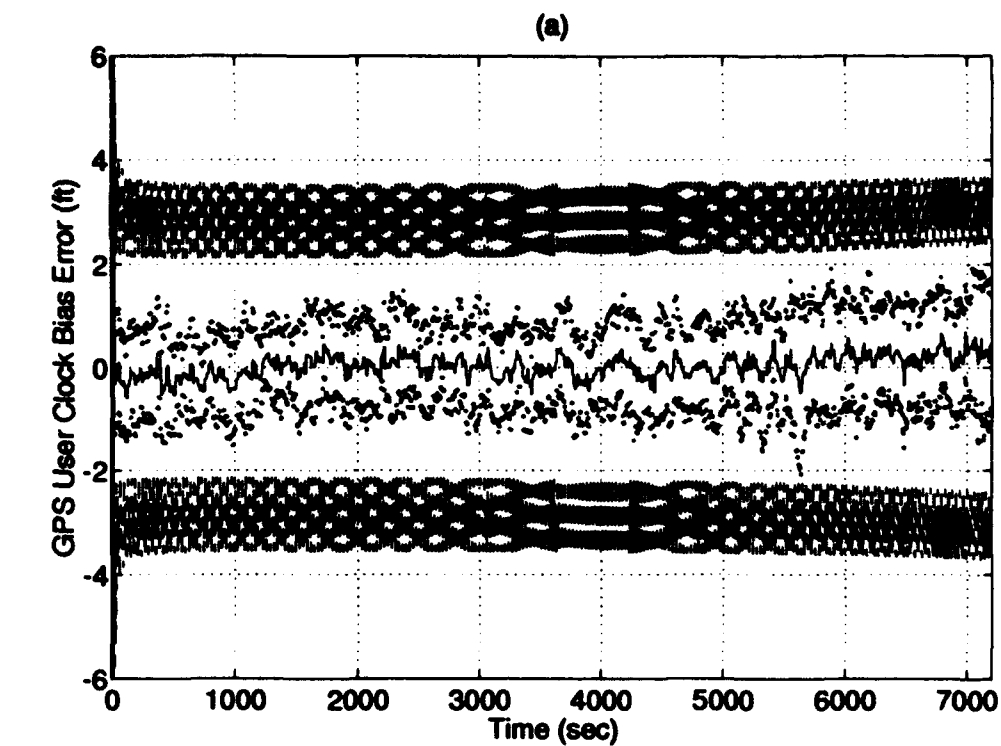
Plot F-8: GPS User Clock Bias/Drift Errors

F-10
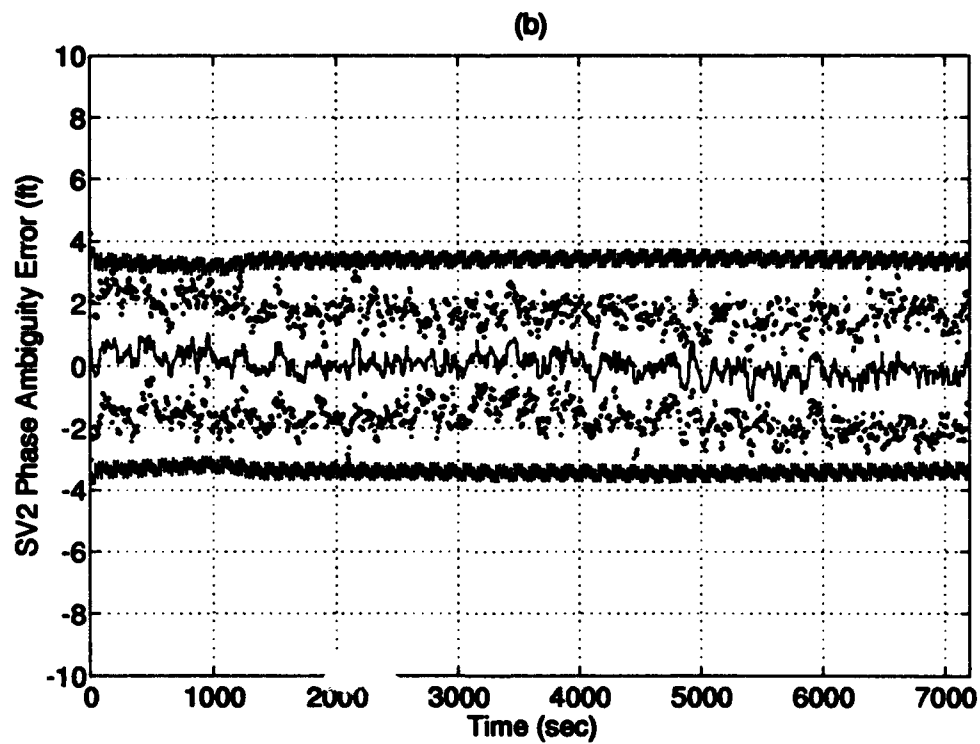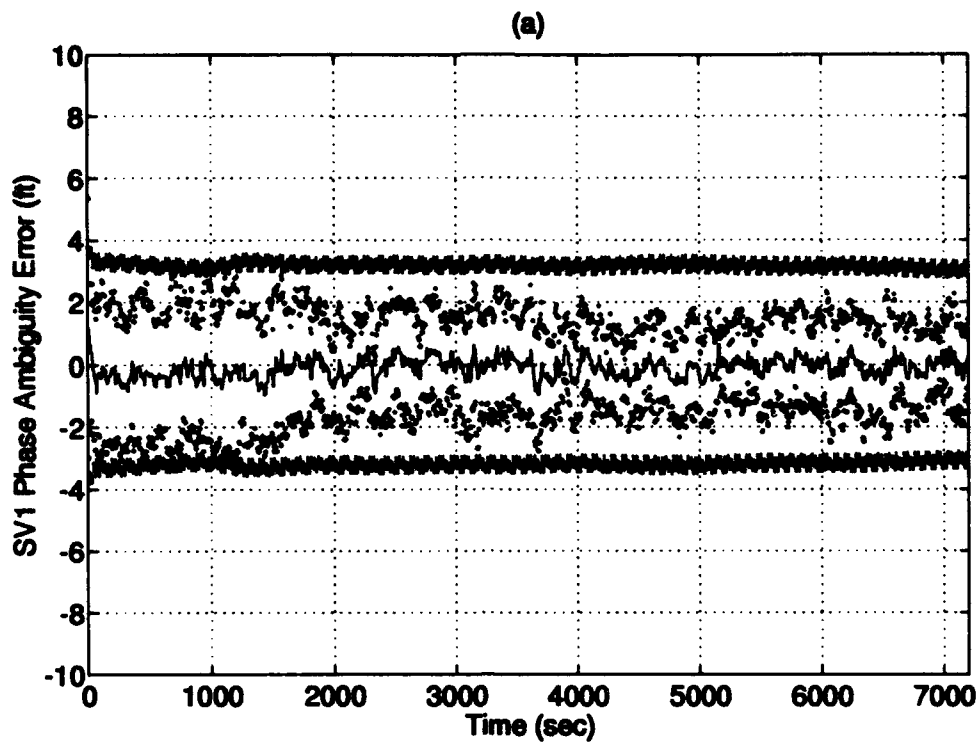
Plot F-9: GPS Satellite 1 and 2 Phase Ambiguity Errors
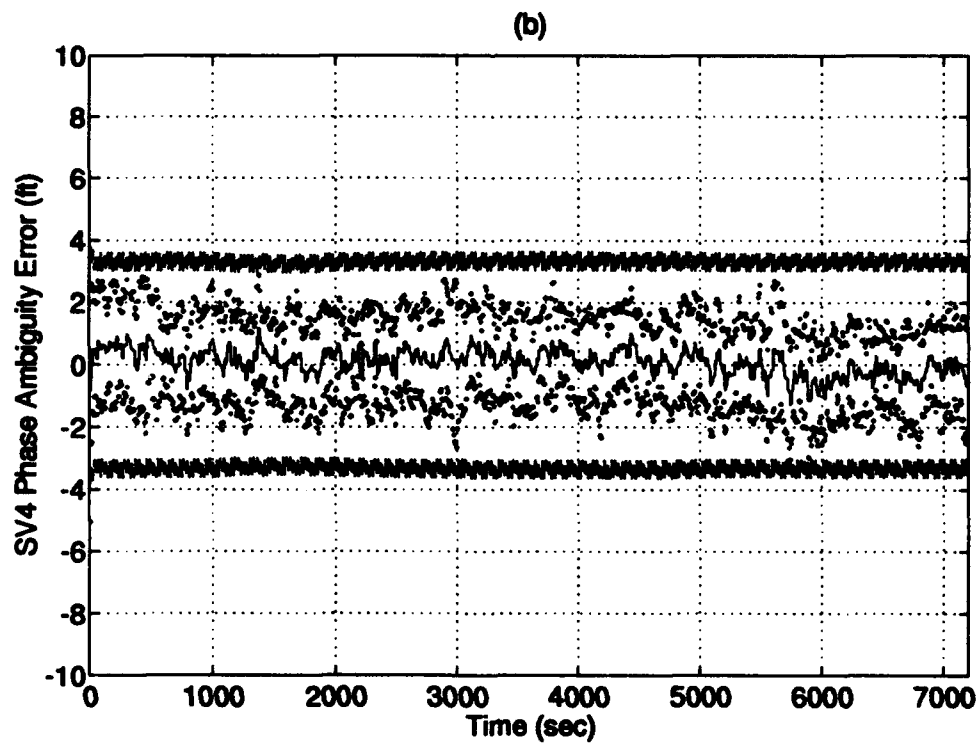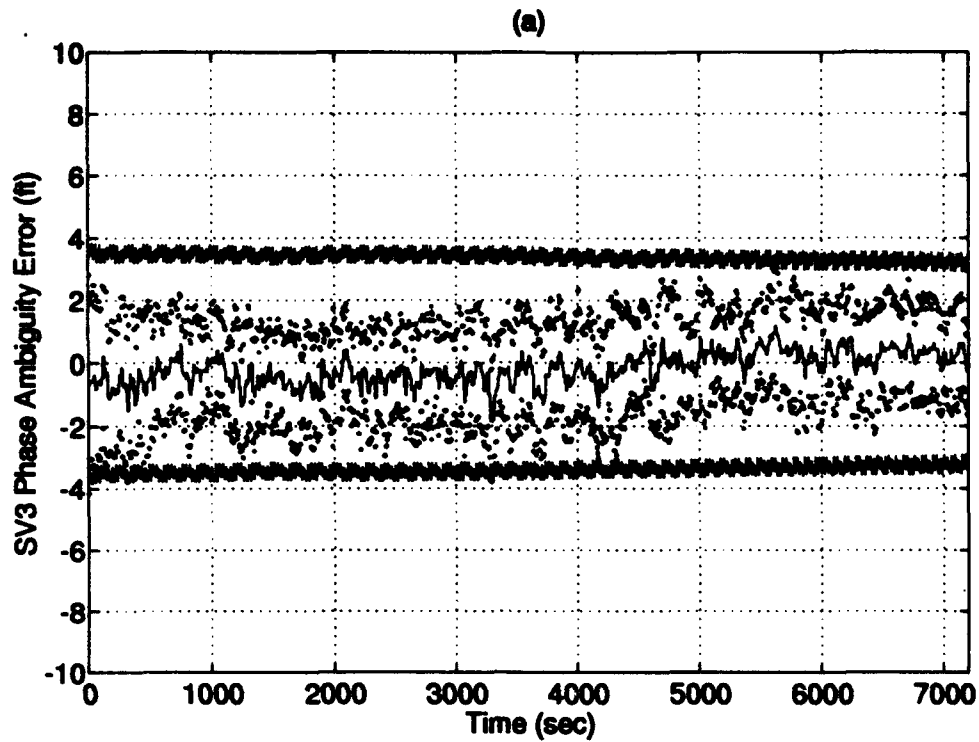
Plot F-10: GPS Satellite 3 and 4 Phase Ambiguity Errors

Appendix G. Loss of Satellite 1 Simulation Results

This appendix presents the results of the PNRS MSOFE simulation study including a simulation of the loss of GPS satellite 1. The simulation utilized the 91-state PNRS truth model and 71-state PNRS filter model derived in Chapter IV of this thesis research. The results are presented in the form of 10 plots:

|		
Plot G-1	(a) - Flight Profile Longitude	
	(b) - Flight Profile Latitude	
	(c) - Flight Profile Altitude	
Plot G-2	(a) - Longitude Error	
	(b) - Latitude Error	
Plot G-3	(a) - Altitude Error	
	(b) - Barometric Altitude Error	
Plot G-4	(a) - North Tilt Error	
	(b) - West Tilt Error	
	(c) - Azimuth Tilt Error	
Plot G-5	(a) - North Velocity Error	
	(b) - West Velocity Error	
	(c) - Vertical Velocity Error	
Plot G-6	(a) - RRS Range Bias Error	
	(b) - RRS Velocity Bias Error	
	(c) - RRS Atmospheric Propagation Delay Error	
Plot G-7	(a) - RRS X Position Survey Error	
	(b) - RRS Y Position Survey Error	
	(c) - RRS Z Position Survey Error	
Plot G-8	(a) - GPS User Clock Bias Error	
	(b) - GPS User Clock Drift Error	
Plot G-9	(a) - Satellite 1 Phase Ambiguity Error	
	(b) - Satellite 2 Phase Ambiguity Error	
Plot G-10	(a) - Satellite 3 Phase Ambiguity Error	
	(b) - Satellite 4 Phase Ambiguity Error	

Each plot shows the results of a 15-run Monte Carlo average of the truth state minus the filter state for the first 1000 seconds of the flight profile, the true +/- one sigma standard deviation of the Monte Carlo simulation, and the filter predicted +/- one sigma standard deviation. The simulation of the loss of GPS satellite 1 begins at the 400 second mark for a duration of 200 seconds.

The following is a legend for the 10 plots:

Line Style	Description
————————	15 Monte Carlo run mean
····························	mean + and - true 1σ
---------------------------	+ and - filter-predicted 1σ
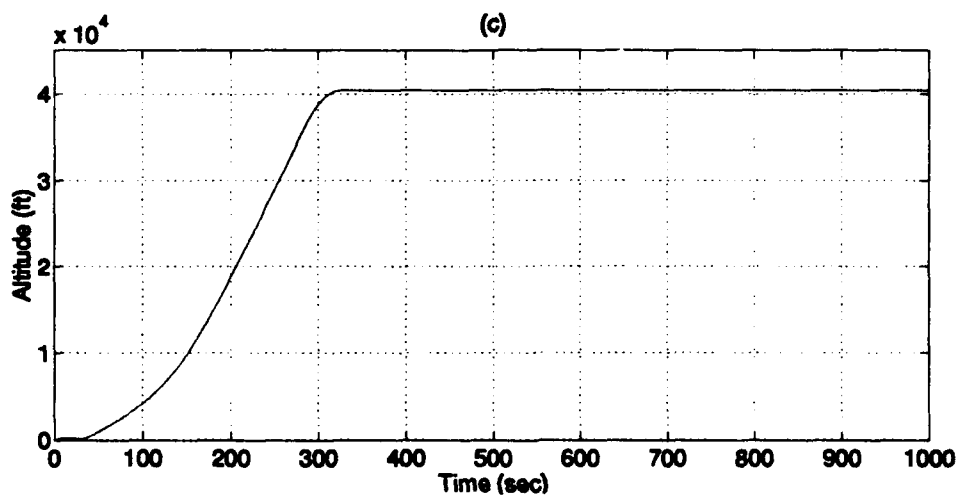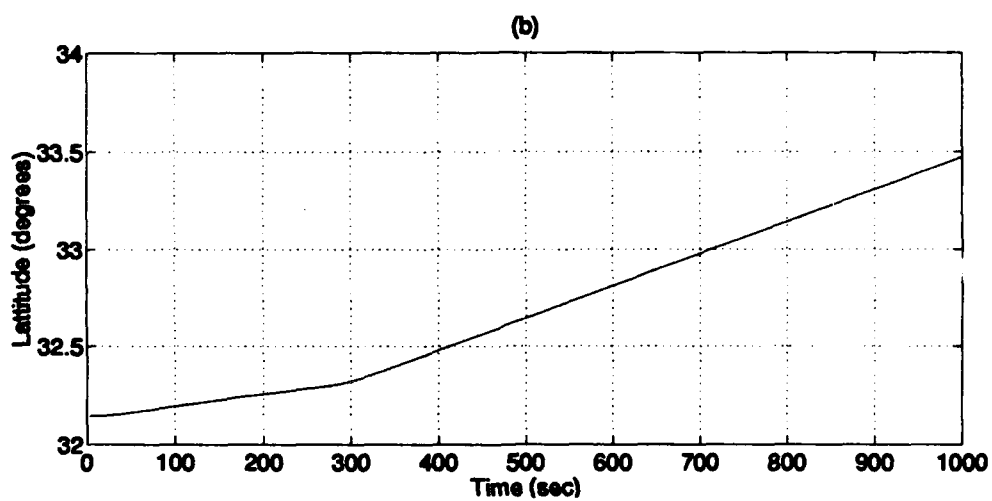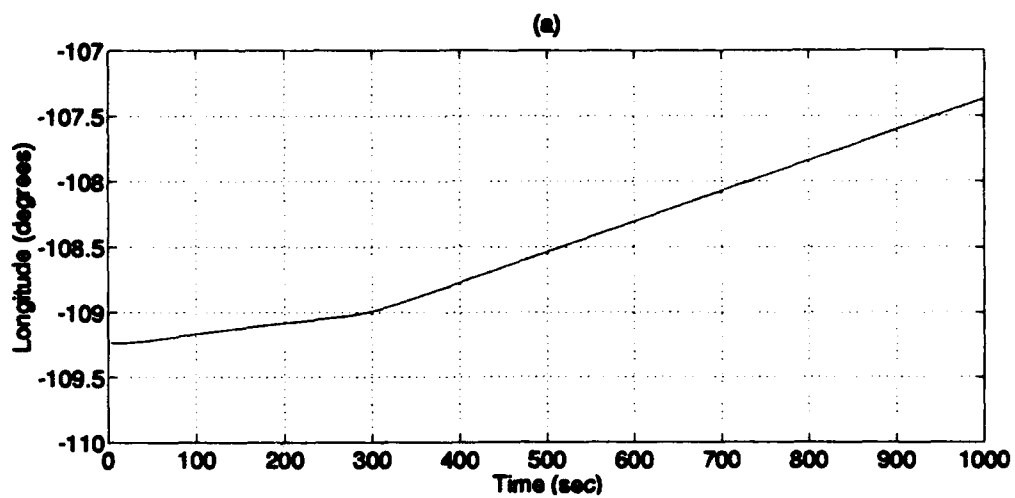
Plot G-1: Flight Profile

G-3

(a)

(b)
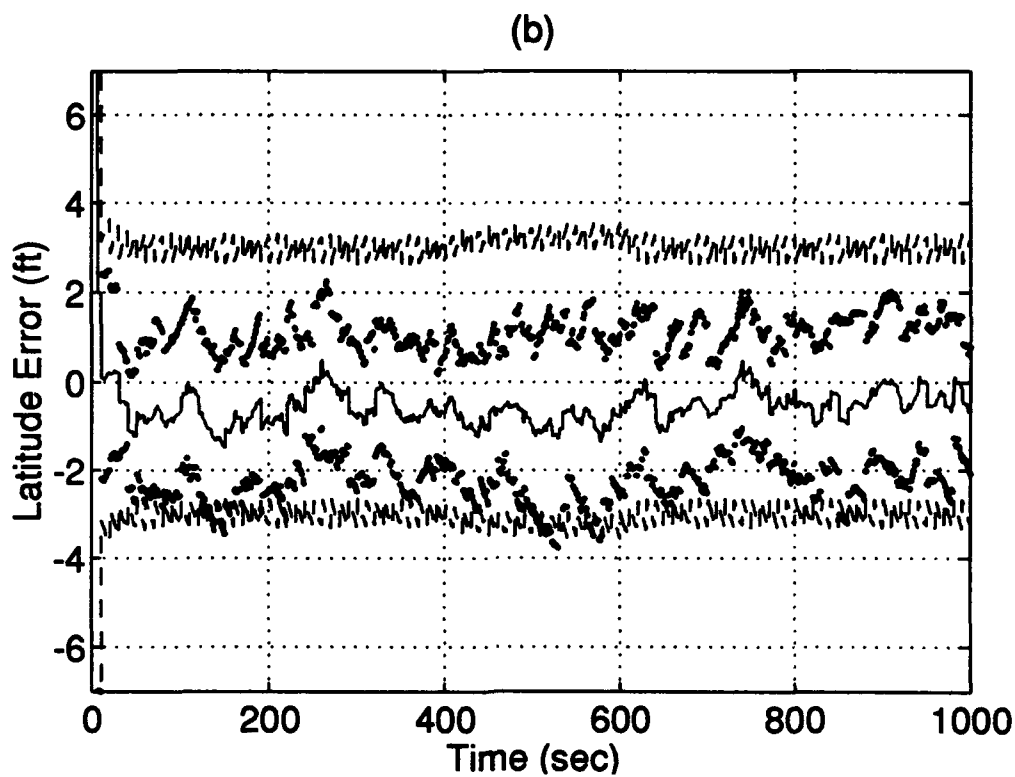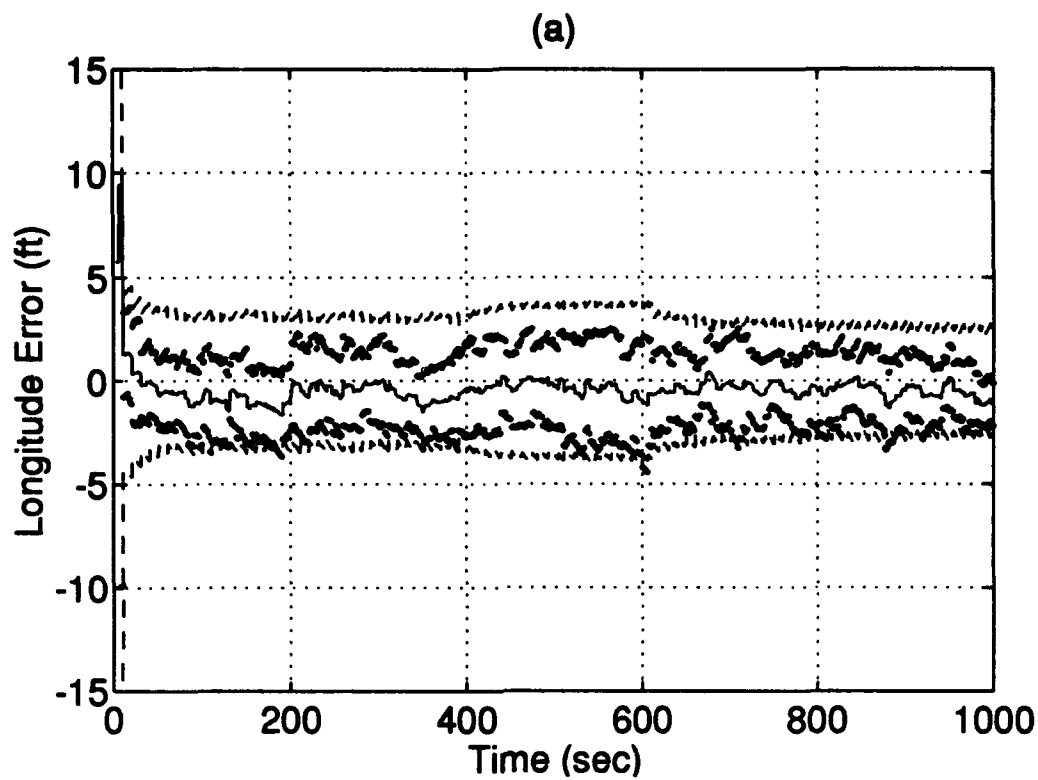
Plot G-2: Longitude/Latitude Errors

G-4

(a)

(b)
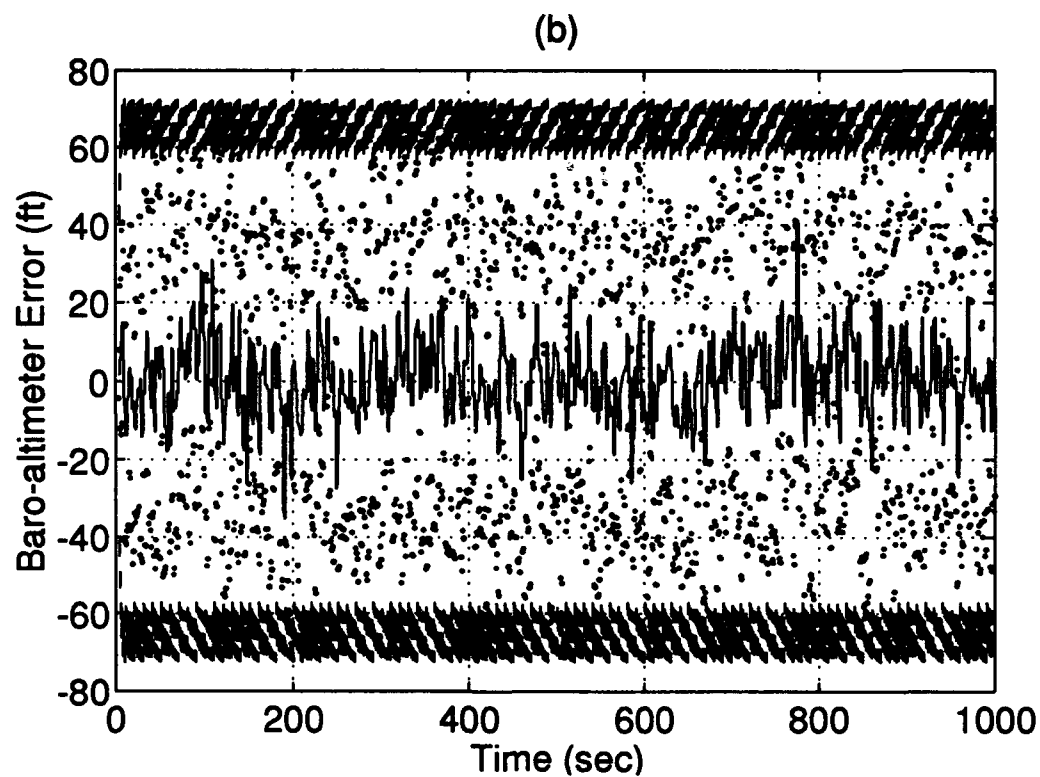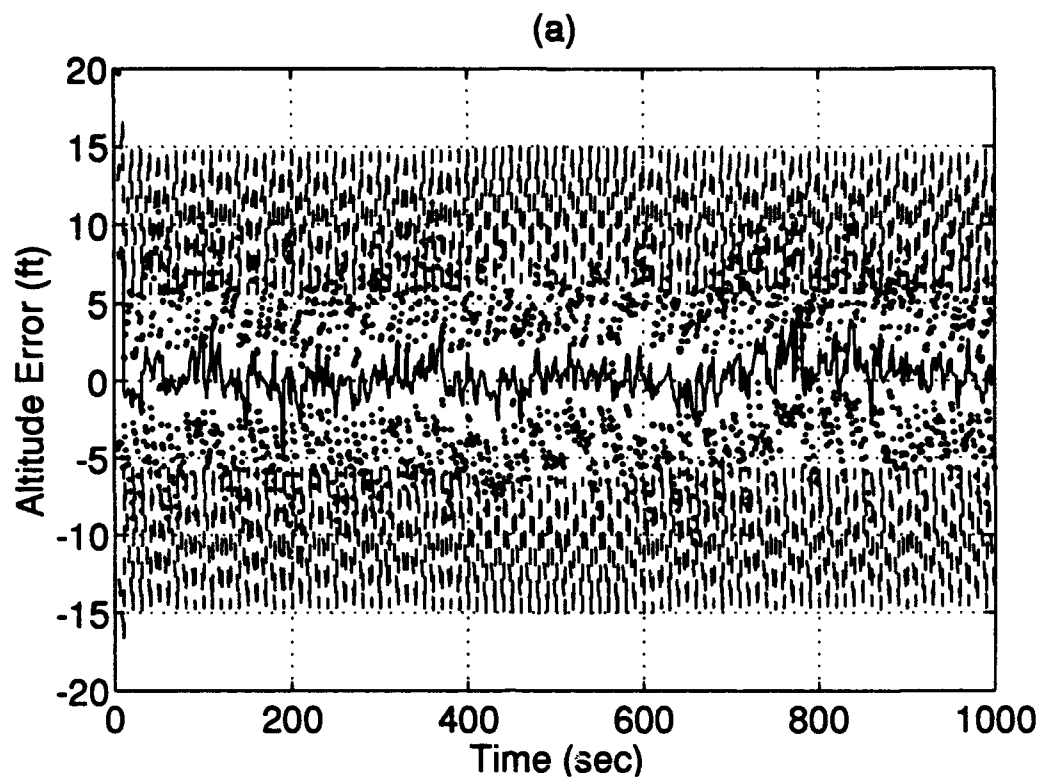
Plot G-3: Altitude/Barometric Altitude Errors
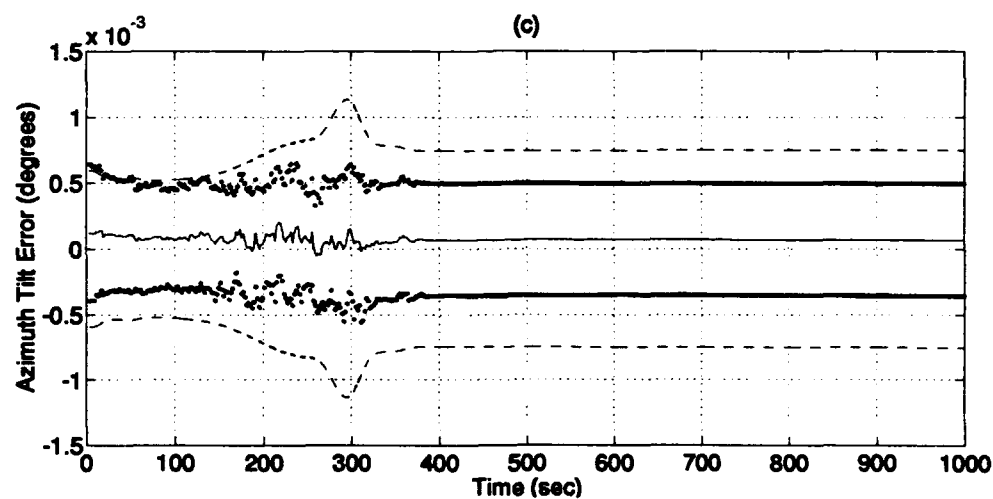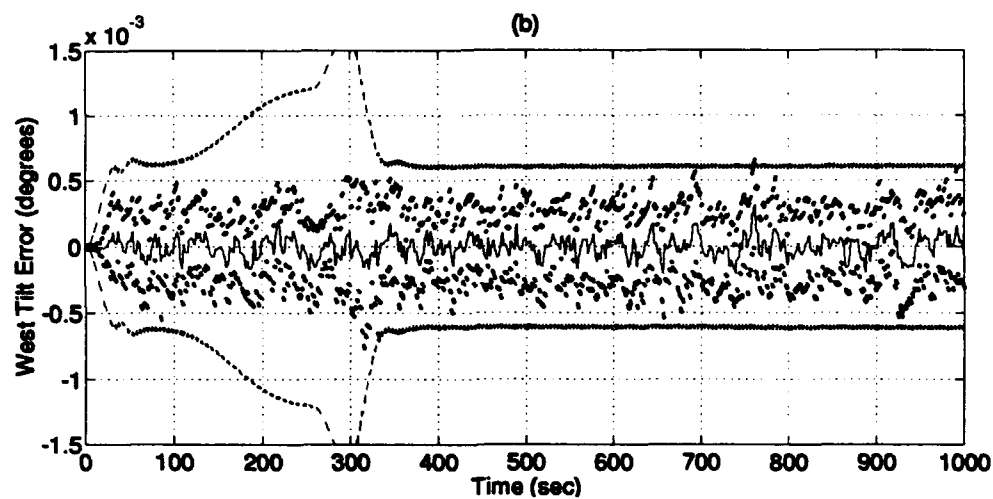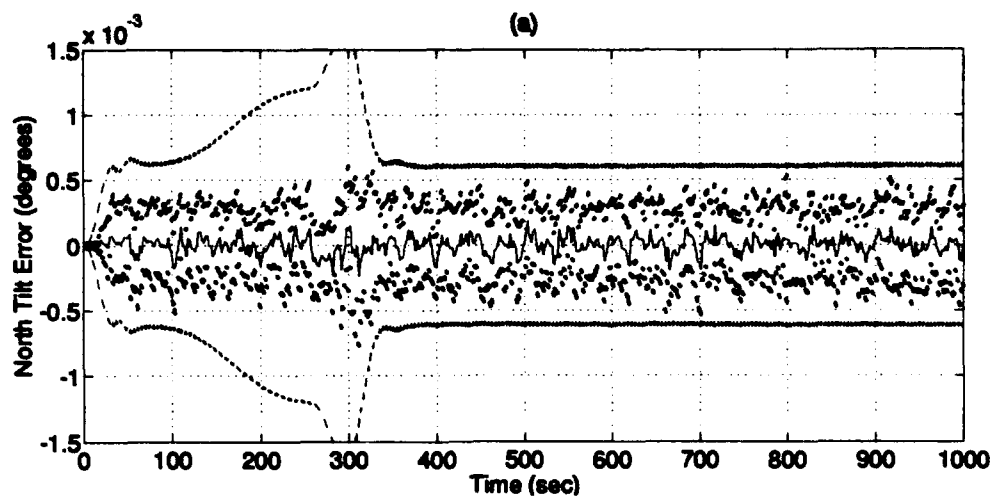
Plot G-4: North/West/Azimuth Tilt Errors
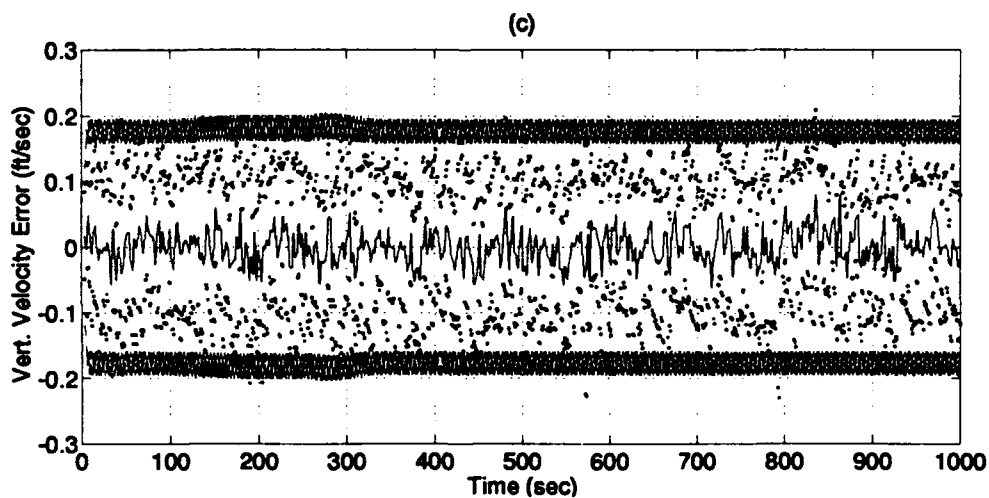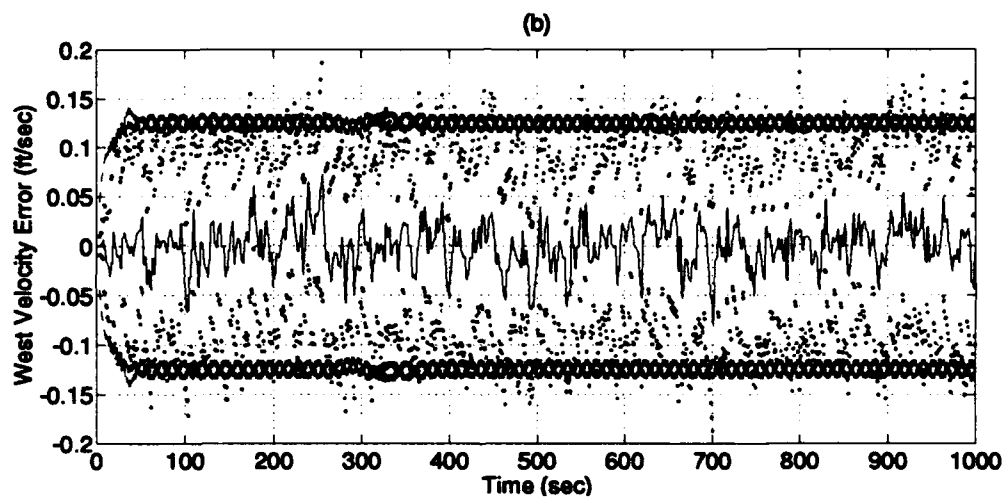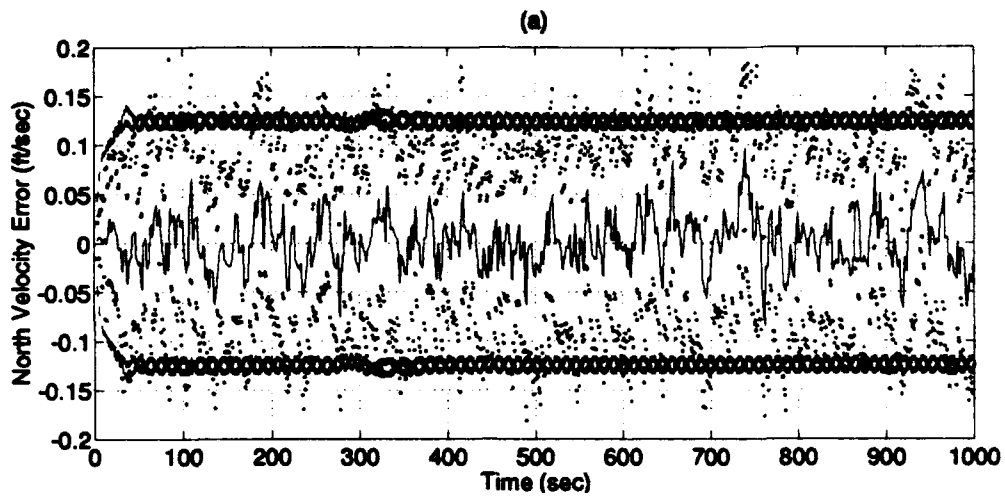
Plot G-5: North/West/Vertical Velocity Errors
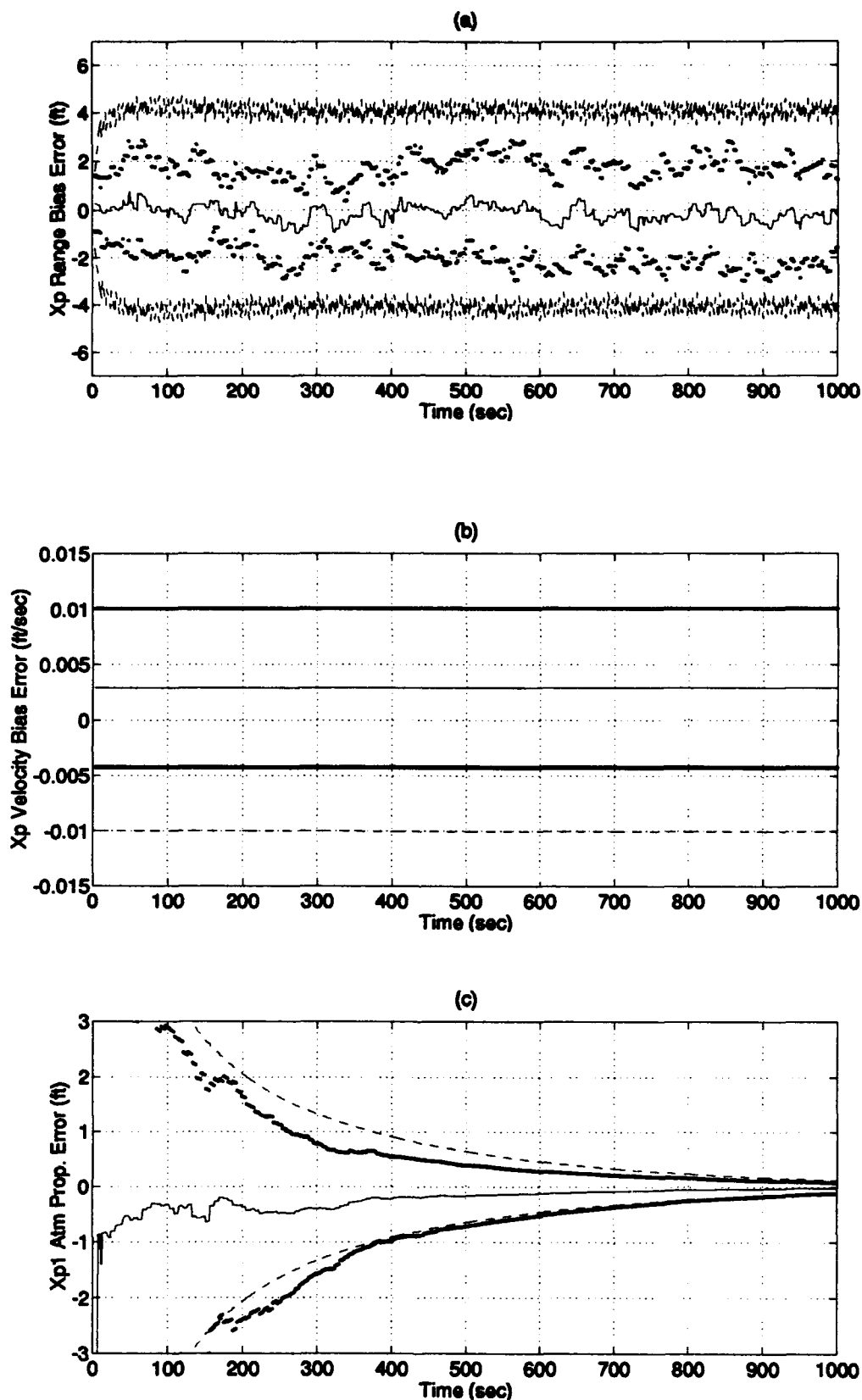
Plot G-6: RRS Range bias/Velocity bias/Atmospheric propagation delay Errors
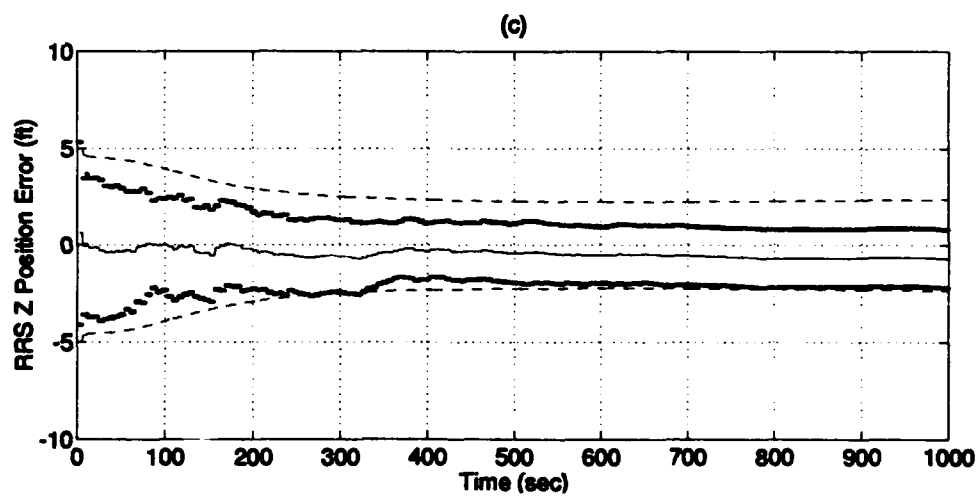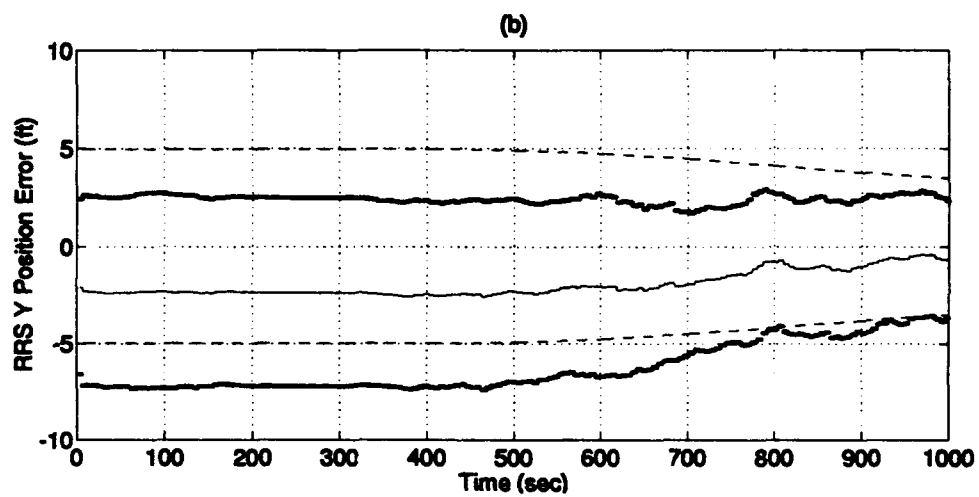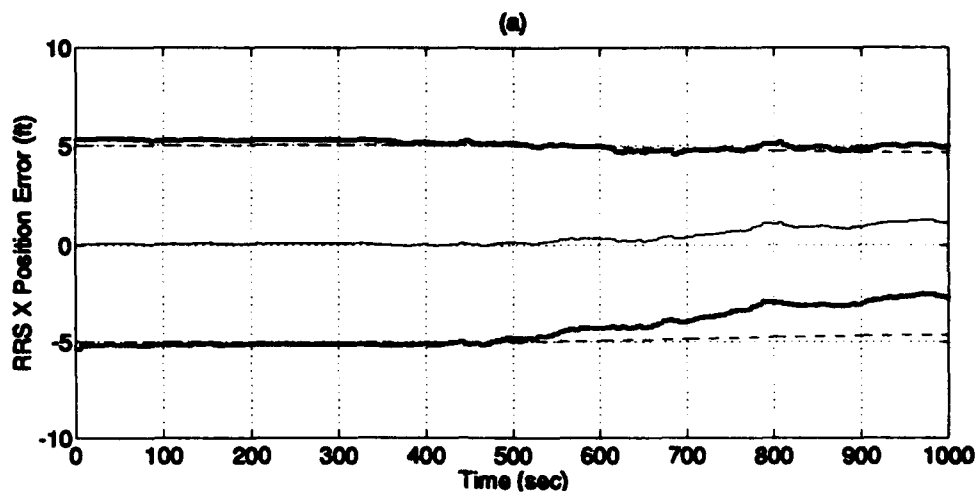
Plot G-7: RRS X/Y/Z Surveyed Position Errors

G-9

(a)

(b)
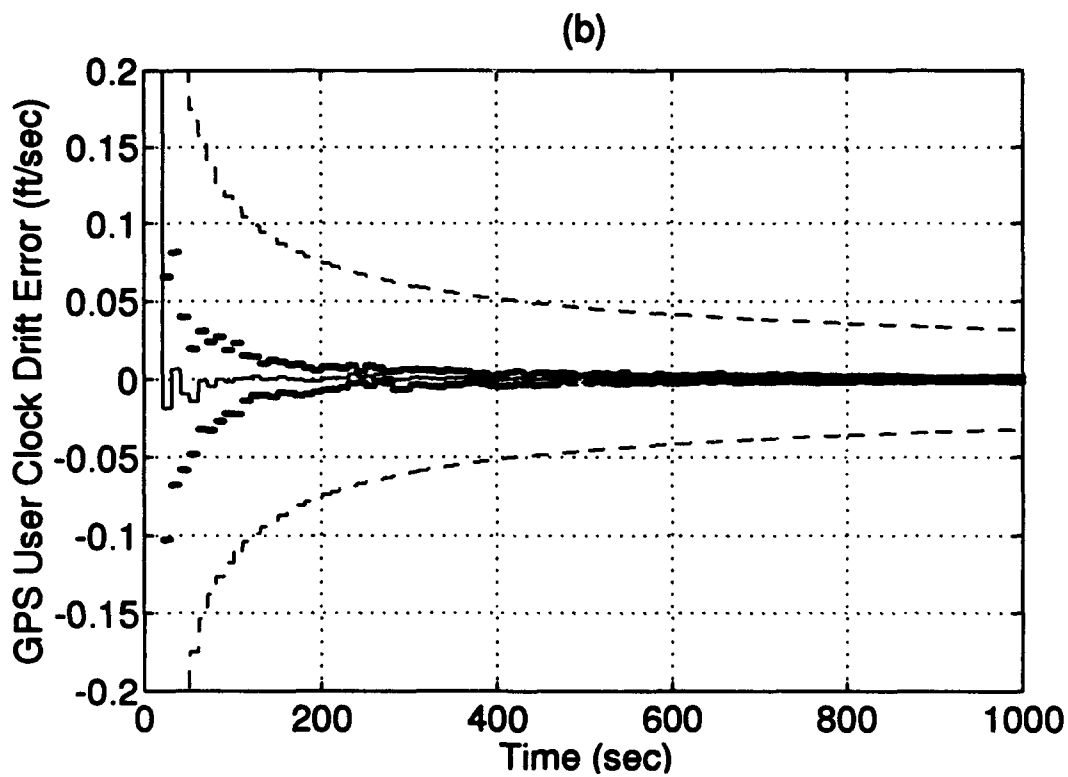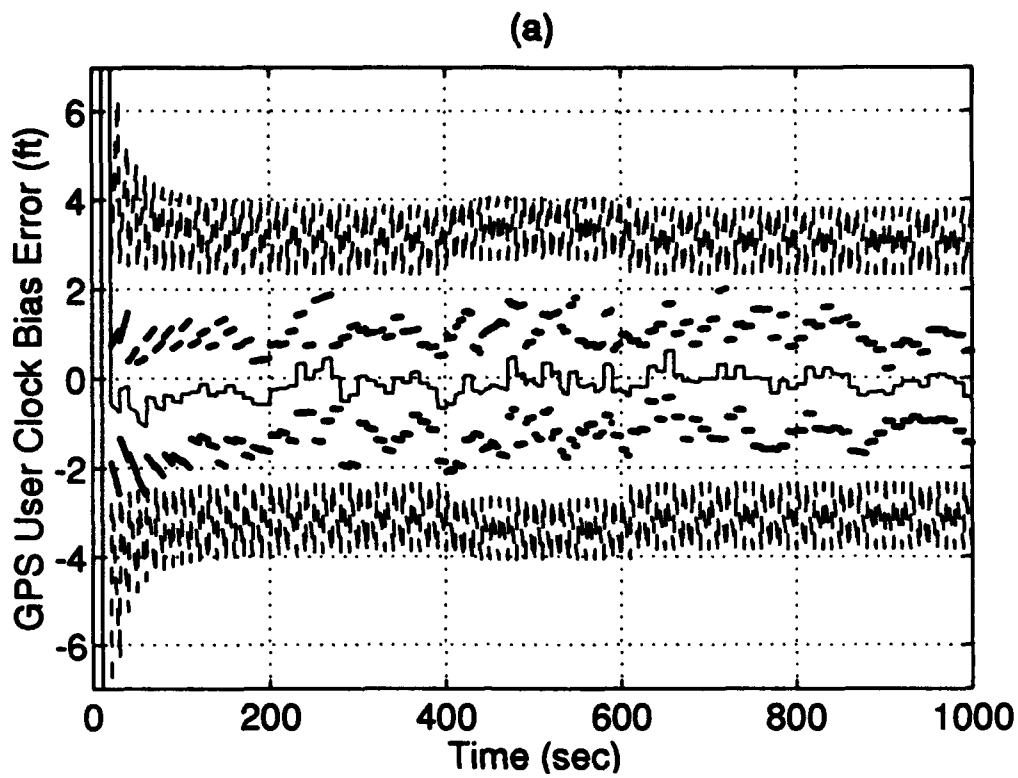
Plot G-8: GPS User Clock Bias/Drift Errors

(a)

(b)
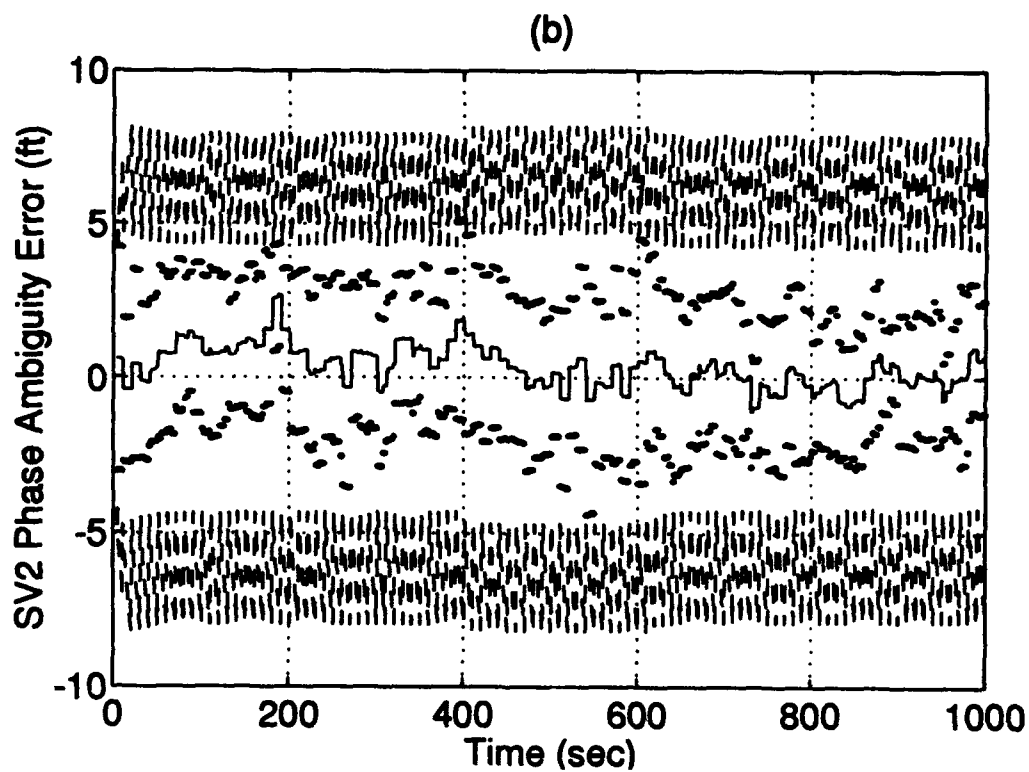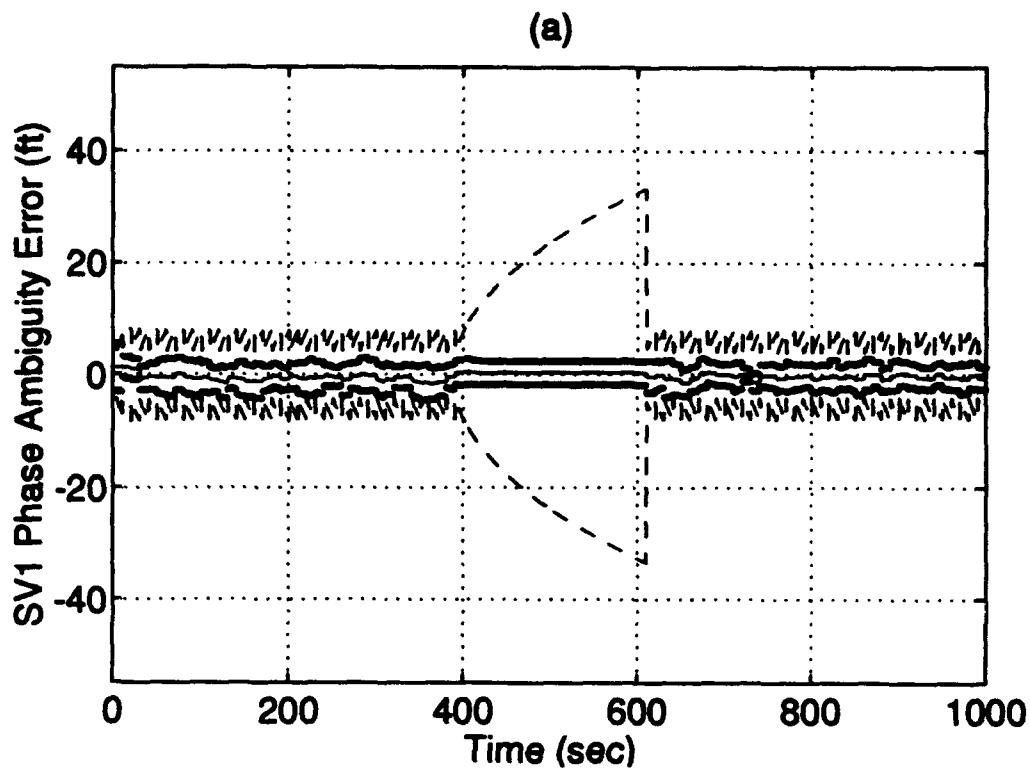
Plot G-9: GPS Satellite 1 and 2 Phase Ambiguity Errors

G-11
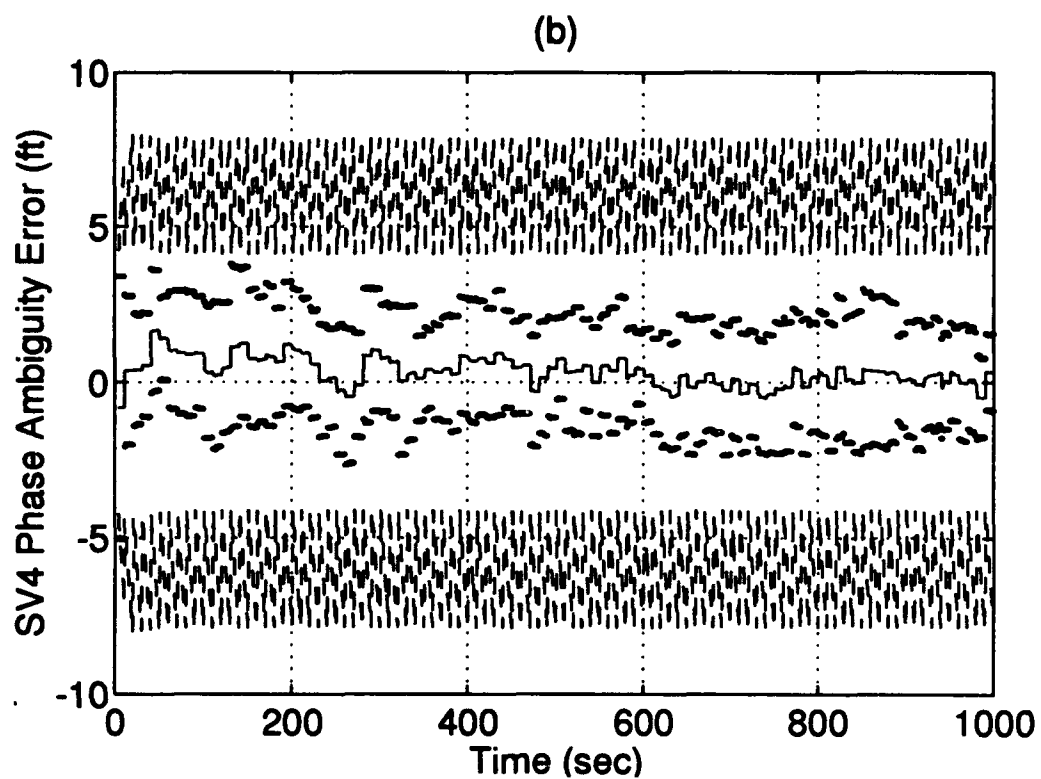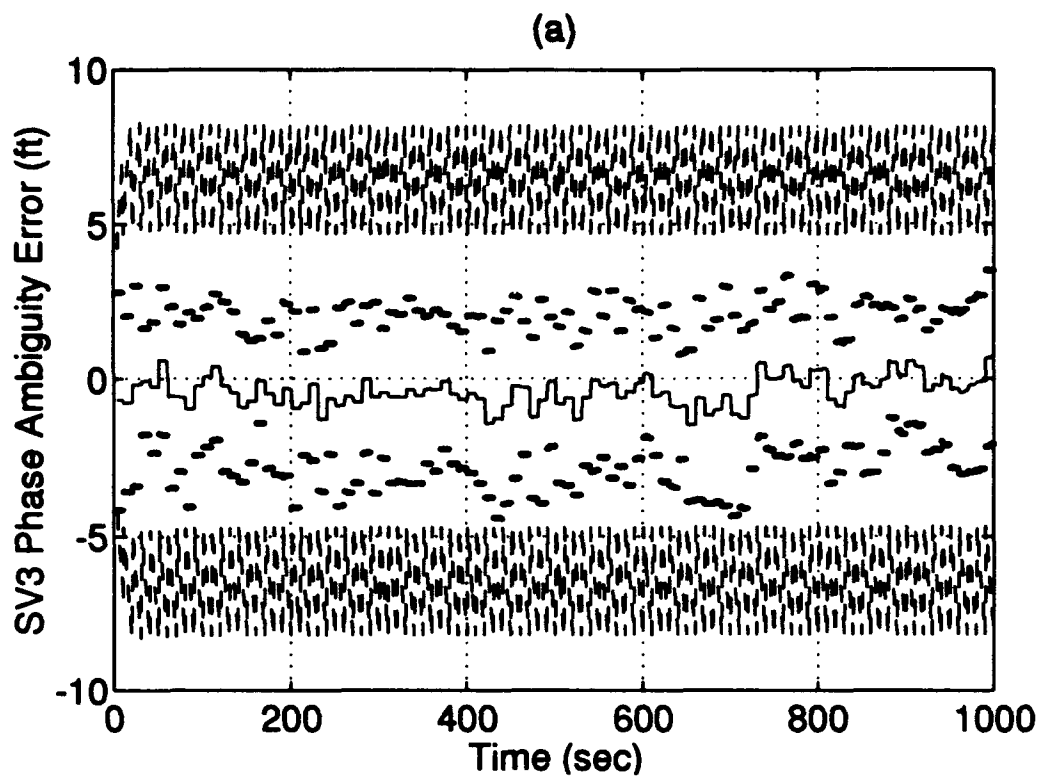
Plot G-10: GPS Satellite 3 and 4 Phase Ambiguity Errors

Appendix H. Large Cycle Slip Simulation Results

This appendix presents the results of the PNRS MSOFE simulation study including a 20 second loss of GPS satellite 1 followed by a cycle slip of 30,000 ft on satellite 1. The simulation utilized the 91-state PNRS truth model and 71-state PNRS filter model derived in Chapter IV of this thesis research. The results are presented in the form of 10 plots:

|	
Plot H-1	(a) - Flight Profile Longitude
	(b) - Flight Profile Latitude
	(c) - Flight Profile Altitude
Plot H-2	(a) - Longitude Error
	(b) - Latitude Error
Plot H-3	(a) - Altitude Error
	(b) - Barometric Altitude Error
Plot H-4	(a) - North Tilt Error
	(b) - West Tilt Error
	(c) - Azimuth Tilt Error
Plot H-5	(a) - North Velocity Error
	(b) - West Velocity Error
	(c) - Vertical Velocity Error
Plot H-6	(a) - RRS Range Bias Error
	(b) - RRS Velocity Bias Error
	(c) - RRS Atmospheric Propagation Delay Error
Plot H-7	(a) - RRS X Position Survey Error
	(b) - RRS Y Position Survey Error
	(c) - RRS Z Position Survey Error
Plot H-8	(a) - GPS User Clock Bias Error
	(b) - GPS User Clock Drift Error
Plot H-9	(a) - Satellite 1 Phase Ambiguity Error
	(b) - Satellite 2 Phase Ambiguity Error
Plot H-10	(a) - Satellite 3 Phase Ambiguity Error
	(b) - Satellite 4 Phase Ambiguity Error

Each plot shows the results of a 15-run Monte Carlo average of the truth state minus the filter state for the first 1000 seconds of the flight profile, the true +/- one sigma standard deviation of the Monte Carlo simulation, and the filter predicted +/- one sigma standard deviation. The simulation of the loss of GPS satellite 1 begins at the 400 second mark for 20 seconds followed by a 30,000 ft cycle slip. Note that the cycle slip was also applied at the 400 second mark.

The following is a legend for the 10 plots:

Line Style	Description
————————————	15 Monte Carlo run mean
··	mean + and - true 1σ
- -	+ and - filter-predicted 1σ
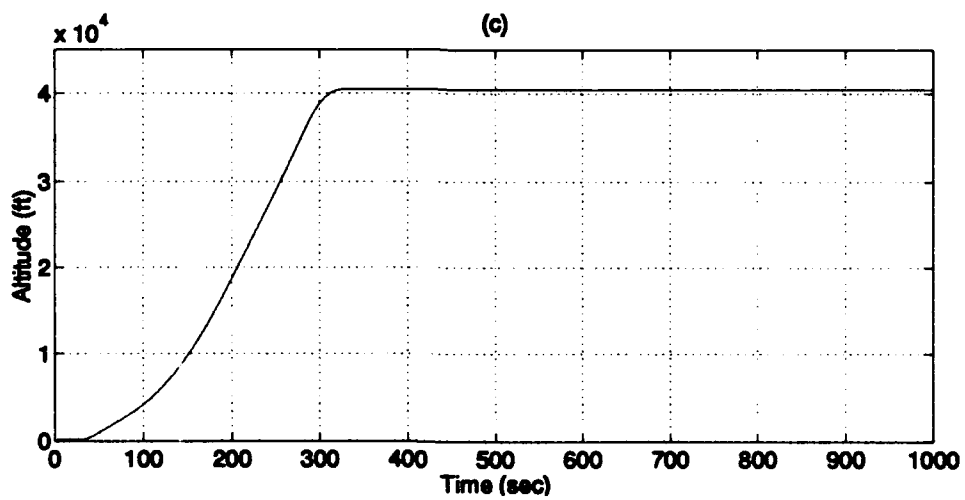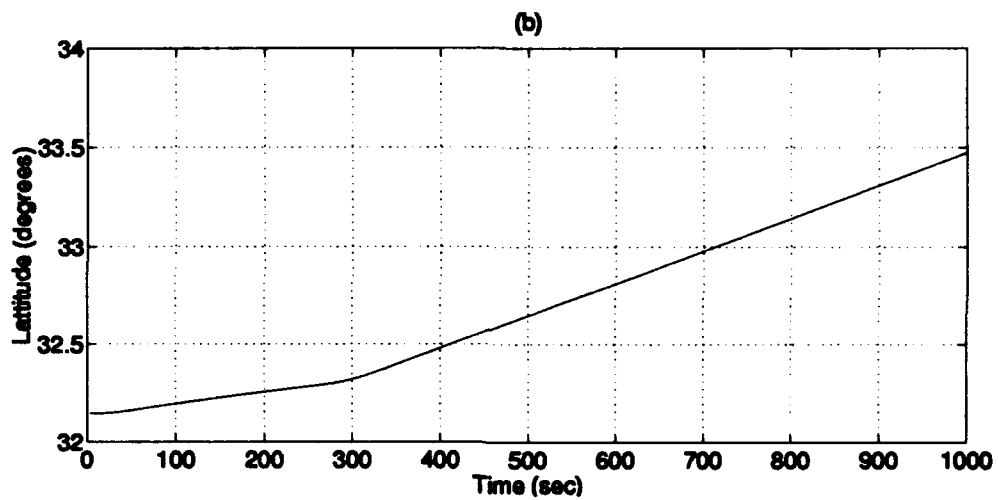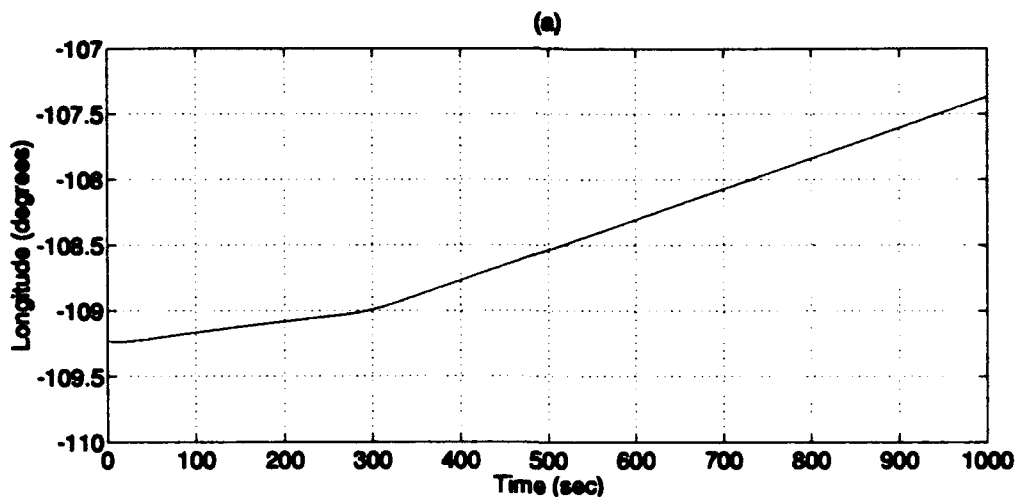
Plot H-1: Flight Profile

H-3

(a)

(b)
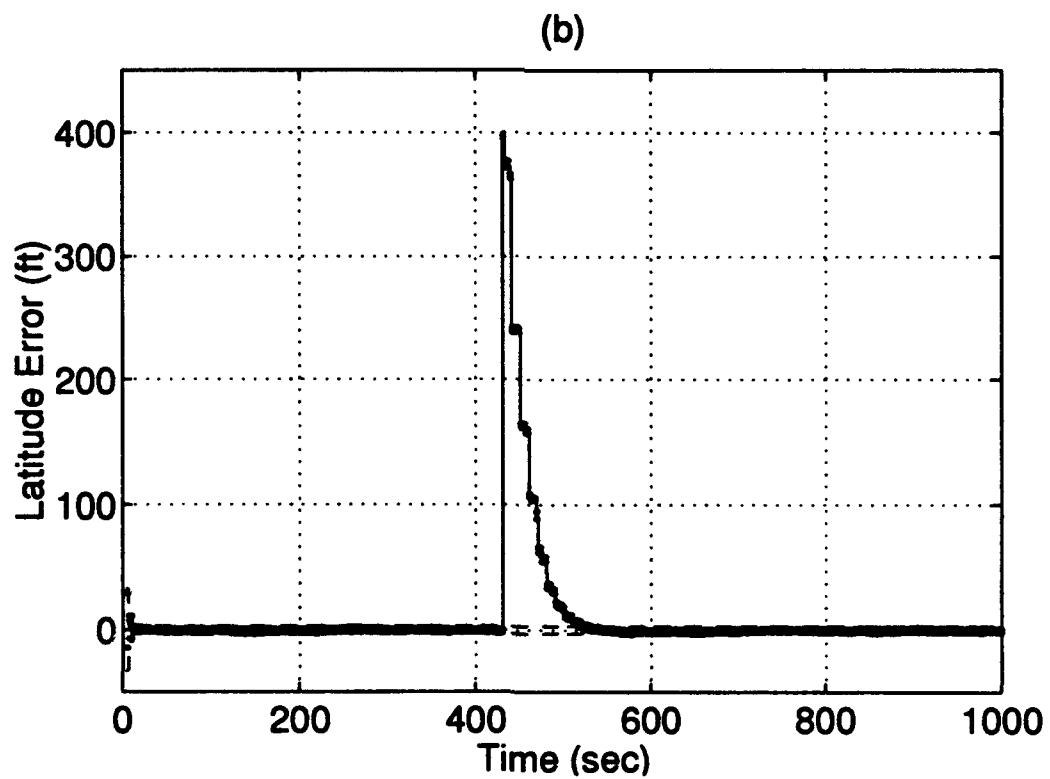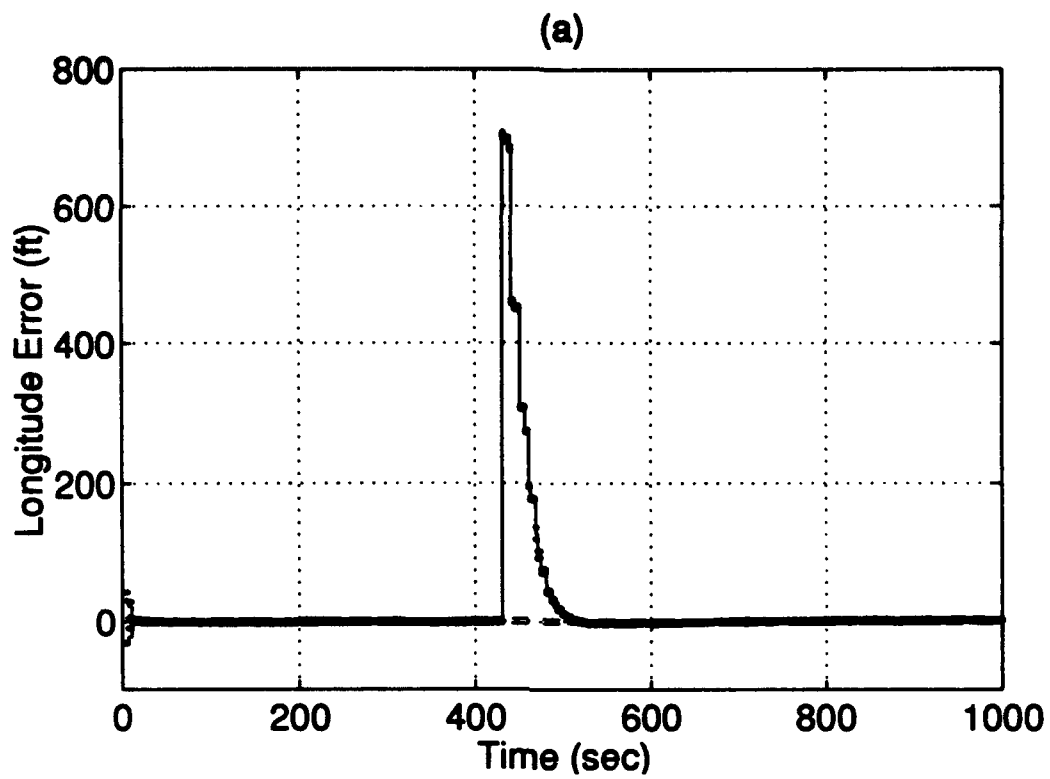
Plot H-2: Longitude/Latitude Errors

H-4

(a)

(b)
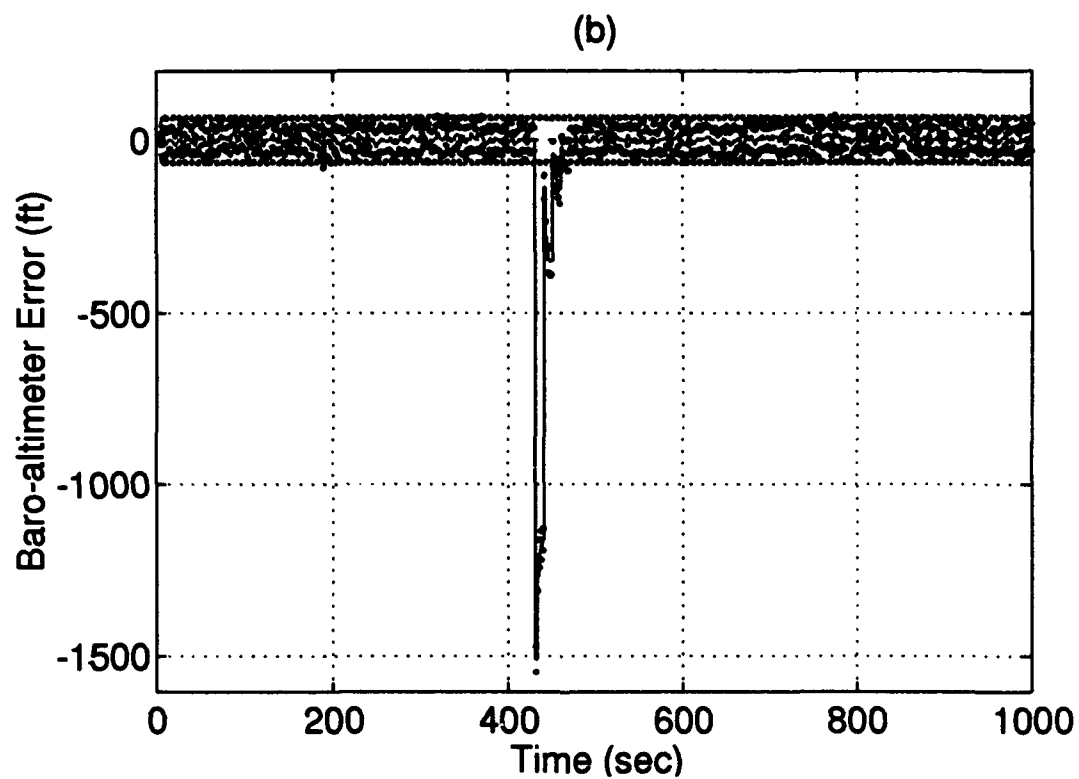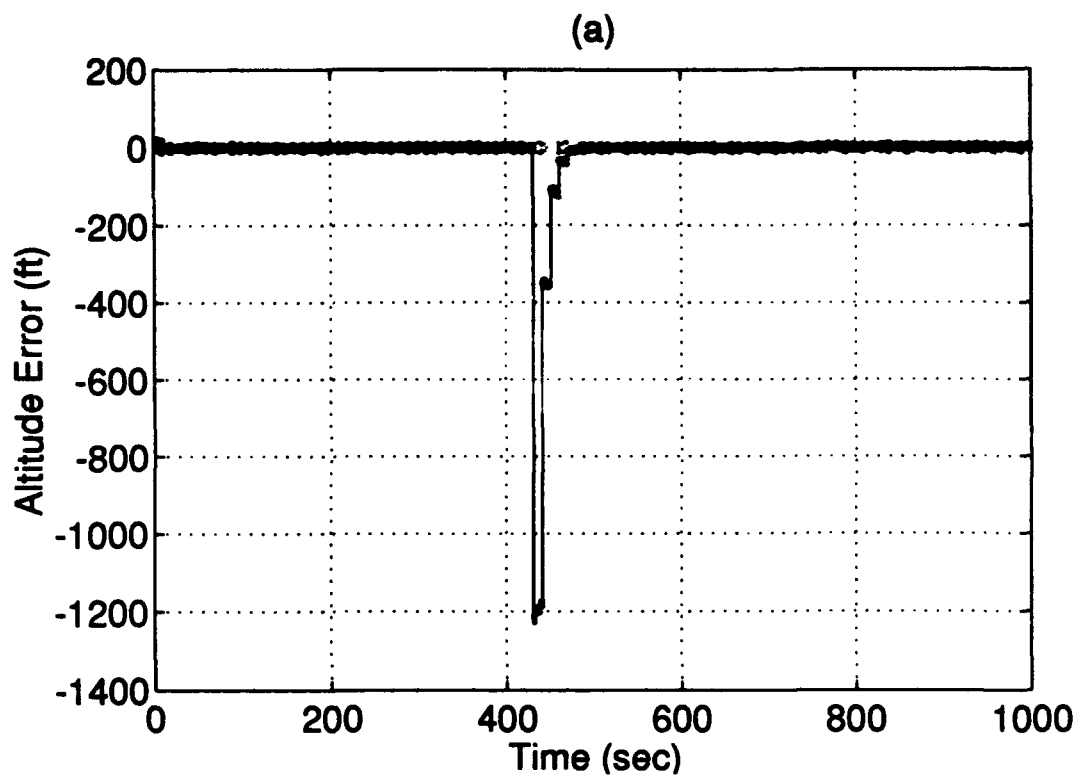
Plot H-3: Altitude/Barometric Altitude Errors

H-5
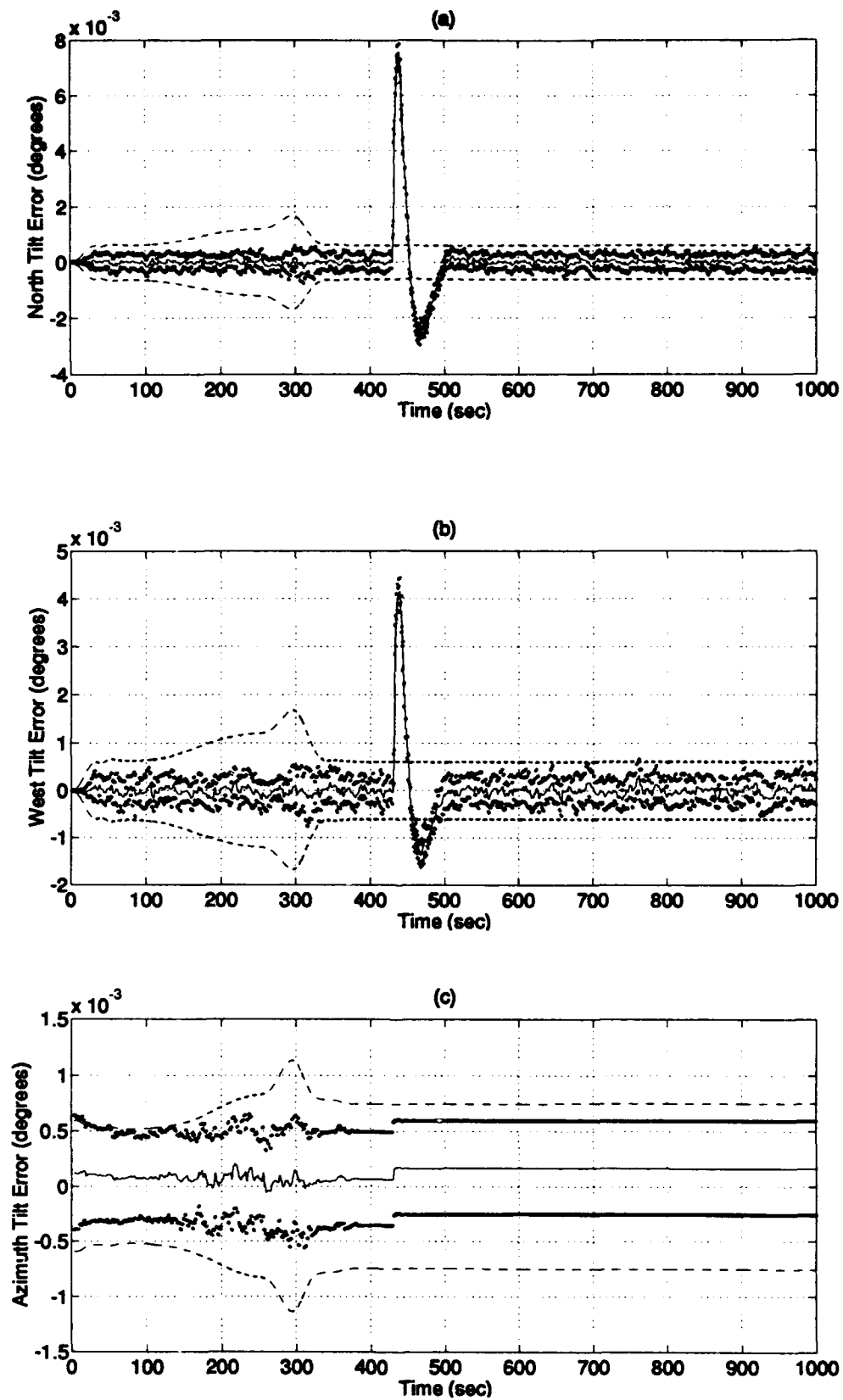
Plot H-4: North/West/Azimuth Tilt Errors
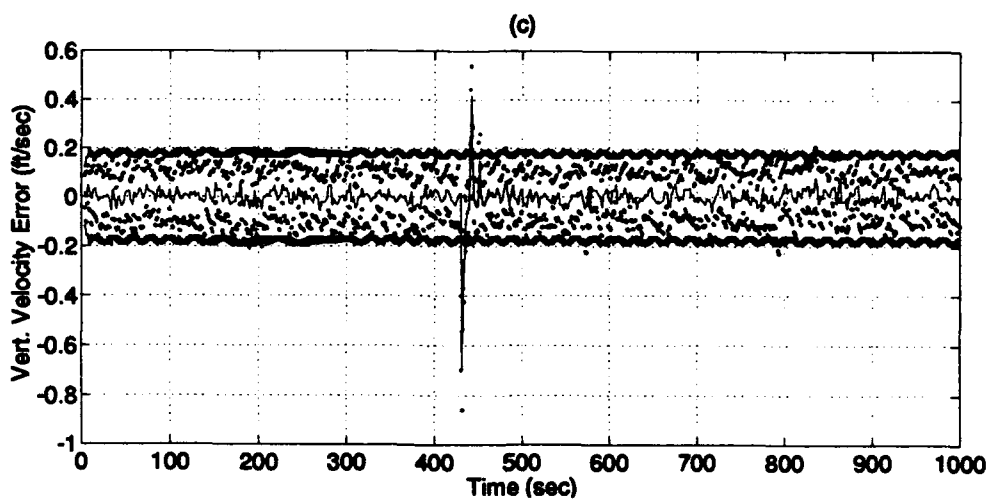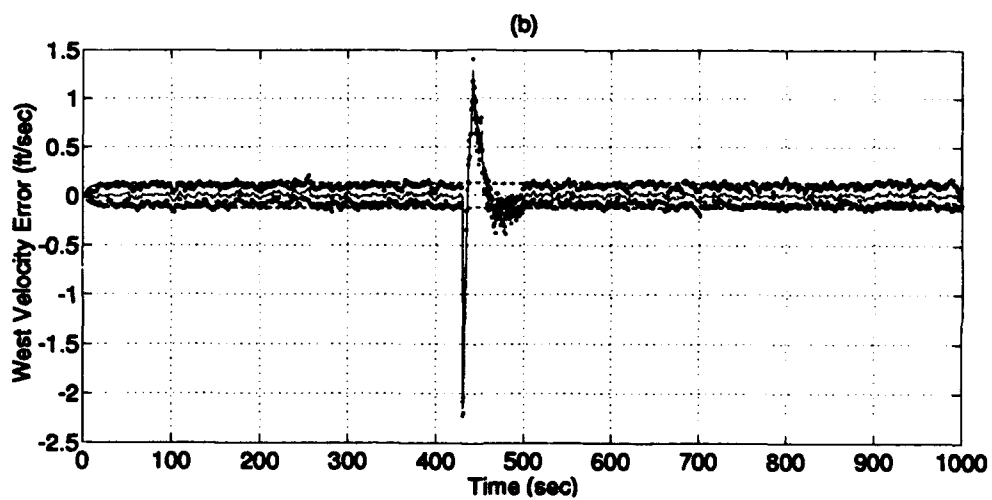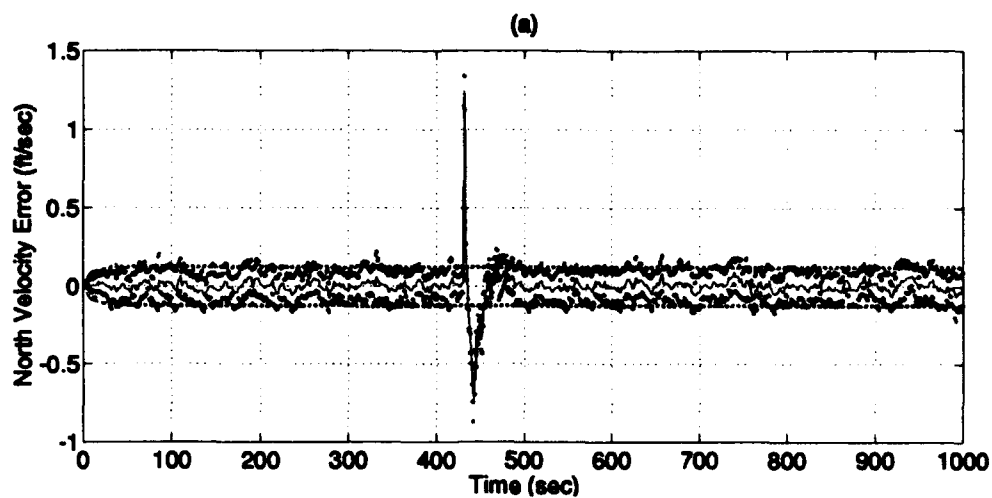
Plot H-5: North/West/Vertical Velocity Errors
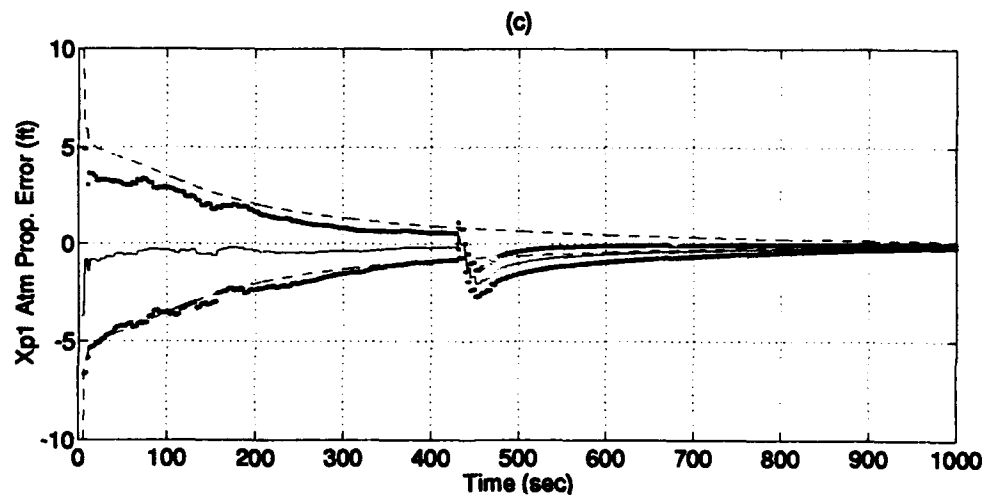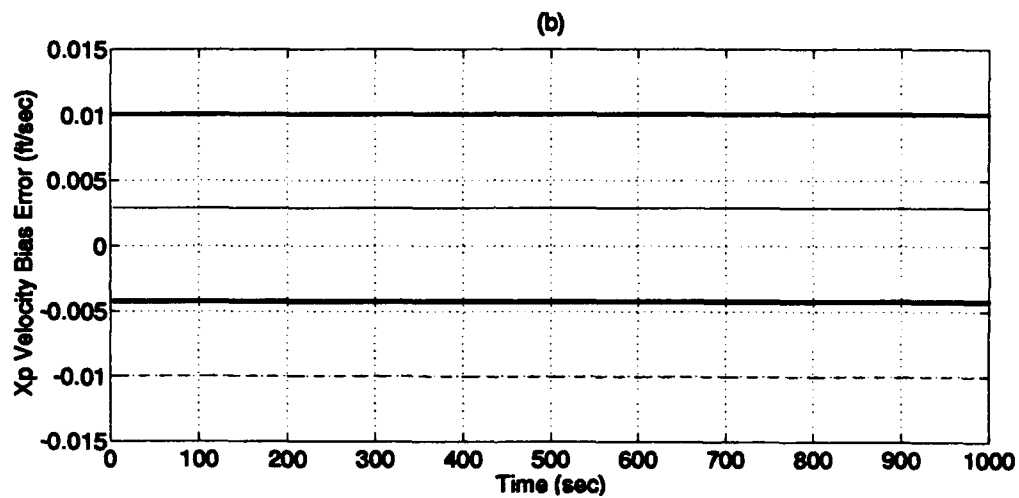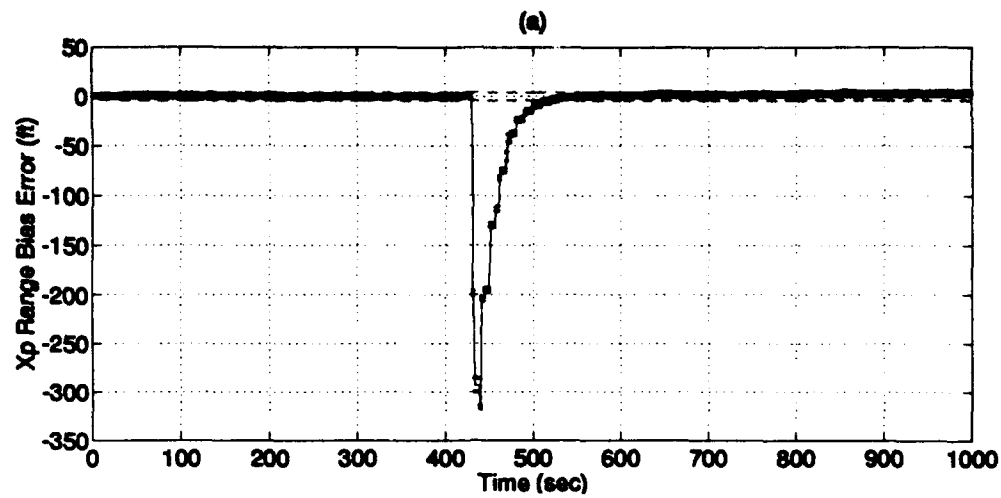
Plot H-6: RRS Range bias/Velocity bias/Atmospheric propagation delay Errors

H-8
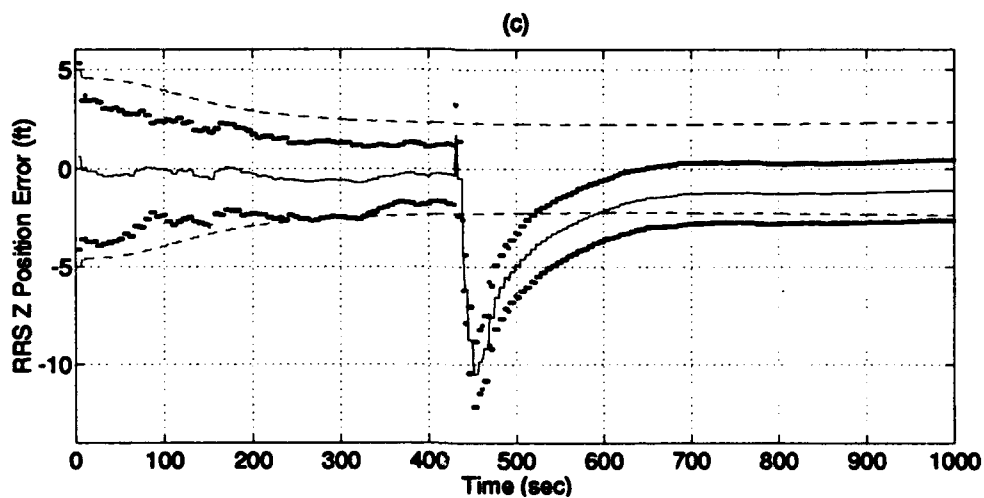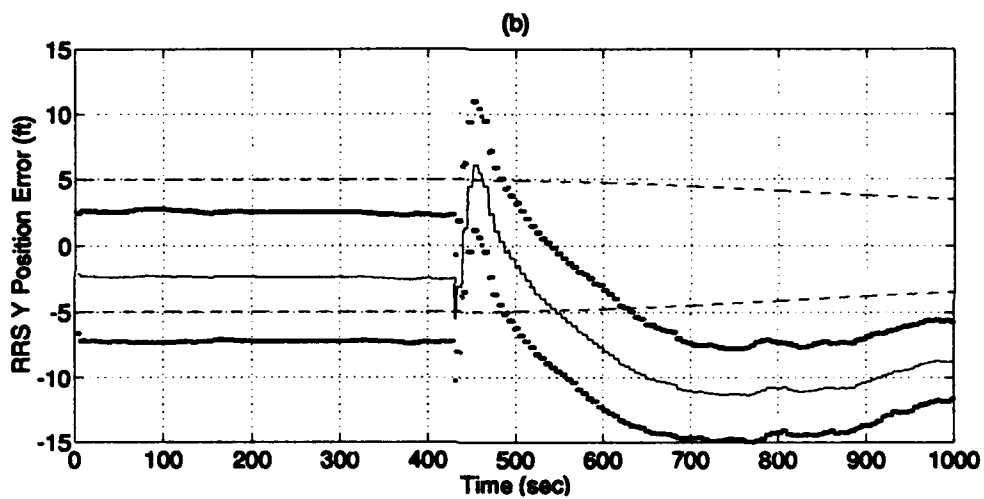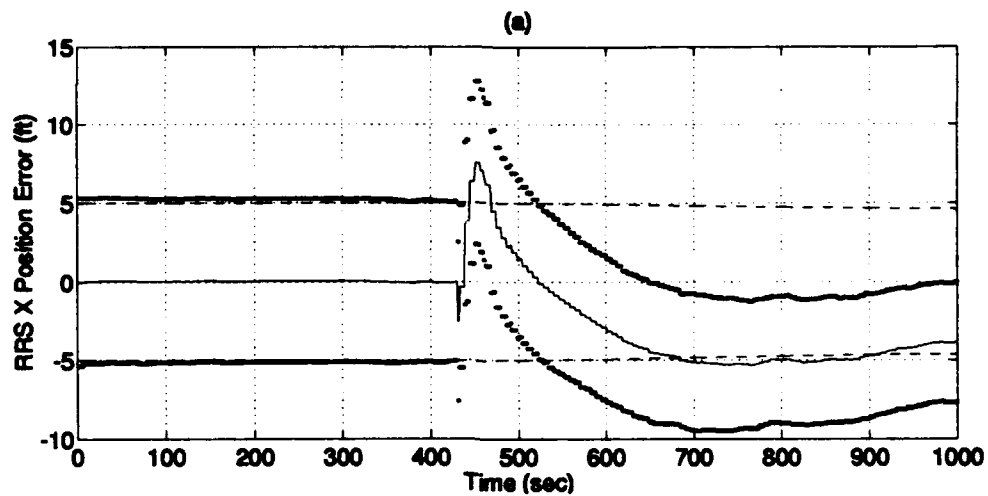
**Plot H-7:** RRS X/Y/Z Surveyed Position Errors
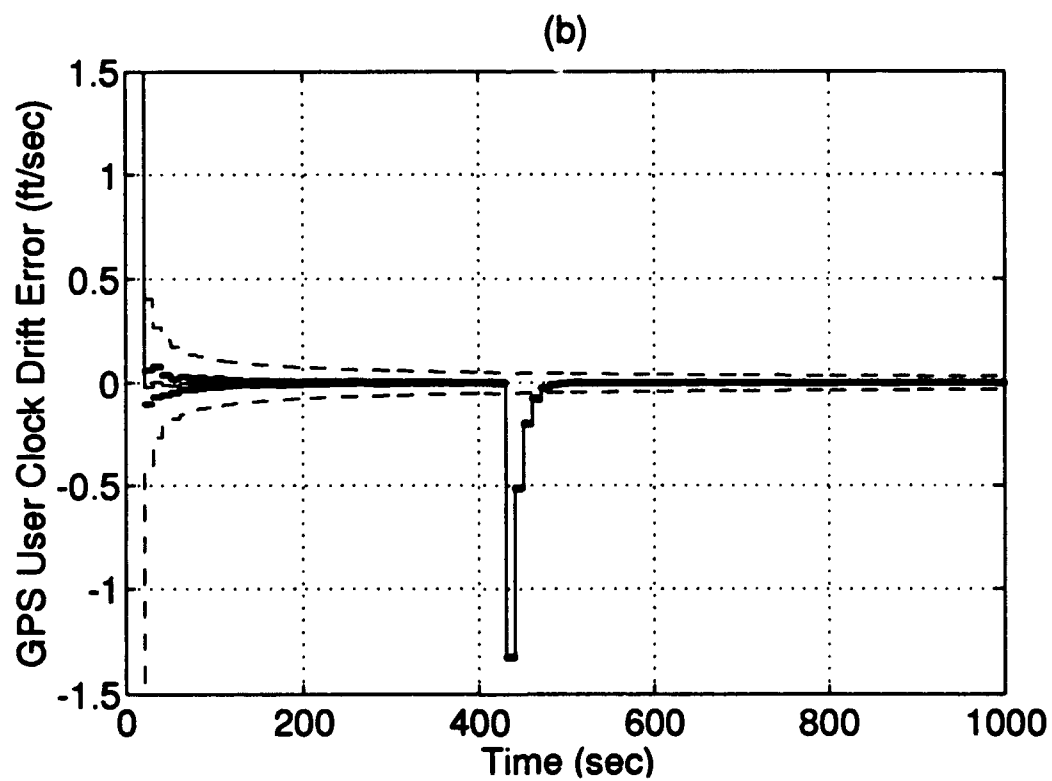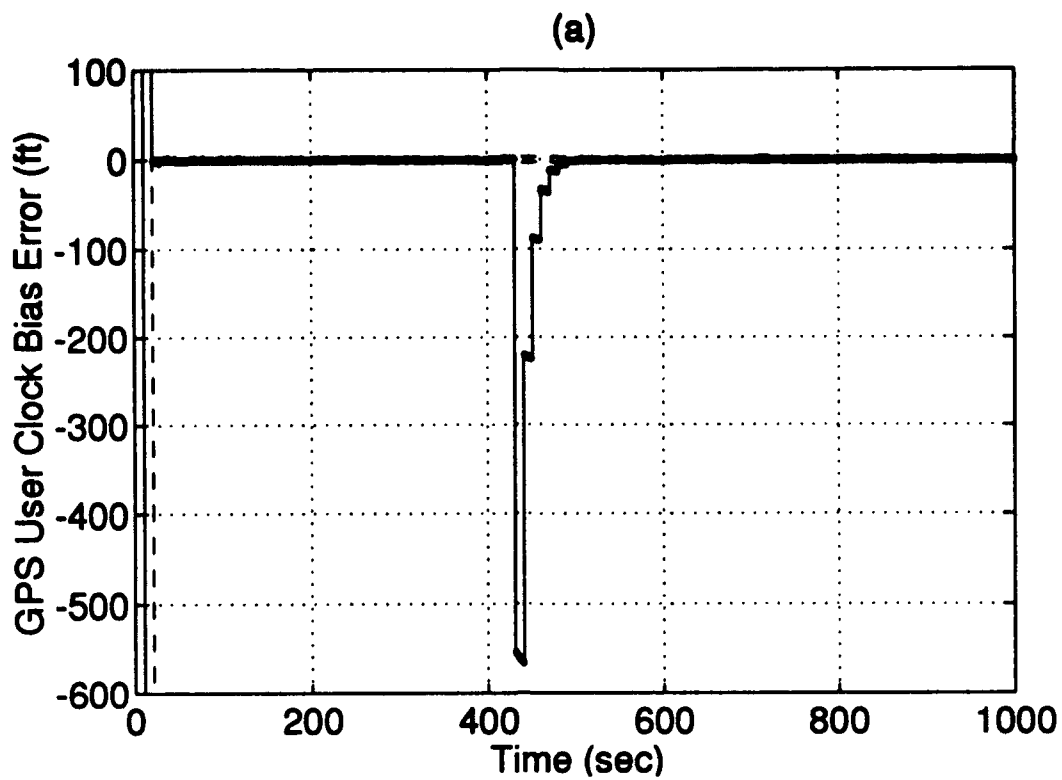
Plot H-8: GPS User Clock Bias/Drift Errors
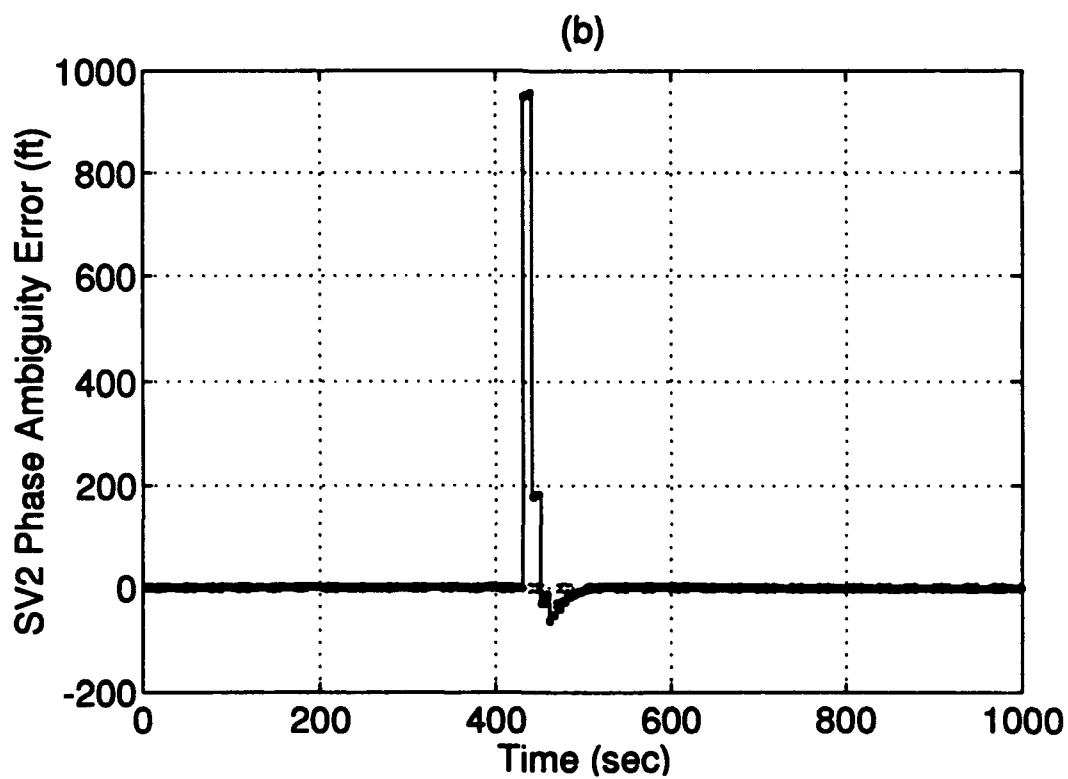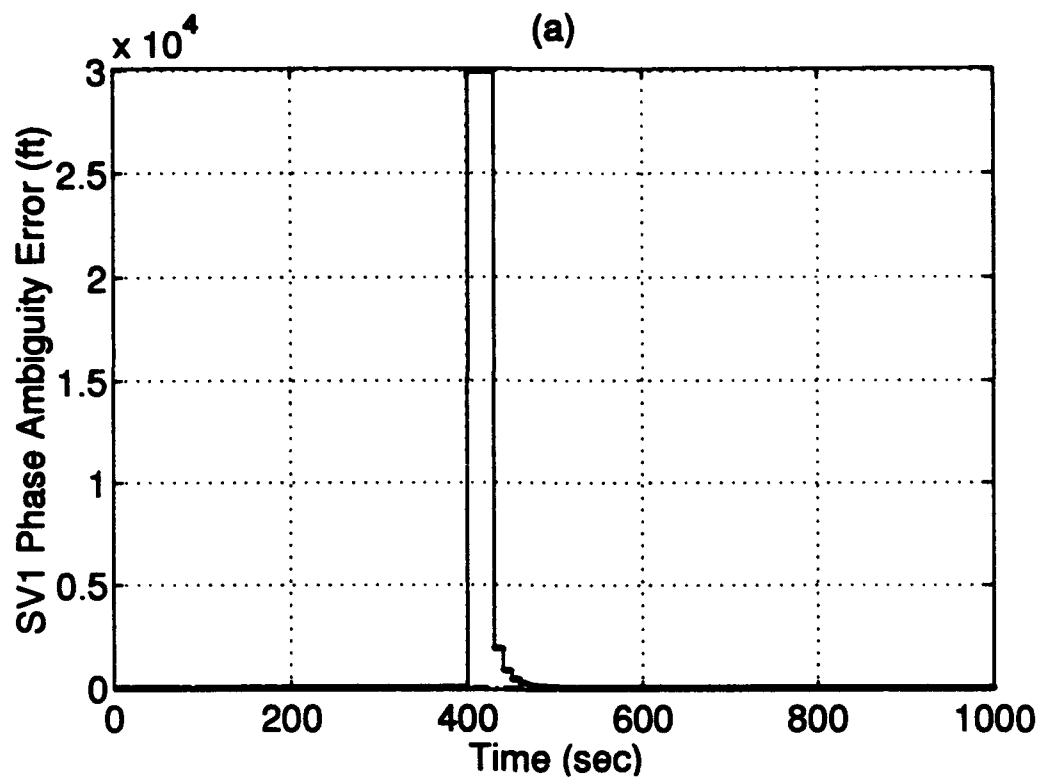
Plot H-9: GPS Satellite 1 and 2 Phase Ambiguity Errors
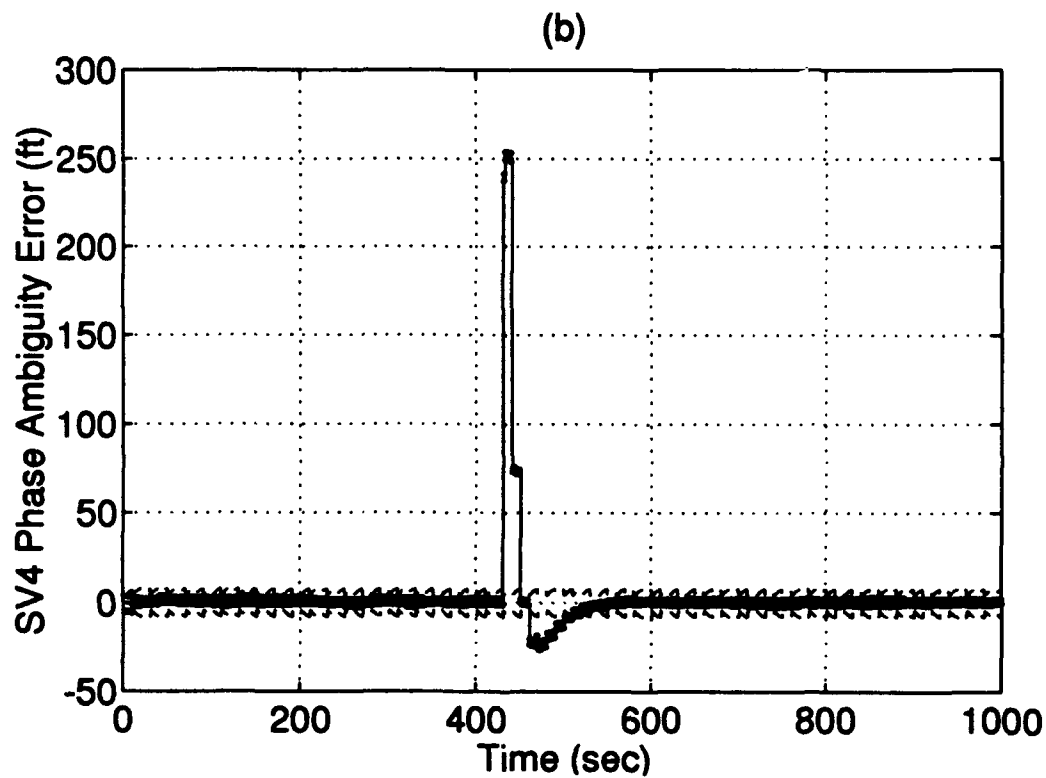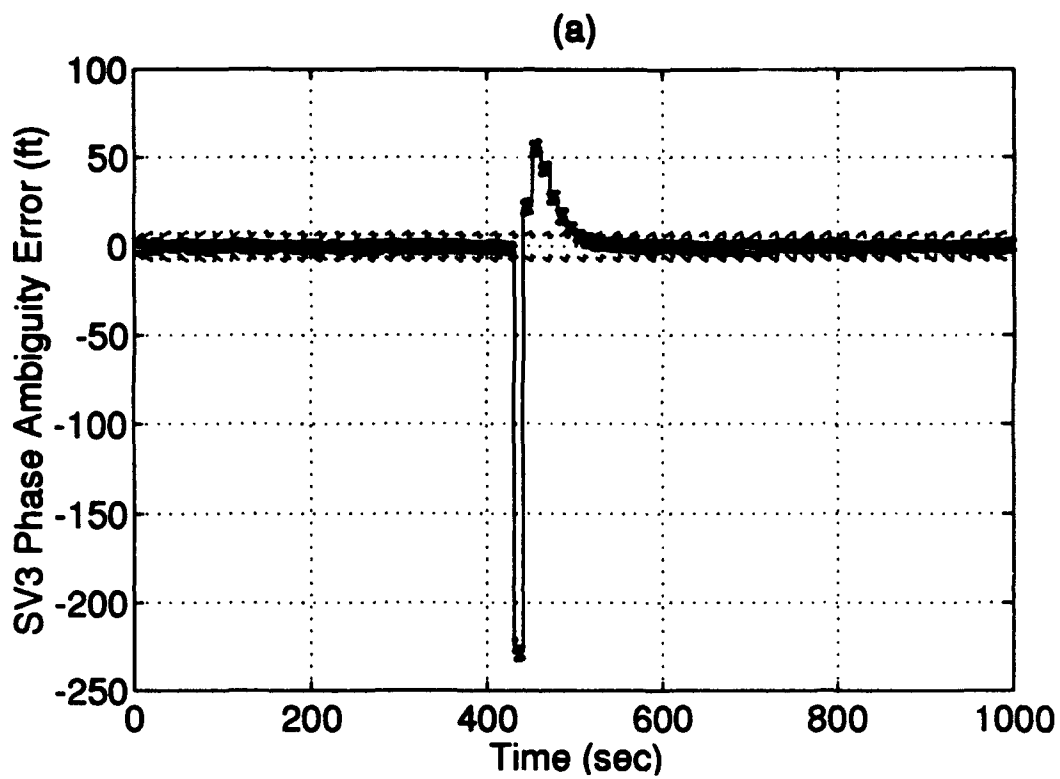
Plot H-10: GPS Satellite 3 and 4 Phase Ambiguity Errors

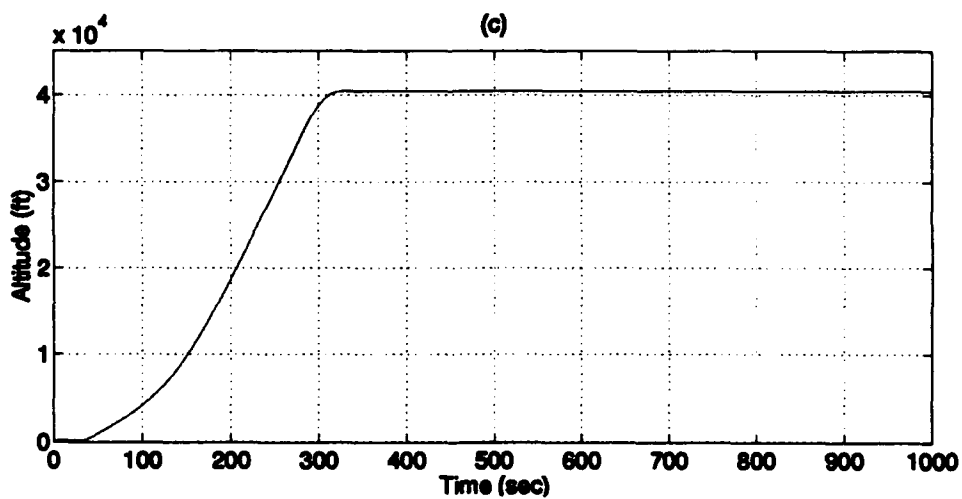## *Appendix I. Large Cycle Slip Simulation Results (Zoomed Time Scale)*

This appendix presents the same results as Appendix H but with a "zoomed" time scale. The 10 plots of Appendix H are shown again here with a time scale of 400 sec to 500 sec in 20 sec increments. The 10 resulting plots are:

Plot I-1   (a) - Flight Profile Longitude
                 (b) - Flight Profile Latitude
                 (c) - Flight Profile Altitude

Plot I-2   (a) - Longitude Error
                 (b) - Latitude Error

Plot I-3   (a) - Altitude Error
                 (b) - Barometric Altitude Error

Plot I-4   (a) - North Tilt Error
                 (b) - West Tilt Error
                 (c) - Azimuth Tilt Error

Plot I-5   (a) - North Velocity Error
                 (b) - West Velocity Error
                 (c) - Vertical Velocity Error

Plot I-6   (a) - RRS Range Bias Error
                 (b) - RRS Velocity Bias Error
                 (c) - RRS Atmospheric Propagation Delay Error

Plot I-7   (a) - RRS X Position Survey Error
                 (b) - RRS Y Position Survey Error
                 (c) - RRS Z Position Survey Error

Plot I-8   (a) - GPS User Clock Bias Error
                 (b) - GPS User Clock Drift Error

Plot I-9   (a) - Satellite 1 Phase Ambiguity Error
                 (b) - Satellite 2 Phase Ambiguity Error

Plot I-10   (a) - Satellite 3 Phase Ambiguity Error
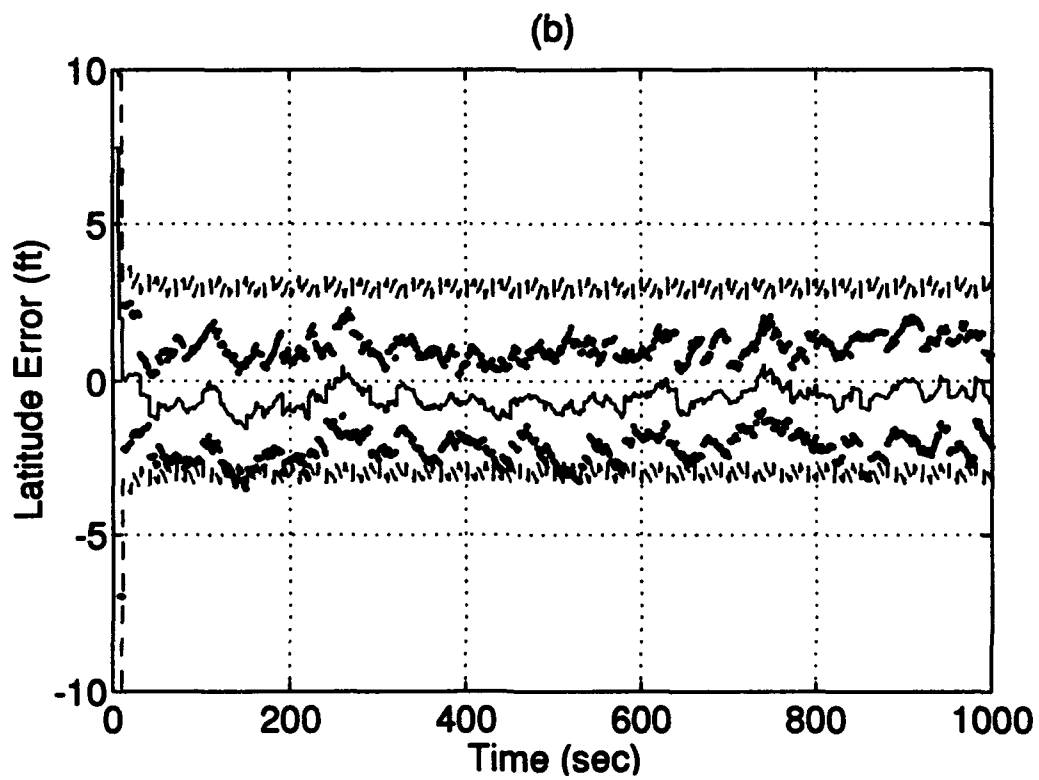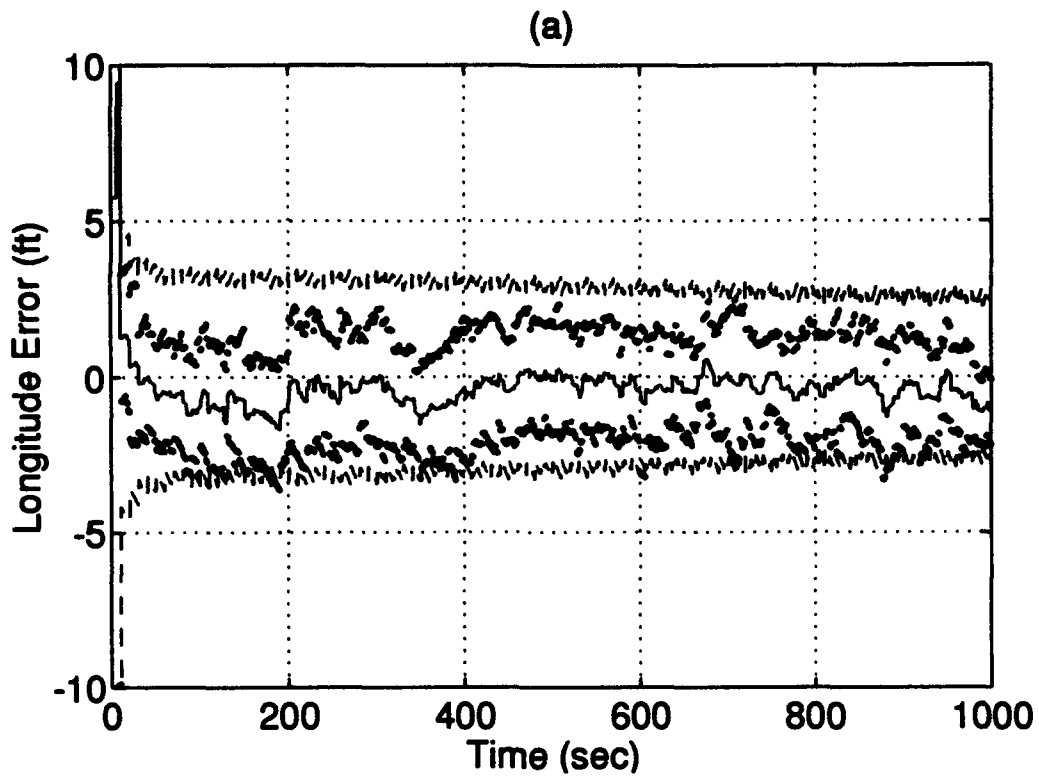   (b) - Satellite 4 Phase Ambiguity Error

Each plot shows the results of a 15-run Monte Carlo average of the truth state minus the filter state for the time period 400 to 500 seconds of the flight profile, the true +/- one sigma standard deviation of the Monte Carlo average, and the filter predicted +/- one sigma standard deviation. The simulation of the cycle slip begins at the 400 second mark with a 20 second loss of GPS satellite 1 followed by a 30,000 ft cycle slip.

The following is a legend for the 10 plots:

Line Style	Description
————————	15 Monte Carlo run mean
··	mean + and - true 1σ
- -	+ and - filter-predicted 1σ
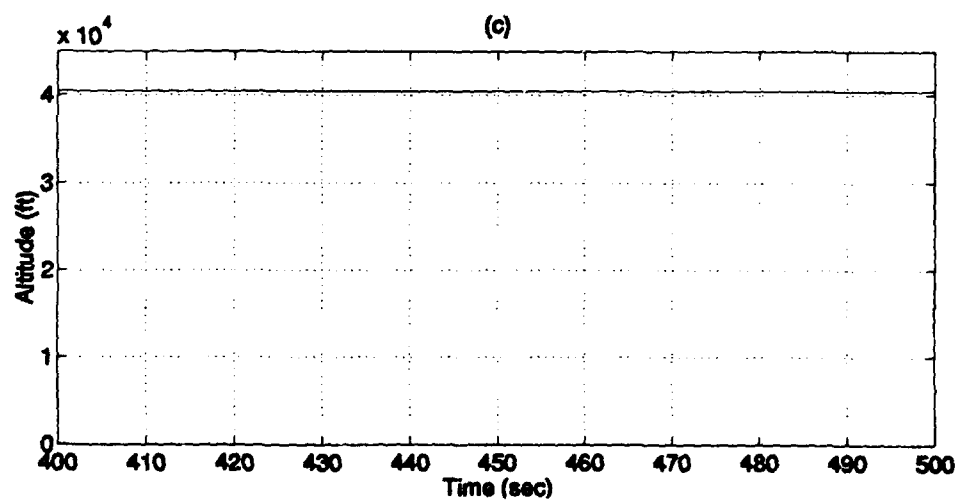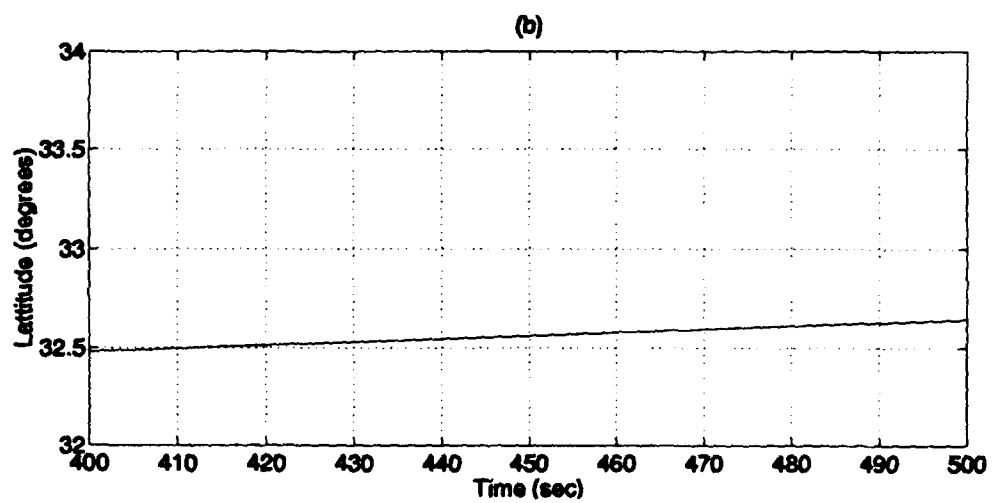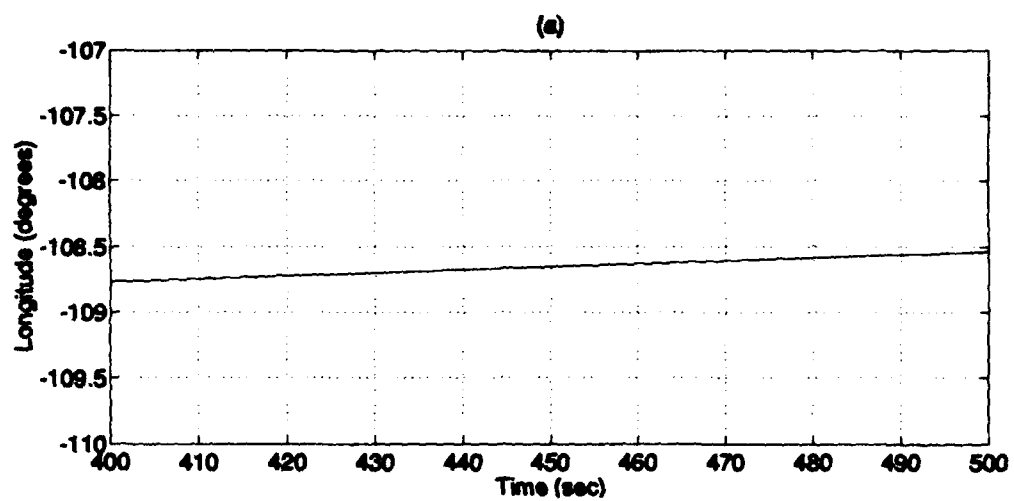
Plot I-1: Flight Profile

I-3

(a)

(b)
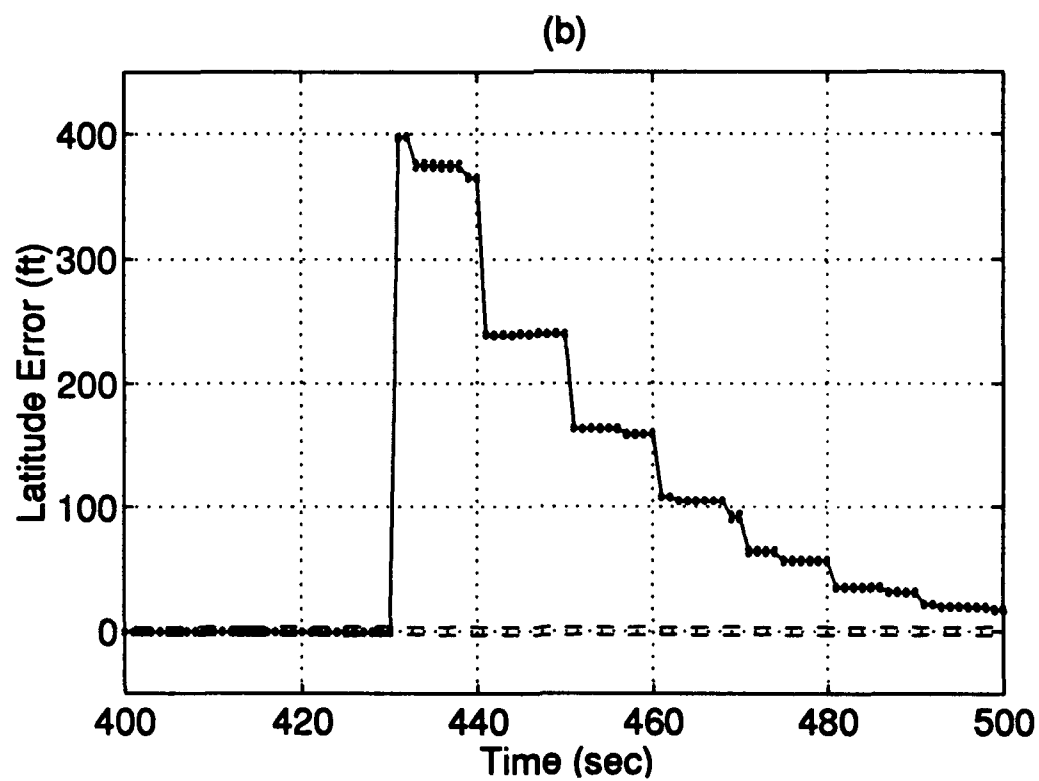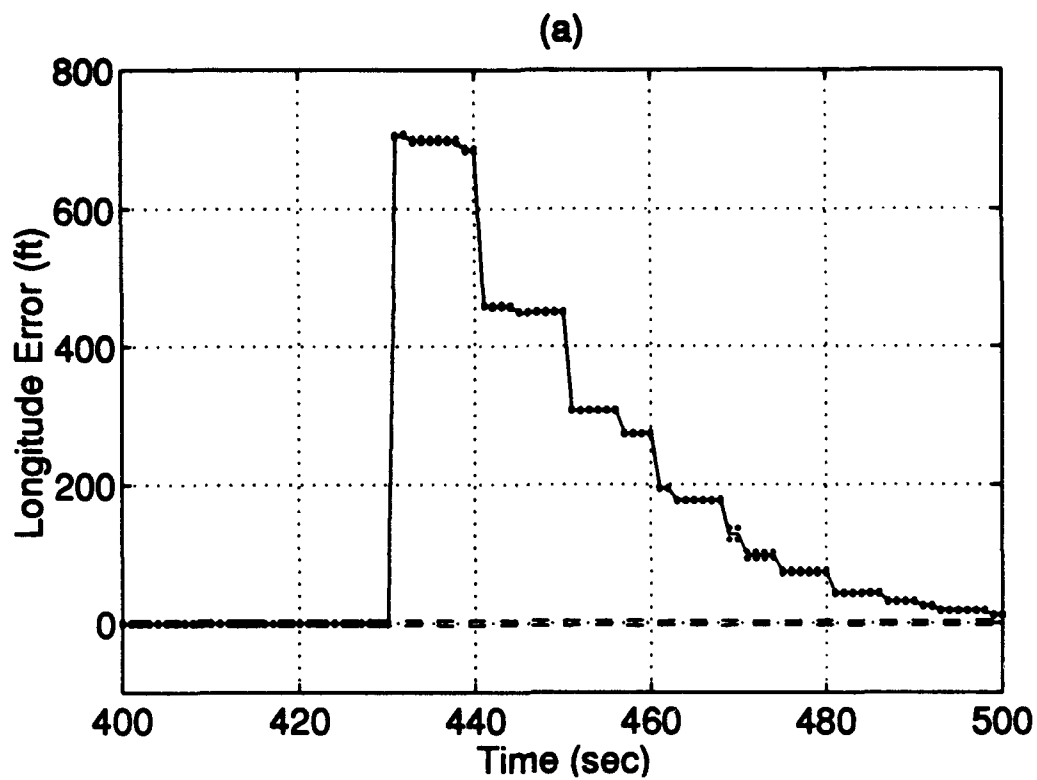
Plot I-2: Longitude/Latitude Errors

I-4
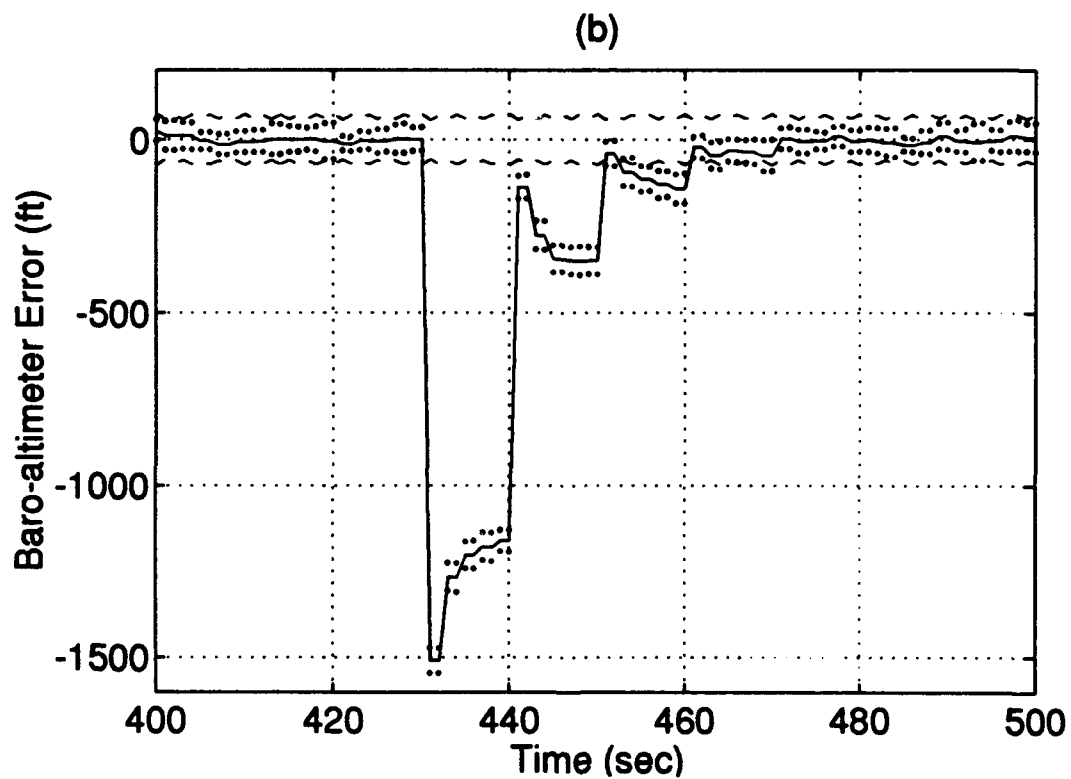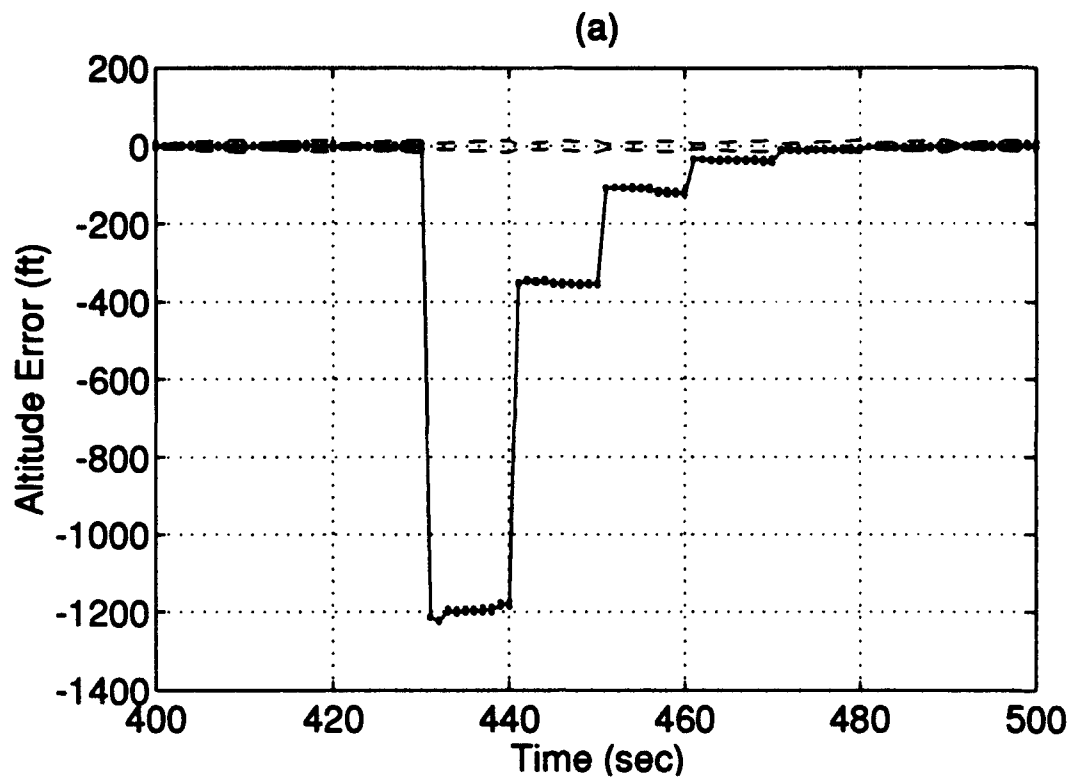
Plot I-3: Altitude/Barometric Altitude Errors

I-5
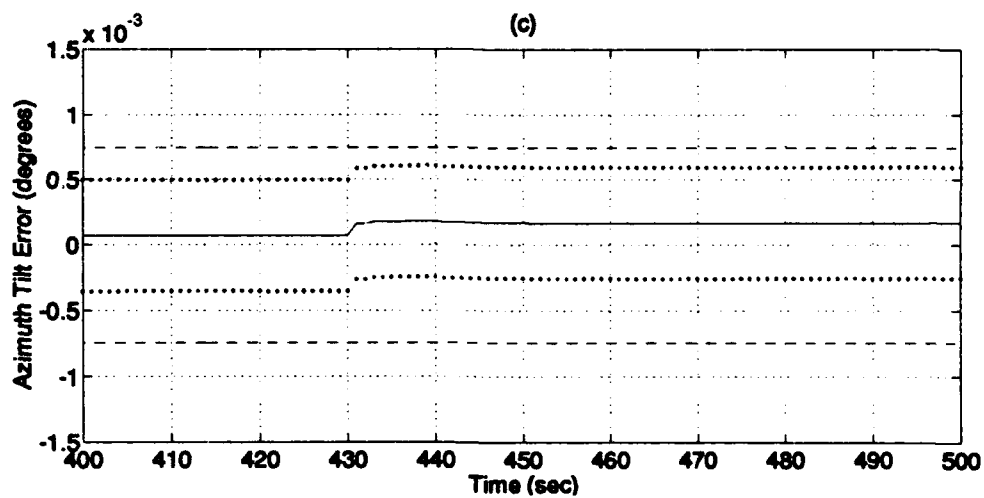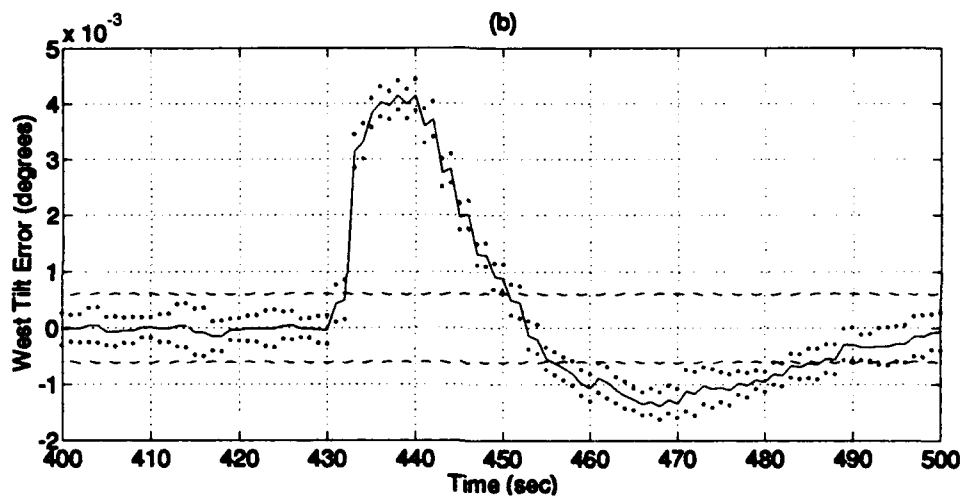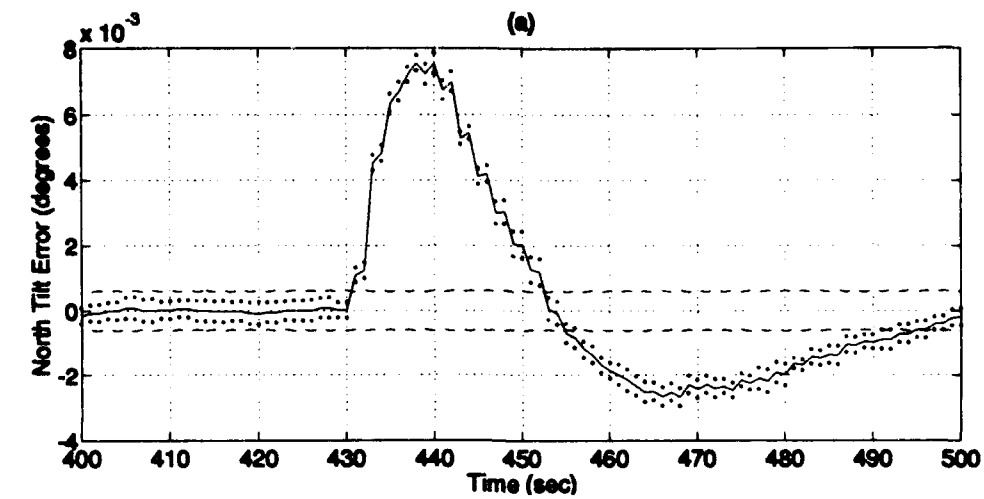
Plot I-4: North/West/Azimuth Tilt Errors
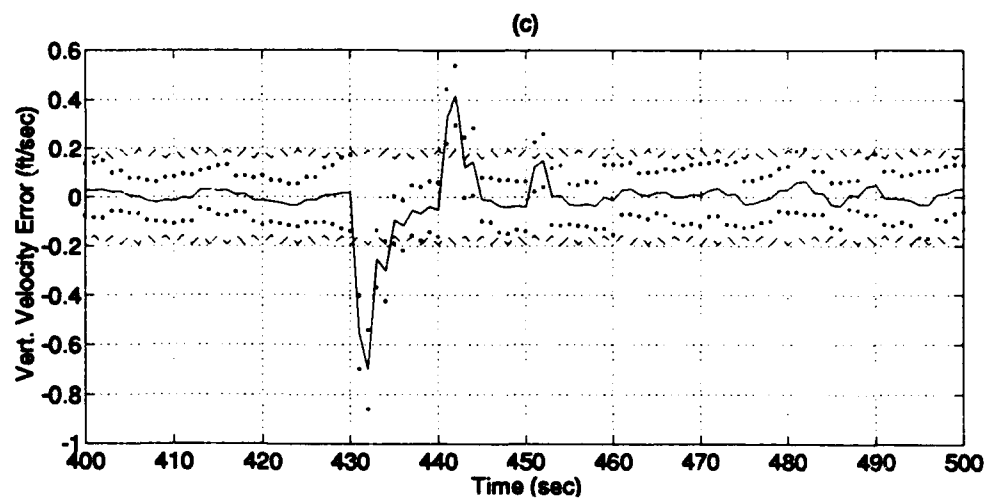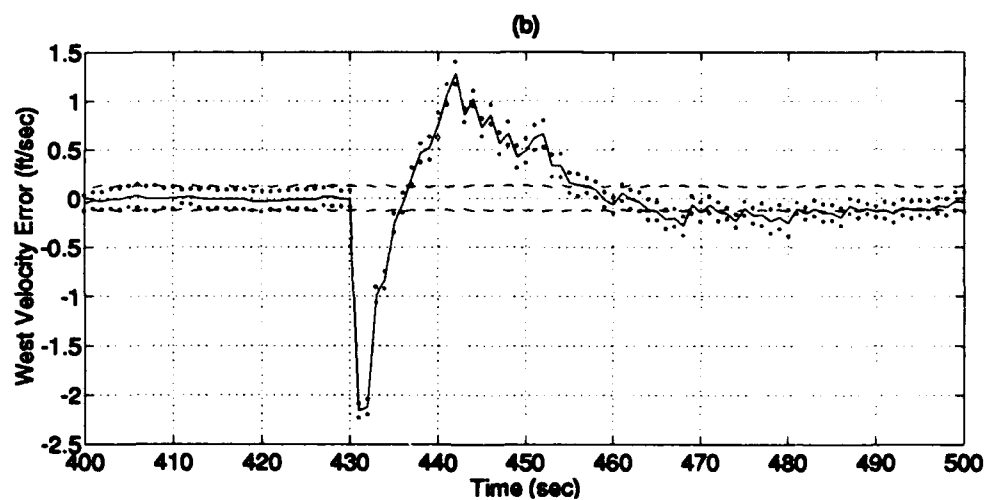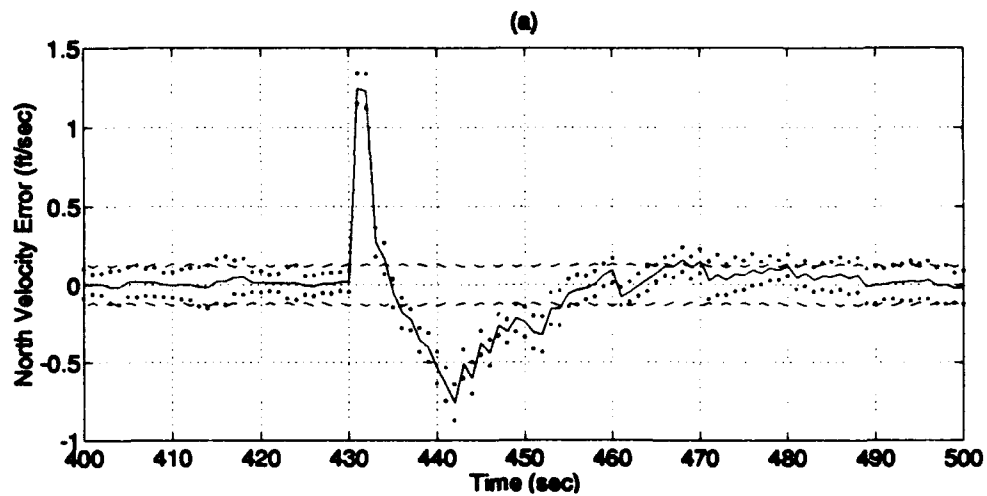
Plot I-5: North/West/Vertical Velocity Errors
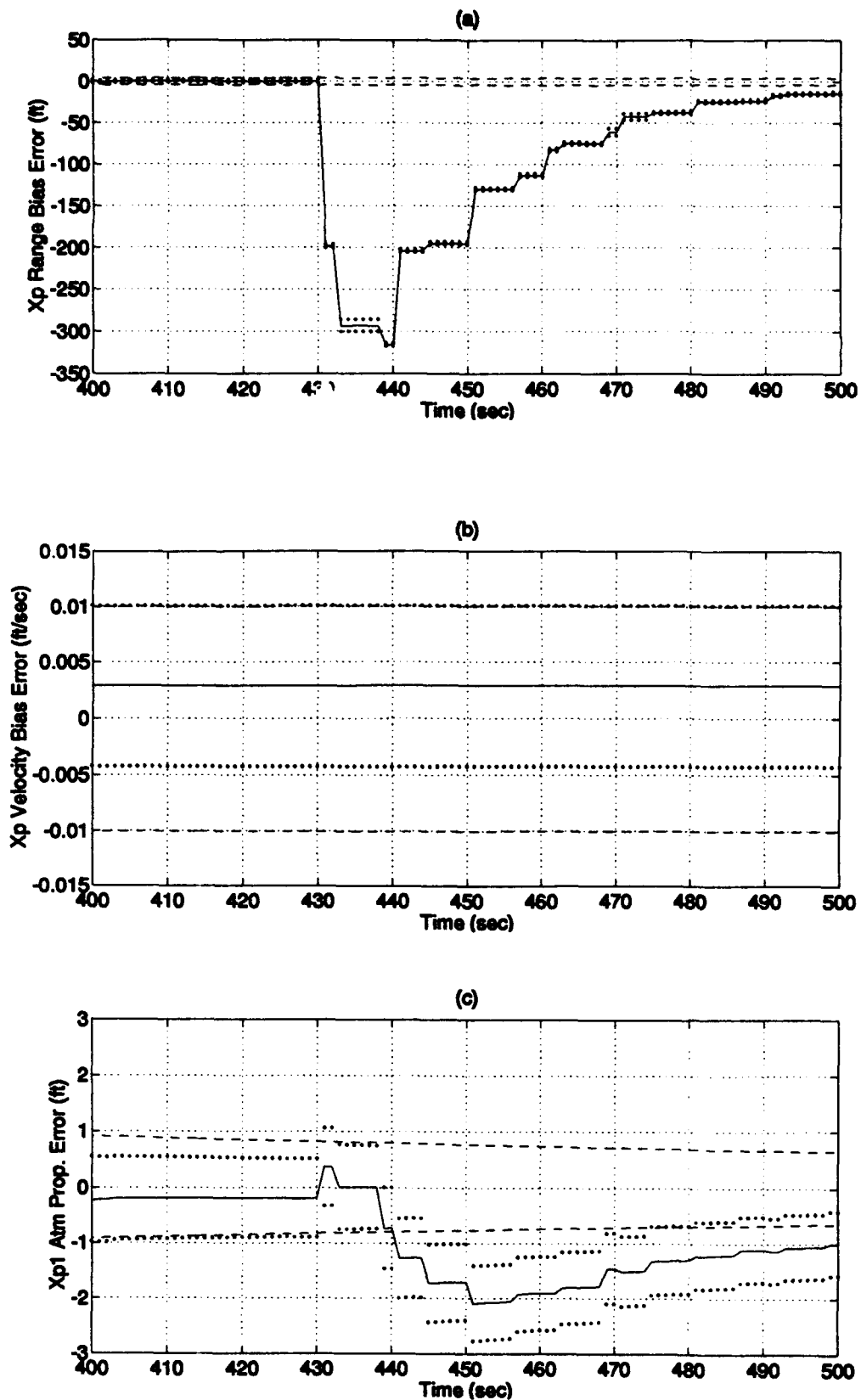
Plot I-8: RRS Range bias/Velocity bias/Atmospheric propagation delay Errors
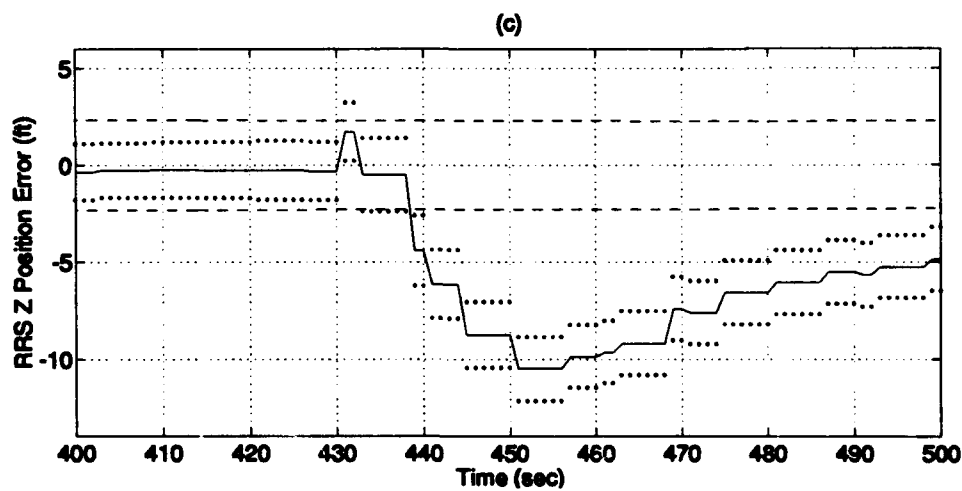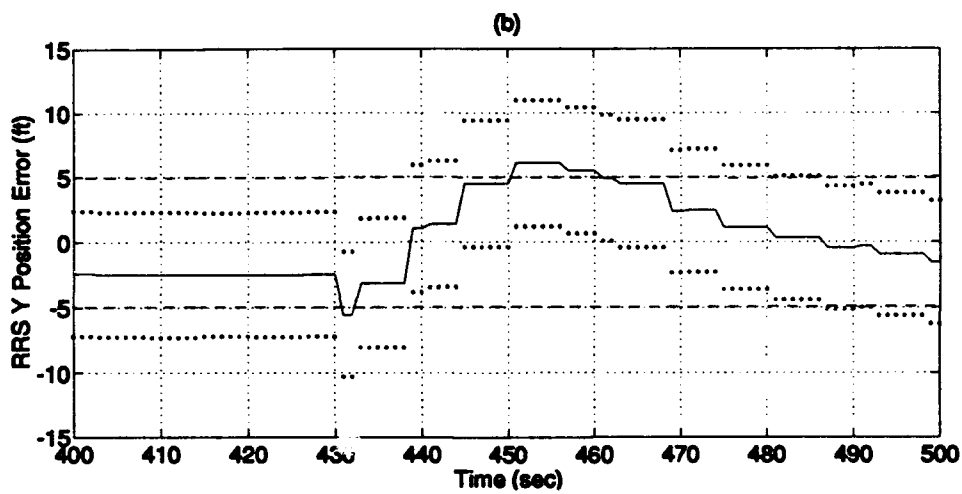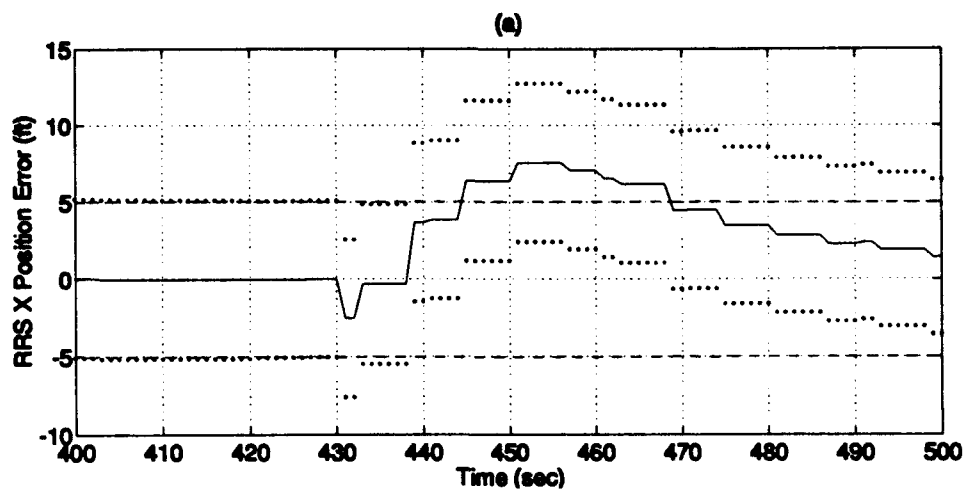
Plot I-7: RRS X/Y/Z Surveyed Position Errors

(a)

(b)
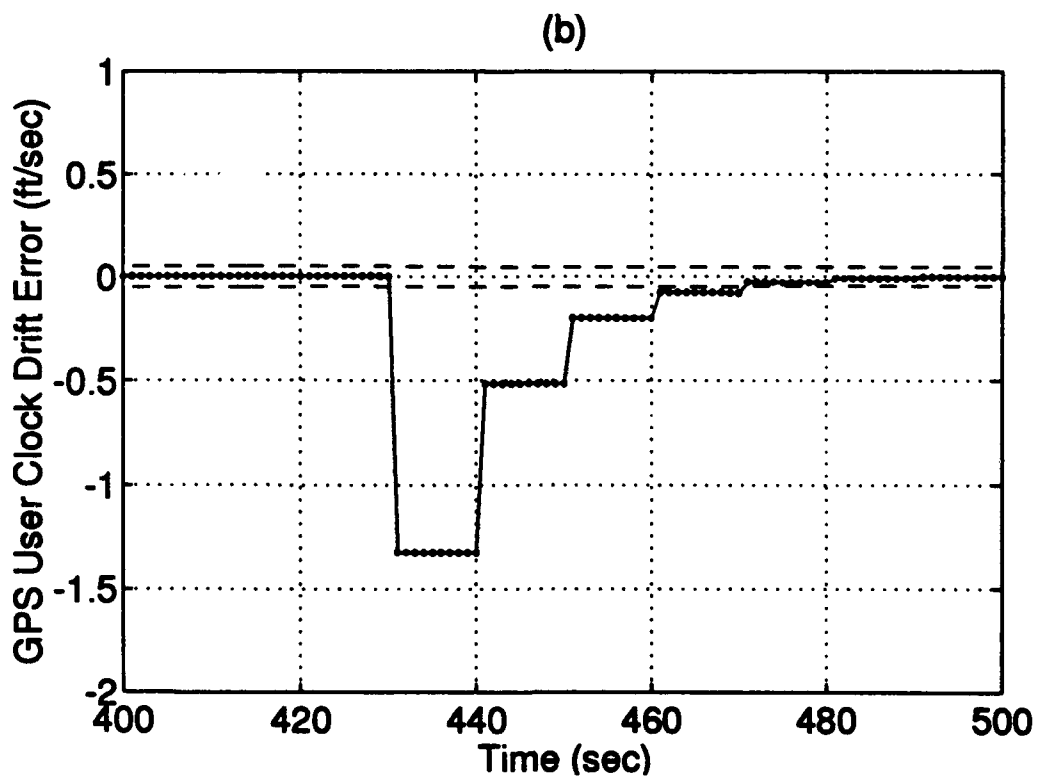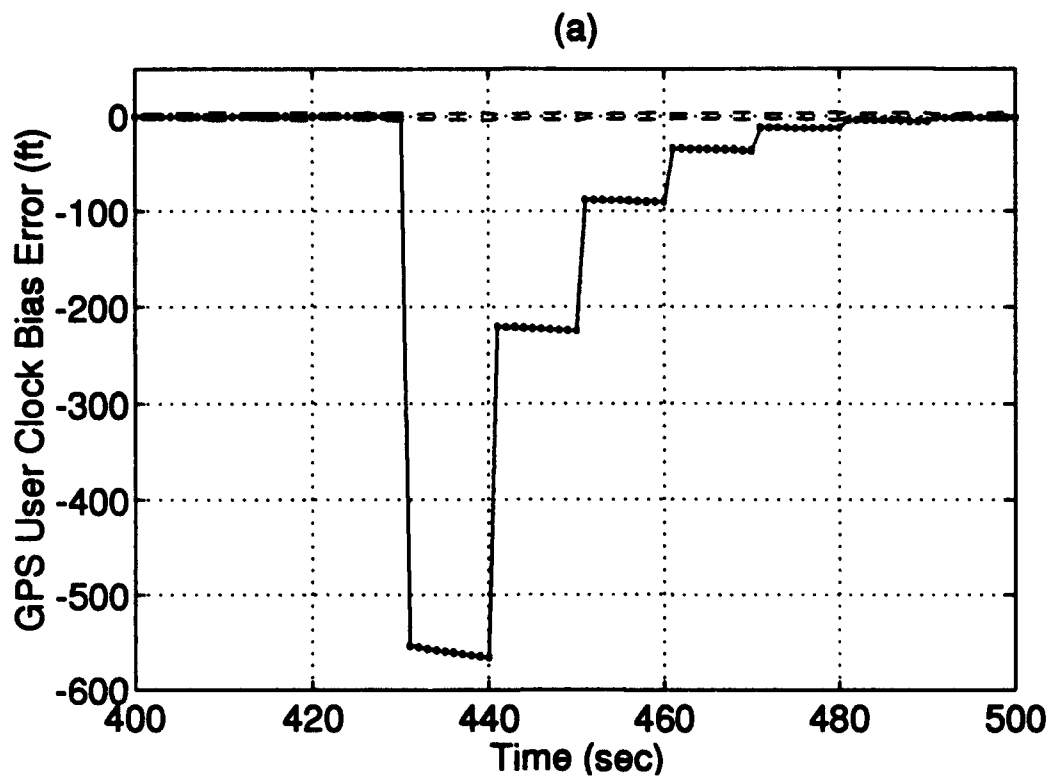
Plot I-8: GPS User Clock Bias/Drift Errors
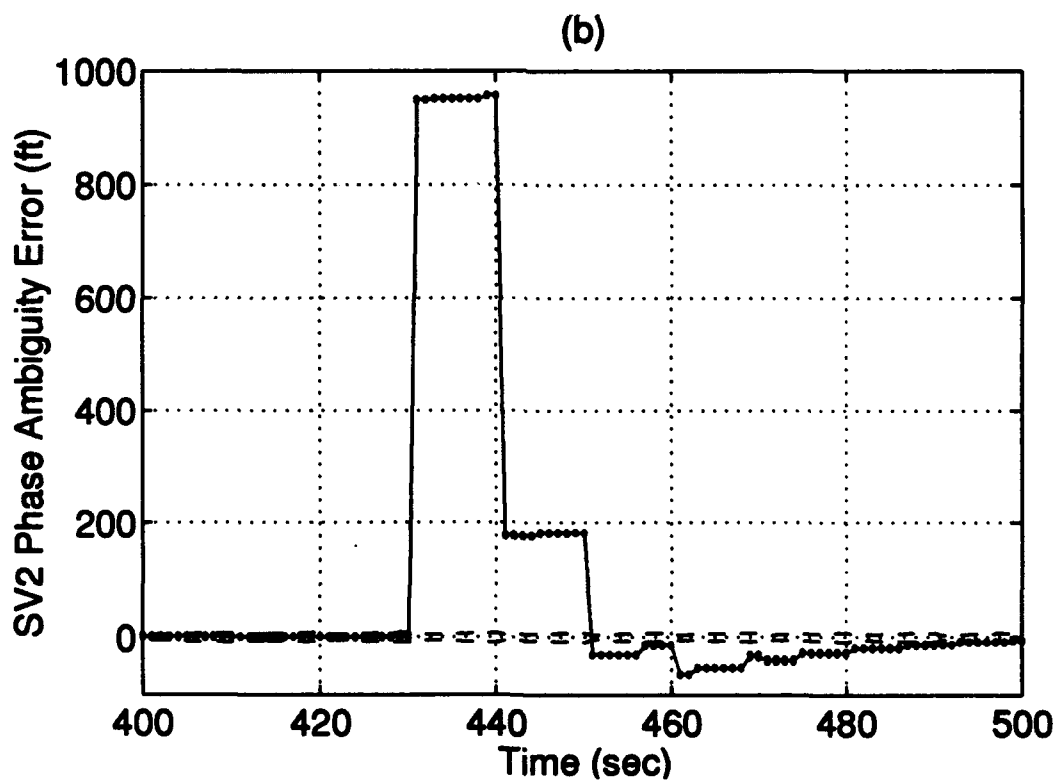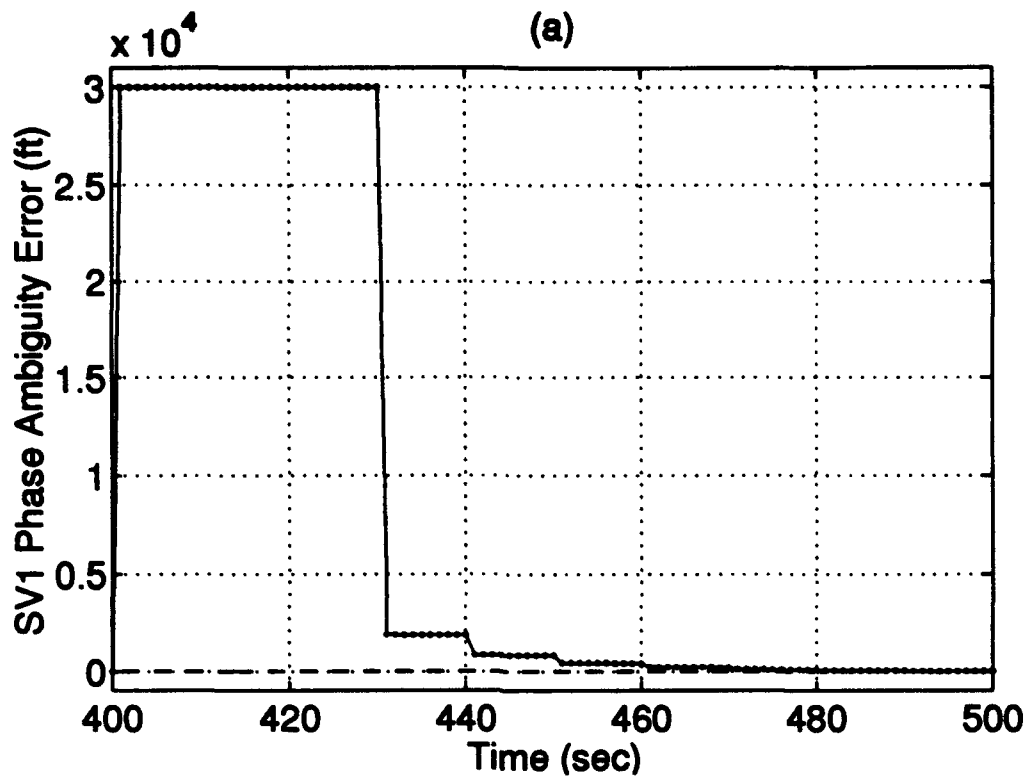
Plot I-9: GPS Satellite 1 and 2 Phase Ambiguity Errors

I-11
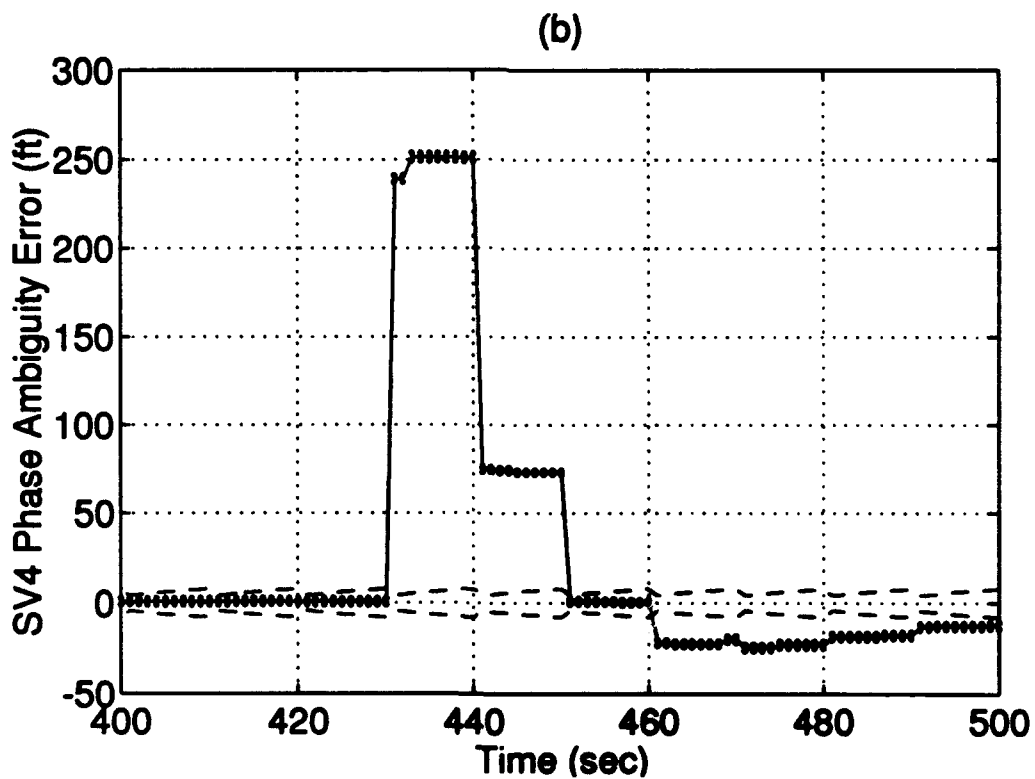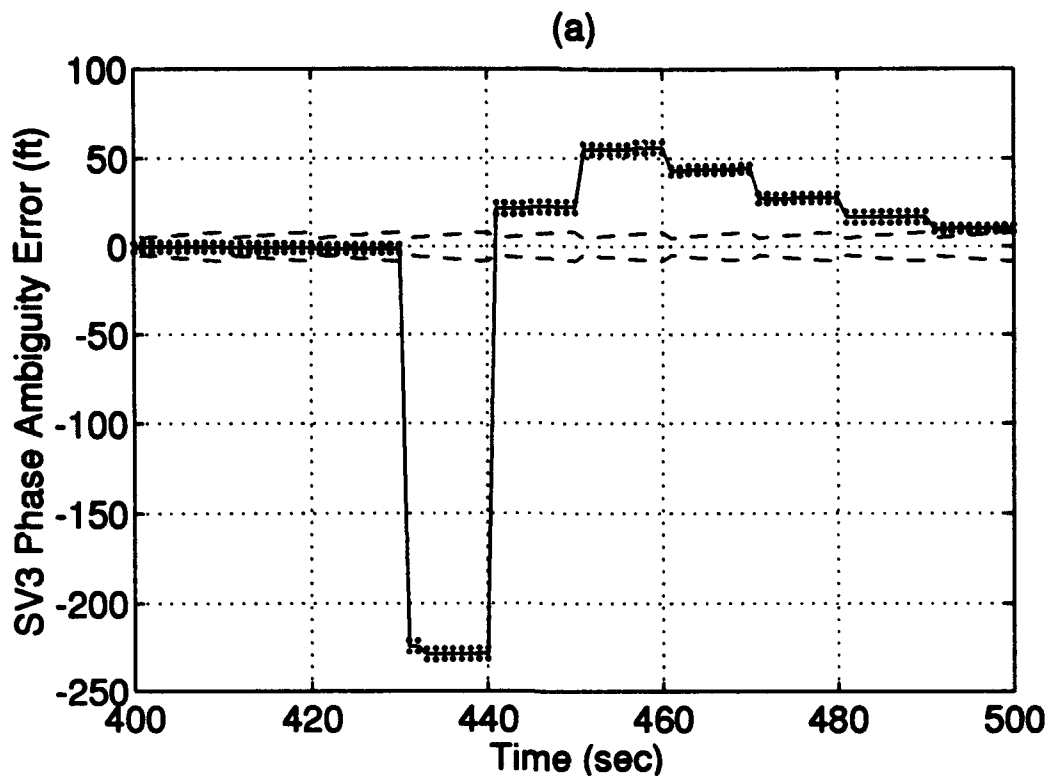
Plot I-10: GPS Satellite 3 and 4 Phase Ambiguity Errors

Appendix J. Small Cycle Slip Simulation Results

This appendix presents the same results of the PNRS MSOFE simulation study including a simulation of a 10 foot cycle slip with no loss of GPS satellite signals. The simulation utilizes the 91-state PNRS truth model and the 71-state filter modelderived in Chapter IV of this thesis research. The results are presented in the form of 10 plots:

Plot J-1 (a) - Flight Profile Longitude
     (b) - Flight Profile Latitude
     (c) - Flight Profile Altitude

Plot J-2 (a) - Longitude Error
     (b) - Latitude Error

Plot J-3 (a) - Altitude Error
     (b) - Barometric Altitude Error

Plot J-4 (a) - North Tilt Error
     (b) - West Tilt Error
     (c) - Azimuth Tilt Error

Plot J-5 (a) - North Velocity Error
     (b) - West Velocity Error
     (c) - Vertical Velocity Error

Plot J-6 (a) - RRS Range Bias Error
     (b) - RRS Velocity Bias Error
     (c) - RRS Atmospheric Propagation Delay Error

Plot J-7 (a) - RRS X Position Survey Error
     (b) - RRS Y Position Survey Error
     (c) - RRS Z Position Survey Error

Plot J-8 (a) - GPS User Clock Bias Error
     (b) - GPS User Clock Drift Error

Plot J-9 (a) - Satellite 1 Phase Ambiguity Error
     (b) - Satellite 2 Phase Ambiguity Error

Plot J-10 (a) - Satellite 3 Phase Ambiguity Error
     (b) - Satellite 4 Phase Ambiguity Error

Each plot shows the results of a 15-run Monte Carlo average of the truth state minus the filter state for the first 1000 seconds of the flight profile, the true +/- one sigma standard deviation of the Monte Carlo simulation, and the filter predicted +/- one sigma standard deviation. The simulation of the cycle slip begins at the 400 second mark.

The following is a legend for the 10 plots:

Line Style	Description
————————————	15 Monte Carlo run mean
··	mean + and - true 1σ
– – – – – – – – – – – – – – – – – –	+ and - filter-predicted 1σ

(a)

(b)

(c)

Plot J-1: Flight Profile

J-3

(a)

(b)

Plot J-2: Longitude/Latitude Errors

J-4
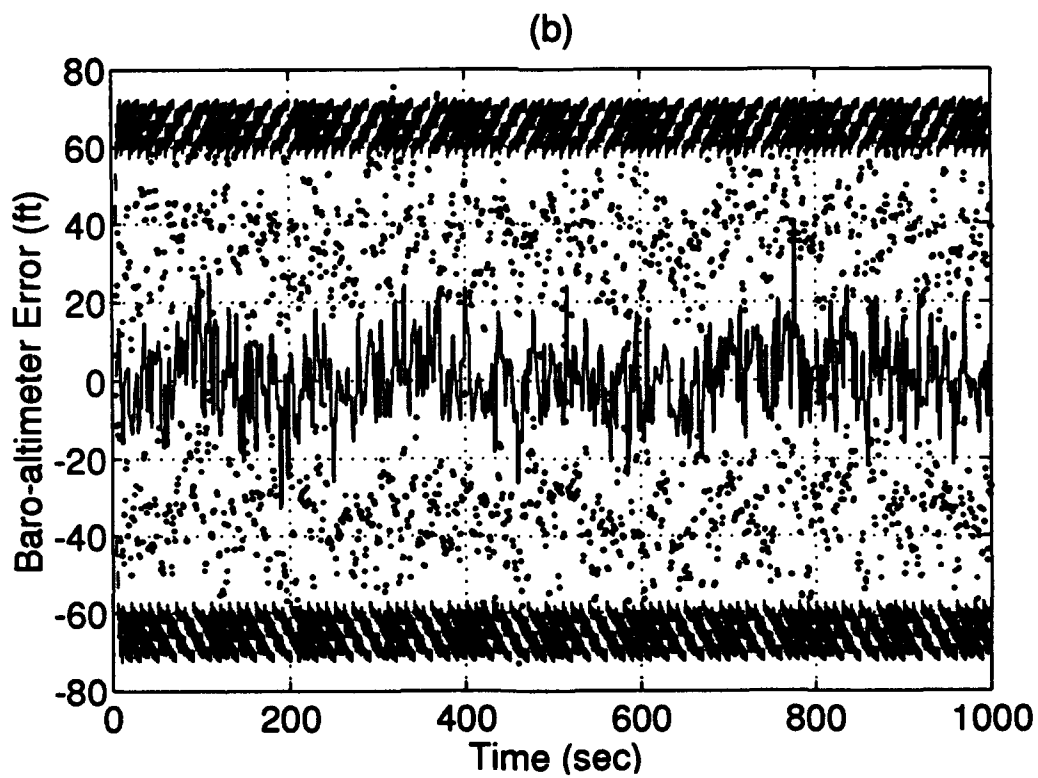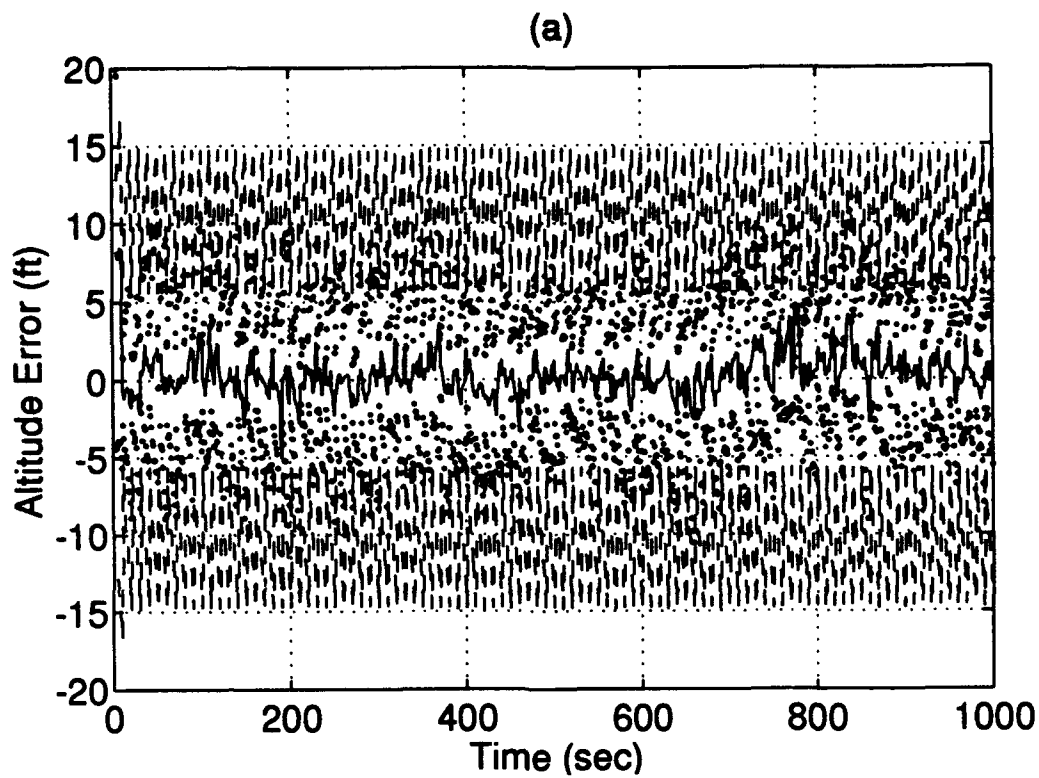
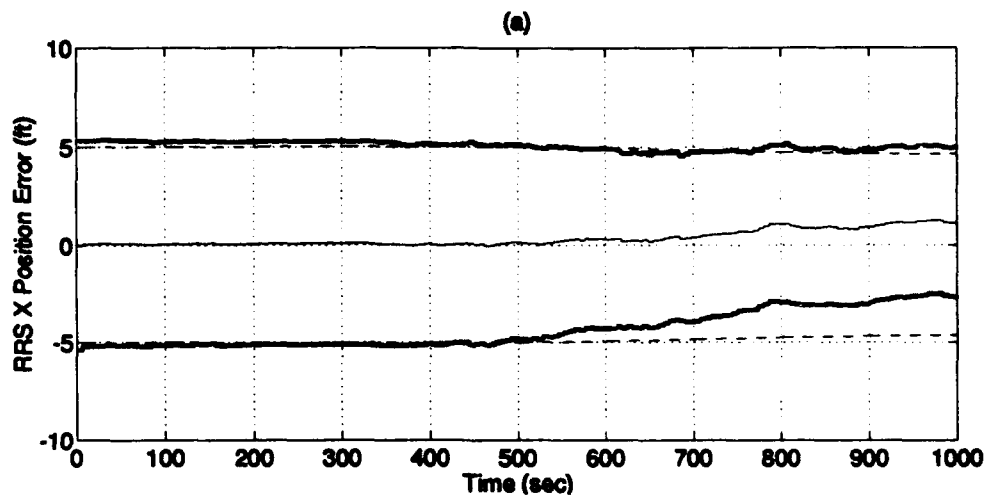**Plot J-3:** Altitude/Barometric Altitude Errors
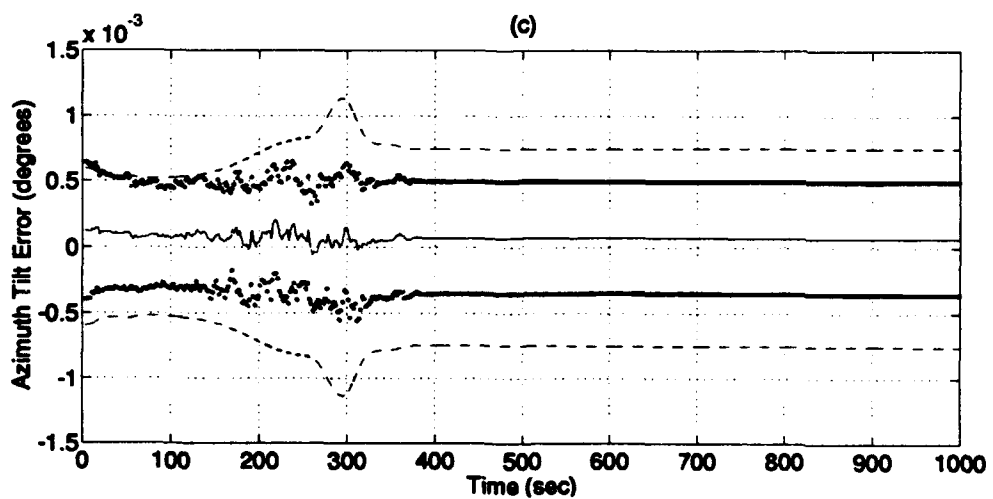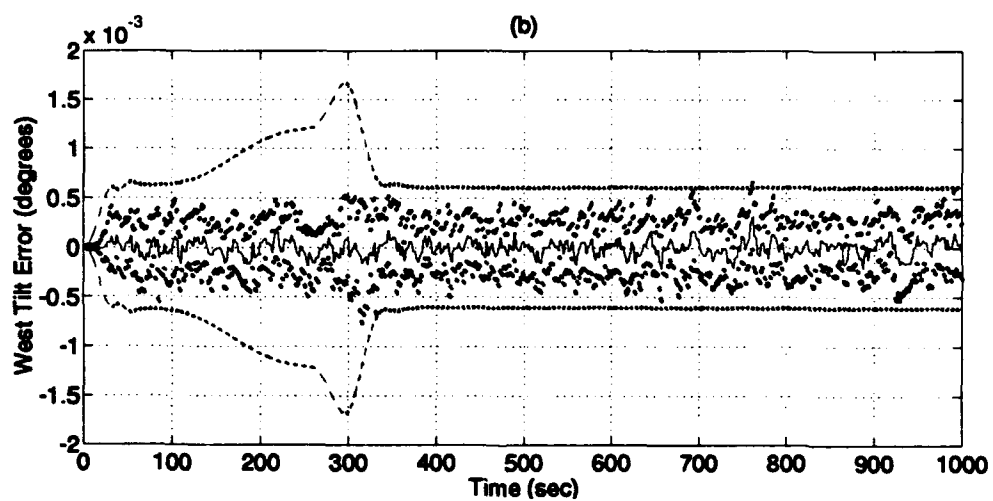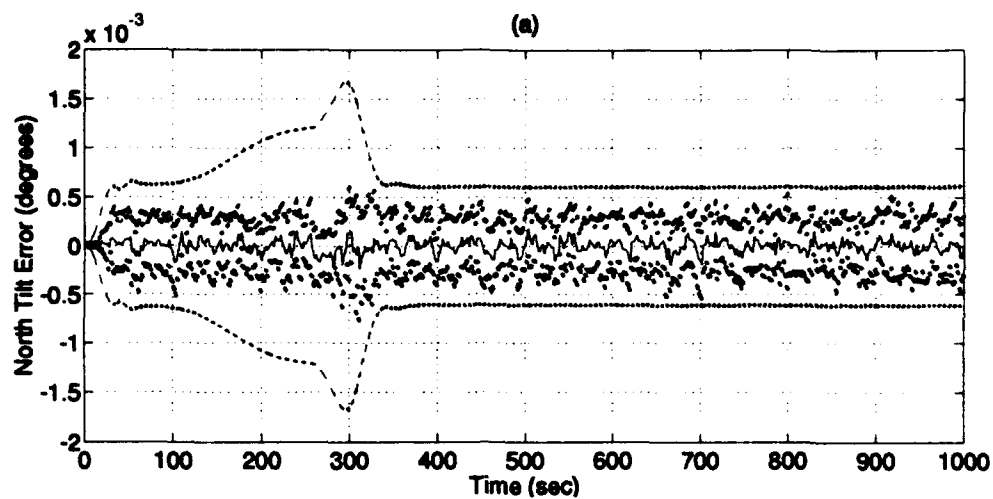
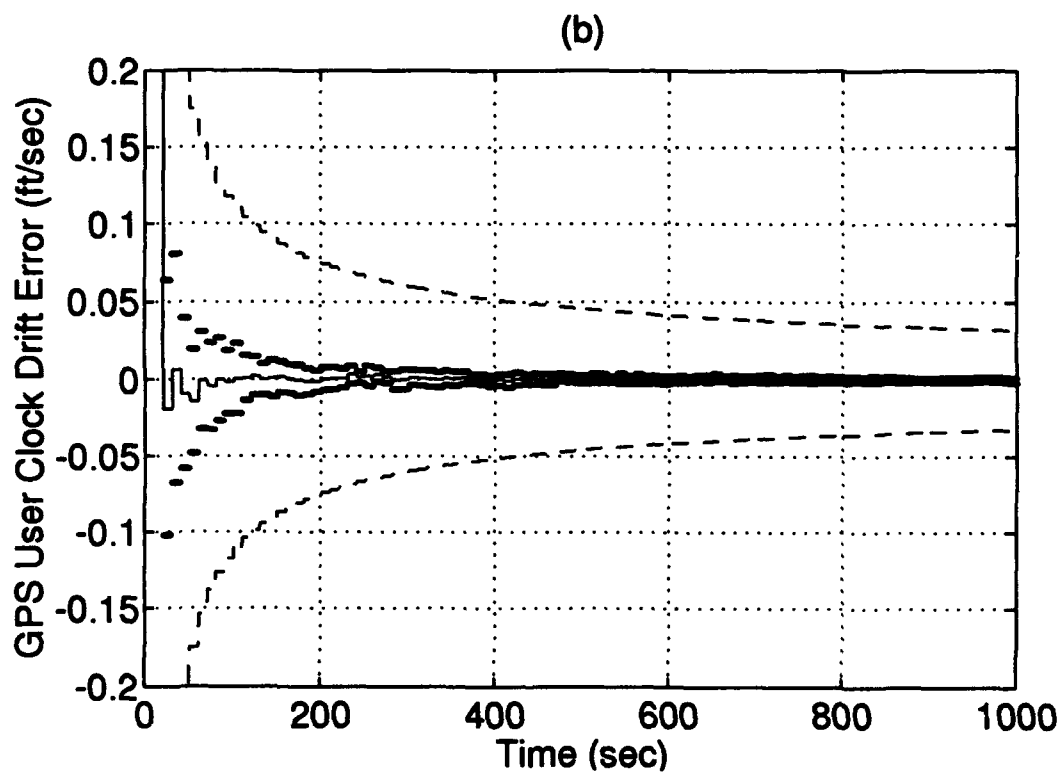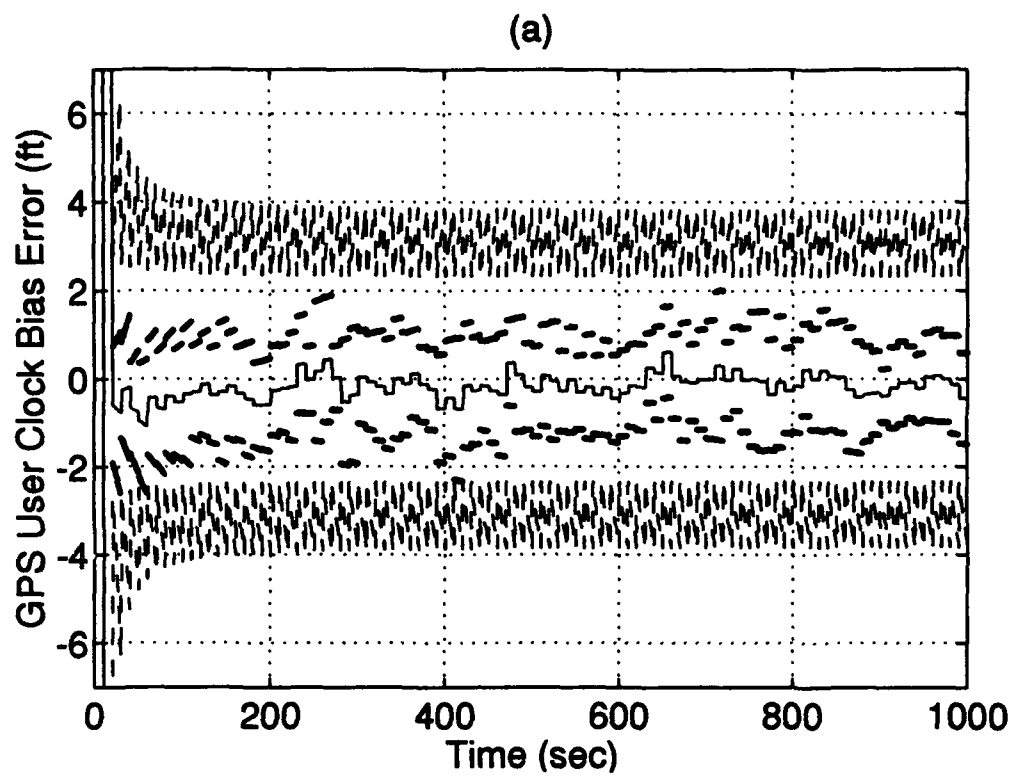**Plot J-4:** North/West/Azimuth Tilt Errors
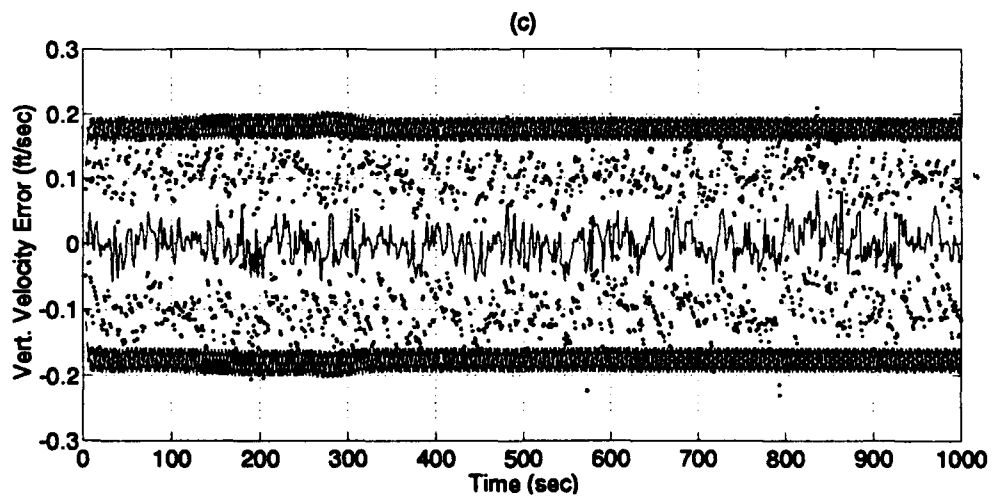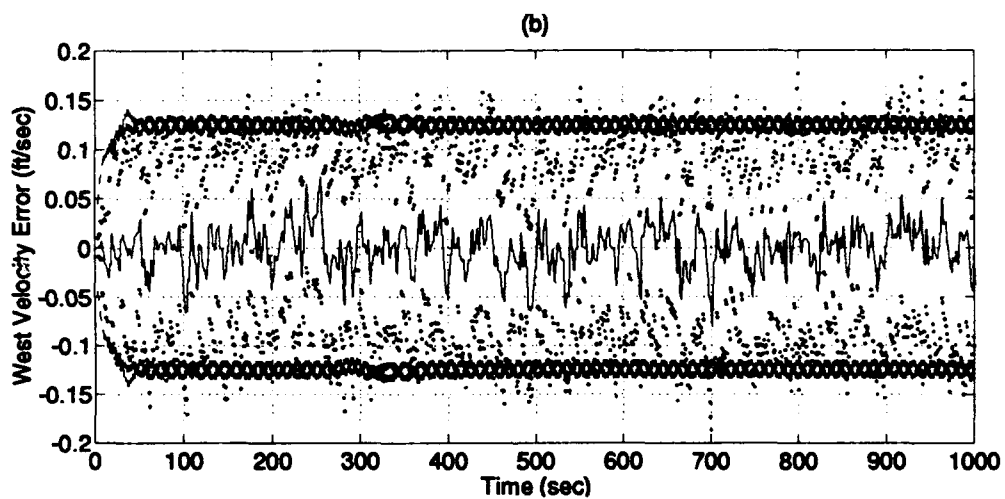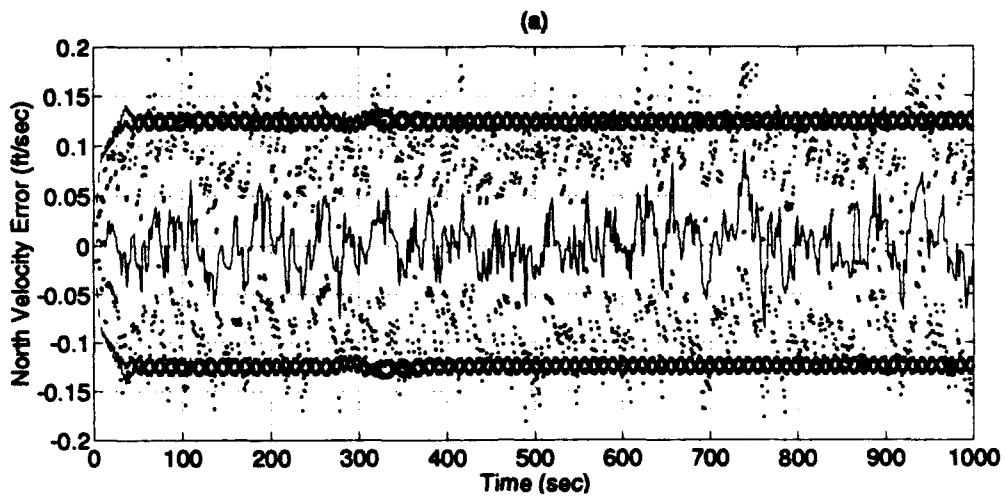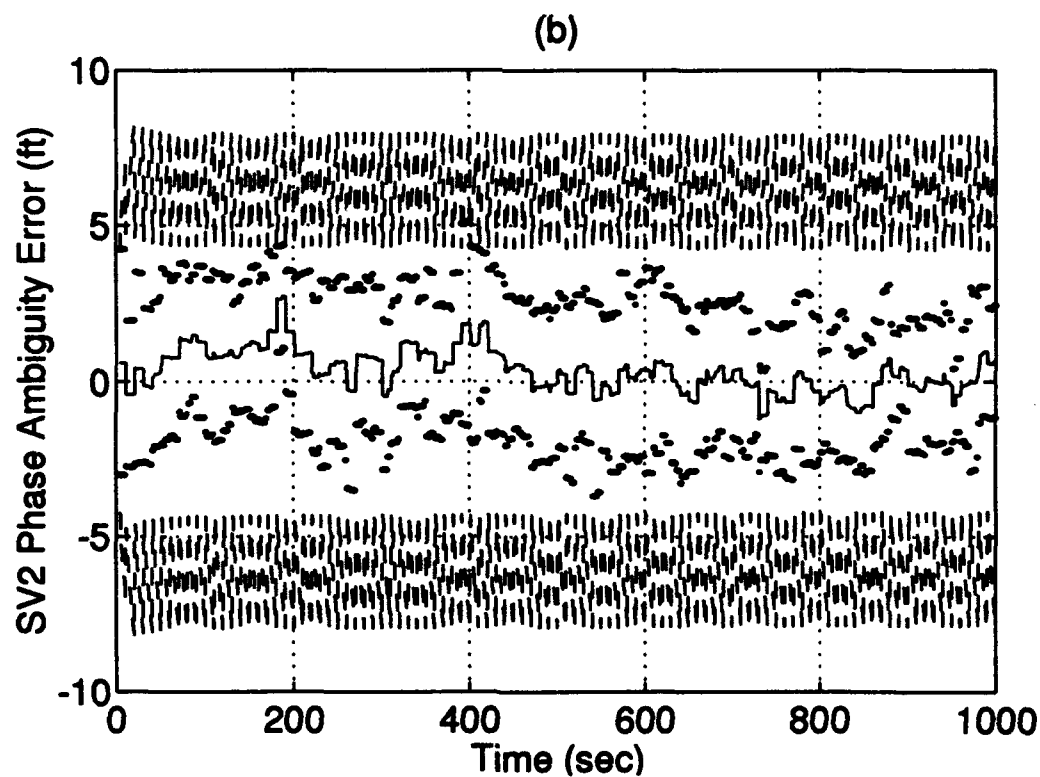
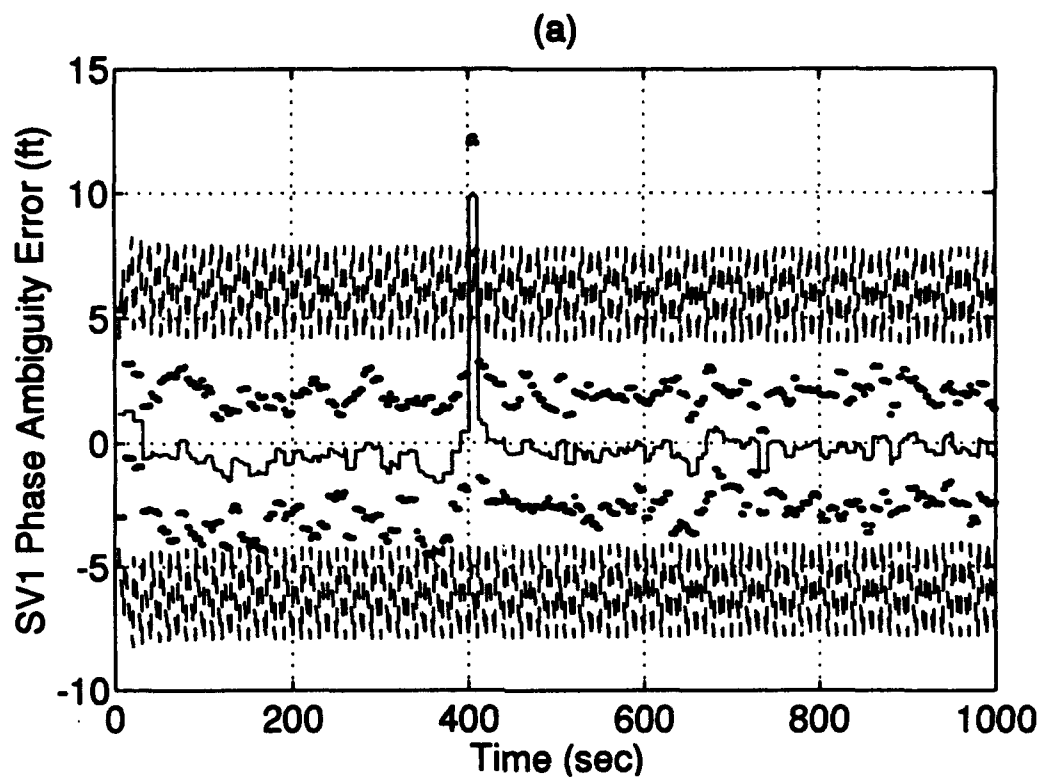**Plot J-5:** North/West/Vertical Velocity Errors
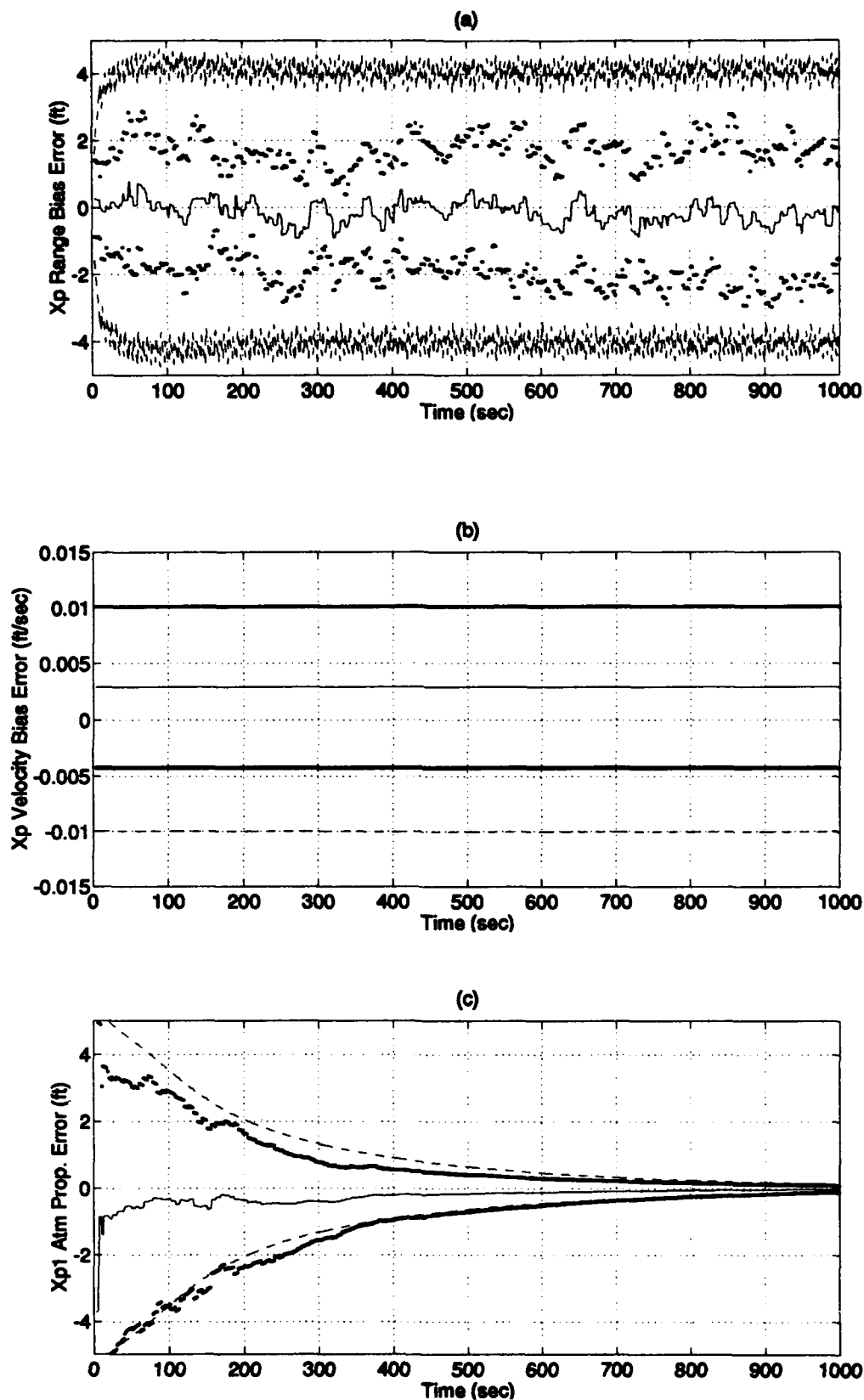
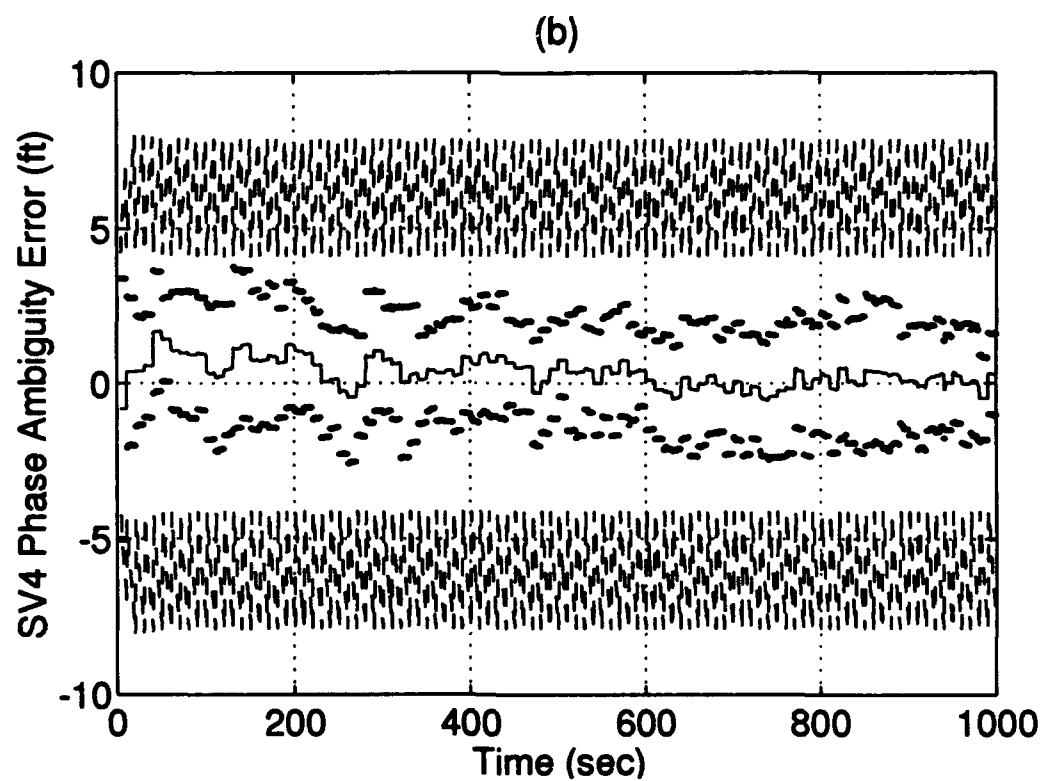**Plot J-6:** RRS Range bias/Velocity bias/Atmospheric propagation delay Errors
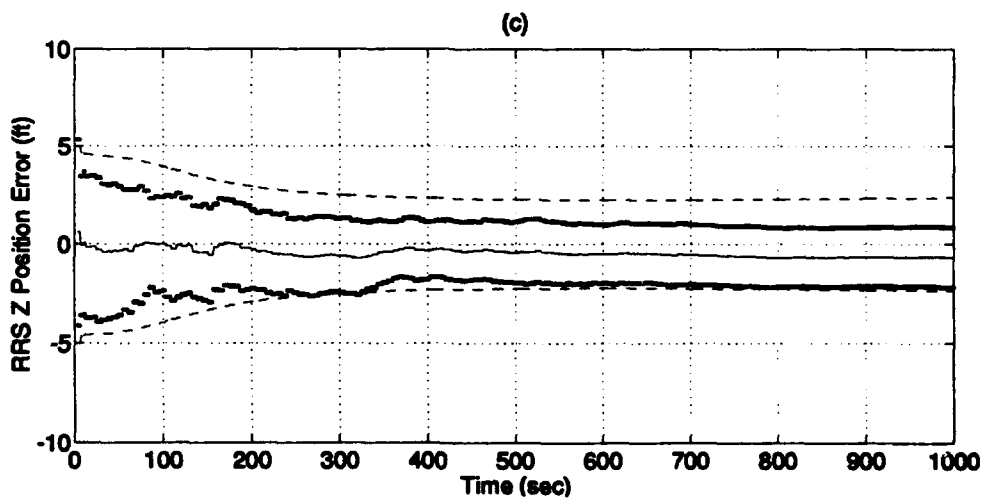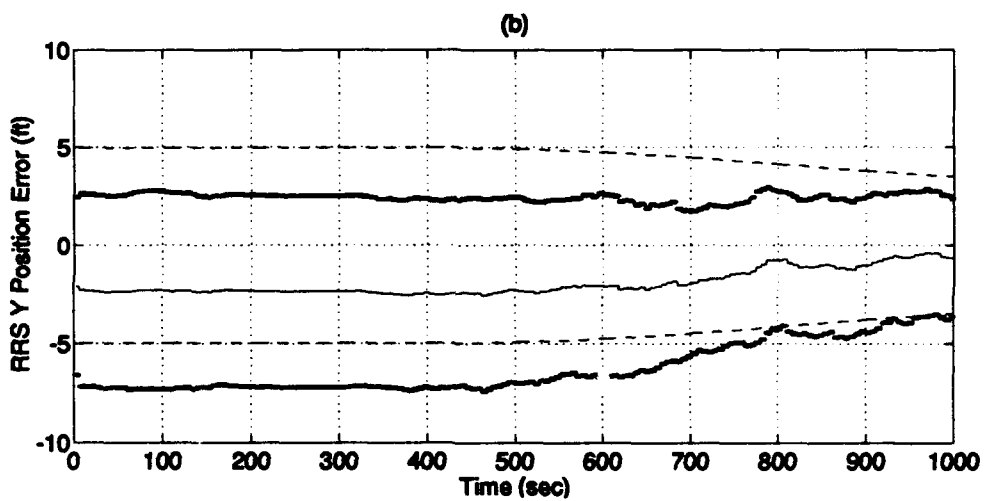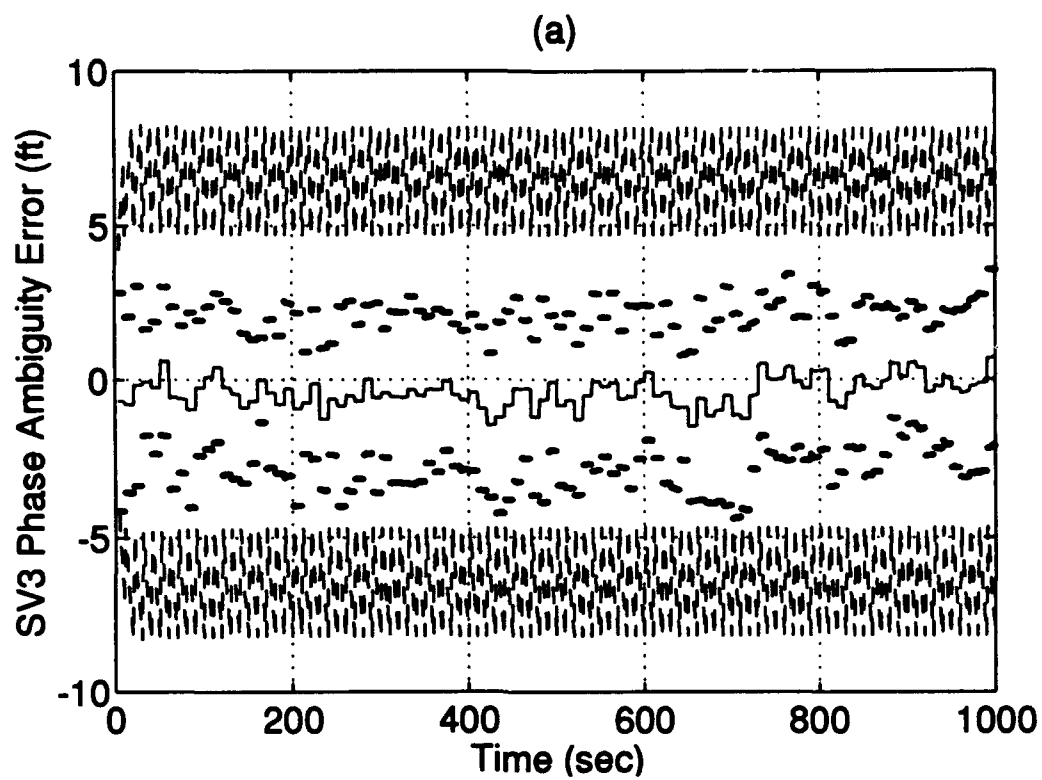
Plot J-7: RRS X/Y/Z Surveyed Position Errors

(a)

(b)

Plot J-8: GPS User Clock Bias/Drift Errors

Plot J-9: GPS Satellite 1 and 2 Phase Ambiguity Errors

Plot J-10: GPS Satellite 3 and 4 Phase Ambiguity Errors

Bibliography

1. Negast, William Joseph. *Incorporation of Differential Global Positioning System Measurements Using an Extended Kalman Filter for Improved Reference System Performance.* MS Degree Thesis, AFIT/GE/ENG/91D-41. School of Engineering, Air Force Institute of Technology (AU), Wright-Patterson AFB OH, December 1991.

2. Solomon, Joseph K. *Development of the Extended Kalman Filter for Advanced Completely Integrated Reference Instrumentation System (CIRIS).* MS Degree Thesis, AFIT/GE/89M-8. School of Engineering, Air Force Institute of Technology (AU), Wright-Patterson AFB OH, March 1989.

3. Snodgrass, Faron Britt. *Continued Development and Analysis of a New Extended Kalman Filter for the Advanced Completely Integrated Reference Instrumentation System (CIRIS).* MS Degree Thesis, AFIT/GE/90M-5. School of Engineering, Air Force Institute of Technology (AU), Wright Patterson AFB OH, March 1990.

4. Stacey, Richard D. *A Navigation Reference System (NRS) Using Global Positioning System (GPS) and Transponder Aiding.* MS Degree Thesis, AFIT/GE/91M-04. School of Engineering, Air Force Institute of Technology (AU), Wright Patterson AFB OH, March 1991.

5. Carlson, Neal and Stanton Musik. *User's Manual for a Multimode Simulation for Optimal Filter Evaluation (MSOFE).* AFWAL-TR-88-1138, Wright-Patterson AFB OH: Avionics Lab, AFWAL/AARN-2, April 1990.

6. Canadian GPS Associates. *Guide to GPS Positioning.* ISBN: 0-920-114-73-3, Fredericton, New Brunswick: University of New Brunswick Graphic Services, May 1987.

7. Counselman, C.C. *Millimeter-Accuracy Satellite Navigation* Scientific report #9, 8 April 1991. Cambridge, MA: Massachusetts Institute of Technology. (AD-A237 736).

8. Mader, Gerald L. "Dynamic Positioning using GPS Carrier Phase Measurements" Manuscripta Geodaetica, 11: pp. 272-277 (1986).

9. Remondi, Benjamin W. "Global Positioning System Carrier Phase: Description and Use" Bulletin Geodesique: 59 pp. 361-377 (1985).

10. Remondi, Benjamin W. *Performing Centimeter-Level Surveys in Seconds with GPS Carrier Phase: Initial Results* NOAA Technical Memorandum NOS NGS-43, October 1985. Rockville, MD.

11. Lachapelle, G. and M Casey. "Use of Phase Data for Accurate Differential GPS Kinematic Positioning" Proceedings of Position, Location, and Navigation Symposium (1988), IEEE pp. 393-398

12. Dance, Scott D. and CIGTF staff. Personal Interviews. Intermetrics Inc., Hollomon A.F.B., NM, June and September 1993.

13. Maybeck, Peter S. *Stochastic Models, Estimation, and Control,* Volume 1. San Diego, CA: Academic Press, 1979.

14. Maybeck, Peter S. *Stochastic Models, Estimation, and Control,* Volume 2. San Diego, CA: Academic Press, 1982.

15. Maybeck, Peter S. *Stochastic Models, Estimation, and Control,* Volume 3. San Diego, CA: Academic Press, 1982.

16. Litton Guidance and Control Systems. *Performance Accuracy (Truth Model/Error Budget) Analysis for the LN-93 Inertial Navigation Unit.* DID No. DI-S-21433 B/T:CDRL No. 1002. Woodland Hills, CA, Jan 1985.

17. Lewantowicz, Zdzislaw H. and Danny W. Keen. "Graceful Degradation of GPS/INS Performance With Fewer Than Four Satellites", *The Institute of Navigation, National Technical Meeting* (Jan 1991).

18. Vasqez, Juan R. *Detection of Spoofing, Jamming, or Failure of a Global Positioning System (GPS).* MS Degree Thesis, AFIT/GE/92D-37. School of Engineering, Air Force Institute of Technology (AU), Wright Patterson AFB OH, December 1992.

19. Mosle, William B. *Detection, Isolation, and Recovery of Failures in an Integrated Navigation System.* MS Degree Thesis, AFIT/GE/93D-28. School of Engineering, Air Force Institute of Technology (AU), Wright Patterson AFB OH, December 1993.

20. Martin, E. H. "GPS User Equipment Error Models." In Janiczek, P. M., editor. *Global Positioning System,* Washington, D. C.: The Institute of Navigation, 1980.

21. Navtech Seminars Inc., "Dynamic Differential GPS", Notebook from Course 311, Alexandria, VA, Dec 1989.

22. Leick, Alfred. *GPS Satellite Surveying*, John Wiley & Sons Inc., 1990. ISBN 0-471-81990-5

23. Van Graas, Frank. Personal Interviews. Ohio University Department of Electrical Engineering, Athens, OH, September 1993.

24. GE-90D, EEng 735 Class. *GPS Aided LN-93 INS*. EEng 735 Class Project Final Report, School of Engineering, Air Force Institute of Technology (AU), Wright Patterson AFB OH, May 1990.

25. Cox Jr., D. B. "Integration of GPS with Inertial Navigation Systems", *Global Positioning System*, Papers Published in *Naviagtion: Journal of the Institute of Navigation*, pages 144-153 (1980).

Vita

Captain Neil Hansen was born on July 26, 1965 in Chatham, New Brunswick (Canada). As what is affectionately known as a "base-brat", he has moved many times and has lived in such places as Montreal, Ottawa, Cold Lake (Alberta), Germany, and Belgium. He graduated from Grand Centre High School (located in Cold Lake, Alberta) in 1983 and moved to Edmonton, Alberta to attend the University of Alberta. He graduated from university in 1987 with a degree in Electrical Engineering. He was accepted out of university into the Canadian Forces as an Aerospace Engineering Officer and, after a year and a half in training systems, received his first assignment at the Aerospace Engineering Test Establishment (AETE) in CFB Cold Lake, Alberta, as a Flight Test Instrumentation Engineer. In 1992, he was selected for post-graduate training and was accepted to the Air Force Institute of Technology, Guidance and Control sequence. In December of 1993, he graduated from AFIT with a Masters of Science degree in Electrical Engineering. Following AFIT, he was assigned to the Director General of Aircraft Engineering and Maintenance (DGAEM), National Defence Headquarters (NDHQ), Directorate of Avionics, Simulators, and Photography (DASP), located in Ottawa, Ontario. He also worked for the 6 months following graduation (on Temporary Duty) at the Central Inertial Guidance Test Facility (CIGTF), Hollomon AFB, New Mexico.

REPORT DOCUMENTATION PAGE

1. AGENCY USE ONLY (Leave blank)	2. REPORT DATE	3. REPORT TYPE AND DATES COVERED
	December 1993	Master's Thesis

4. TITLE AND SUBTITLE

Incorporation of Carrier Phase Global Positioning System Measurements into the Navigation Reference System for Improved Performance

5. FUNDING NUMBERS

6. AUTHOR(S)

Neil Peter Hansen, Captain, Canadian Forces (Air)

7. PERFORMING ORGANIZATION NAME(S) AND ADDRESS(ES)

Air Force Institute of Technology, Wright-Patterson AFB, OH, 45433-6583

8. PERFORMING ORGANIZATION REPORT NUMBER

AFIT/GE/ENG/93D-40

9. SPONSORING / MONITORING AGENCY NAME(S) AND ADDRESS(ES)

46th Test Wing, Holloman AFB, NM, 88330-5000

10. SPONSORING / MONITORING AGENCY REPORT NUMBER

11. SUPPLEMENTARY NOTES

12a. DISTRIBUTION / AVAILABILITY STATEMENT

Approved for public release; distribution unlimited

12b. DISTRIBUTION CODE

13. ABSTRACT (Maximum 200 words)

In order to quantify the performance and accuracy of existing navigation systems, the U.S. Air Force has been using the Completely Integrated Reference Instrumentation System (CIRIS) as a baseline. CIRIS combines information from an inertial navigation unit, a barometric altimeter, and a range/range-rate system of ground transponders to obtain a navigation solution. This research explores the possibilities of enhancing CIRIS by adding measurements obtained from the Global Position System (GPS). Pure pseudorange measurement updates to the CIRIS Extended Kalman Filter form the basis of the Navigation Reference System (NRS). Applying differential corrections to the pseudorange measurements forms the basis of the Enhanced Navigation Reference System (ENRS). The addition of Carrier-Phase GPS measurements to the ENRS forms the basis of the Precision Navigation Reference System (PNRS). Analysis of these three systems is performed using a software package known as Multimode Simulation for Optimal Filter Evaluation (MSOFE). The performance of the three filters are compared as well as the PNRS's performance when subjected to cycle slips. Results of the simulations indicate that the PNRS can provide an improved navigation solution over CIRIS, the NRS, and the ENRS and the filter is stable for large cycle slips and small cycle slips are negligible.

14. SUBJECT TERMS

Carrier Phase, Cycle Slip, Differencial GPS, Global Positioning System, GPS, Kalman Filter, Navigation Reference System, MSOFE, Integration.

15. NUMBER OF PAGES

216

16. PRICE CODE

17. SECURITY CLASSIFICATION OF REPORT	18. SECURITY CLASSIFICATION OF THIS PAGE	19. SECURITY CLASSIFICATION OF ABSTRACT	20. LIMITATION OF ABSTRACT
Unclassified	Unclassified	Unclassified	UL